Variability in the Polar Vortex and its Interaction With the Climate System



Oscar B. Dimdore-Miles

Hertford College

University of Oxford

A thesis submitted for the degree of

Doctor of Philosophy

October 2021

Abstract

Variability in the strength of the Northern Hemisphere stratospheric polar vortex is an important climate feature. Strong vortex conditions, as well as disruptions of the vortex, known as sudden stratospheric warmings (SSW), are associated with significant tropospheric and surface variations. This makes them an important feature for improving the skill of seasonal weather forecasts. This thesis addresses some ongoing research questions regarding the nature of variations in the polar vortex and their interactions with the wider climate system.

First, multi-decadal variability of SSW events is examined in a 1000-yr pre-industrial simulation of a coupled global climate model. A wavelet spectral decomposition method shows that hiatus events (intervals of 5 years or more with no SSWs) and consecutive SSW events (extended intervals with at least one SSW in each year) vary on multi-decadal timescales with the most persistent spectral feature appearing at a period of 90 years. This long-term SSW variability is found to be associated with similar variations in amplitude and vertical coherence of the stratospheric quasi-biennial oscillation (QBO), likely via the well-known Holton-Tan link where the QBO has an in-season influence over the vortex.

Interactions between multi-decadal variability in vortex strength and modes of surface and ocean variability are subsequently examined. Intervals that exhibit persistent anomalous vortex behaviour are found to lead to oscillatory responses in the Atlantic Meridional Overturning Circulation (AMOC). These AMOC responses peak in magnitude at lags of 2-3 years and ∼17 years following the vortex anomalies. The vortex-AMOC interaction is characterised by non-stationary variations at periods of 30 and 50 years and involves a corresponding modulation of the North Atlantic Oscillation (NAO). Using the relationship between persistent vortex behaviour and the AMOC response established in the model, the contribution of the observed 8-year SSW hiatus interval in the 1990s to the recent negative trend in AMOC observations is estimated. This analysis suggests that approximately 30% of the trend may have been caused by the SSW hiatus. The AMOC is also found to vary on longer timescales, similar to the 90-year SSW variability, but this periodicity is not present in the NAO signal. An additional mechanism is proposed where long-term variations in the AMOC influence the vortex via a pathway involving the equatorial Pacific and QBO.

Finally, the role that vertical coherence in the QBO plays in its teleconnections is investigated using a set of climate model experiments that impose a perpetually deep and shallow QBO. While the magnitude of the vortex and surface responses to the QBO is significantly larger in the deep QBO experiment compared to the shallow experiment, they are of the opposite sign to those shown in previous work. The origin of these unexpected responses is explored, and the perpetual deep QBO is shown to induce unrealistically large anomalies in the equatorial semi-annual oscillation (SAO). The discrepancy is consistent with a modulation of the vortex and surface response from the SAO region, but showing this explicitly is challenging. Further experiments with imposed SAO conditions, as well as the QBO, are proposed to help establish the true nature of these teleconnections.

Acknowledgements

Foremost thanks must go to to my supervisors, Lesley Gray and Scott Osprey. Your generosity, technical advice and personal guidance over the past four years has been unrivalled. Lesley - your belief in my ability and understanding of some of my struggles has had more of a positive effect on my life than you probably know. Scott - your laughter, energy and enthusiasm for research is truly infectious. I can safely say I wouldn't have made it anywhere near this point had it not been for the two of you, thank you both.

Thanks also goes to those at AOPP and beyond, especially other members of the Stratosphere and Climate group, for engaging discussions that shaped the research in this thesis - Matt Brown, Jorge Garcia-Franco, Josh Dorrington, Helena Cotterill, Beatriz Monge-Sanz, Stergios Misos, Matt Patterson, Tim Woolings, Blanca Ayarzagüena as well as many others. I am also grateful for the NERC DTP in environmental research for funding my project.

Thanks must also go...

to my mum and dad, my grandparents, Harri and Georgia for your unwavering support and belief (and bringing Cassie to visit).

to Ella, Louis and Hamish for being fantastic housemates at 47 Oatlands Road and for your companionship through the highs and lows of a PhD.

to Cameron, Josh and Ben for the fantastic years studying at the University of Edinburgh, for giving me the confidence to continue in physics and for always providing an outlet to vent my frustrations with the subject.

to Hertford college CC and RFC for four fantastic seasons and to OPCC for providing a weekly lifeline through which I could temporarily forget the mental stress of my PhD and focus on the mental stress of having to bat every Saturday.

Contents

List of acronyms and abbreviations **13**

1 Introduction **15**
1.1 Overview and aims 15
1.2 Relation to published work 17
1.3 Thesis structure 18

2 Background **19**
2.1 The stratospheric polar vortex 20
2.2 Atmospheric waves 22
2.2.1 Other atmospheric waves 27
2.3 Sudden Stratospheric Warmings 28
2.4 The equatorial stratosphere 32
2.5 External influence on the vortex 36
2.5.1 The Holton-Tan effect 37
2.5.2 The Aleutian Low 38
2.5.3 ENSO and tropical SSTs 39
2.6 Downward influence of the vortex 41
2.6.1 The Northern Annular Mode 41
2.6.2 Tropospheric and surface variability 43
2.7 Multi-decadal climate variability 46
2.7.1 Atlantic variability 46
2.7.2 Pacific variability 49

3 Origins of multi-decadal variability in sudden stratospheric warming events 51
3.1 Introduction . . . 51
3.2 Data and methods . . . 54
3.2.1 Model configuration . . . 54
3.2.2 Reanalysis data . . . 55
3.2.3 Wavelet analysis . . . 58
3.2.4 Cross wavelet spectra . . . 61
3.2.5 Hilbert transform . . . 62
3.2.6 Statistical methods . . . 63
3.2.6.1 Student's t-test . . . 63
3.2.6.2 Correlation analysis . . . 64
3.2.6.3 Linear regression analysis . . . 64
3.2.6.4 EOF analysis . . . 66
3.2.6.5 SSW statistics . . . 67
3.2.7 Model diagnostics . . . 69
3.3 Modes of stratospheric variability . . . 70
3.4 Regression analysis . . . 79
3.5 Long-term variability of the polar vortex . . . 81
3.6 Surface forcing of polar vortex variability . . . 85
3.7 Vortex-QBO interactions . . . 91
3.8 Summary and discussion . . . 98

4 Interactions between the stratospheric polar vortex and Atlantic circulation 105
4.1 Introduction . . . 105
4.2 Data And methods . . . 108
4.2.1 Model configuration and observation data . . . 108
4.2.2 Model diagnostics . . . 109
4.3 In-season surface responses to anomalous vortex events . . . 113
4.4 Surface impacts of persistent vortex anomalies . . . 116
4.5 Response to strong and weak vortex intervals . . . 121
4.6 Non-stationary variability . . . 124
4.7 Surface forcing of the stratosphere . . . 130
4.8 Contribution of the stratosphere to recent AMOC changes . . . 134
4.9 Sensitivity to NAM thresholds and filtering . . . 140
4.10 Summary and discussion . . . 148

5 The role of vertical structure in QBO teleconnections 153
5.1 Introduction 153
5.2 Model configuration 156
5.2.1 Nudging 158
5.3 QBO characteristics 162
5.4 Other atmospheric characteristics 166
5.5 Surface responses to deep and shallow QBOs 170
5.6 Vortex responses to the QBO 174
5.7 The role of the SAO region 184
5.8 Results in the context of previous work 190
5.9 Summary and discussion 195

6 Conclusions 201
6.1 Summary of results 201
6.2 Limitations and further investigations 205

Bibliography 211

List of Figures

2.1 climatological ZMZW and seasonal cycle in the vortex (ERA-Interim) 21
2.2 10 hPa NH GPH for a stable, split and displaced vortex (ERA-Interim) 30
2.3 Equatorial ZMZW from ERA-Interim 32
2.4 Schematic of equatorial wave-mean flow interactions 34
2.5 Arctic Oscillation surface pattern NCEP/NCAR reanalysis 43
2.6 Composites of the NAM about anomalous vortex events in ERA40 . . 44

3.1 Channel profiles for satellite retrievals assimilated by ERA-Interim . . 57
3.2 SSWs per NH winter season in the UKESM pi-control 71
3.3 Vortex ZMZW and SSW time series from UKESM pi-control 73
3.4 Time-height profiles for equatorial ZMZW from the UKESM pi-control 74
3.5 ZMZW composite differences between QBO phases in the pi-control. . 76
3.6 Histogram of SSWs per winter in different QBO phases. 77
3.7 ZMZW anomaly composites for different phases of ENSO and the AL 79
3.8 Wavelet power spectrum for the SSW per NH winter time series . . . 82
3.9 Wavelet power spectrum for Dec-Mar 5-year mean SSW time series . 83
3.10 Wavelet power spectrum of Nov-Mar 5-year mean SSW time series) . 85
3.11 Wavelet spectrum of 5-year smoothed Niño3.4 index 86
3.12 Wavelet power spectrum of the Niño3.4 index 87
3.13 Wavelet power spectra of tropical basin SST indices. 88
3.14 Wavelet power spectrum for 5-year smoothed AL index 89
3.15 Wavelet power spectrum for 5-year smoothed PDO index 91
3.16 Wavelet cross power spectrum between AL index and SSW time series 91
3.17 QBO time series and associated wavelet power spectra 92
3.18 QBO amplitude time series and associated wavelet power spectra . . 94
3.19 Wavelet spectra for the deep QBO amplitude 95
3.20 cross-spectrum of deep QBO amplitude and low rate SSW_{5yr} 97

4.1 Surface response patterns to anomalous NAM_{10} events. 115
4.2 NAM_{10} and Gaussian smoothed NAM_{10} time series 117
4.3 Lagged response of the AMOC index to persistent NAM_{10} intervals. . 118

4.4 Lagged response of the NAO, heat flux and ocean T to NAM_{10} intervals. 120
4.5 Lagged responses to strong and weak NAM_{10} intervals 123
4.6 Wavelet power spectrum of smoothed NAM_{10} index 125
4.7 Wavelet power spectrum of the AMOC at 50°N 127
4.8 Wavelet power spectrum of the AMOC at 30°N 128
4.9 Wavelet power spectrum of the AMOC at 45°N 128
4.10 Wavelet power spectrum of the NAO 129
4.11 Power spectra for the QBO amplitude and associated surface metrics 132
4.12 Time series of NAO, NAM_{10} and AMOC from the ERA5 and RAPID 135
4.13 Regression of NAM_{10} extreme magnitude vs AMOC anomaly at 50°N 137
4.14 PDFs for NAM_{10} extreme vs lagged AMOC correlation 138
4.15 Regression of NAM_{10} extreme magnitude vs AMOC anomaly at 30°N 140
4.16 σ/threshold/lag parameter grids for AMOC responses to NAM_{10} intervals 143
4.17 PDFs for strong NAM_{10} extreme vs AMOC for different σ/threshold . 145
4.18 PDFs for weak NAM_{10} extreme vs AMOC for different σ/threshold . 147

5.1 Idealised QBO winds used for nudging experiments 161
5.2 Equatorial ZMZW time-height profiles from QBO experiments 163
5.3 Equatorial ZMZW and nudging winds from the deep QBO 165
5.4 Equatorial ZMZW and nudging winds from the shallow QBO 166
5.5 Climatological seasonal cycle of the SAO in QBO experiments 168
5.6 SSWs per NH winter season in QBO experiments 169
5.7 MSLP composites under QBO phases in the pi-clim cntrl simulation . 171
5.8 MSLP composites under QBO phases in the deep QBO simulation . . 173
5.9 MSLP composites under QBO phases in the shallow QBO simulation 174
5.10 ZMZW composites under QBO phases in the pi-clim cntrl simulation 176
5.11 ZMZW composites under QBO phases in ERA-Interim 178
5.12 ZMZW composites under QBO phases in the deep QBO simulation . 180
5.13 ZMZW composites under QBO phases in the shallow QBO simulation 181
5.14 EP flux composites under QBO phases in the deep QBO simulation . 183
5.15 Equatorial ZMZW anomaly time-height profiles from QBO experiments 185
5.16 ZMZW composites under easterly and westerly SAO anomalies 187
5.17 EP flux composites under USLM QBO phases (deep QBO simulation) 189
5.18 MSLP composites under 50 hPa QBO phases in the pi-control simulation 191
5.19 MSLP composites under deep QBO phases in the pi-control simulation 192
5.20 ZMZW composites under QBO phases in the pi-control simulation . . 194

List of acronyms and abbreviations

AL Aleutian Low
AMOC Atlantic Meridional Overturning Circulation
AMV Atlantic Multidecadal Variability
AO Arctic Oscillation
BDC Brewer Dobson Circulation
CMIP3 Coupled Model Intercomparison Project Phase 3
CMIP6 Coupled Model Intercomparison Project Phase 6
CMIP5 Coupled Model Intercomparison Project Phase 5
CP Central Pacific
EastP East Pacific
ECMWF European Centre for Medium-Range Weather Forecasts
ENSO El Niño–Southern Oscillation
EOF Empirical orthogonal function
EP Eliassen-Palm
ERA-interim ECMWF Reanalysis-Interim dataset (1979–2019)
ERA5 5th ECMWF Reanalysis-Interim dataset (1979–2019)
GCM General circulation model
HT Holton-Tan
MSLP Mean sea-level pressure
NA North Atlantic
NAM Northern annular mode
NAO North Atlantic oscillation
NH North Hemisphere
PDO Pacific Decadal Oscillation (pattern)
PNA Pacific-North American (pattern)
PV Potential vorticity
QBO Quasi-biennial oscillation
QG Quasi-geostrophic
QGPV Quasi-geostrophic Potential vorticity
SAO Semiannual Oscillation
SH Southern Hemisphere

SST Sea Surface Temperature
SSW Sudden stratospheric warming
TEM Transformed Eulerian-mean
UKESM UK Earth System Model
USLM Upper stratosphere/ lower mesosphere

CHAPTER 1

Introduction

1.1 Overview and aims

There is a variety of reasons that the Northern Hemisphere (NH) stratospheric polar vortex warrants significant scientific study. Variations in its strength, particularly disruption events known as Sudden Stratospheric Warmings (SSWs), are among the most dramatic dynamical events observed in the Earth's atmosphere. They also play an important role in stratosphere-troposphere coupling as they both respond to and influence variations in surface weather and climate. Despite significant developments in the understanding of vortex variability in the last three decades, some key features of this phenomenon are still not fully explained. Namely:

- The nature of variability in the strength of the vortex, including the frequency of SSWs, is yet to be fully diagnosed. This is particularly an issue when considering variations on decadal to multi-decadal timescales.
- the full extent of interactions between the vortex and other parts of the climate system such as the equatorial stratosphere, troposphere, surface and ocean is

also not understood.

These are significant and ongoing issues in the field. Research efforts are often hampered by the limited observational record and works rely heavily on state of the art climate models for diagnosis of climate behaviour. While it is beyond the remit of this work to provide comprehensive resolutions to these issues, this thesis aims to contribute to the understanding of variability in polar vortex strength on multiple timescales as well as the role such variability plays in coupling between the vortex and other parts of the climate system. This understanding is not only motivated by scientific curiosity. Vortex variations and SSWs play a key role in seasonal to sub-seasonal forecasts of NH weather [*Scaife et al.*, 2016]. As a result, an improved understanding of their variability and coupling could aid in improving predictability of the climate system. The primary original contributions to this field of study contained in this thesis are as follows:

- Chapter 3 considers multidecadal variability in the occurrence of SSW events in a 1000 year pre-industrial control simulation of a coupled general circulation model (GCM). A wavelet spectral decomposition analysis is utilised to identify non-stationary periodic variations in events corresponding to periods around 90 years as well as less persistent signals at 60-year scales. Possible origins for this variability are examined and it is shown that similar variations in the amplitude and vertical coherence of the equatorial winds, the Quasi-Biennial Oscillation (QBO), are likely driving signals in SSWs. This represents a potential novel source of predictability of SSW events.

- Chapter 4 considers the influence of multi-decadal vortex variations found in chapter 3 on surface variability with a particular focus on low-frequency modes in the North Atlantic region. Co-variations are found between the appearance of intervals of winters which exhibit the same type of anomalous behaviour (strong

or weak) and the Atlantic Meridional Overturning Circulation (AMOC) on 50 and 30 year timescales. This interaction appears to involve a pathway through the vortex's influence over tropospheric circulation and the North Atlantic Oscillation. This result builds on previous work suggesting a similar connection and demonstrates the key role non-stationarities may play in the teleconnection. It also suggests a potentially key role of the stratosphere in recent observed trends in the AMOC.

- Chapter 5 presents an analysis of the role that vertical coherence in the Quasi-Biennial Oscillation plays in its teleconnections using a set of relaxation experiments. A GCM simulation which imposes a high degree of vertical coherence in the QBO exhibits larger responses in the polar vortex and surface than other simulations. However, these surface and vortex responses are of opposite sign to those shown by numerous previous works. The origin of these unexpected patterns in the simulation is investigated and a key role for the winds in the upper stratosphere / lower mesosphere (USLM) is suggested. In this case, unrealistically large USLM anomalies and their influence over teleconnections may obscure other pathways involved although this is difficult to show explicitly. Further GCM experiments which rectify these issues with the USLM are required to isolate the precise mechanisms involved in QBO teleconnections.

1.2 Relation to published work

Chapter 3 broadly corresponds to a paper written by myself, Lesley Gray and Scott Osprey and published in Weather and Climate Dynamics [*Dimdore-Miles et al.*, 2021a]. However, the analysis presented here includes an extension to the published work and has been rewritten for inclusion in this thesis. Chapter 4 corresponds to *Dimdore-Miles et al.* [2021b], a paper written by myself, Lesley Gray, Scott Osprey, Jon Robson, Bablu

Sinha and Rowan Sutton which is currently under review in Atmospheric Chemistry and Physics. A paper based on the work in chapter 5 is currently being constructed and will hopefully be submitted in the near future. In all papers, I conducted the analysis, was in charge of all writing and generated all figures. I am extremely grateful to all my co-authors for their input and comments during the writing of these papers as well as all those involved in reviewing both works (all of whom are anonymous).

1.3 Thesis structure

Chapter 2 presents a background overview of middle atmospheric dynamics and the variability in the polar and equatorial stratosphere including SSWs and the QBO. This includes the current understanding of these modes and their interactions as well as their variability on decadal to multi-decadal timescales. It also outlines some of the key features of current understanding of stratosphere-troposphere coupling. This includes interactions between the stratosphere and the North Atlantic Oscillation, Aleutian Low, El Niño Southern Oscillation as well as oceanic modes such as the Atlantic Meridional Overturning Circulation. Results from the original analysis summarised above are presented in chapters 3, 4 and 5. These chapters also include an outline of the analysis tools and data utilised in each investigation. Conclusions, as well as possible further work, are presented in chapter 6.

CHAPTER 2

Background

The Stratosphere is a layer of the Earth's atmosphere characterised by increasing temperatures with height. This feature distinguishes it from the lowest layer of the atmosphere, the troposphere, and makes it stable to vertical convection. As a result, the stratosphere exhibits significantly different dynamical behaviour to the troposphere. The stratosphere is bounded by the tropopause from below and the stratopause above. The height of these bounds varies latitudinally with tropopause heights ranging from $\sim$17-18km at the equator to $\sim$6km near the polar regions. While the stratosphere and troposphere are characterised separately, current understanding of atmospheric dynamics incorporates elements of coupling between the layers. This chapter outlines the key points of this understanding including dynamics of the polar and equatorial stratosphere, stratosphere-troposphere coupling as well as surface variability relevant to the stratosphere. It also introduces the time variability of dynamical features in the stratosphere, a key theme in the work presented in this thesis.

2.1 The stratospheric polar vortex

During Northern Hemisphere (NH) winter, the NH polar stratosphere is plunged into polar night. As a result, it experiences a net cooling effect through the emission of longwave infrared radiation to space and the absence of shortwave solar radiation available for absorption. This significant cooling increases the meridional temperature gradient ($\frac{\partial T}{\partial y}$) between the polar region and the tropics. This causes an increase in the vertical shear of zonal wind according to the thermal wind balance relation,

$$\frac{\partial u_g}{\partial z} = -\frac{R}{fH}\frac{\partial T}{\partial y}, \tag{2.1}$$

where u_g is the geostrophic zonal wind velocity (the wind resulting in a balance between Coriolis and pressure gradient forces), z is the height coordinate, R is the specific gas constant ($R = 8.31 JK^{-1}mol^{-1}$) and H is the atmospheric scale height, the gain in altitude which leads to a reduction in atmospheric pressure by a factor of e given by $H = RT_r/g$ (g = acceleration due to gravity and T_r is a reference temperature). f in equation 2.1 is the Coriolis parameter under a beta plane approximation which is given by

$$f = f_0 + \beta y = 2\Omega sin(\phi_0) + 2\Omega cos(\phi_0)\frac{y}{a}, \tag{2.2}$$

where ϕ_0 is a reference latitude, Ω is the rotation rate of the Earth and a is the Earth's radius. This increase in vertical shear in u_g leads to a strong, stratospheric, westerly flow circumnavigating the North Pole during boreal winter months. This feature is known as the NH polar vortex or polar night jet. Henceforth we refer to this feature as simply "the vortex".

The vortex contains a core of cold polar air in which temperatures can drop to around 200K in the lower stratosphere according to the European Centre for Medium

Range Weather Forecasting (ECMWF) interim reanalysis data set (referred to as ERA-Interim, *Uppala et al.* [2005]). Wintertime zonal wind speeds are found to reach up to approximately $70ms^{-1}$ on the 10 hPa level at a latitude of 60°N. Figure 2.1a shows the climatological zonal mean (averaged over all longitudes) zonal wind (ZMZW) from ERA-Interim for the December-February period. It exhibits the traits set out above with a persistent zonal westerly wind above the 30 hPa level and northward of ∼20°N. The troposphere exhibits two subtropical westerly jets which show lower peak magnitude winds of around $30ms^{-1}$ on approximately 90 hPa level. Also included is figure 2.1b showing the seasonal cycle in daily winds at 60°N on the 10 hPa level (near the edge of the vortex). On average, the vortex forms in early September and breaks down to be replaced with summer easterlies in mid-April. These winds show a large degree of variability across different seasons (figure 2.1b, faint blue lines) with some seasons exhibiting anomalously strong westerly flow and others even exhibiting easterlies for a portion of the season. These effects are due to the action of atmospheric waves on the vortex and are described fully in the following section.

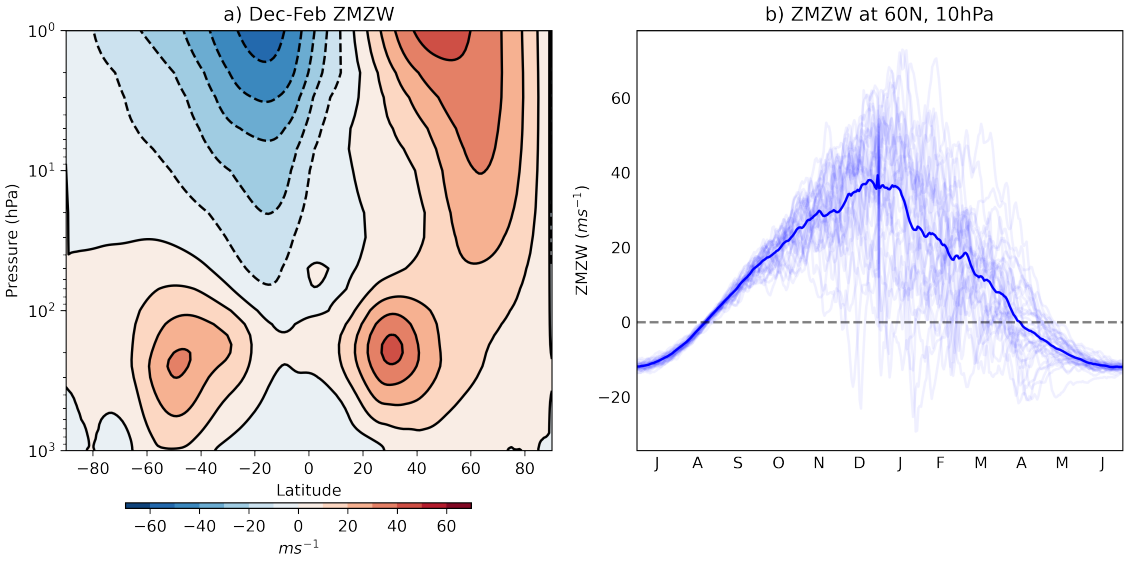


Figure 2.1: **a**: Dec-Feb climatological ZMZW, the zonal wind averaged over all longitudes, from ERA-Interim dataset between 1979 and 2018. **b**: Seasonal cycle in ZMZW at 60°N on the 10 hPa level from the same dataset. The thick blue line indicates the seasonal cycle and faint blue lines signify winds from individual years.

2.2 Atmospheric waves

Atmospheric wave is the term generally used for deviations from the zonal mean dynamical state and these phenomena, often referred to as Rossby waves, play a key role in the variability of the vortex. These waves are generated in the troposphere when air flowing over variations in topography (orographic waves) or through other mechanisms such as interactions with convection fronts and latent heat release (non-orographic waves) deviate from purely zonal flow. Variations in the Coriolis parameter with latitude act as a restoring force thus generating wave disturbances. Perturbations originating near the surface can propagate vertically into the stratosphere altering large scale circulation features via wave drag as they transfer momentum to the background flow.

Large scale Rossby waves are known as planetary waves and exhibit wavelengths of the order of $\sim 1000km$. The propagation of these waves can be described using the quasi-geostrophic (QG) approximation for fluid in hydrostatic balance with low (< 0.1) Rossby number, $R_0 = U/f_0L$, where U and L are characteristic zonal velocity and length scales respectively. Under this framework, the quasi-geostrophic potential vorticity (QGPV) equation states that in the absence of friction and diabatic heating, the QGPV, q, is conserved following the geostrophic wind [*Andrews et al.*, 1987]. I.e.

$$D_g q = 0, \tag{2.3}$$

where D_g is the operator,

$$D_g = \frac{\partial}{\partial t} + u_g \frac{\partial}{\partial x} + v_g \frac{\partial}{\partial y}, \tag{2.4}$$

and q can be written in terms of the stream function, ψ, in the QGPV framework as

$$q = f_0 + \beta y + \nabla^2\psi + \frac{\partial}{\partial z}\left(\frac{f_0^2}{N^2}\frac{\partial\psi}{\partial z}\right), \tag{2.5}$$

where N is the Brunt–Väisälä frequency, the frequency of vertical motion of a parcel of air in a stable atmosphere given by $N^2 = \frac{g}{\theta_0}\frac{\partial\theta}{\partial z}$ [1]. ψ is related to u_g and v_g, the zonal and meridional components of geostrophic wind by $u_g = -\frac{\partial\psi}{\partial y}$ and $v_g = -\frac{\partial\psi}{\partial x}$. Under a further approximation of small disturbances from a uniform zonal flow, $\overline{u}$, ψ is given by

$$\psi = -\overline{u}y + \psi', \tag{2.6}$$

where ψ' is the contribution to the stream function from the small deviation from $\overline{u}$. This approximation allows equation 2.5 to be linearised to

$$\left(\frac{\partial}{\partial t} + \overline{u}\frac{\partial}{\partial x}\right)\Gamma\psi' + \beta\frac{\partial\psi'}{\partial x} = 0, \tag{2.7}$$

where Γ is the operator

$$\Gamma = \nabla^2\psi + \frac{\partial}{\partial z}\left(\frac{f_0^2}{N^2}\frac{\partial}{\partial z}\right). \tag{2.8}$$

It can be shown that this equation has wave-like solutions whose vertical propagation is only supported if the following condition is satisfied:

$$\overline{u} - c = \frac{\beta k}{k^2 + l^2 + \frac{f_0^2 m^2}{N^2}} < \overline{u}_c = \frac{\beta k}{k^2 + l^2}, \tag{2.9}$$

[1] θ is the potential temperature, the temperature of a parcel of air of current absolute temperature, T, which is transferred adiabatically from a pressure level, p to a reference level, p_0 (usually 1000 hPa) given by $\theta = T\left(\frac{p_0}{p}\right)^{R/c_p}$ (c_p is the heat capacity of air at fixed pressure). θ_0 is a reference potential temperature.

where $\overline{u}_c$ is a critical velocity corresponding to the background flow when $m = 0$, c is the phase speed and k, l and m are the meridional, zonal and vertical wavenumbers of the wave respectively. Also imposing $m^2 > 0$ (positive vertical wavenumber), which implies that $\overline{u} - c > 0$, gives the Charney-Drazin criterion for the vertical propagation of planetary waves [*Charney and Drazin*, 1961],

$$0 < \overline{u} - c < \overline{u}_c, \tag{2.10}$$

which reduces to $0 < \overline{u} < \overline{u}_c$ for waves with 0 phase speed relative to the ground. This result implies that vertical propagation can only occur through background westerly zonal flow with a magnitude less than some critical value, $\overline{u}_c$, which depends on the horizontal wavenumbers of the wave. More specifically, equation 2.9 shows that smaller wave-numbers (larger wavelengths) favours greater propagation. As a result, the spectrum of waves propagating vertically from the troposphere to the stratosphere is dominated by disturbances of wavenumbers 1-3 (referred to as wave-n disturbances). The condition that $\overline{u} - c > 0$, which is necessary for the equality in equation 2.9 to hold, also dictates that westerly phase speed waves ($c > 0$) cannot propagate into the stratosphere under this framework.

The Charney-Drazin criterion also leads to the definition of a critical layer of the atmosphere as the layer at which the background zonal flow no longer supports propagation of a given wave (i.e. where $\overline{u} \sim \overline{u}_c$). When a wave encounters a critical layer, much of the linear dynamical behaviour proposed in equation 2.7 breaks down as the waves' amplitude grows too large to support continued propagation and it dissipates, transferring momentum to the background flow through so-called wave-mean flow interactions. These interactions are often associated with large scale responses. For example, the repeated transfer of easterly momentum from the planetary-scale Rossby waves to the background stratospheric flow in the NH requires a temperature

adjustment via the thermal wind relation (equation 2.1). This is achieved via a large-scale meridional circulation with descent at high latitudes which forms the major parts of the Brewer-Dobson circulation (BDC) [*Butchart*, 2014]. There, therefore, exists a two-way interaction between the background flow and wave disturbances in the atmosphere: the magnitude of $\overline{u}$ relative to $\overline{u}_c$ dictates the propagation of waves through the troposphere into the stratosphere and waves significantly influence the background wind upon dissipation at a critical layer.

Wave-mean flow momentum deposition, which is key for understanding stratospheric dynamical variability, can be quantified via the introduction of a variable known as the Eliassen-Palm (EP) flux. In the QG framework as above, equations for the zonal mean momentum and buoyancy (b) budget can be expressed as

$$\frac{\partial \overline{u}}{\partial t} = f_0 \overline{v} - \frac{\partial}{\partial y} \overline{u'v'} + \overline{X} \tag{2.11}$$

and

$$\frac{\partial \overline{b}}{\partial t} = -N^2 \overline{w} - \frac{\partial}{\partial y} \overline{v'b'} + \overline{Q}, \tag{2.12}$$

where the overbar denotes zonal mean quantities and deviations from this (eddy quantities) are denoted by primes. $\overline{X}$ and $\overline{Y}$ represent dissipative forces on the flow (in this case friction and diabatic heating respectively) and $\overline{u'v'}$ and $\overline{v'b'}$ represent the meridional eddy fluxes of momentum and buoyancy respectively.

In order to decouple these equations (as they both feature v'), the mean residual circulation, the difference between zonal mean flow and contributions from eddy-mean flow interactions is introduced. These are known as the Transformed Eulerian Mean (TEM) meridional and vertical velocities, denoted by $\overline{v^*}$ and $\overline{w^*}$ respectively [*Andrews*

and McIntyre, 1976]. They are expressed as

$$\overline{v^*} = \overline{v} - \frac{\partial}{\partial z}\left(\frac{\overline{v'\theta'}}{\frac{\partial\overline{\theta}}{\partial z}}\right) \tag{2.13}$$

$$\overline{w^*} = \overline{w} + \frac{\partial}{\partial y}\left(\frac{\overline{v'b'}}{\frac{\partial\overline{\theta}}{\partial z}}\right). \tag{2.14}$$

Under these transformations, the decoupled equations can be written as

$$\frac{\partial\overline{u}}{\partial t} - f_0\overline{v^*} = (\nabla \cdot F) + \overline{X} \tag{2.15}$$

and

$$\frac{\partial\overline{b}}{\partial t} + N^2\overline{w^*} = \overline{Q}, \tag{2.16}$$

where

$$F = -\overline{u'v'}\mathbf{j} + f_0\frac{\overline{v'\theta'}}{\frac{\partial\overline{\theta}}{\partial z}}\mathbf{k} \tag{2.17}$$

is the Eliassen-Palm flux which can be thought of as the flux of wave activity in the meridional and vertical directions ($\mathbf{j}$ and $\mathbf{k}$ represent unit vectors in the y and z directions) [*Andrews and McIntyre*, 1976]. These equations indicate that EP flux convergence ($\nabla \cdot F < 0$) signifies momentum transfer from eddies to the background flow via wave dissipation (e.g. when breaking occurs). Conversely, flux convergence ($\nabla \cdot F > 0$) indicates wave growth at the expense of momentum of the mean flow. Closer inspection of these TEM equations (equations 2.15 and 2.16) shows that a viable solution is $\overline{v}^* = \overline{w}^* = 0$ in the absence of wave driving and frictional forces. In a real atmosphere, these two terms are non-zero and the NH wave activity outlined above results in an induced poleward meridional and vertical downward circulation

at high latitudes balanced by upward residual transfer of air at the equator. These residual circulations form part of the BDC [*Butchart*, 2014].

2.2.1 Other atmospheric waves

In addition to planetary-scale Rossby waves outlined in previous sections, other types of waves play a vital role in stratospheric variability. Gravity waves arise due to buoyancy variations and, similarly to planetary waves, can be forced through airflow over variations in topography (orographic) or convection fronts (non-orographic). These waves exhibit length scales significantly shorter than planetary waves as well as those scales resolvable in general circulation models (GCMs). As a result of these resolution issues, their effects are parameterised in most models and appear in the dissipative force term ($\overline{X}$) in equation 2.11.

Kelvin waves are equatorially-trapped disturbances caused primarily by latitudinal variations in Coriolis term. In these regions, geostrophic balance does not apply and the waves exhibit a westerly phase velocity. Dissipation of these waves contributes westerly momentum to the background flow. Finally, Rossby-gravity waves exhibit different behaviour for small and large length scales (or horizontal wavenumber, k). For small k (large length scale), they reduce to Rossby wavelike disturbances, similar to planetary-scale Rossby waves outlined in the previous section in which variations in Coriolis parameter with latitude act as the restoring force. For large k (shorter length scales), they behave as gravity waves (those for which the restoring force is gravity). Rossby-gravity waves typically have easterly phase velocity and contribute easterly momentum to the background flow upon dissipation [*Andrews and McIntyre*, 1976].

2.3 Sudden Stratospheric Warmings

While the vortex generally exhibits strong, westerly flow over boreal winter, it can be significantly disrupted and even reversed on sub-seasonal timescales (see individual season winds on figure 2.1b). This reversal occurs due to the dissipation of planetary waves which transfer easterly momentum to the background flow. If this wave forcing is large enough such that the vortex becomes significantly disrupted (and reversed) an event known as a sudden stratospheric warming (SSW) occurs. Such events are named as they are associated with significant and rapid increases in middle atmosphere NH polar cap temperature ($\sim 50K$ over a few days) which is required following significant easterly momentum transfer to the mean flow by the thermal wind relation (equation 2.1) and achieved by the descent of air at polar latitudes, causing an adiabatic increase in temperature. These events were first observed in radiosonde data in *Scherhag* [1952]. In observation-based datasets SSWs occur at an average rate of approximately 6.2 events per decade [*Butler et al.*, 2017] and represent one of the largest modes of interannual variability in the NH stratosphere.

Matsuno [1971] was the first work to introduce a dynamical model linking the action of planetary waves and the occurrence of SSWs. The framework developed by this work is still largely accepted today and describes the mechanisms involved in the life cycle of an SSW as follows: First, a burst of planetary wave activity is generated in the troposphere through a combination of airflow over topography and interactions with convection fronts. Waves subsequently propagate into the stratosphere in accordance with the Charney-Drazin criterion (equation 2.10). When these waves encounter a critical layer (normally one which exhibits stronger westerlies than $\overline{u}_c$ as the undisturbed vortex is strong), these waves break and dissipate easterly momentum to the background zonal flow. As a result, the westerly vortex decelerates and, if stratospheric conditions are appropriate or the planetary wave activity is strong

enough, even reverses. As a result, new critical layers are formed (where $\overline{u} = 0$) at a level below that of the original reversal. Subsequent waves now dissipate and can act to reverse the background flow at this lower critical layer. This process repeats and the critical layers can descend into the lower stratosphere. Once the critical layer lies near the tropopause, planetary waves are effectively prevented from entering the stratosphere stopping further deceleration of the vortex. With wave driving of the vortex prevented, radiative cooling of the stratosphere subsequently brings polar cap temperatures back down and the strong westerly flow of the vortex recovers.

While this framework of dynamical processes involved in SSWs is relatively well accepted, there are contrasting hypotheses regarding the triggering mechanisms which initiate events. The primary mechanism suggested as the trigger is a rapid injection of wave activity from the troposphere which is large enough to significantly disrupt the vortex [*Matsuno*, 1971; *Limpasuvan et al.*, 2004; *Manney et al.*, 2009; *Nishii et al.*, 2009; *Kuttippurath and Nikulin*, 2012]. An alternative hypothesis is that the state of the stratosphere itself also plays a key role in triggering events. Many studies support this phenomenon and have shown SSWs preceded by moderate levels of wave driving from the troposphere which is subsequently amplified through non-linear resonance mechanisms with the stratospheric background flow [*Esler and Scott*, 2005; *Scott and Polvani*, 2006; *Esler and Matthewman*, 2011].

The framework of *Matsuno* [1971] provides a mechanism by which SSWs occur through the interaction between planetary waves and the zonal mean background flow. However, further studies show that as well as zonal mean disturbance, the 2D geometry of the vortex (i.e. the latitude-longitude plane on a given pressure level) is altered significantly during these events and this provides a method of event classification [*Lehtonen and Karpechko*, 2016; *Mitchell et al.*, 2011a; *Seviour et al.*, 2013]. During events, the vortex can either be displaced from its stable configuration, an example of which is provided in figure 2.2a, to one in which its centroid shifts to a lower latitude

(figure 2.2b) or split into two daughter vortices each of which exhibits a core of high PV air (figure 2.2c).

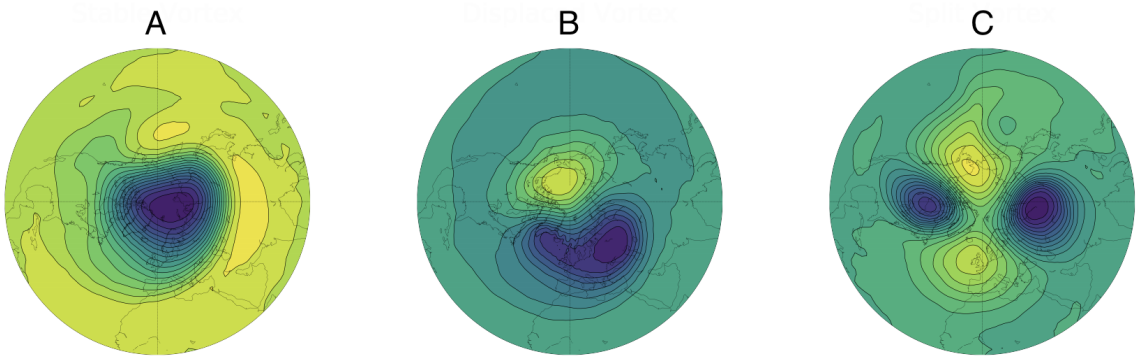


FIGURE 2.2: Geopotential Height over the NH hemisphere polar cap on the 10 hPa level from ERA-Interim showing three vortex configurations: Stable on 21/11/2008 (**A**), displaced on 22/02/2008 (**B**) and split on 24/01/2009 (**C**).

It is shown in *Seviour et al.* [2013] that the type of deformation occurring broadly depends on the wavenumber of the dominant planetary waves involved with wave-1 disturbances more associated with displacement events and wave-2 with split events. Other studies utilising this vortex geometry approach note that SSWs are preceded by planetary wave breaking on the edge of the vortex in the so-called "surf zone" which strips high PV air off the edge of the vortex thus sharpening its PV edge [*McIntyre and Palmer*, 1983]. Further works examine this phenomenon in the context of vortex preconditioning in which its geometry preceding SSWs promotes subsequent disruption. This geometry varies depending on whether the trigger for an event is considered as tropospheric wave bursts, in which case preconditions are generally a weak but westerly vortex which promotes propagation [*Nishii et al.*, 2009; *Kuttippurath and Nikulin*, 2012], or resonance with the stratospheric state in which case specific preconditions for split and displacement events are observed [*Charlton and Polvani*, 2007; *Bancalá et al.*, 2012]. The framework provided by *Matsuno* [1971] as well as insights from geometry analysis gives a picture of the processes involved in these remarkable dynamical events. The role SSWs play in two way stratosphere-troposphere coupling as well as their

links to surface variability are discussed fully in sections 2.5 and 2.6.

While many works into SSWs utilise observation-based data, the observational record is relatively short (ERA-Interim is available from 1979-2019) and GCMs remain one of the most useful tools for developing a better understanding of the nature of these events. As a result, representing SSWs realistically in models is also key to this understanding. Multi-model comparisons of representation of SSW events have shown that large scale GCMs, including Coupled Model Intercomparison Project phase 5 (CMIP5) models, reproduce the vortex well but display a large degree of variation in SSW frequency [*Butchart et al.*, 2011; *Kim et al.*, 2017]. Over the whole season, models with a well-resolved stratosphere (high top) record higher numbers of SSWs and, unsurprisingly, a mean frequency closer to that exhibited by reanalysis than those with a crude representation of the stratosphere (low top). However, there appears a significant overestimation of early winter warmings (November) in high top models compared to reanalysis [*Kim et al.*, 2017]. More recent studies utilising CMIP6 models report further variation in model SSWs and, in particular, disagreement across models in the response of SSW occurrence to anthropogenic forcing [*Ayarzagüena et al.*, 2020] which may originate from the different treatment of physical processes underlying these events. *Charlton et al.* [2007] and *Schmidt et al.* [2013] show that most GCM's struggle to obtain the correct sub-seasonal distribution of SSWs, with events occurring more uniformly across winter months compared to reanalysis in which the majority of events are recorded in January and February. The cause of this systematic bias is not well understood. A persistent problem in the past with simulating seasonal SSW distributions was the so-called "cold pole problem", with SSWs occurring too late in the season due to an overly strong early winter vortex [*Pawson et al.*, 2000; *Charlton et al.*, 2007]. This has largely been corrected by the introduction of improved gravity-wave parametrisation schemes *Garcia et al.* [2017]. However, the schemes utilised in most GCMs are still relatively simple and there is a conflict between achieving a good

representation of the polar regions (i.e. SSW frequency) and dynamical variability in the equatorial region [*Eichinger et al.*, 2020] which is outlined in the following section. Both are forced through a GCM's gravity wave scheme.

2.4 The equatorial stratosphere

Another region that exhibits key modes of stratospheric dynamical variability is the equatorial region. The most notable of these modes are the quasi-biennial oscillation (QBO) in the zonal flow which varies with a frequency of approximately 28-29 months between the 100 hPa and 10 hPa levels and the semiannual oscillation (SAO) of zonal wind which cycles more regularly with a frequency of 6 months around the 1 hPa level and above (figure 2.3) [*Baldwin and Dunkerton*, 1991].

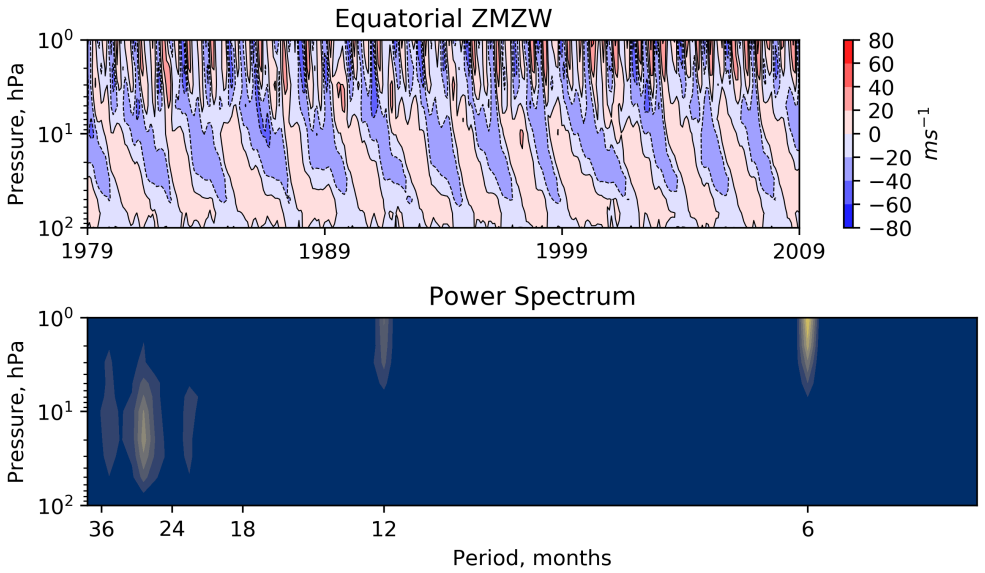


FIGURE 2.3: Equatorial ZMZW averaged between 5° S–5° N latitude (top) and associated Fourier power spectrum (bottom) from a 30-year sample from the ERA-Interim dataset between 1979 and 2009. A 30-year sample of data is provided to demonstrate the stalling of descending QBO phases.

A periodic reversal of equatorial stratospheric winds was first measured using balloon-based observations in *Ebdon* [1960]; *Ebdon and Veryard* [1961] and *Reed* [1965] however the QBO and its mechanisms were first fully classified as a phenomenon by

Lindzen and Holton [1968]. These studies found a set of descending shears of easterly and westerly ZMZW above the equator between approximately the 10 hPa and 100 hPa pressure levels. These seminal studies made use of a short observational record (approximately 5 years) and later works with longer datasets were able to establish the key features of the oscillation [*Baldwin et al.*, 2001; *Pascoe et al.*, 2005; *Schenzinger et al.*, 2017]. These include an approximate period of 28.1 months (with a range of 22-40 months) and an asymmetry in the rate of descent of the westerly and easterly phases - slower descending easterly winds are caused by increased equatorial upwelling associated with this phase [*Pascoe et al.*, 2005]. The oscillation is generally zonally symmetric [*Belmont and Dartt*, 1968] and has a latitudinal extent of approximately 12° half width at half maximum [*Baldwin et al.*, 2001].

The primary cause of the oscillation is the interaction of waves outlined in section 2.2 with the background zonal flow. To analyse the action of these disturbances, it is useful to consider a pair of equatorial waves with phase speeds of $+c$ and $-c$ respectively (figure 2.4, *Plumb* [1984]). These waves propagate or dissipate according to the difference between their phase speed and the background flow, $\overline{u}$. If $\overline{u}$ approaches $+c$ or $-c$ at a given height, the respective wave will deposit momentum of the same sign as its phase speed onto the background flow. This means that, for a background wind profile like that shown in 2.4a, westerly momentum is deposited at the bottom of a zone of westerly low altitude background wind, while easterly phase speed waves pass through and are deposited above on easterly flow. This causes the shear zone to descend and reduces the width of the layer of the westerlies enough to allow viscous diffusion to eradicate the westerly winds completely near the surface. This leads to the profile in figure 2.4b where westerly waves pass through the flow and easterlies deposit momentum. Finally, westerly waves begin to accelerate flow from high levels descending (as seen in schematic c) to finally force the background profile to figure 2.4d which is the inverse of schematic a. The asymmetry in descent speed between

phases of the QBO is accounted for by the induced meridional circulation associated with each phase. An easterly QBO in the lower stratosphere induces a poleward meridional circulation at the same level [*Plumb*, 1984; *Baldwin et al.*, 2001] as well as an acceleration in upwelling over the equator, this slows the descent of the QBO easterlies [*Reed*, 1965]. The converse is true for a westerly phase in the lower stratosphere.

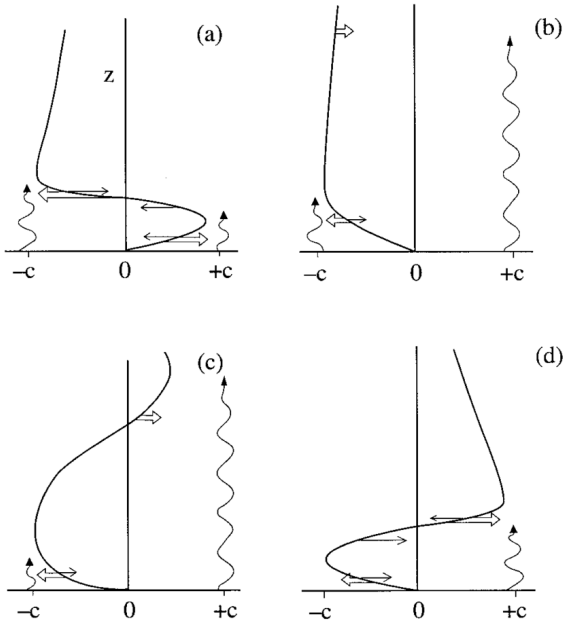


FIGURE 2.4: Schematic of equatorial wave-mean flow interactions for two example wave disturbances (phase speeds $\pm c$) from *Plumb* [1984]. Solid continuous lines show the background flow of the QBO in developing phases, wavy arrows indicate propagation of the two waves, double arrows show momentum deposition on the mean flow from wave breaking, single arrows indicate viscous-driven acceleration.

Above the 10 hPa pressure level, a different dominant mode of dynamical variability can be observed - the semiannual oscillation (SAO) [*Garcia et al.*, 1997]. This mode is categorised by two easterly and two westerly phases each calendar year with maximum amplitudes of approximately 30 ms^{-1}. These peak amplitudes are observed near the 1 hPa level and also exhibit vertically descending shear zones like the QBO. While the QBO is purely driven by local equatorial wave-mean flow interactions, the SAO phases are driven by a combination of physical processes. The westerly phases, observed near the equinoxes, are thought to be caused by the action of a combination

of Kelvin waves (∼70% of variability) and smaller-scale inertia-gravity waves (the remaining ∼30% of variability) [*Dunkerton*, 1979; *Hitchman and Leovy*, 1988]. The easterly phase, observed at the two solstices, is the result of meridional advection of (summer hemisphere) easterlies from the BDC [*Holton and Wehrbein*, 1980]. The easterly phases of the SAO also exhibit an asymmetry in amplitudes with the NH winter solstice phase stronger than its summer counterpart [*Dunkerton*, 1979]. This is due to a stronger BDC in NH winter which leads to greater advection of easterlies to the equatorial region, leading to a stronger easterly SAO phase compared to NH summer. The periodicity of the SAO is therefore tied (through its easterly phase) to the seasonal cycle, unlike the QBO which has 'quasi-periodicity' because its period is determined by the amplitude of wave forcing. The westerly SAO phases show a similar asymmetry, NH winter westerlies are marginally weaker than their summer counterparts. This is due to increased gravity wave activity in NH autumn (Sep-Nov) compared to NH spring (Mar-Jun) [*Ray et al.*, 1998].

Significant research efforts have been conducted to understand and improve the representation of these equatorial modes of variability in GCMs. The first work to produce QBO like variability in a GCM was *Takahashi* [1996] yet subsequent works have highlighted the difficulty in reproducing this mode due to the specific set of conditions required for it to be simulated [*Baldwin et al.*, 2001]. Many studies have explored the importance of parameterised gravity waves for the production of a QBO and found them generally important [*Giorgetta et al.*, 2006; *Osprey et al.*, 2010]. However, explicitly resolved waves were sufficient to produce a QBO in some high-resolution simulations of the Model for Interdisciplinary Research on Climate (MIROC) [*Kawatani et al.*, 2011]. Despite much research on the topic, only a small fraction of CMIP5 models captured an internally generated QBO-like variation [*Charlton-Perez et al.*, 2013]. As a result, the QBO initiative (QBOi) has been devised to produce a "recipe book for simulating a reliable QBO" using CMIP6 simulations and a set

of standardised evaluation metrics [*Butchart et al.*, 2018]. Recent Work under the remit of the QBOi [*Bushell et al.*, 2020] has suggested that the majority of CMIP6 GCMs exhibit a mean QBO period of near or less than the 28 months observed in reanalysis. The asymmetry in descent rates of easterly and westerly phases is not replicated successfully in some models, implying that the induced meridional circulation associated with the QBO may be problematic or that there may exist biases in the annual cycle in equatorial upwelling and its synchronisation with the QBO. Overall, the work suggests that the treatment of non-orographic gravity waves is the primary source of discrepancy in the QBO across models [*Bushell et al.*, 2020]. QBOi also considers the representation of the SAO in its models. *Smith et al.* [2019] presents representations from 11 models submitted to CMIP6 which vertically extend to the stratopause (the SAO region). These models are generally able to reproduce the seasonal variation (amplitude and phase) of winds compared to observations. However, the work notes that climatological winds of most models exhibit an easterly bias in the upper stratosphere which is attributed to an under-representation of small scale parameterised westerly phase speed waves. Despite the work of QBOi and other studies, there still remains significant open questions regarding representations of QBO and SAO in GCMs. How these equatorial modes interact with the vortex also remains a somewhat open question and is discussed in the following section.

2.5 External influence on the vortex

While the NH vortex is confined to the NH stratosphere, variability in its strength can be influenced remotely by the troposphere, the surface and other parts of the stratosphere. The role of such influence on the vortex has been explored extensively in previous literature however the nature of dynamical coupling is not fully understood.

2.5.1 The Holton-Tan effect

There exists a large body of literature examining the nature of the QBO and its interaction with the climate system; of particular relevance for the work presented in this thesis is how this mode couples with variability in the vortex. An association between the phase of the QBO and the strength of the vortex was first proposed by *Holton and Tan* [1980] and *Holton and Tan* [1982] who found that the vortex exhibited a strengthening when the QBO near the 50 hPa level was in its westerly phase (QBOW) compared to its easterly phase (QBOE). This link, usually referred to as the Holton-Tan (HT) effect, has been reported in subsequent studies with more comprehensive observations as well as in modelling studies using GCMs including the Met Office Hadley Centre Model 2 (HadGEM2) [*Watson and Gray*, 2014] and other Met Office models [*Garfinkel et al.*, 2018]. Separate modelling studies also report a HT effect [*Baldwin and Dunkerton*, 1991; *Pascoe et al.*, 2005; *Lu et al.*, 2008].

A number of physical mechanisms have been proposed to account for the observed coupling between the QBO and the vortex. Most notable is the hypothesis that during westerly phases, the zero wind line (the latitude at various heights at which the NH mid-latitude winter westerlies meet the summer easterlies) is shifted southwards [*Holton and Tan*, 1980]. This leads to a greater latitudinal dispersion of planetary wave activity as waves generated in the mid-latitudes are permitted to propagate vertically and equatorward (according to the Charney-Drazin criterion, equation 2.10) thus decreasing their dissipative effect on the vortex. The converse argument can be made for easterly QBO phases when the zero-wind line lies further north and the planetary waves are guided more directly towards the vortex [*Lu et al.*, 2014]. Indications of this effect may manifest in EP-flux divergence at different latitudes for each QBO phase however, studies that have tested this mechanism show varied results. *Hamilton* [1998] finds a significant difference in latitudinal distribution of

EP-flux divergence between QBO phases in accordance with the mechanism proposed above however *Hu and Tung* [2002] and *Gray et al.* [2004] suggest the mechanism only takes effect during certain winter months, namely a stronger link is observed in early winter (Sep-Nov) compared to mid or late winter. Furthermore [*Garfinkel et al.*, 2012a] present the idea of the HT effect competing with other phenomena such as the meridional circulation associated with QBO phases leading to variations in the strength of QBO-vortex coupling. *Lu et al.* [2014] examines this further and shows that the strength of the HT effect is transient in nature; the coupling is weakened if a broader and stronger vortex is present in NH winter due to divergence of wave activity generated by eddies within the vortex itself. This diverts wave activity equatorward, an opposite driving mechanism to that of the HT link. These competing processes are thought to temporarily reduce the influence of the QBO on the vortex.

2.5.2 The Aleutian Low

Vortex variability has also been closely associated with variations in winter surface climate that can determine the strength of mid-latitude tropospheric wave driving. Among the most notable of these is the climatological low-pressure system over the Aleutian Islands in the Bering sea - the Aleutian low (AL). The AL is a key indicator of Pacific climate variability with teleconnections to both tropical and mid-latitude climate [*Tsuyoshi and Shingo*, 1989; *Trenberth and Hurrell*, 1994; *Zhang et al.*, 1997]. The intensity of the AL has been shown to modulate vertical planetary wave propagation into the vortex region [*Woo et al.*, 2015; *Garfinkel et al.*, 2010; *Manzini et al.*, 2006]. Anomalously low pressure leads to an increase in Rossby wave amplitude with height [*Woo et al.*, 2015] which can lead to stratospheric wave breaking and momentum deposition on the vortex associated with SSW occurrence. The effect has been found in the reanalysis study of *Hu and Guan* [2018] which attribute positive trends in vortex strength to a less intense AL and resulting weakening in wave-1

planetary wave flux into the stratosphere. Subsequent modelling studies report similar connections between AL indices and winter mean vortex strength as well as the occurrence of SSW events [*Kren et al.*, 2016].

2.5.3 ENSO and tropical SSTs

Further surface features linked to vortex variability involve tropical sea surface temperatures (SSTs). For example, the SST anomalies over the Eastern Pacific region associated with the El Niño Southern Oscillation (ENSO) have been shown to induce a stratospheric vortex circulation response via a pathway involving the AL [*Domeisen et al.*, 2019]. A positive ENSO phase is associated with a deepening of the AL (anomalously low pressures over the AL region) which promotes stronger planetary wave forcing of the middle atmosphere. This teleconnection has been found extensively in observation-based studies [*Garfinkel and Hartmann*, 2008; *Ineson and Scaife*, 2009; *Smith and Kushner*, 2012] as well as modelling studies [*Bell et al.*, 2009; *Domeisen et al.*, 2015; *Manzini et al.*, 2006; *Richter et al.*, 2015]. However, the connection's robustness has also been shown to vary between ENSO events [*Deser et al.*, 2017; *Iza et al.*, 2016], between decades [*Osprey et al.*, 2019] and even within a single season (early vs late winter) [*Ayarzagüena et al.*, 2018] suggesting elements of non-stationarity in the teleconnection. Furthermore, there is a degree of asymmetry in the vortex response to anomalous positive (El Niño) and negative (La Niña) phases; SSWs occur at equal rates during winters of each ENSO phase and both at a higher rate than in neutral ENSO winters in the NCEP-NCAR reanalysis [*Butler and Polvani*, 2011; *Garfinkel et al.*, 2012b]. The elevated SSW rates during both ENSO phases are suggested to be due to sampling variability given the short observational record and further studies report a more linear ENSO-SSW connection in model simulations [*Polvani et al.*, 2017] with no significant increase in SSW rates associated with La Niña winters in high-top CMIP5 models [*Song and Son*, 2018]. El Niño winters' association

with increased SSWs and a weaker winter vortex are consistent across model and observations [*Manzini et al.*, 2006; *Richter et al.*, 2015].

Additional studies consider the role of ENSO indices evaluated over different regions of the equatorial Pacific in coupling with the vortex. Two of these so-called "flavours" of ENSO variation are the central Pacific (CP) ENSO and the East Pacific (EastP) ENSO which are defined by taking average SSTs over different longitudinal ranges in the equatorial Pacific and identified as separate modes of SST variability in the clustering analysis of *Johnson* [2013]. *Kao and Yu* [2009] also analyse these modes and show they represent the 1st (CP) and 2nd (EastP) Empirical Orthogonal Functions (EOFs, see section 3.2.6.4), which indicate patterns of maximum variance, of interannual equatorial Pacific SST variations in the HadISST dataset. The same work finds that the EP pattern exhibits greater inter-decadal variability than its CP counterpart. Other works examine the teleconnections with the stratosphere associated with each type of pattern; *Iza and Calvo* [2015] examine vortex responses to patterns in a combined ERA-Interim and ERA40 dataset and show significant correlation with both EastP and CP ENSO indices. However, the surface signal associated with CP El Niño conditions is more associated with a lower AL than the EP pattern in seasons where SSWs occur. Differences in vortex and mid-latitude wave activity responses to EastP and CP patterns are also shown in modelling studies [*Hegyi and Deng*, 2011] and in NCEP NCAR reanalysis [*Sung et al.*, 2014], highlighting probable differences in the physical mechanisms associated with each type of index.

SSTs in other regions also exhibit elements of coherence with the vortex. *Rao and Ren* [2018] show that Tropical Atlantic SSTs give rise to a vortex response although it is highly variable throughout the season while *Fletcher and Kushner* [2011], *Fletcher and Kushner* [2013] and *Rao and Ren* [2016] propose a tropical Indian Ocean (TIO) connection: Positive TIO SST anomalies lead to a reduced strength of the AL that weakens the Rossby wave forcing of the vortex, an opposite effect to the ENSO-vortex

connection where positive SST anomalies lead to vortex weakening. SST variability in the Northern Pacific basin, commonly labelled the Pacific Decadal Oscillation (PDO), has also been associated with the vortex (see section 2.7.2 for full details of this mode). The PDO has been shown to exert influence over stratospheric variability primarily through alteration of the AL with negative PDO phases associated with enhanced vertical and meridional propagation of planetary waves towards the vortex [*Mantua et al.*, 1997; *Rodionov et al.*, 2005; *Rao et al.*, 2019]. This Association is reported in both observation and modelling based studies [*García-Herrera et al.*, 2006; *Kren et al.*, 2016; *Hu and Guan*, 2018].

2.6 Downward influence of the vortex

So far, we have presented evidence for the influence of surface and tropospheric forcing on the vortex. Indeed, this was the sole view of stratosphere-troposphere coupling before the early 1990s when a selection of studies began to identify statistical coherence between vortex anomalies and subsequent patterns in the eddy-driven jet and NH surface patterns [*Kodera et al.*, 1990; *Nigam*, 1990]. Since then, significant evidence has emerged in support of a two-way dynamical relationship between the atmospheric layers with influence of the stratosphere on modes of tropospheric and surface variability.

2.6.1 The Northern Annular Mode

A key concept in the study of the vortex influence on the troposphere and surface is that of the Northern Annular Mode (NAM). The NAM is regarded as the leading mode of dynamical variability in the NH extra-tropical atmosphere [*Thompson and Wallace*, 1998, 2000; *Baldwin and Dunkerton*, 1999] and is usually defined as the leading EOF pattern (see section 3.2.6 for full details on EOF analysis) of NH geopotential heights (GPH) at various pressure levels [*Baldwin and Dunkerton*, 1999]. The projection of

this pattern onto the GPH fields gives a principal component (PC) index for the NAM. While these GPH fields are generally defined on 2D grids (in the latitude-longitude plane) many studies have been able to decrease computational expense by computing the NAM using zonal mean GPH fields [*Baldwin and Thompson*, 2009].

In the stratosphere, variations in the NAM broadly correspond to changes in winter vortex strength with the leading pattern resembling that of a strong, stable and zonally symmetric vortex [*Baldwin and Dunkerton*, 1999]. On tropospheric pressure levels, variability in the strength and latitude of the tropospheric jet dominates [*Limpasuvan and Hartmann*, 1999]. This makes the NAM a useful quantity for measuring the interactions between stratospheric and tropospheric variability as, in a single metric, it captures changes in distinct dynamical features of the NH winter stratosphere and troposphere (the vortex and the jet). The surface NAM pattern, often referred to as the Arctic Oscillation (AO), resembles the well-known dipole structure over the Atlantic, the North Atlantic Oscillation (NAO) [*Hurrell et al.*, 2003]. This mode consists of two centres of action over the Azores and Icelandic regions which are displayed in figure 2.5a. In addition to the NAO characteristics, the surface NAM also exhibits a centre over the AL region in the North Pacific. There is some debate regarding the relative roles of the NAO and AL sections of the AO pattern. Namely, whether the two features are truly coupled or can exist independently [*Deser*, 2000; *Ambaum et al.*, 2001] as well as how this may change under anthropogenic forcing [*Hamouda et al.*, 2021]. The AO pattern is shown in figure 2.5a along with the corresponding PC index.

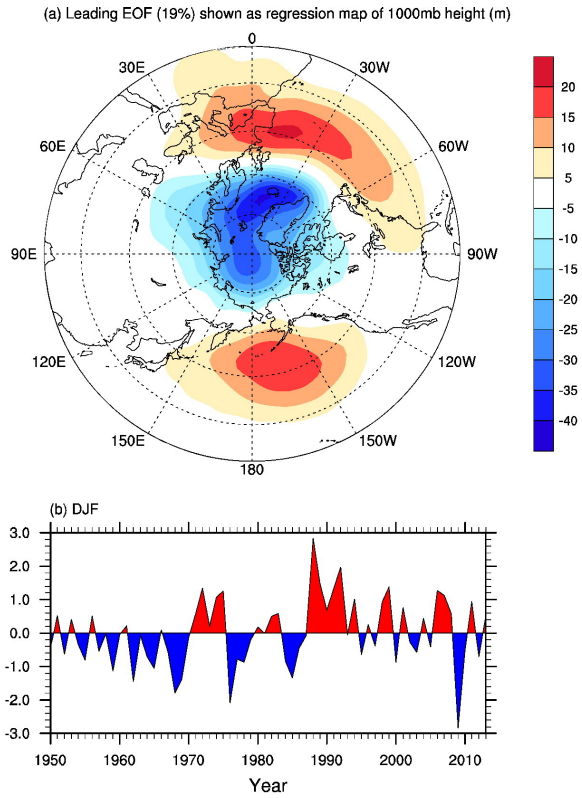


Figure 2.5: The Surface NAM pattern (also referred to as the Arctic Oscillation) derived by *Hegyi and Deng* [2011] using GPH data from the NCEP/NCAR (National Center for Environmental Prediction/National Center for Atmospheric Research) reanalysis dataset. **(a)** shows the leading EOF pattern of monthly mean GPH on the 1000 hPa level from the 1979-2000 period. The percentage quoted in parentheses indicates the fraction of the variance in GPH explained by the lead EOF. **(b)** shows the principal component time series generated by projecting the pattern in **(a)** onto the winter (Dec-Feb) surface GPH anomalies from the same dataset.

2.6.2 Tropospheric and surface variability

The notion of vortex influence over tropospheric and surface climate variability was first fully analysed in the seminal work of *Baldwin and Dunkerton* [2001] which demonstrated a steady downward propagation of NAM anomalies from the middle stratosphere to the surface following strong and weak vortex events (SSWs) in the ERA40 reanalysis dataset (figure 2.6). The surface perturbations associated with an anomalously weak (strong) vortex were shown to persist intermittently for approximately 60 days after the event and project significantly onto the negative (positive)

pattern of the NAO and AO. Subsequent studies have corroborated these results: *Domeisen* [2019] show using ERA40 and ERA-Interim datasets that approximately 2/3 SSW events are followed either by a switch from positive to negative NAO or a persistent negative NAO pattern. *Charlton-Perez et al.* [2018] consider this coupling from the perspective of tropospheric weather regimes and find, in both ERA-Interim and the ECMWF Integrated forecast model, a 40-60% increase in the probability of transition to a negative phase of the NAO given a 1 standard deviation reduction in vortex strength.

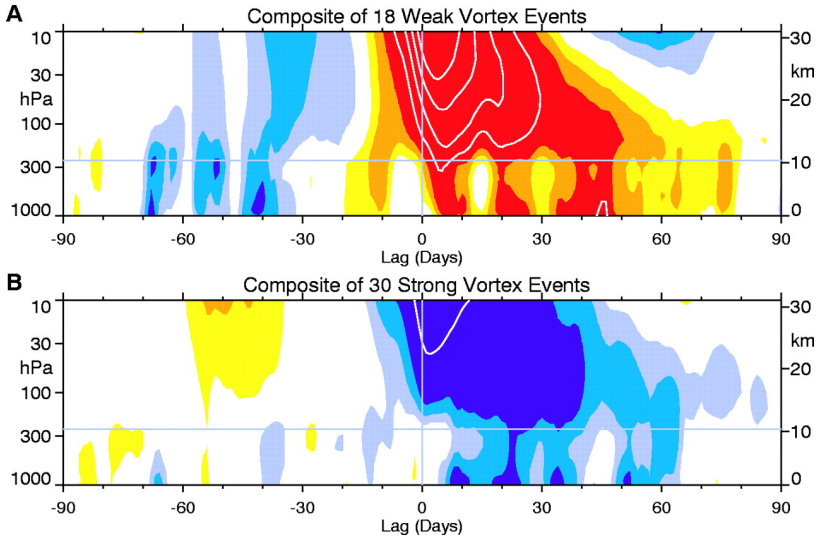


FIGURE 2.6: Figure from *Baldwin and Dunkerton* [2001]: Time-height composites of the NAM about anomalous weak (A) and strong (B) vortex events in the ERA40 dataset. Events are defined when NAM values cross -3.0 (weak) and +1.5 (strong). Coloured contours are spaced at 0.25 NAM intervals while white contours are spaced at 0.5. Only NAM values with a magnitude greater than 0.25 are shown. Vertical lines denote the central date of the vortex event and horizontal lines the approximate height of the tropopause.

SSWs' projection onto negative NAO phase probability has subsequently been shown to influence NH winter temperatures. *Thompson et al.* [2002] show in NCEP–NCAR reanalysis that SSWs are followed by a 60-day interval of anomalously low surface temperatures in eastern North America, northern Europe, and eastern Asia. Subsequent observational studies find similar response patterns to SSWs [*Kolstad et al.*, 2010; *King et al.*, 2019; *Lehtonen and Karpechko*, 2016] and the effect

can also be seen in GCM simulations [*Tomassini et al.*, 2012; *Lehtonen and Karpechko*, 2016]. Equally, the absence of an SSW, when the vortex is relatively undisturbed by waves propagating from the troposphere so that the vortex is unusually strong and cold, also has significant impacts on surface weather [*Shaw and Perlwitz*, 2013; *Lawrence et al.*, 2020]. Further impacts of SSWs on tropospheric circulation include an equatorward shift and deceleration of the North Atlantic eddy-driven jet stream which correspond to negative tropospheric NAM anomalies [*Hitchcock and Simpson*, 2014; *Maycock et al.*, 2020]. Links with persistent atmospheric blocking events are also shown in observation and modelling studies [*Davini et al.*, 2014; *Vial et al.*, 2013]. On the other hand, *Taguchi* [2008] finds no significant link between the phenomena however this work only considers hemisphere-averaged blocking and studies mentioned above that show shown significant links with the stratosphere (*Davini et al.* [2014] and *Vial et al.* [2013]) consider regional blocking metrics.

Although the composite analysis of *Baldwin and Dunkerton* [2001] indicates an average downward propagation of stratospheric anomalies, the same work demonstrates that only a fraction of vortex events perturb tropospheric and surface NAM signals. The cause of this fraction is not fully understood: *Mitchell et al.* [2011b] and *Seviour et al.* [2016] propose, using reanalysis and CMIP5 model data, that split vortex events have a greater probability of penetrating through the tropopause and exhibit a larger response at the surface than displacement events. However, *Maycock and Hitchcock* [2015] carry out a similar analysis on a large ensemble of pre-industrial control model runs (1000 years worth of simulation) and find no statistically significant difference between the vertical profiles of the two event types. Other works suggest that increased wave activity in the mid to lower troposphere preceding an event can influence its downward impact. *Nakagawa and Yamazaki* [2006] demonstrate anomalously high wavenumber two activity associated more with propagating events while *White et al.* [2019] find that 2/3 of events preceded by enhanced planetary wave

activity in the lower troposphere are propagating. However, the authors acknowledge that this attribute could not be used deterministically to predict whether a given event will propagate into the troposphere. Despite the lack of full understanding regarding downward propagation of vortex events, their influence on surface patterns is relatively well represented in modern GCMs [*Baldwin et al.*, 2021]. Idealised modelling studies using the Model of an Idealized Moist Atmosphere (MIMA) are able to show a direct downward influence of SSW events on the NAO by imposing disturbed vortex conditions and measuring the surface response [*White et al.*, 2020]. Similar results are obtained in *Gerber et al.* [2009] which utilises a similar method. However, some works note that simple models tend to over-represent the persistence of surface anomalies [*Gerber et al.*, 2008a,b] indicating that a complex combination of factors not captured by simplified model setups likely cause the varying degrees of propagation for different SSWs.

2.7 Multi-decadal climate variability

In the majority of studies covered thus far, the vortex and its interactions with the wider climate system are considered within each NH winter, and variability in its strength is considered primarily on interannual timescales. However, there is a growing body of evidence in support of modes of variability on multi-decadal timescales in the climate system. Here, we outline some of the most well-studied of these modes.

2.7.1 Atlantic variability

A domain often associated with multi-decadal timescale variations is the ocean, primarily due to the high degree of thermal inertia present in ocean systems. One of the primary modes of variability in ocean circulation is the Atlantic Meridional Overturning Circulation (AMOC) which consists of a northward transfer of warm, saline water that occurs in the top 2km of the Atlantic Ocean (the "upper cell")

accompanied by a corresponding return flow of southward transport at lower depths, the "lower cell" often referred to as the North Atlantic Deep Waters (NADW) [*Kuhlbrodt et al.*, 2007; *Xu et al.*, 2014; *Buckley and Marshall*, 2016]. The AMOC is thought to be a key driver of North American and European surface variability via modulation of Atlantic sea surface temperatures (SSTs) and heat transport [*Knight et al.*, 2005; *Delworth and Mann*, 2000; *Frierson et al.*, 2013; *Frankignoul et al.*, 2013]. It has been shown to influence a diverse range of features such as European summertime temperatures [*Sutton and Hodson*, 2005], biogeochemical conditions in the northwest Atlantic [*Lavoie et al.*, 2019] as well as abrupt climate shifts in paleoclimate records [*Alley*, 2007; *Cheng et al.*, 2009].

The strength of the AMOC has been shown to vary significantly on decadal-centennial timescales [*Delworth et al.*, 1993; *Biastoch et al.*, 2008; *Tulloch and Marshall*, 2012; *Menary et al.*, 2012]. *Biastoch et al.* [2008] show, using a suite of ocean models with varying resolutions, that these characteristic timescales are likely due to the complex interaction of different driving mechanisms including wind and thermohaline forcing as well as subarctic deep water formation which is transferred to the tropical Atlantic. Both modelling and observational studies link the AMOC to the Atlantic Multidecadal Variability (AMV), a prominent mode of variability in subpolar North Atlantic SSTs with a period of 60-80 years in observations [*Zhang et al.*, 2019]. For example, the observation-based study of *McCarthy et al.* [2015a] shows that the decadal-scale changes in the AMOC lead to similar fluctuations in the AMV through alterations in subpolar gyre heat content, a finding that backs up the earlier modelling study of *Delworth and Mann* [2000] which proposed a similar mechanism.

Multiple potential drivers of AMOC variability at different timescales have been studied extensively in both observations and modelling studies. On intra-annual to inter-annual timescales, variability in the AMOC has been closely associated with wind variations over the North Atlantic region through Ekman-transport anomalies

or wind stress curl forcing [*Wang et al.*, 2019; *McCarthy et al.*, 2012; *Mielke et al.*, 2013; *Yang*, 2015]. On inter-annual to decadal timescales, AMOC variability has been associated with buoyancy anomalies in the subpolar region, particularly in the Labrador Sea [*Delworth et al.*, 1993; *Medhaug et al.*, 2012]. This mechanism is linked to variability in mixed-layer depth, the depth of the upper ocean layer where salinity, density and temperature are approximately uniform [*de Boyer Montégut et al.*, 2004], particularly in NH winter [*Böning et al.*, 2006; *Biastoch et al.*, 2008; *Robson et al.*, 2012; *Wang et al.*, 2015]. Mixed-layer anomalies in the Labrador Sea are an indication of the strength of deep convection in this region, which is associated with AMOC variations in modelling studies [*Eden and Willebrand*, 2001; *Eden and Jung*, 2001] and observations [*Latif and Keenlyside*, 2011].

Recent studies on the observed AMOC have shown a negative trend in circulation strength of approximately $-2.7Sv$ ($1Sv = 10^6 m^3 s^{-1}$) between 2004 and 2012 [*Smeed et al.*, 2018] before a marginal recovery after 2012 [*Smeed et al.*, 2019]. Modelling studies have proposed a key role for anthropogenic forcing in AMOC slowdown over the 20th century and into the future [*Liu et al.*, 2017; *Bakker et al.*, 2016; *Liu et al.*, 2019] however the magnitude of this contribution as well as others carries significant uncertainties. Research efforts into understanding these AMOC trends rely heavily on GCMs and subsequently their representation of the AMOC. Recent studies (e.g. *Robson et al.* [2020]) evaluate the representation of the AMOC in a modern GCM (the UK Earth System Model in this case) and find it is able to realistically simulate key features of the AMOC over the historical period but under-represents decadal-scale variability compares to observations. It also underestimates the size of the recent trends reported in *Smeed et al.* [2018, 2019]. The same issue is reported in a suite of CMIP5 models in *Roberts et al.* [2014].

2.7.2 Pacific variability

An analogous mode of SST variability to the AMV can be observed in the Pacific basin labelled the Pacific Decadal Oscillation (PDO, *Mantua et al.* [1997]). This mode is often defined using the leading EOF and associated PC of North Pacific SSTs (however, a simpler box average over the same region index is also utilised). This mode is shown to exhibit spectral power at a range of frequencies in a suite of CMIP5 models which show little consensus as to the characteristic timescale of variations [*Newman et al.*, 2016]. Other studies into the spectral features of the PDO report significant non-stationary regime behaviour [*Overland et al.*, 2006; *Fleming*, 2014] as well as variations between 20 and 70-year periods utilising paleoclimate proxy records [*Biondi et al.*, 2001]. Despite these works, there remains an open question as to the true characteristic timescale of PDO variations and *Newman et al.* [2016] suggest this is likely because this mode is not simply a single phenomenon but the result of a complex combination of physical processes.

A variety of mechanisms are proposed to drive PDO variations. For example, *Frankignoul and Hasselmann* [1977] show a possible role of stochastic atmospheric forcing (effectively white noise) from the AL region whose effect is integrated over time due to the long memory of the ocean. Links to the tropical Pacific are also explored with *Strong and Magnusdottir* [2009] showing an influence of ENSO SSTs via modulation of the AL particularly in boreal winter (when ENSO peaks). The ENSO-PDO connection may also contribute to decadal timescale fluctuations in the PDO as *Alexander et al.* [2002] and *Alexander and Scott* [2008] show using GCM integrations that 1/4-1/2 of PDO variability originates in the tropical Pacific. Low-frequency (longer than a decade) co-variability between ENSO and the PDO is also shown in other observational and modelling studies [*Vimont*, 2005; *Chen and Wallace*, 2015].

The PDO has been shown to influence stratospheric variability primarily through alterations in AL intensity and subsequent modulation of planetary wave driving of the vortex [*Kren et al.*, 2016; *Kang and Tziperman*, 2017; *Hu and Guan*, 2018]. PDO and ENSO like SST variations have been shown to perturb the vortex in numerous modelling studies [*Kren et al.*, 2016; *García-Herrera et al.*, 2006]) however the role of decadal-scale variations in such teleconnections are less well explored and is one of the aims of the original work presented in this thesis.

The set of multi-decadal features outlined in this section is not exhaustive within the climate system however the AMOC, AMV and PDO represent some of the most well-studied modes which exhibit variations on this timescale. The aim of analysis in chapters 3 and 4 is to determine whether the vortex and equatorial stratosphere exhibit similar multi-decadal variability as well as to establish how these signals may interact with the modes outlined above.

CHAPTER 3

Origins of multi-decadal variability in sudden stratospheric warming events

Much of the work presented in this chapter is based on *Dimdore-Miles et al.* [2021a] however the analysis here has been extended.

3.1 Introduction

Despite a significant body of work aimed at understanding the nature of vortex variability including SSWs, variations in this mode on decadal to multi-decadal timescales is not well understood. A formal diagnosis of such variability as well as a better understanding of factors that influence it may help to improve the predictability of SSWs and subsequently NH mid-latitude surface climate [*Kidston et al.*, 2015].

There is some evidence of vortex variations with periods longer than a year in the observational record. In reanalysis datasets, SSWs occur at an average rate of ∼0.6 events/winter but this varies markedly within the record [*Butler et al.*, 2015] suggesting the possibility of variability on much longer timescales. For example, observational studies have noted a hiatus in the 1990s when very few major SSW

events occurred [*Butler et al.*, 2015; *Pawson and Naujokat*, 1999; *Shindell et al.*, 1999] while, in contrast, the early 21st century displayed a remarkable number of consecutive winters containing SSW events [*Manney et al.*, 2005]. Other studies have addressed the notion of low-frequency variations in the vortex using GCMs. *Garfinkel et al.* [2017] analyse decadal-scale variations in vortex strength in a set of historical simulations and propose that an observed hiatus in Eurasian surface warming was most likely due to variability in midwinter vortex strength. Similarly, *Cohen et al.* [2009] find decadal-scale variations in planetary wave forcing of the vortex in a suite of CMIP3 models as well as NCEP–NCAR reanalysis. Whether the vortex variability was forced by greenhouse gas concentrations or arose through internal variability in these studies was not fully established but *Garfinkel et al.* [2015] used a subset of the simulations analysed in *Garfinkel et al.* [2017] and linked a decadal trend (1980-2009) in late winter vortex strength to SST variability. On the other hand, *Seviour* [2017] analysed observed variations between 1980 and 2016 and concluded that the vortex variability was primarily internally generated. Other studies also point towards internally generated decadal fluctuations in vortex strength: *Manzini et al.* [2012] explore causes of 20-year period variability in a simulation with prescribed, pre-industrial SSTs. They propose that given the boundary conditions in the simulations are fixed, such variability must be internally generated. Finally, *Butchart et al.* [2000] suggest that decadal variability in vortex strength, as well as SSW frequency, may originate from feedbacks caused by the non-linear nature of boreal winter stratospheric dynamics.

On longer timescales, *Schimanke et al.* [2011] note variations in SSW occurrence with periods of approximately 52 years in a multi-century GCM integration and demonstrated coherent variability in other parts of the climate system, including vertically propagating planetary wave activity, Eurasian snow cover and Atlantic SSTs. However, despite providing some indications of externally driven variability, results

from this study are not conclusive, since the GCM used (EGMAM: ECHO-G with Middle Atmosphere Model) exhibits significant bias in mean SSW rate compared to reanalyses (2 events per decade compared to ∼6 in reanalysis). The authors also note that further simulations are required to understand this variability.

Multi-decadal scale variations in climate features that couple with the vortex have also been explored. There are clear decadal variations in the period and phase transition timing of the QBO [*Pascoe et al.*, 2005; *Anstey and Shepherd*, 2008; *Yang and Yu*, 2016]. These may be linked to variations in the degree of 'stalling' of the QBO phase descent, which can cause more or less persistent wind direction at a given level. A number of studies have also noted the transient nature of the strength of the HT relationship outlined in section 2.5.1 [*Lu et al.*, 2008, 2014; *Anstey and Shepherd*, 2008; *Osprey et al.*, 2010]. *Lu et al.* [2008, 2014] show that the mid-latitude waveguide is modulated by the shape of the vortex so that planetary waves are diverted further equatorwards when the vortex is anomalously strong and wide, and this could temporarily reduce the influence of the QBO on the vortex. The Aleutian Low (AL, see section 2.5.2) also varies significantly on decadal to multi-decadal timescales. *Overland et al.* [1999] note that 10-year mean values of SLP over the AL region exhibit fluctuations of up to 35% of the climatological mean. Subsequent studies corroborate the presence of these decadal-scale fluctuations: *Sugimoto and Hanawa* [2009] and *Minobe* [1999] show 20-year fluctuations in intensity and centre of action of the AL while *Raible et al.* [2005] propose a 50-60 year trend in AL intensity, suggesting the existence of even longer timescale variability.

Although substantial effort has been applied to characterising SSWs and their underlying mechanisms, there is little understanding of periods of hiatus (such as that in the 1990s) and consecutive-event years (early-mid 2000s), primarily because of the short record of reliable observations as well as the complexities and often non-stationary nature of the multiple observed teleconnections. Much longer time series are required

to successfully identify and understand the source of decadal and multi-decadal scale variability. In the meantime, analysis of variability and teleconnections in long climate model simulations may help to understand these processes.

In this chapter, we analyse long-term variability of the stratospheric polar vortex in a 1000-year pre-industrial control (pi-control) simulation of the UK Earth System Model (UKESM). The absence of external forcings such as greenhouse gas increases, volcanic and solar variations allows us to examine sources of long-term variability that are internally generated within the climate system. We identify intervals containing high and low SSW rates and analyse their variability, with a focus on multi-decadal scales. A variety of techniques are employed to examine associations with those parts of the climate system that are known to exhibit long-term memory, namely the tropical region over the ocean and the AL which both retain such memory through their close association with SSTs. In particular, a wavelet spectral decomposition and cross-spectrum analysis are employed to overcome some of the difficulties with non-stationary signals that may arise. We also investigate interactions between the vortex and the QBO as a potential source of internally-driven variability.

3.2 Data and methods

3.2.1 Model configuration

For analysis of multi-decadal variability in the vortex and SSWs, we utilise a simulation of the first version of the UK Earth System Model (henceforth referred to as UKESM), a configuration of the MetOffice unified model (the UM) [*Mulcahy et al.*, 2018]. UKESM is a stratosphere resolving coupled ocean-atmosphere-land-sea ice model. The atmospheric component is GA7.1 with 85 vertical levels from the surface to na altitude of 85km, 35 of which are above 18km [*Walters et al.*, 2019; *Williams et al.*, 2018]. The model is run at N96 horizontal resolution (approximately 1.25° × 1.875°

or ∼135 km near the equator). The ocean model used is GO6.0 [*Storkey et al.*, 2018] which contains 75 levels and runs at 1° × 1.875° horizontal resolution. Land surface and sea-ice processes are represented by JULES [GL7.0, *Walters et al.*, 2019] and CICE [GSI8.1, *Ridley et al.*, 2018] models respectively, while ocean biochemistry is added through MEDUSA [*Yool et al.*, 2013]. UKESM also includes a fully interactive chemistry scheme via coupling with the UK Chemistry and Aerosols model [UKCA, *Mulcahy et al.*, 2018].

We utilise a 1000-year pre-industrial control (pi-control) simulation of UKESM submitted to CMIP6 which is spun-up to achieve initial model equilibrium following the method outlined in *Yool et al.* [2020]. This run is forced using CMIP6 pre-industrial values for concentrations of major GHGs (global mean 284.317ppm CO_2, 808.25ppb CH_4, 273.02ppb N_2O). While there are no volcanic eruptions in the simulation, background stratospheric volcanic aerosols are set to climatological values between 1850 and 2014 estimated from satellite products and other model simulations [*Menary et al.*, 2018]. We choose a pi-control for this analysis to examine internal variability in SSWs on multi-decadal timescales.

3.2.2 Reanalysis data

To verify that the model reproduces relevant features of the climate system we compare it with an observation-based dataset produced by the ECMWF - ERA-Interim *Dee et al.* [2011]. The ERA-Interim dataset is produced by a 4D-Var data assimilation method of a wide range of observations [*Uppala et al.*, 2005]. These include surface measurements, aircraft campaign data, radiosonde readings and satellite observations. The 4D-var data assimilation process involves supplying the ECMWF's Integrated Forecast System (IFS) initial conditions from observations, letting the model evolve for a timestep and re-initialising for the next step with a combination of output and updated observations [*Courtier et al.*, 1998; *Bouttier and Kelly*, 2001]. This update is

carried out by minimising a cost function defined to capture the difference between the latest model output and observations for that corresponding time. ERA-Interim provides data on 60 vertical levels at a maximum horizontal resolution of ∼80 km (approximately 0.7° × 0.7°) from 1979-2019 [*Berrisford et al.*, 2011]. We utilise data on this maximum horizontal resolution grid with data sampled from 37 standard pressure levels outlined in *Berrisford et al.* [2011] between 1000 hPa and 1 hPa.

The majority of observations assimilated for ERA-Interim are satellite-based radiance retrievals. These are gained from nadir sounding satellites which measure spectral radiances (energy detected at different wavelengths). A single detection device will consist of several channels which detect radiation from different wavelengths. Different atmospheric layers absorb and emit at different wavelengths so measuring over a range of channels can build up a vertical profile of a variable such as temperature. However, the atmospheric layers that are detected by each channel may overlap resulting in measurements from multiple channels being used in the retrieval of a given layer. A weighting is applied to the channels at each height to account for the proportion of the total measurement that should be contributed by each channel. Channel weighting profiles (see figure 3.1) are generally Gaussian (for nadir Satellites) in pressure coordinates [*Fujiwara et al.*, 2017], the width of which signifies the vertical extent of the channel. The vertical resolution of the retrievals is determined by the density of channels covering a particular height range.

During the ERA-Interim period, the set of observations used for assimilation have developed significantly. Between 1979 and 1998 only limited satellite-based radiance retrievals are available to produce profiles. These satellite observations are primarily provided by the Stratosphere Sounding Unit (SSU) and Microwave Sounding Unit (MSU) which are parts of the Television Infrared Observation Satellite (TIROS) Operational Vertical Sounder (TOVS) suite. The SSU possesses only 3 channels (figure 3.1a) and therefore provides data at relatively coarse vertical resolution. Over

this period, ERA-Interim relies heavily on direct measurement techniques such as radiosondes, dropsondes and aircraft [*Fujiwara et al.*, 2017] which bring possible biases from the influence of shortwave solar heating on temperature sensors in radiosondes as well as warmer tendencies in aircraft-based observations compared to radiosondes [*Ballish and Kumar*, 2008]. After 1998, more extensive satellite-based measurements are available for assimilation and are incorporated in ERA-Interim. The new satellite products include improved versions of the SSU and MSU as a part of the Advanced TIROS Operational Vertical Sounder (ATOVS) suite which provides profiles derived from the Advanced Microwave Sounding Unit A (AMSU, figure 3.1b) from which ERA-Interim calculates profiles using 11 channels (channels 5-14 from AMSU). ERA-Interim also makes use of a number of other satellite-based instruments which are fully outlined in [*Fujiwara et al.*, 2017]. Possible sources of biases in these satellite-based observations include orbital drift and calibration offsets [*Simmons et al.*, 2014].

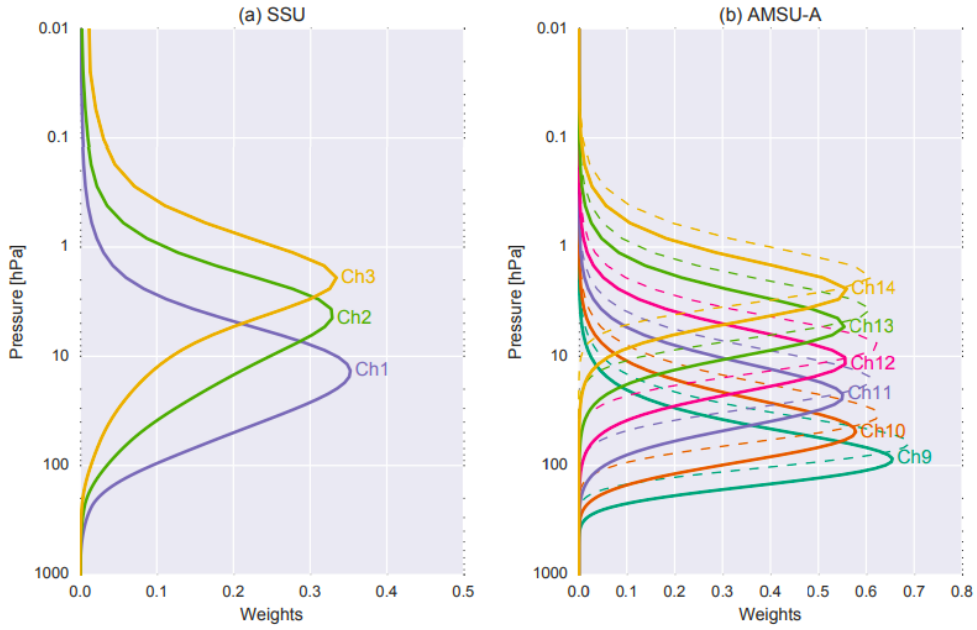


Figure 3.1: Figure from *Fujiwara et al.* [2017]. **Left**: Channel weighting profiles for the TOVS Stratospheric Sounding Unit (SSU) used for ERA-Interim dataset in the period 1979-2005. **Right**: Weighting profiles from the ATOVS-suite Advanced Microwave Sounding Unit (AMSU) which provides measurements for ERA-Interim from 1998-present. Solid lines represent near-nadir profiles and dashed lines signify limb profiles (taken at an angle of 48.33°).

As a result of including additional observations for assimilation after 1998, ERA-Interim shows a shift in temperature structure of the middle and upper stratosphere between the two periods. Caution is therefore advised when using this data for trend analysis [*Long et al.*, 2017] however such an analysis does not form part of the work in this thesis. Zonal wind fields show little change across the periods. Additionally, ERA-Interim struggles (as the majority of modern reanalyses do) to constrain phase transition timing of the QBO correctly [*Kawatani et al.*, 2016]. Comparisons with wind profiles derived from a single radiosonde station (Singapore at 1°N, 104°E), which covers a large majority of the reanalysis period, show that ERA-Interim also exhibits biases in the amplitude of both QBO phases. These biases reduce significantly with the transition to the use of ATOVS [*Kawatani et al.*, 2016; *Long et al.*, 2017]. Similar biases and improvements over the TOVS-ATOVS period are also observed for representation of the SAO *Baldwin and Gray* [2005]. These biases must be taken into account when considering comparisons in stratospheric circulation between ERA-Interim and GCMs. Nonetheless, *Long et al.* [2017] stress that these datasets are in broad agreement with other major reanalyses in the stratosphere and lower mesosphere.

3.2.3 Wavelet analysis

In order to study possible multi-decadal variability in SSW occurrence, we utilise a wavelet analysis method based on *Torrence and Compo* [1998]. Such an analysis can be used to examine time series which displays non-stationary spectral power over multiple frequencies [*Daubechies*, 1990] giving it a useful advantage over more traditional Fourier methods for spectral analysis. The wavelet transform of a uniform 1-dimensional time series, x, of length N and timestep δt is given by the convolution between the series

and a scaled and translated version of a wavelet function ψ_0 (equation 3.1)

$$W_n(s) = \sum_{n'=0}^{N-1} x_{n'} \psi^* \left[(n' - n) \frac{\delta t}{s} \right], \tag{3.1}$$

where $*$ denotes the complex conjugate and s is the wavelet scale indicating the frequency of the wavelet. Varying s and translating along the time scale (the index n), W_n indicates the amplitude of signals at different scales and their variation in time. *Torrence and Compo* [1998] suggest an approach to varying the scale s as increasing in powers of 2 according to

$$s_j = s_0 2^{j \delta j}, j = 0, 1, ..., J \tag{3.2}$$

$$J = \delta j^{-1} log_2 \left(\frac{N \delta t}{s_0} \right), \tag{3.3}$$

where s_0 is the shortest resolvable scale of a signal, J corresponds to the longest and δj is the scale resolution. The translated and scaled wavelet has the form

$$\psi^* \left[(n' - n) \frac{\delta t}{s} \right] = \left(\frac{\delta t}{s} \right)^{1/2} \psi_0 \left[(n' - n) \frac{\delta t}{s} \right] \tag{3.4}$$

and we select the form of ψ_0 following the recommendation of *Torrence and Compo* [1998] as a Morlet wavelet, an oscillatory function enveloped by a Gaussian which is expressed as

$$\psi_0(p) = \pi^{-1/4} e^{i \omega_0 p} e^{\frac{p^2}{2}}. \tag{3.5}$$

The advantages of using a Morlet wavelet for analysing signals in climate time series is discussed in *Lau and Weng* [1995] in which the authors acknowledge that, while truly physical signals should be detected regardless of which wavelet basis is

chosen, for best results, one should adopt a wavelet function reminiscent of the real signal. They show that, when a Morlet wavelet form is utilised, spectral decomposition methods can detect common forms of behaviour exhibited in the variability of time series associated with the Earth's climate. These include time variations in period and amplitude of signals, abrupt changes in periodicity (sudden regime shift to different spectral behaviour) and some forms of rapid changes in series over time. These forms of behaviour are most likely relevant for our analysis of SSWs, therefore we proceed with a wavelet of this form.

It is computationally quicker to compute the wavelet transform in discrete Fourier space. By the convolution theorem, the transform reduces to multiplication

$$W_n(s) = \sum_{k=0}^{N-1} \hat{x}_k \hat{\psi}^*(s\omega_k) e^{i\omega_k n\delta t}, \tag{3.6}$$

where $\hat{x}_k$ and $\hat{\psi}$ are the discrete Fourier transforms of the time series x (equation 3.7) and the wavelet function (equation 3.8) respectively. These quantities are given by

$$\hat{x}_k = \frac{1}{N} \sum_{n=0}^{N-1} x_n e^{\frac{-2\pi ikn}{N}} \tag{3.7}$$

$$\hat{\psi}(s\omega_k) = \left(\frac{2\pi s}{\delta t}\right) \pi^{-1/4} H(\omega_k) e^{-(s\omega_k - \omega_0)^2/2} \tag{3.8}$$

where $H(\omega_k)$ is the Heavyside function and $\hat{\psi}$ is normalised to have unit energy when integrated over all ω. The square modulus of the wavelet transform gives the wavelet power spectrum which indicates the relative strength of signals in the time series as a function of signal period and discretised time. To directly compare spectra of different indices, we normalise all time series by subtracting the mean and dividing by its standard deviation before performing the wavelet transform. To effectively compare spectral power across a range of frequencies, we additionally scale the power

spectrum by dividing by the scale parameter (s_j defined above) associated with each frequency. This is done following the methodology of *Liu et al.* [2007] which shows that un-scaled spectra exhibit a bias towards overestimated powers at longer periods and that an effective comparison across timescales is possible with such scaling. We also define a confidence interval for wavelet power observed at a given period and time for a series by assuming a mean background spectrum corresponding to that of a first-order autoregressive (AR1, red noise) process modelled by

$$x_n = \alpha x_{n-1} + z_n, \tag{3.9}$$

where α is the lag-1 autocorrelation of the time series and z_n is Gaussian white noise. *Torrence and Compo* [1998] show that such a process's wavelet power spectrum is χ^2 distributed and therefore can be used to define a 95% confidence interval for any observed power.

3.2.4 Cross wavelet spectra

The cross wavelet spectrum of two time series x and y with associated wavelet spectra W_n^x and W_n^y gives a measure of coincident power (the same period at the same time points) between the series. It is given by

$$|W_n^{xy}(s)| = |W_n^{x*}(s)W_n^y(s)|, \tag{3.10}$$

where $W_n^{x*}(s)$ is the complex conjugate of the wavelet power spectrum of x [*Grinsted et al.*, 2004]. The complex argument of $W_n^{xy}(s)$ gives the local phase difference between signals in x and y in frequency-time space. The phase relationship between the two time series can be represented by a vector that subtends an angle representing the phase difference: On all plots of cross-spectra, arrows to the right (left) denoted signals which are in-phase (π out of phase) and correlated (anti-correlated). Vertical arrows

indicate a phase relationship of $\frac{\pi}{2}$ between the time series, so that the evolution of one is correlated with the rate-of-change of the other. As for individual power spectra, we define a confidence interval for which cross power of a larger amplitude is deemed significant (>95% confidence interval) by comparing power exhibited by time series with a theoretical red noise process. The cross power of two such AR1 processes is theoretically distributed such that the probability of obtaining cross power greater than a set of red-noise processes is

$$D\left(\frac{|W_n^{xy}(s)|}{\sigma_x\sigma_y} < p\right) = \frac{Z_\nu(p)}{\nu}\sqrt{P_k^x P_k^y}, \tag{3.11}$$

where σ denotes the standard deviation of each time series, Z is the confidence interval defined by p ($Z = 3.999$ for 95% confidence), ν is the degrees of freedom for a real wavelet spectrum ($\nu = 2$) and P_k^x is the theoretical Fourier spectrum of the AR1 process with the same autocorrelation structure as x. For a given wavenumber k, this can be expressed as

$$P_k = \frac{1-\alpha^2}{|1-\alpha e^{2i\pi k}|^2}. \tag{3.12}$$

3.2.5 Hilbert transform

We utilise a signal processing method known as a Hilbert transform to calculate the instantaneous phasor amplitude of a QBO time series. The Hilbert transform of a time series $x(t)$ can be expressed as

$$\tilde{x} = Hil[x(t)] = \frac{1}{\pi t} * x(t), \tag{3.13}$$

where ˜ denotes the transformed series, * signifies a convolution and t is discretised time. Conversely, the original time series can be recovered using an inverse transform

expressed as

$$x(t) = Hil^{-1}[\tilde{x}(t)] = -\frac{1}{\pi t} * \tilde{x}(t). \tag{3.14}$$

A complex signal which consists of $x(t)$ and its transform is known as the analytic signal of x and can be used to calculate an instantaneous phasor amplitude, $A(t)$, of the signal. $X(t)$ can be expressed as

$$X(t) = x(t) + \tilde{x}(t)i = A(t)e^{i\theta}, \tag{3.15}$$

where $A(t)$ is the instantaneous amplitude of the signal and $\theta(t)$ is the instantaneous phase angle - a measure of signal progression through a cycle at time t.

3.2.6 Statistical methods

3.2.6.1 Student's t-test

Much of the analysis presented in this chapter, and indeed in the whole thesis, involves comparisons of composite and mean quantities. A two-tailed Student's t-test is implemented to test the null hypothesis that two sampled quantities, x_1 and x_2, with means $\overline{x}_1$ and $\overline{x}_2$ and standard deviations σ_1 and σ_2 are drawn from the same underlying normal distribution. A t statistic is defined by $t = \frac{\overline{x}_1 - \overline{x}_2}{\sigma_{12}\sqrt{\frac{1}{n_1}+\frac{1}{n_2}}}$ where n_i is the number of samples for quantity i and σ_{12} is the pooled variance for the two quantities given by $\sigma_{12} = \sqrt{\frac{\sigma_2^2(n_2-1)+\sigma_1^2(n_1-1)}{n_1+n_2-2}}$. The significance level for the difference in means can then be estimated by comparing the value of t with a Student's t-distribution to give an associated p value. Differences which give a p value greater than a deemed level (normally 95%) are deemed significant in which case the null hypothesis of identical means is rejected to this level.

3.2.6.2 Correlation analysis

We use a standard measure of linear monotonic statistical association between two time series, the correlation coefficient, r [*Freedman et al.*, 2007]. the r-value between 2 time series, x and y, is defined as the normalised covariance between the series -

$$r = \frac{\Sigma(x_i - \overline{x})(y_i - \overline{y})}{\Sigma(x_i - \overline{x})^2 \Sigma(y_i - \overline{y})^2}, \tag{3.16}$$

where $\overline{x}$ and $\overline{y}$ are the means of the corresponding time series and all sums are over the index, i, which refers to each element of the time series. r can take values ranging from -1 (anti-correlated) to 1 (correlated) and describes the degree to which changes in one variable (x) are associated with changes in the other (y). We also calculate a significance level for a calculated value of r using a similar t statistic as outlined in the previous section. In this case, this t statistic takes the form $t = \frac{r\sqrt{n-2}}{\sqrt{1-r^2}}$ where r is the measured correlation coefficient and n is the number of data points in each time series [*Freedman et al.*, 2007]. Similarly to with a Student's t-test, The significance level for a measured r can be estimated by comparing the value of t with a t-distribution to give an associated p value and r values which give a p value greater than 95% are deemed significant in which case the null hypothesis of no monotonic linear association between x and y is rejected to this level.

3.2.6.3 Linear regression analysis

We employ a multi-linear regression technique to give an estimate of the relative contributions to SSW variability from the QBO, ENSO and the AL following the method outlined in *Krzywinski* [2015]. We model an SSW time series of length n which we denote y as

$$\hat{y} = \beta_0 + \beta_1 QBO + \beta_2 ENSO + \beta_3 AL, \tag{3.17}$$

where β_j denotes the coefficient of the corresponding index and $\hat{y}$ is the prediction of y. We calculate the best estimate for each β using an ordinary least square (OLS) estimator which minimises the sum of squared residual error (SSE) between the predicted $\hat{y}$ and the real time series y with respect to each coefficient. The SSE is given by $SSE = \sum_i^n (\hat{y}_i - y_i)^2$ [*Kim*, 2018].

We can compare the estimated magnitude of the coefficient for each index to analyse the respective contributions to SSW variability. We can also calculate standard error ranges for β estimates. An estimated value of a true β_j (denoted by $\hat{\beta}_j$) carries a standard error given by

$$se(\hat{\beta}_j) = \sqrt{\frac{SSR}{n-k}(X^T X)^{-1}_{jj}}, \tag{3.18}$$

where SSR is the regression sum of squares which measures the sum of squared deviations of predicted values from the mean y value, $\overline{y}$. This is given by $SSR = \sum_i^n (\hat{y}_i - \overline{y})^2$ where k is the number of predictors used in the linear model (in this case 3) and X is an $n \times k$ matrix consisting of the predictor indices. We also define significance levels for $\hat{\beta}_j$ using a one-tailed t statistic (similar to above) with $n - k$ degrees of freedom to test the null hypothesis that $\hat{\beta}_j = 0$. The t statistic is given by $t = \frac{\hat{\beta}_j}{se(\hat{\beta}_j)}$. We also define the coefficient of determination, R^2, of the model which gives the proportion of the variance in the dependant variable (in this case the SSW time series) accounted for by the contributions from the predictor indices (multiplied by their respective coefficients).

A potential pitfall of implementing this regression analysis is the possibility of significant covariations between predictor indices. If the variance of a given predictor is increased due to covariability with other independent variables, the standard error on the coefficient's estimate, $se(\hat{\beta}_j)$, may be artificially inflated leading to difficulties in deriving meaningful findings from the model. A method for quantifying the severity

of this multicollinearity issue for a given regression model is the variance inflation factor (VIF) [*Akinwande et al.*, 2015]. VIF_j, indicates the degree to which $se(\hat{\beta}_j)$ is increased through the effects of all other predictors. It is given by $VIF_j = \frac{1}{1-R_j^2}$ where R_j^2 is the coefficient of determination of a separate linear regression model with predictor j (the AL, for example) as the dependant variable and all other predictors from the original regression model as the independent variables. For the example of the AL (j = 3), this model is given by

$$AL = k_1 QBO + k_2 ENSO, \tag{3.19}$$

where $k1$ and $k2$ are the estimates on coefficients of the secondary model. A value of $VIF_j >\sim 5$ indicates that multicollinearity has significantly increased the standard error on $\hat{\beta}_j$ and that the estimates of coefficients for the original model may be compromised by this effect. A $VIF_j > 1$ indicates a marginal effect from multicollinearity.

3.2.6.4 EOF analysis

We also utilise a method for diagnosing patterns of variability in a quantity defined on a spatial and temporal grid. Such a method, known as Empirical Orthogonal Function (EOF) analysis decomposes a function, y, into a set of basis functions that indicate the spatial patterns that maximise variance in y.

if y is defined on N time points and M spatial points then the time anomalies of y, defined as $y' = y - \overline{y}$ ($\overline{y}$ = the time mean of y at each spatial point) can be expressed as an $N \times M$ matrix denoted as Y. The EOFs, e_n, are subsequently defined as the eigenvectors of the covariance matrix of Y, $C = \frac{1}{N-1} Y^T Y$, such that $Ce_n = \lambda_n e_n$. λ_n is the eigenvalue which can be used to indicate the proportion of total variance in y explained by the EOF e_n. Such a metric, the variance fraction, is given as $v_n = \frac{\lambda_n}{\Sigma_i \lambda_i}$ - the ratio of a given eigenvalue to the sum of all eigenvalues. EOFs are ordered by

eigenvalue size such that EOF1 explains the largest fraction of the total variance. Projecting the matrix Y back onto a given EOF, e_n, gives the n^{th} principal component (PC) time series given by $PC_n = Ye_n$. For many applications of EOF analysis for diagnosing climate variability, the first 2 EOF patterns sufficiently explain the variance in quantities such as mean sea level pressure (MSLP) or geopotential height. In the work presented here, we utilise EOF and PC analysis to construct climate variability indices such as the NAM, NAO and AL.

3.2.6.5 SSW statistics

In order to assess the model's representation of vortex variability, we introduce a statistical framework that uses parametric and bootstrapping methods to assess significance levels for differences in SSW abundance across datasets. First, a parametric approach which assumes that the occurrence of any number of SSWs (denoted as N) in a given number of winters (denoted by k) can be modelled as a Poisson process and is distributed as

$$P(N(k) = n) = \frac{(\lambda k)^n}{n!} e^{-\lambda k}, \tag{3.20}$$

where λ is the intensity of the Poisson process calculated as the mean SSW rate over k winters. For two such processes with intensities λ_1 and λ_2 the difference in intensity, $\Delta\lambda$ can be expressed as

$$\Delta\lambda = \frac{\lambda_1 - \lambda_2}{\sqrt{\frac{\lambda_1}{k_1} + \frac{\lambda 2}{k_2}}}, \tag{3.21}$$

where k_i is the number of instances of the process i (number of winters sampled). *Charlton et al.* [2007] suggest that if a pair of Poisson processes are recorded for more than 30 instances each then $\Delta\lambda$ can be assumed to be normally distributed. *Gu et al.* [2008] and *Huffman* [1984] present an alternative test for the significance of

$\Delta\lambda$ in cases where the datasets underlying each process are of different lengths (i.e. for comparing model and reanalysis data). For this analysis, we introduce the test statistic

$$W(X_1, X_2) = 2\frac{\sqrt{X_1 + 3/8} - \sqrt{\rho(X_2 - 3/8)}}{\sqrt{1+\rho}}, \tag{3.22}$$

where ρ is the ratio of observation lengths of the datasets and X_i is the number of observations of events (number of SSWs) in dataset i. W is distributed an with associated p-value,

$$P = 1 - 2\psi(W(X_1, X_2)), \tag{3.23}$$

where $\psi(W)$ is the cumulative distribution function of the normal distribution. This statistic provides a parametric test for significance between different SSW rates and the associated p-value is referred to as P_{para} to distinguish it from other tests.

Additionally, we utilise a bootstrapping approach to test significance in SSW rate differences. For this method we assume two datasets produce a set of time series of the number of SSWs in each winter. These are denoted as $[X1, X2.....X_k]$ and $[Y1, Y2.....Y_j]$ and the mean SSW rate can be expressed as $\mu_X = \frac{\sum[X_1, X_2.....X_k]}{k}$. A confidence interval for an observed difference in mean SSW rate ($\Delta\mu = \mu_X - \mu_Y$) can be constructed by forming a pooled dataset, $Z = [X_1, X_2, ...X_k, Y_1, Y_2, ...Y_j]$ and randomly choosing (without replacement) synthetic datasets of the same length as X and Y from Z and subsequently calculating synthetic mean differences. Repeated choosing can build up a distribution for mean differences and a confidence interval for the real difference, $\Delta\mu$. We perform a set of 10000 random choices for this statistical test and the associated p-value is referred to as P_{boot}.

3.2.7 Model diagnostics

We utilise the definition of an SSW event from *Butler et al.* [2015]. An event is recorded when the ZMZW at 60°N on the 10 hPa level transitions from westerly to easterly during NH winter months (November - March). The day on which this reversal occurs is referred to as the central date. After this date, the ZMZW must recover to westerly for at least 10 consecutive days (which is the approximate radiative timescale of the mid-stratosphere) before another event can be recorded. If, after the central date, the ZMZW does not recover to westerly for at least 20 consecutive days before the end of April, the warming is classified as a final warming. While we do record all events in extended winter (Nov-Mar) for an initial analysis of mean SSW rates, we use mid-late winter warmings (Dec-Mar) for our analysis of multi-decadal variability and interaction with other climate variables (this choice is addressed in section 3.3).

We analyse variability in tropical SSTs in four regions identified by *Scaife et al.* [2017] as key to affecting Rossby wave propagation and interactions with stratospheric winds. The regions are defined as the Tropical Atlantic ($5°S$-$5°N, 60°W$–$0°W$), Tropical East Pacific ($5°S$–$10°N, 160°$–$270°E$), Tropical West Pacific ($5°S$–$25°N, 110°$–$140°E$) and Tropical Indian Ocean ($5°S$–$10°N, 45°$–$100°E$). Additionally, we calculate an El Niño Southern Oscillation (Niño3.4) index as the SST anomaly in the region $5°S$-$5°N, 170°W$–$120°W$ following *Trenberth and Stepaniak* [2001]. We use an index to track the intensity of the AL based on the method of *Chen et al.* [2020]. The AL index is defined as the first PC of winter mean sea level pressure (MSLP) anomalies averaged over the region $120°$–$240°E, 20°$–$70°N$. We employ an EOF-based method as opposed to a fixed box average to allow for the fact that the centre of the model AL may not line up well with observations. The month range used for studies into AL-vortex teleconnections varies somewhat with *Overland et al.* [1999] using both Jan-Feb and Nov-Mar while *Hu and Guan* [2018]

use a core winter metric (Dec-Feb). Unless stated otherwise we use the same month range as our SSW definition (Dec-Mar); for all analyses, tests were performed to check that the results were not unduly sensitive to the choice. An index for the Pacific Decadal Oscillation (PDO) was determined following the methodology of *Mantua et al.* [1997] using the leading PC of Pacific basin (120°–240°E) SST anomalies poleward of 20°N. Finally, a QBO index was defined by a variety of measures (see section 3 for further discussion), using the monthly mean ZMZW averaged between ±5° latitudes at various stratospheric pressure levels (15 hPa, 20 hPa, 30 hPa, 50 hPa, 70 hPa) as well as two 'deep QBO' indices computed by taking the average of the ZMZW between 15-30 hPa (as in *Andrews et al.* [2019]) and between 20-50 hPa to identify QBO phases that exhibit winds of the same sign over a relatively large vertical extent.

3.3 Modes of stratospheric variability

We begin by analysing the representation of modes of stratospheric variability in the UKESM pi-control simulation. The winter polar stratospheric vortex exhibits substantial variability. In some years the westerly winds of the vortex are relatively strong and undisturbed while in other years the vortex is weakened by wave disturbances that in extreme cases can lead to SSWs. The average Nov-Mar SSW rate over the full 1000 years of the UKESM simulation is 0.54 events/winter (figure 3.2a). This represents a marginal underestimation compared to ERA-Interim (0.62 events/winter between 1979 and 2019) but is within 1 standard error of the observations and the difference in SSW rates is not deemed significant to the 95% level under both the parametric and bootstrapping significance tests outlined in section 3.2.6.5 ($P_{para} = 0.162$ and $P_{boot} = 0.159$).

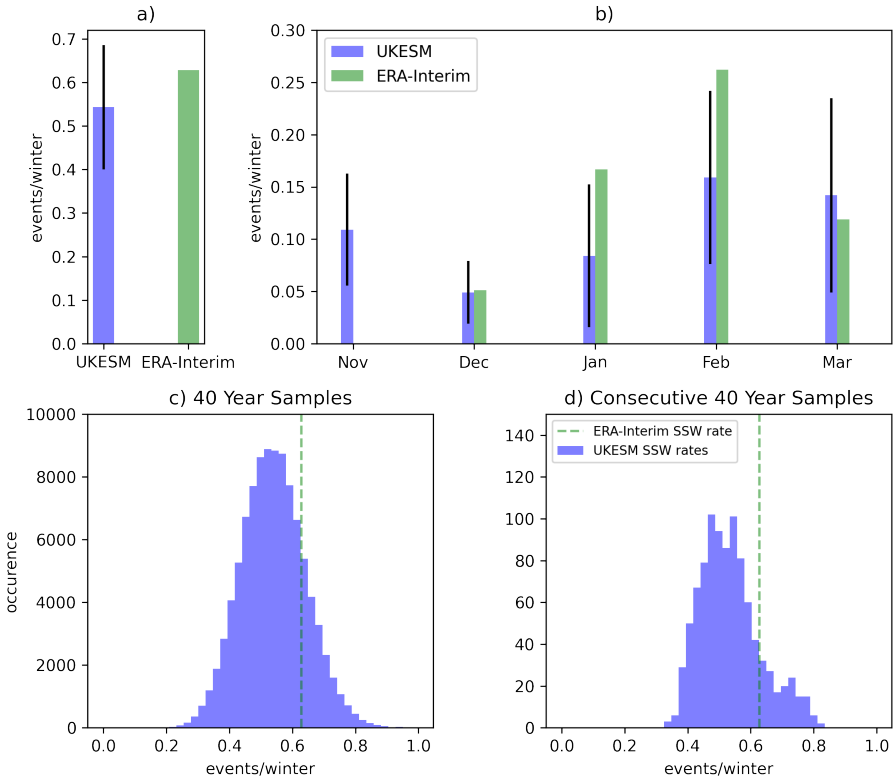


Figure 3.2: **a**: SSWs per NH winter season in the UKESM pi-control and the ERA-Interim datasets. **b**: SSW rates separated by months. Error bars on a and b are derived using a bootstrap resampling method in which random selections of 40 years (the length of the reanalysis dataset) are chosen from the SSW data and the SSW rate recorded to build a PDF of events per season. 100000 such resamples are carried out and the 95 and 5 percentile values are used as error bounds. This PDF is shown in blue bars in panel **c**. **d**: PDF of SSW rates in consecutive 40-year intervals of the UKESM simulation (blue bars). The SSW rate in ERA-Interim is indicated by the green dashed line in panels c and d.

This is also reflected in the bootstrapped PDFs of both consecutive and non-consecutive 40-year random samples of the simulation (figures 3.2c and d) in which the SSW rate in ERA-Interim lies within the top 10 percentile value. The PDF of consecutive 40-year intervals (figure 3.2d) exhibits elements of double peak behaviour with a secondary peak corresponding to rates of 0.75 events/winter. This suggests that within the simulation there exist 40-year intervals with significantly different SSW rates implying the possibility of variability in these events on 40-year timescales and above. The model adequately represents the seasonal distribution of SSWs compared to the

reanalysis dataset, as shown in figure 3.2b, but exhibits too many warming events in November and an underestimation of Jan and Feb warming rates (see *Andrews et al.* [2020] and *Menary et al.* [2018] for further details). This bias is well known and relatively common in GCMs [*Charlton et al.*, 2007; *Ayarzagüena et al.*, 2020]. On the other hand, we note that validation of this pre-industrial control simulation with ERA-Interim data is not optimum. The sample sizes of the ERA-Interim data and the model are very different and could give rise to differences in distributions [*Horan and Reichler*, 2017] but our use of the different significance testing methods attempts to account for this difference. the ERA-Interim SSW rates may also be influenced by anthropogenic forcing, the impact of which is not well understood [*Ayarzagüena et al.*, 2020]. In all analyses presented in the following sections, tests have been performed to ensure that the results are not sensitive to the inclusion or exclusion of November SSW rates.

The model exhibits variability in SSW frequency comparable to observations, including both hiatus and consecutive SSW intervals. Figure 3.3 shows a sample 40-year interval of the polar vortex zonal wind strength and SSW occurrence from the UKESM simulation compared with a similar length from the ERA-Interim reanalyses. An extended interval of mainly westerly anomalies indicating a strengthened vortex and lack of SSWs can be seen towards the end of the 40-year interval, similar to the 1990s in ERA-Interim when only 2 SSW events were recorded in the decade. The simulation contains 8 such hiatus intervals with at least 10 consecutive years with no SSWs, the longest of which lasts 16 years. On the other hand, the simulation only contains 2 intervals in which 10 consecutive years exhibit at least 1 SSW. However, if the threshold interval width for identifying hiatus and consecutive-SSW intervals is shortened from 10 to 5 years, then 9 consecutive-SSW intervals and 25 hiatus intervals are found. These statistics indicate that UKESM is not only able to reproduce the mean state characteristics of SSW events but also decadal-scale variations in SSW

rate, underlining its suitability for this study.

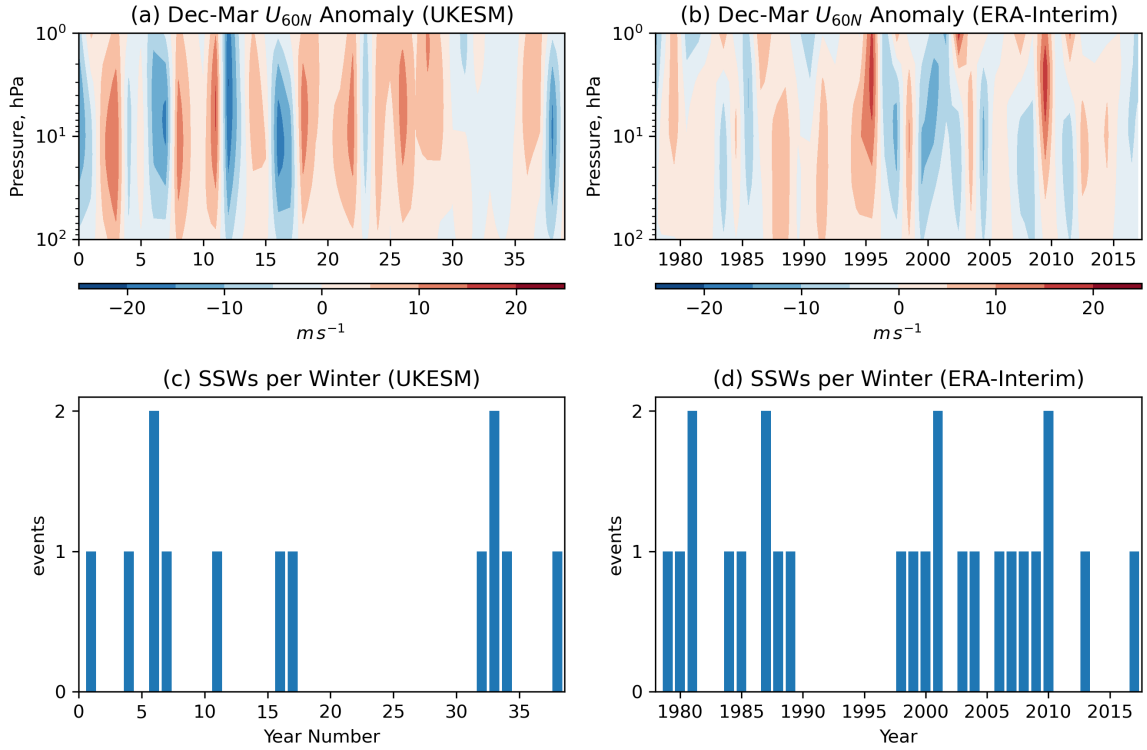


Figure 3.3: (a, b): Dec-Mar annual mean ZMZW anomaly from the climatological mean at 60° N from a 40-year sample from the pre-industrial control simulation of UKESM (a) and the ERA-Interim dataset between 1979 and 2018 (b). (c, d): Time series of SSWs recorded per winter season in the same datasets.

The second major mode of stratospheric variability is the QBO at equatorial latitudes which is present at all times of the year. Figure 3.4 shows the equatorial wind time series from a sample 40-year interval of the simulation compared with the ERA-Interim dataset. The mean period of the oscillation is longer than observed, at ∼38 months compared to ∼28 months in ERA-Interim [*Kawatani et al.*, 2016]. As a result, the vertical shear zones descend less rapidly than observed. There is also a westerly bias at low levels where the QBO-E phase does not extend sufficiently deep into the lower stratosphere, which is a common bias in many models [*Bushell et al.*, 2020]. The descending shear zones also appear more regular than observed but there is nevertheless some evidence of decadal-scale variations e.g. in the degree of stalling

at 30 hPa, although not as pronounced as in the observations.

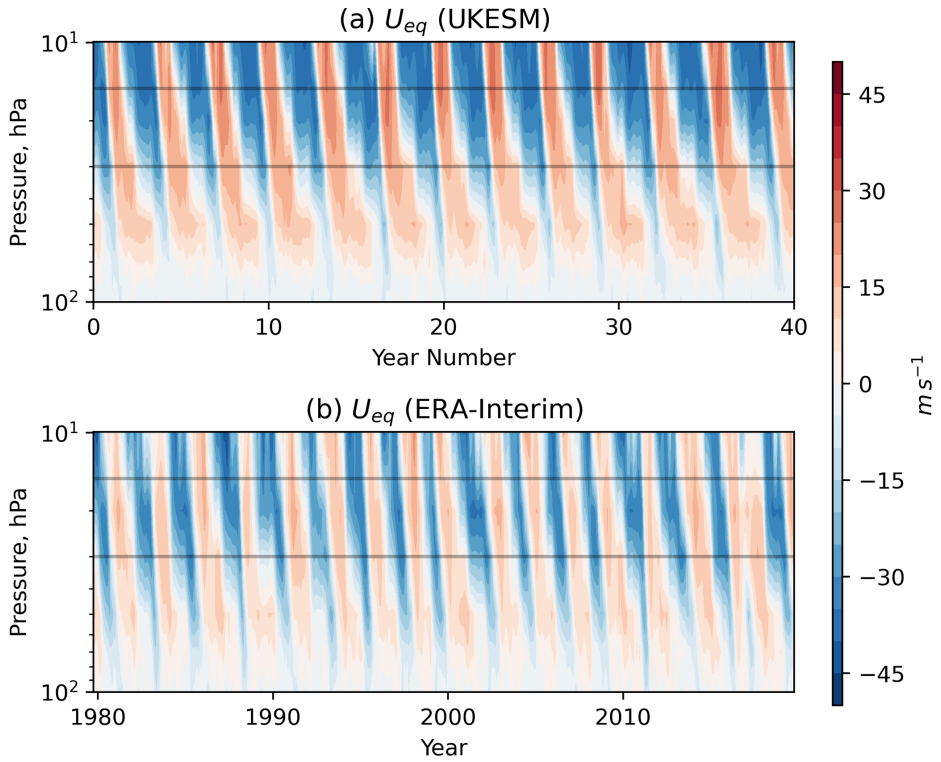


FIGURE 3.4: ZMZW averaged between 5° S–5° N latitude from a 40-year sample of the pre-industrial control simulation of UKESM **(a)** and the ERA-Interim dataset between 1979 and 2018 **(b)**. Horizontal lines mark the 15 hPa and 30 hPa levels between which the deep QBO metric employed by *Andrews et al.* [2019] is defined.

There is evidence of coupling between the two major modes of stratospheric variability in the model, giving rise to a Holton-Tan relationship [*Anstey and Shepherd*, 2014]. Figure 3.5 shows height-latitude cross-sections of NH winter ZMZW differences between QBO E-W composites defined at various equatorial levels. The familiar pancake structure of alternating easterly/westerly differences is present at equatorial latitudes, indicative of the QBO phase but there is also a response at high latitudes. In good agreement with observations, the largest high latitude response amplitude is seen when the QBO is defined at 50 hPa, with anomalously weaker polar vortex strength in QBO-E than in QBO-W years. Higher levels (15 hPa and 20 hPa) show little significant QBO-vortex coupling. For comparison, we also show in figure 3.5 the

composite different response for QBO composites selected on the basis of the average QBO winds over a greater depth of the equatorial atmosphere (15-30 hPa and 20-50 hPa). We note that while this QBO definition will select some of the same years as in the separate single-level composite definitions, it is specifically designed to identify only QBO phases that have extended vertical coherence, following [*Gray et al.*, 2018] and *Andrews et al.* [2019], so the resulting composite differences in figure 3.5 will not necessarily be an average of the corresponding single-level differences. Interestingly, the 15–30 hPa deep-QBO selects years that exhibit not only a weaker polar vortex in QBO-E but also a weaker sub-tropical tropospheric jet (see 200 hPa, 30°-40°N). This results in a more coherent response in the mid-latitude troposphere and at the surface, in excellent agreement with the results of *Gray et al.* [2018] and *Andrews et al.* [2019].

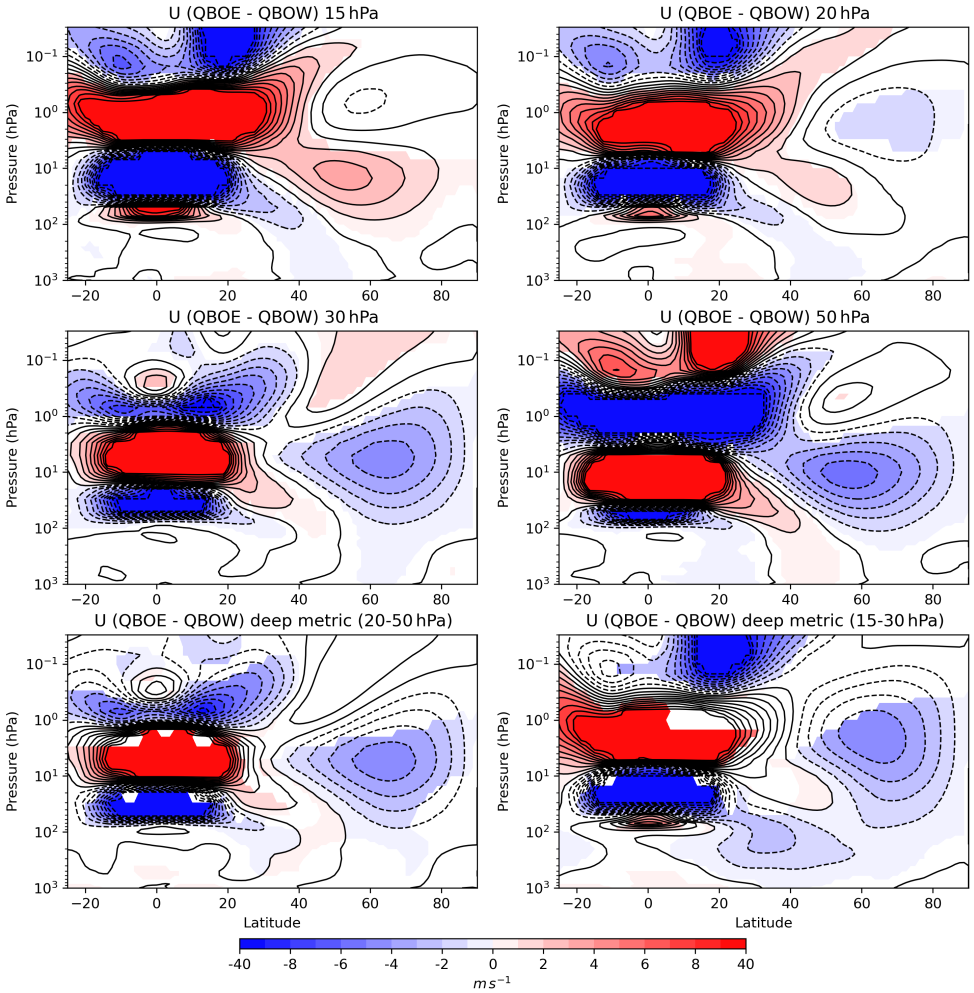


FIGURE 3.5: Dec-Mar ZMZW composite differences between QBO East and QBO West phases on individual levels as well as using two deep QBO metrics. The phase of the QBO is defined as any Sep-Nov equatorial (5° S–5° N average) ZMZW that exceeds a magnitude of 5 m s^{-1}. Coloured shading indicates differences significant above the 95% confidence level under a 2 tail Student's t-test.

The presence of the Holton-Tan relationship is also seen in the modelled frequency of SSWs (figure 3.6). Significantly higher rates are observed in QBO-E winters than QBO-W. Also notable is the asymmetry in the abundance of QBO-E and QBO-W winters - nearly twice as many QBO-E winters are observed compared to QBO-W under all phase definitions (figure 3.6, legends). This suggests an element of phase locking between the QBO and the seasonal cycle possibly associated with seasonal variations in the strength of mean equatorial upwelling or mid-latitude planetary wave

forcing in winter [*Pascoe et al.*, 2005; *Gruzdev and Bezverkhny*, 2000; *Rajendran et al.*, 2016] resulting in QBO phase transitions that occur preferentially in certain months.

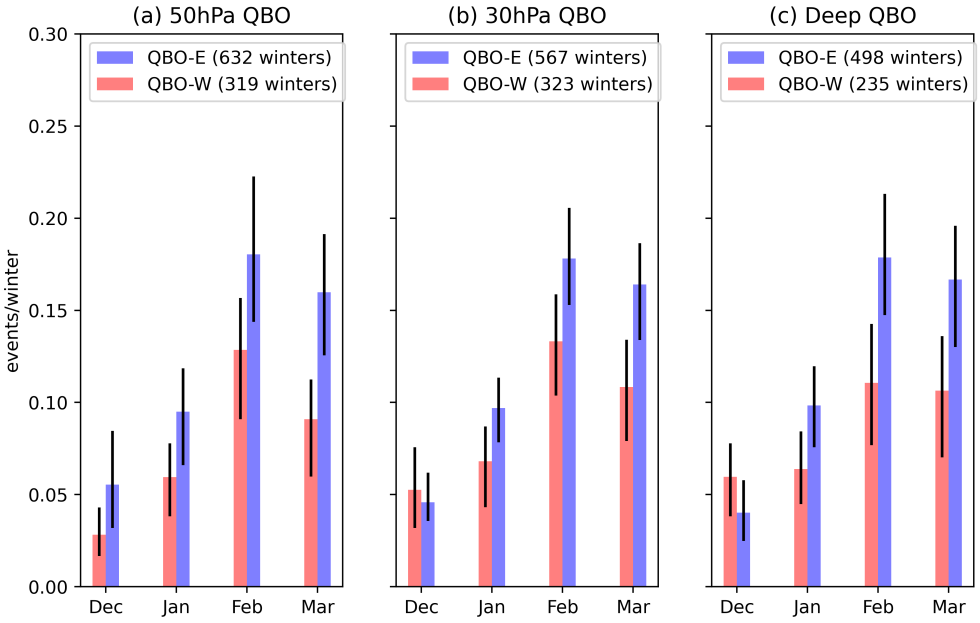


Figure 3.6: SSWs per winter season for years exhibiting QBO-E and QBO-W conditions in early winter (Sep-Nov) defined on different pressure levels (a,b) as well as using the deep metric (c), the vertical mean between 15 and 30 hPa defined in *Andrews et al.* [2019]. The QBO phase is defined as any Sep-Nov equatorial (5° S–5° N average) ZMZW that exceeds a magnitude of 5 $\mathrm{m\,s^{-1}}$. Error bars on all plots are derived using the same bootstrapping method outlined in figure 3.2

There is also evidence of in-season coupling between the vortex and phases of ENSO as well as the AL. Composites of ZMZW under different Niño3.4 conditions (figures 3.7a and b) shows a response from vortex winds to the 2 types of anomalous ENSO behaviour. The vortex appears significantly stronger under La Niña conditions and weaker under El Niño, a result which is consistent with numerous studies from both observations and other models (see section 2.5.3). As is noted in *Polvani et al.* [2017], the vortex response to ENSO in the model appears more linear than those generally found in observation-based studies; the magnitude of responses to each phase is similar. In contrast, the vortex response to different signs of the AL (figures 3.7c and d) index is highly asymmetric. The vortex is considerably weakened under

anomalously negative AL values (corresponding to a more intense Aleutian Low) while the positive AL phase leads to only a marginal strengthening in vortex winds. This may be due to the proposed mechanism by which the AL influences the vortex, via alteration of planetary wave propagation into the stratosphere. This provides modulation of the weakening mechanism of the vortex under negative AL but not a strengthening under positive - simply an absence of wave fluxes. Nevertheless, these AL composites are consistent with the findings of studies outlined in section 2.5.2 which report a weakened vortex under negative AL conditions. Both sets of composites indicate that the model is able to reproduce expected in-season vortex responses from these key modes of surface variability, further suggesting its suitability for analysis of the external influence on the vortex from these modes on multi-decadal timescales.

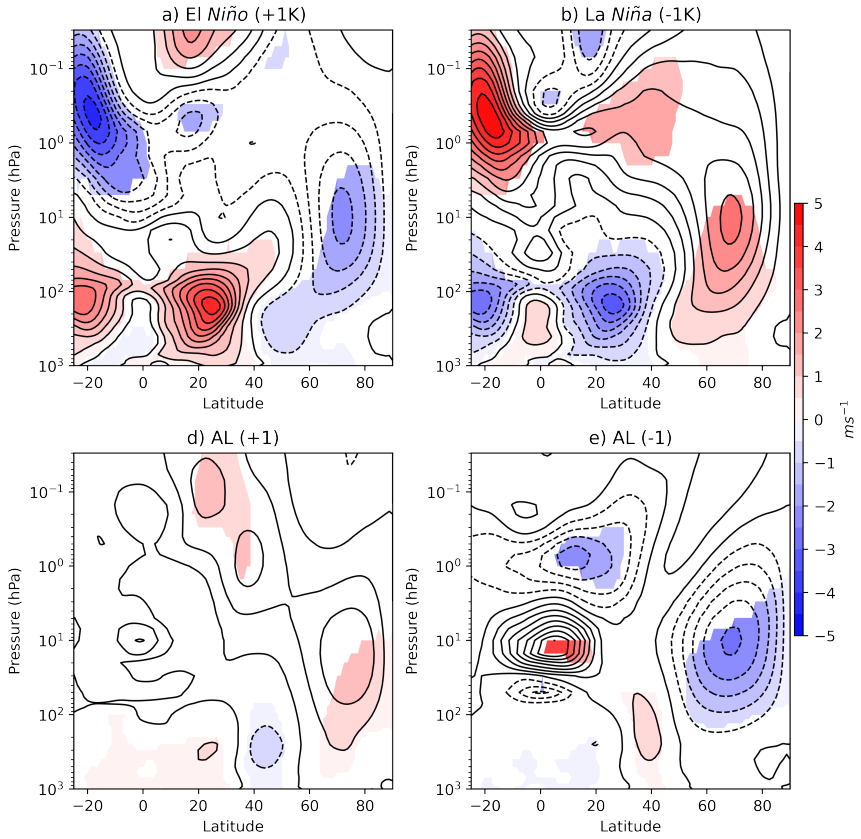


Figure 3.7: Dec-Mar ZMZW anomaly composites for positive (El Niño) and negative (La Niña) phases of the Niño3.4 index evaluated in Sep-Nov (a, b) and the AL index evaluated in Dec-Feb (c, d). The phase of Niño3.4 is defined as an SST anomaly of greater magnitude than 1K and the AL phase as an index value derived using the PC-based definition of greater magnitude than 1. Coloured shading indicates anomalies significant above the 95% confidence level under a 2-tailed Student's t-test.

3.4 Regression analysis

We next employ multi-linear regression analysis to measure the relative contributions to the time series of SSWs per year (as in figure 3.3) from the QBO, ENSO and the AL. The results from this analysis are summarised in table 3.1. Sensitivity experiments were performed to identify the optimum averaging lagged response by the vortex to each index: the deep 15-30 hPa QBO index and Niño3.4 indices were both defined using early winter (Sep-Nov) averages while the AL index was defined using Dec-Mar

averages. The coefficients are all significant to the 95% level but are relatively small and the R^2 score is only 0.047 indicating these variables account for only a small portion of the variability in the SSW time series. While results from this multi-linear regression analysis are easy to interpret, the approach does not directly tackle the problem posed in this study, that of multi-decadal variability in SSWs and its origins, for two main reasons: Firstly, regression analysis assumes stationarity i.e. it provides a measure of stationary contributions to variability and will only highlight signals that are relatively persistent for the whole simulation. Secondly, it analyses variability in the time series at all timescales simultaneously, so that the results are dominated by the timescales with larger amplitude variations. This means that the results in table 3.1 are most likely dominated by the shorter (inter-annual) timescales and any small amplitude variations at longer timescales will not be revealed. The latter can be addressed to some extent by smoothing or filtering the time series, as discussed in the next section, but this requires prior knowledge of which frequencies are of interest. Furthermore, co-variability in predictor indices of a regression model may lead to spuriously large errors on coefficients. This may be an issue here as *Rao et al.* [2019] note correlations between ENSO and the AL. The VIF for each predictor (see section 3.2.6.3), which gives an indication of this issue in a linear model, is greater than 1 indicating a moderate degree of co-variation with other predictors which may further hamper the efficacy of this regression method [*Akinwande et al.*, 2015]. An alternative and superior approach to this problem employs wavelet analysis, described more fully in the next section, which successively examines different frequency intervals to identify the presence of signals thus avoiding dominance by one particular frequency, and also measures the time evolution of the signal so that non-stationary signals can also be identified.

SSW regression		
Regression Variable	Coefficient	p-value
Niño3.4	$0.1625^{+}_{-}0.035$	0.0002
AL	$-0.0927^{+}_{-}0.04$	0.048
deep QBO	$-0.1993^{+}_{-}0.03$	0.0001

Table 3.1: Summary of results from regression analysis of SSWs per NH winter time series.

3.5 Long-term variability of the polar vortex

A more comprehensive assessment of the long-term variability of SSWs can be made using a wavelet power spectrum approach outlined in section 3.2.3. We count the number of SSWs in each winter season (Dec-Mar) and calculate the corresponding wavelet power spectrum, shown in figure 3.8. As described above, the analysis highlights the presence of power in the signal as a function of frequency (period in years, along the y-axis) and as a function of time (year of simulation along the x-axis). As expected, there is an intermittent but relatively persistent signal with a period of around 2-4 years throughout the simulation, corresponding to the period of the QBO which supports the presence of a Holton-Tan relationship between the QBO and the polar vortex in the model. The so-called 'global power spectrum' (i.e. the time average of the wavelet spectrum) shown on the right of figure 3.8 shows that the signal is on the boundary of the 95% statistical significance. Other signals at periods near 20-30 years are similarly intermittent and manifest as a peak in the time-averaged spectrum that is also near the 95% significance boundary. There is also a feature at periods between ∼60-90 years in the interval between 400-800 years. This feature shows statistical significance (based on comparisons between power in the spectrum and that of an AR1 process with the same autocorrelation structure as the series being analysed) for around 300 years of the 1000-year simulation but does not cross the significance threshold for the time-averaged spectra. There is a possible limitation of

this wavelet methodology due to the discrete nature of the time series being analysed (time points take values 0/1/2). The Morlet wavelet is a continuous function and, as a result, convolution with a highly discretised series may alias features on the resulting wavelet spectra. This limitation must be considered when drawing conclusions from the wavelet spectra and is discussed further below.

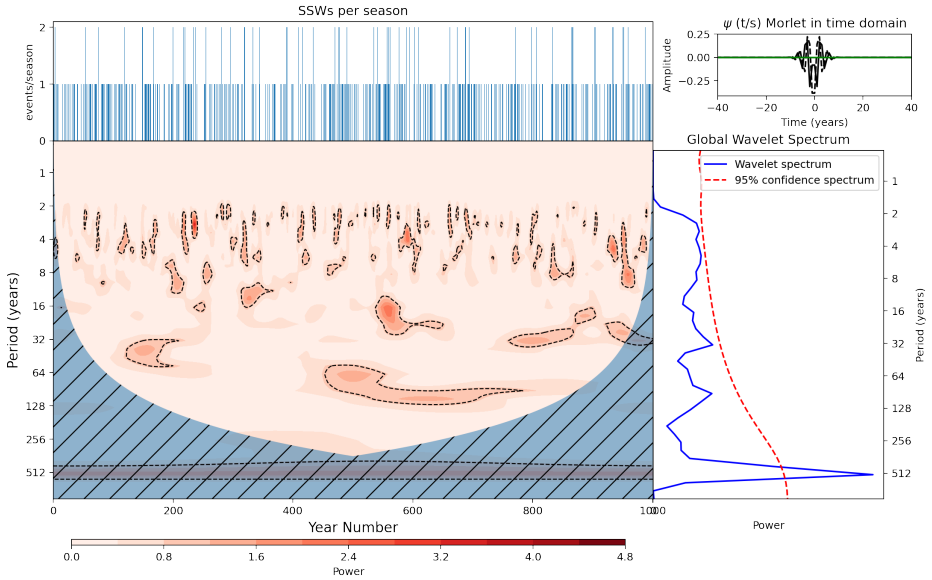


FIGURE 3.8: **Top left**: SSW events per Dec-Mar season in UKESM **Bottom left**: Wavelet power spectrum of time series in top left. Hatching represents an area outside the cone of influence in which edge effects are significant and power should not be considered. Black dashed contours represent the 95% confidence level assuming mean background AR1 red noise. **Top Right**: Morlet wavelet used for the wavelet transform in the time domain. **Bottom right:** Global power spectrum, the wavelet power averaged over the whole simulation (blue line), and global 95% confidence spectrum (red dashed line).

The focus of this study is on the longer-term time variations to understand the source of variability characterised by hiatus intervals (no SSWs over an extended period) and consecutive-event intervals (at least one SSW every year for an extended period). We, therefore, apply low-pass filtering to the time series of SSWs per season using a 5-year rolling window and examine the spectral characteristics of this smoothed series (which we refer to henceforth as SSW_{5yr}). This averaging is similar to the standard practice of smoothing daily data to remove the noise associated with daily

weather variations, thus isolating longer seasonal timescales. It also decreases the impact of the time series discretisation and therefore reduces the chance of introducing spurious spectral features on the wavelet power spectrum which could be otherwise encountered when analysing the un-smoothed time series.

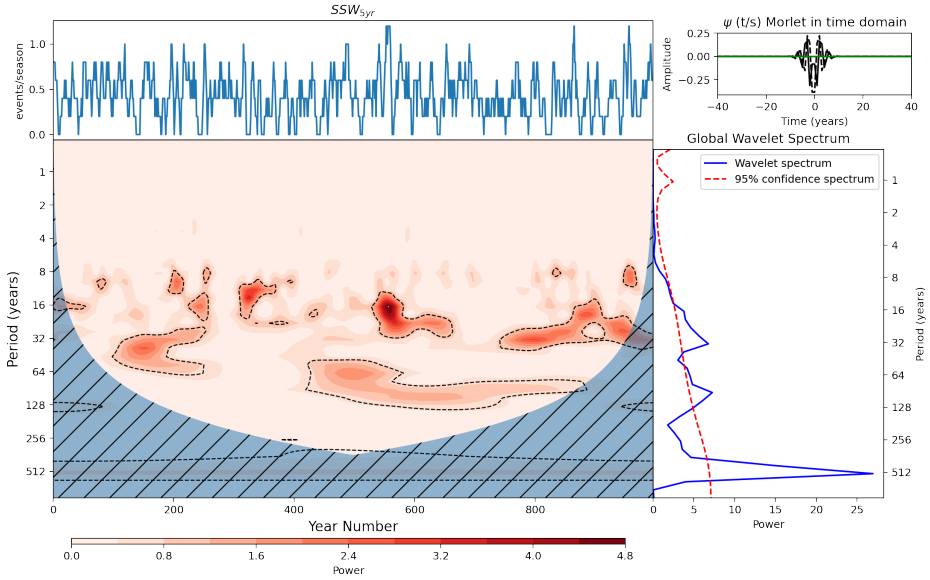


Figure 3.9: **Top left**: SSW events per Dec-Mar season in UKESM smoothed using a 5-year running mean. **Bottom left**: Wavelet power spectrum of time series in top left. Hatching represents an area outside the cone of influence in which edge effects are significant and power should not be considered. Black dashed contours represent the 95% confidence level assuming mean background AR1 red noise. **Top Right**: Morlet wavelet used for the wavelet transform in the time domain. **Bottom right:** Global power spectrum, the wavelet power averaged over the whole simulation, and global 95% confidence spectrum.

The wavelet power spectrum of SSW_{5yr} (figure 3.9) shares many of the characteristics of the spectra of the un-smoothed series (figure 3.8), but the longer period signals are now more clearly evident, as expected. The SSW_{5yr} wavelet spectrum shows the same two broad regions of statistically significant maxima corresponding to signal periods of ∼20-30 years and ∼60-90 years but with increased significance both locally and in the time average. For example, the feature around 90-year period appears significant for 450 years in SSW_{5yr} compared to 350 years before smoothing. One possible explanation for this increase lies in our definition of the significance

level on power which is dependent on the lag-1 autocorrelation of the time series. Introducing a 5-year averaging window will increase the autocorrelation, possibly leading to a less strict significance level. However, this is unlikely because the significance level is constructed using a red noise process with the same autocorrelation as the series. This means that for SSW_{5yr}, the threshold for 95% confidence level increases with increasing period more steeply than in the un-smoothed case and yet the power exhibited at those long periods in SSW_{5yr} nevertheless achieves higher statistical significance. This indicates that the smoothing has enhanced the visibility of a real signal in the SSW_{5yr} time series that was less visible in the un-smoothed time series. As a check for robustness, we also include the SSW_{5yr} wavelet spectrum including the over-represented November SSW events (figure 3.10). It looks similar to the spectrum shown in figure 3.9 but contains more persistent power on the 8-32 year timescales. The feature noted on the Dec-Mar SSW_{5yr} wavelet spectrum on $\sim$60-90 years timescales is also present with persistent power for around 450 years of the simulation at these periods. We proceed with the Dec-Mar SSWs for the analysis of possible drivers of this variability as the cause of the November SSW bias in the model is not fully understood and may make the attribution of signals more difficult.

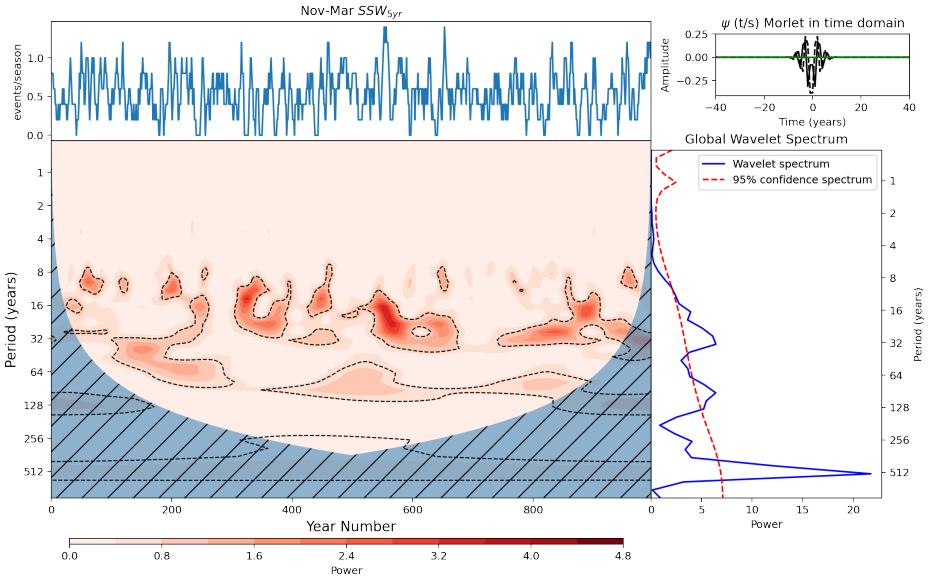


Figure 3.10: Like figure 3.9 for the Nov-Mar SSWs per NH winter season time series smoothed with a 5-year rolling window.

3.6 Surface forcing of polar vortex variability

In the absence of external forcing mechanisms such as greenhouse gas or anthropogenic aerosol forcing, the presence of long-term variability such as the 60-90 year periodicity seen in SSW_{5yr} (figure 3.9) suggests a source of long-term internal variability from within the climate system.

The most obvious potential driver of such long-timescale variability is the ocean due to its high degree of thermal inertia. Previous work has identified coupling between tropical SSTs and the polar vortex, such as the relationship to ENSO conditions (see section 2.5.3). The model exhibits an expected connection between ENSO and the vortex on interannual timescales indicated by the regression analysis results (table 3.1) and ZMZW composites for El Niño and La Niña winters (figures 3.7a and b). Figure 3.11 shows the wavelet power spectrum for the 5-year smoothed Sep-Nov ENSO 3.4 index as well as the cross power spectrum with SSW_{5yr}. We use the early NH winter

ENSO index to capture the lagged response of the vortex to this mode of variability. The ENSO index is slowly varying so will likely remain in the same state between early and mid-winter. We also smooth the ENSO index for the purposes of calculating the cross-spectrum with SSW_{5yr}. (The spectrum of the un-smoothed Niño3.4 index is provided in figure 3.12 and shows significant power in the expected period range of 4-7 years [*Santoso et al.*, 2017]).

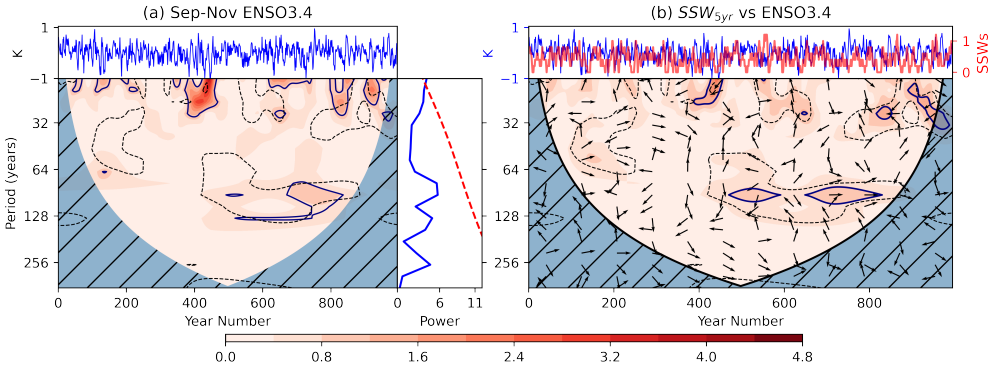


FIGURE 3.11: **(a, top)**: Niño3.4 time series, **a, bottom left**: Wavelet power spectrum (shaded contours represent wavelet power and navy contours the 95% significance level compared to an AR1 process), **a, bottom right**: global wavelet power spectrum (blue) and 95% confidence level (dashed red). **b**: cross-spectra between SSW_{5yr} and the Niño3.4 index. **b, top**: Niño3.4 and SSW_{5yr} time series. **b, bottom**: Cross power spectrum. Shading indicates cross power, navy contours the 95% confidence interval and arrows the relative phase angle between signals in the time series (to the right: in phase, vertically upwards: $\frac{\pi}{2}$ out of phase with SSWs leading, to the left: π out of phase, vertically downwards: $\frac{\pi}{2}$ out of phase Niño3.4 leading). Black, dashed contours on both spectra represent the 95% confidence intervals for the wavelet power spectrum of SSW_{5yr}.

The smoothed Niño3.4 index shows intermittent power at periods around 16 years which appears significant in the global spectrum. It also exhibits a small signal coincident with the 90-year variability in SSW_{5yr} however, this feature only persists for around 100 years of the simulation. The cross-spectrum between the two series (figure 3.11b) reveals that the coincidence in signals at the 90-year period, while significant under our test, is marginally prominent but only covers a small proportion of significant signals in SSW_{5yr}. This suggests there may be some contribution from ENSO to the observed SSW variability but it is only marginally significant and on its

own it cannot explain the signal in SSW_{5yr} that persists for 450 years. The source of this ENSO signal at 90-year periods is unclear, although *Newman et al.* [2016] propose the PDO as a low pass filtered version of ENSO which suggests the possibility of connection between the modes on long timescales. The spectrum for a PDO index is analysed below.

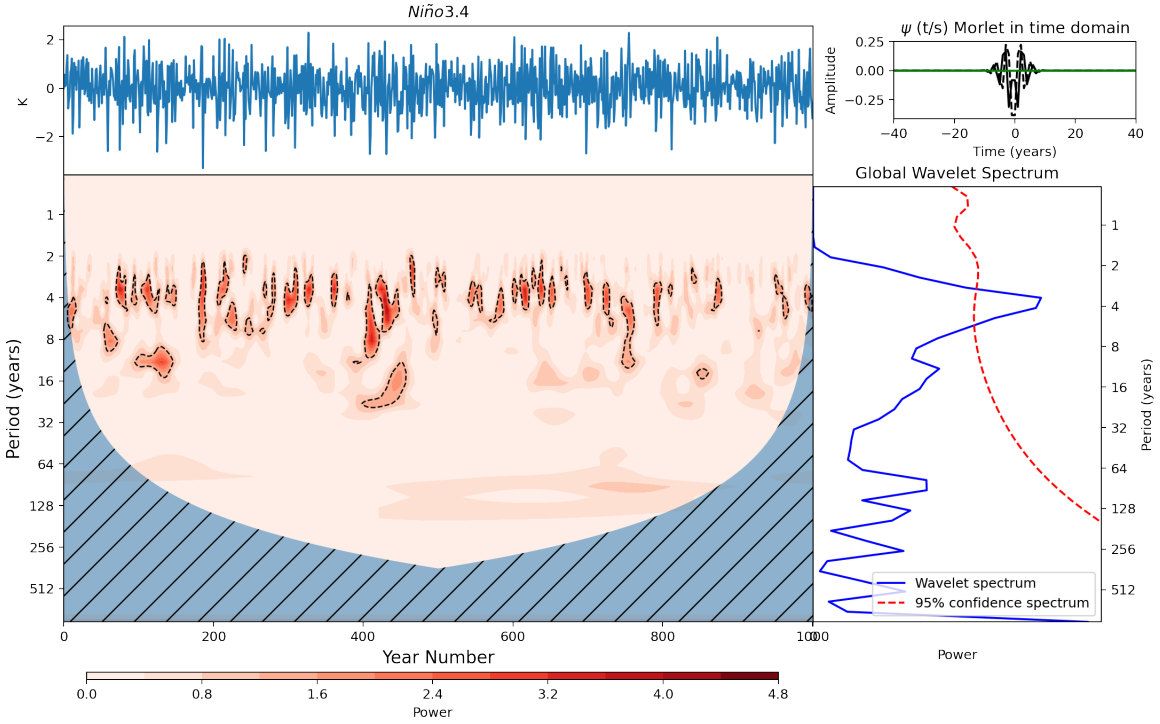


FIGURE 3.12: Like figure 3.8 for the Sep-Nov Niño3.4 index

In the interest of completeness, we also explore the long-term variability of other tropical ocean regions and their potential teleconnections with the polar vortex. Four additional tropical regions were selected based on those identified by *Scaife et al.* [2017] and outlined in section 3.2.7. While all four regions show some elements of multi-decadal variability (figure 3.13), particularly the Tropical Atlantic with a peak period of approximately 140 years for 700 years of the simulation, none of the spectra show variability that coincides well with that of SSW_{5yr}. There is some overlap of the Atlantic and Tropical East Pacific spectra with the regions of significant periodicity at

around 60-90 years in the SSW_{5yr} spectrum but, like the Niño3.4 index, the overlaps between the series are minimal and cannot reasonably explain the vortex signal, especially the signal with a period of approximately 90 years that persists in SSW_{5yr} for around 450 years (figure 3.13 dashed contours).

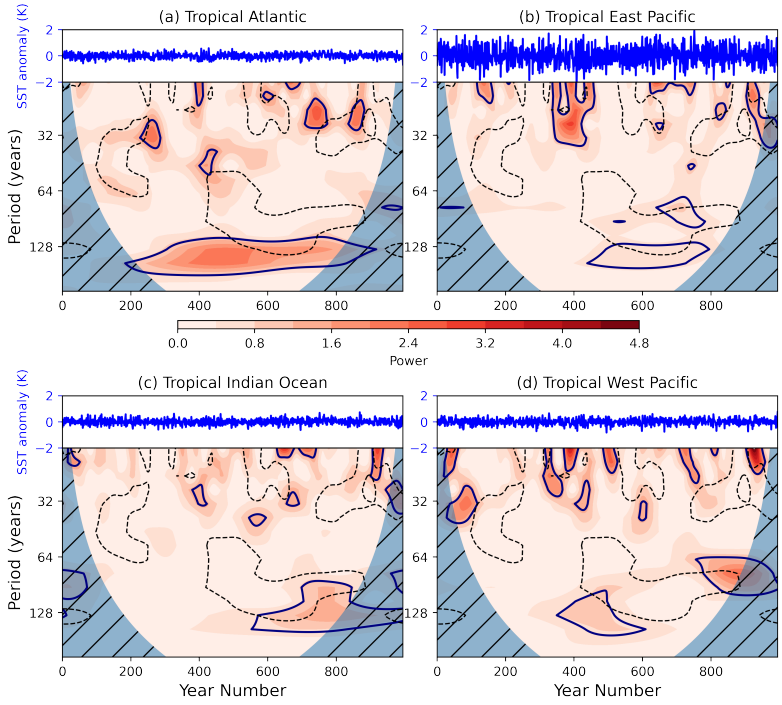


FIGURE 3.13: Sep-Nov SST anomaly time series and associated wavelet power spectrum for Tropical Atlantic (5° S–5° N, 60° W–0° W), Tropical East Pacific (5° S–1° N, 160° E–270° E), Tropical West Pacific (5° S–25° N, 110° E–140° E) and Tropical Indian Ocean (5° S–10° N, 45° E–100° E). Shading indicates wavelet power, navy contours show the 95% confidence level when the power is compared to and AR1 red-noise process and dashed contours indicate the 95% confidence level for the power spectrum of SSW_{5yr}.

The strength of the AL has also been used as an indicator of tropospheric wave forcing and its influence on the polar vortex [*Woo et al.*, 2015]. We perform a similar wavelet and cross-spectrum analysis using an index based on the strength of the modelled NH winter (Dec-Mar) AL (see section 3.2.7 for details). The wavelet power spectrum for the 5-year smoothed AL index (figure 3.14a) exhibits elements of periodic

signals with maximum power corresponding to a period of around 55 years (between 40-60 years) but with fairly minimal overlap with the regions enclosed by the 95% confidence level in the corresponding SSW_{5yr} wavelet analysis (dashed contours). AL indices derived from different winter months give similar spectral patterns (not shown). The cross-spectral analysis between the AL and SSW_{5yr} (figure 3.14b) highlights this relatively small region of overlap in the interval between years 400-500. However, the phase relationship, indicated by the arrows in that region of overlap is difficult to interpret. The proposed physical mechanism of coupling between the AL and the vortex [*Woo et al.*, 2015] involves an association between a deeper AL (i.e. lower pressure and hence a negative anomaly) with increased frequency of SSWs. This negative correlation would give rise to arrows pointing to the left if the relationship was present. In contrast, the upward arrows in figure 3.14b indicate a $\frac{\pi}{2}$ phase difference between the indices on these 60-year timescales, suggesting that peaks in SSW_{5yr} variations are associated with maximum rates of change of the AL index at the same periods.

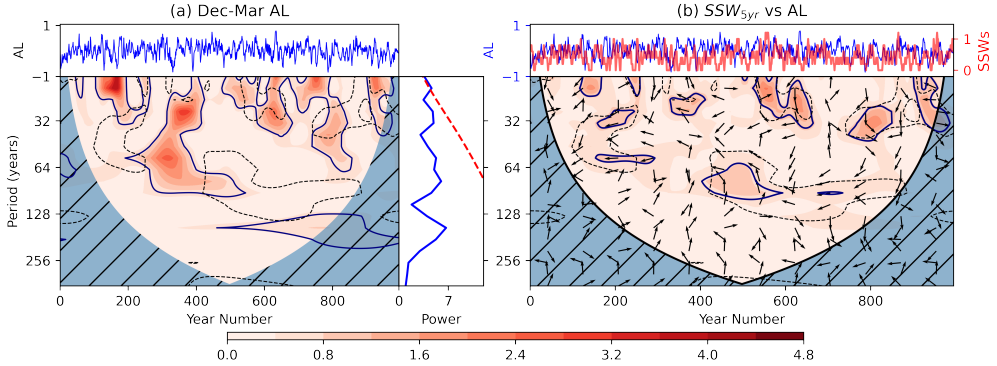


Figure 3.14: Like figure 3.11 for the Dec-Mar AL index smoothed with a 5-year window. **a**: AL time series and associated wavelet power spectrum. **b**: Cross power spectrum between AL and SSW_{5yr}.

The spectra of the AL as well as that of the Niño3.4 index (figure 3.11) shares some features with that of the PDO (figure 3.15), particularly on the 90-year timescale. This is consistent with studies into these modes of variability which find significant

correlations between the PDO and AL [*Mantua et al.*, 1997; *Rodionov et al.*, 2005] as well as studies that examine the influence of the PDO on vortex strength through a pathway involving the AL and ENSO [*Rao et al.*, 2019]. Despite this possible pathway, the relatively short time interval of overlap between the AL and SSW_{5yr} signals at the 60-year period, the absence of any significant signal around the 90-year period, together with the inconsistent phase relationships, points to a conclusion that AL forcing is unlikely to be the primary driver of long-term variability in SSW_{5yr}. Indeed, examination of the cross-spectrum between the un-smoothed AL and SSW indices (figure 3.16) shows little indication of a coherent relationship between periodic signals in the two indices at any timescale. Finally, while the regression results of the un-smoothed indices give a significant coefficient for the AL (table 3.1), its magnitude is small compared to that of Niño3.4 and the deep QBO, the uncertainty on the coefficient is large and the associated p-value is close to the 95% significance boundary. The weak relationship between the AL and SSWs is unexpected due to the well-acknowledged influence of the AL over planetary wave flux in the upper troposphere [*Woo et al.*, 2015]. To attempt to address this, we also analyse an AL metric evaluated as the area-weighted average over a box recommended by *Garfinkel et al.* [2012b] who use an SSW precursor region in 500 hPa height defined by 52.5°–72.5°N, 165°–195°E. However, we find a lower correlation between this measure and our SSW time series than between the original EOF-based metric and SSWs - $r = -0.21$ for the EOF-based AL which is deemed significant to the 95% level by the t-test outlined in section 3.2.6.2. In contrast, $r = -0.13$ for the box-based AL which is deemed not significant to the same level.

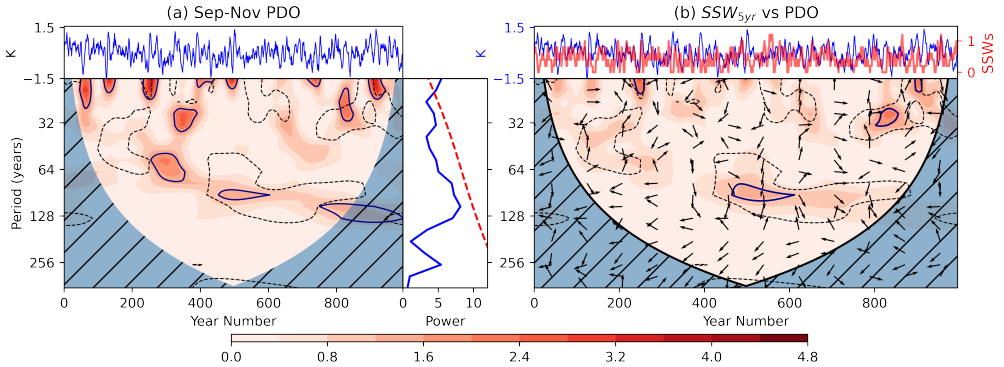


FIGURE 3.15: Like figure 3.11 for the Sep-Nov PDO index smoothed with a 5-year window. **a**: PDO time series and associated wavelet power spectrum. **b**: Cross power spectrum between PDO and SSW_{5yr}.

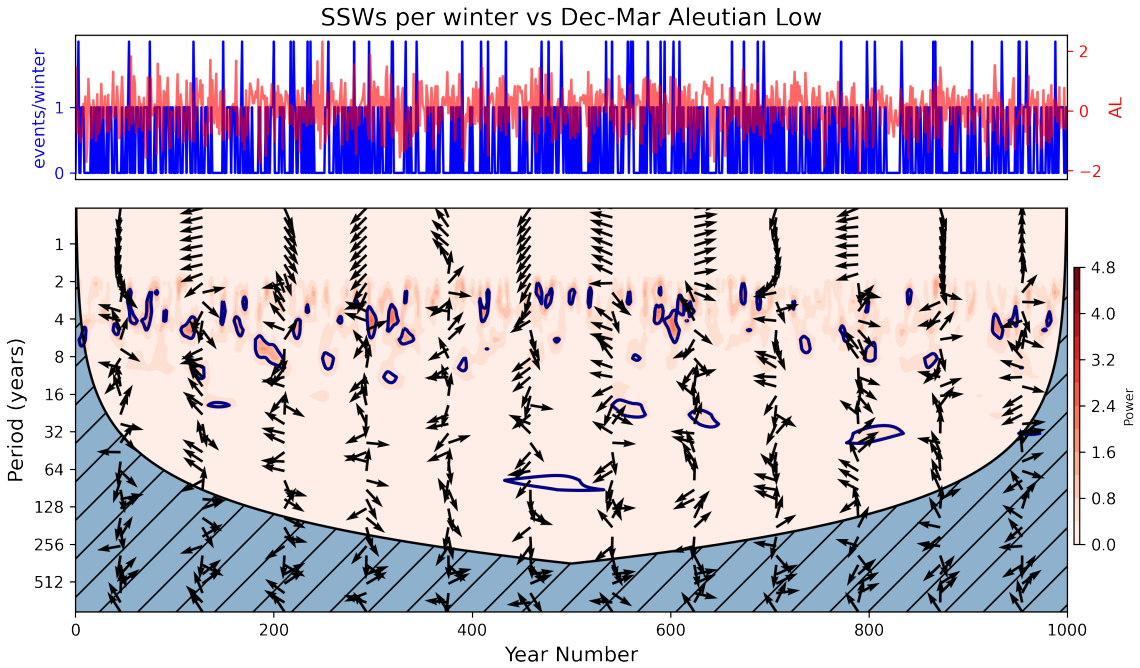


FIGURE 3.16: **Top**: December–March AL index (red) and SSWs per NH winter (blue) time series. **Bottom** Cross-wavelet power spectrum between the two time series.

3.7 Vortex-QBO interactions

Despite some coincident signals between tropical SSTs, AL and SSW_{5yr}, long-term variability in these surface indices are unable to fully account for the multidecadal

signals in SSW frequency. An additional potential source of internally generated long-term variability may reside within the stratosphere. Studies have noted relatively long-term variations in the strength of the Holton-Tan relationship [*Lu et al.*, 2008, 2014; *Osprey et al.*, 2010] although the cause of these variations is not well understood. In order to investigate this figure 3.17 shows the wavelet power spectrum of early winter (Sep-Nov) QBO winds evaluated at selected levels. Since the QBO evolves relatively slowly, employing Sep-Nov averaged winds provides a reasonable representation of the QBO and also allows us to evaluate the in-season lagged relationship between the QBO and subsequent occurrence of an SSW. There is a clear signal between 2 and 4 years for the majority of the simulation, as expected, but no prominent power at longer periods, confirming that there is no significant long-term variability in the periodicity of the QBO winds that could explain the long-term variations in SSW_{5yr} via the Holton-Tan relationship.

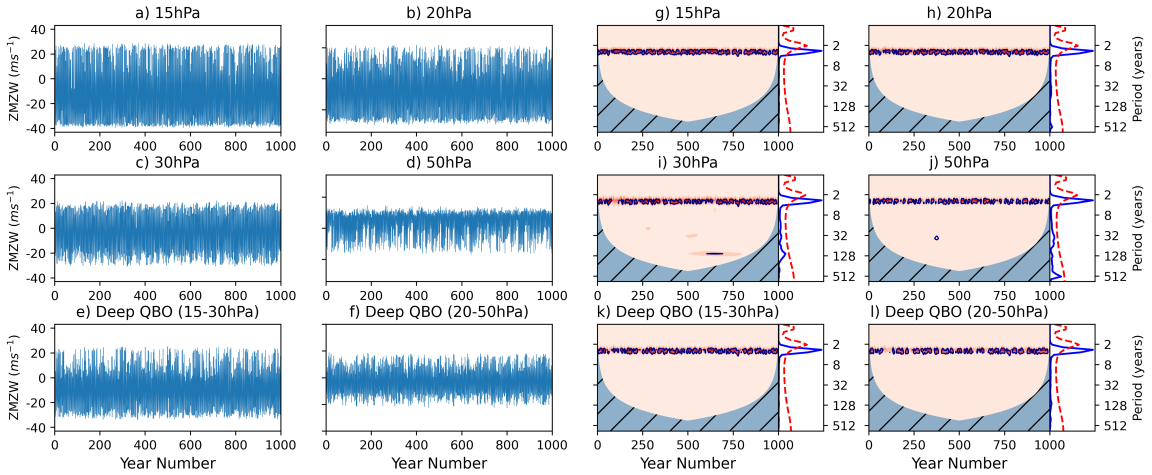


FIGURE 3.17: (a-f): Sep-Nov mean ZMZW averaged between 5°S–5°N latitude on different pressure levels (a-d) and deep metrics averaged between 15–30 hPa (e) and 20–50 hPa (f). (g-l): Wavelet power spectra for each time series shown in (a-f). Shading represents wavelet power with a colour scale the same as that seen in figure 3.9 and navy contours indicate regions of significant power (>95% confidence interval) compared to a background AR1 process.

While the wavelet analysis technique is able to isolate and reveal frequency modulations very well, it is less suited to examine amplitude modulations which are clearly evident by eye in some of the QBO index time series. For example, both the 20 hPa and deep (15-30 hPa) QBO time series show multi-decadal variations in the magnitude of the westerly phase while the easterly phase amplitudes are relatively uniform in time. Similarly, the 50 hPa and 30 hPa time series show amplitude modulation predominantly in the easterly phase. This amplitude modulation can be highlighted by taking the Hilbert Transform of each QBO time series (figure 3.18a-f). Wavelet analysis of the transformed QBO time series now shows significant power on multidecadal timescales (figure 3.18g-l). In particular, the 20 hPa and deep QBO time series exhibit signals coincident in time and around similar periods (60-90 years) to those observed in SSW_{5yr}. On the other hand, the QBO indices based on equatorial winds at 50 hPa or 30 hPa show minimal power at these periods, despite showing a strong intraseasonal HT relationship (figure 3.5). Given that the 15-30 hPa deep QBO index exhibits both multidecadal timescale variability and a strong intraseasonal HT coupling, we continue further analysis of the SSW-QBO interactions using the 15-30 hPa index.

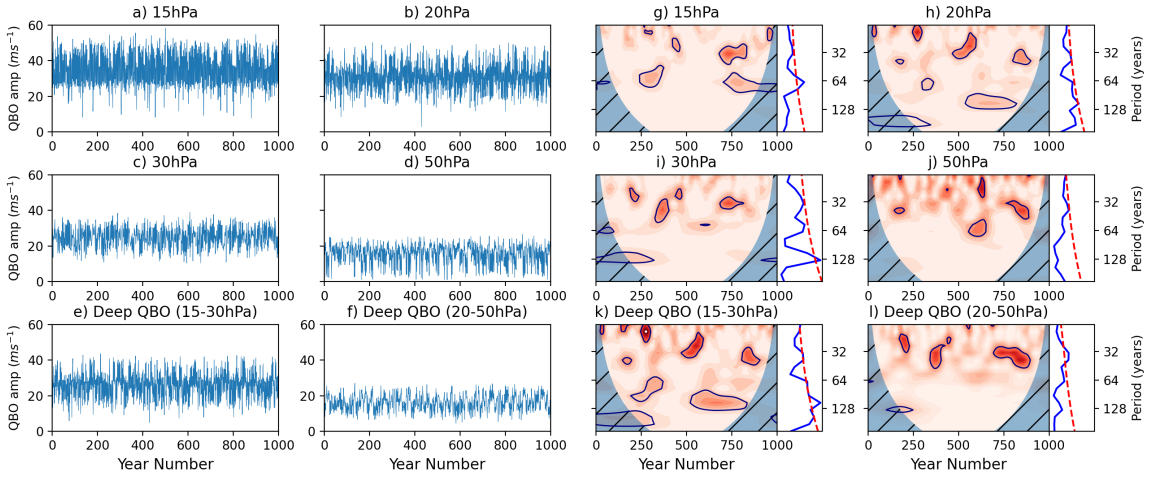


FIGURE 3.18: (a-f): Hilbert amplitude of Sep-Nov mean ZMZW averaged between 5° S–5° N latitude on different pressure levels (a-d) and deep metrics averaged between 15–30 hPa (e) and 50–20 hPa (f). (g-l): Wavelet power spectra for each time series shown in (a-f). Shading represents wavelet power with a colour scale the same as that seen in figure 3.9 and navy contours indicate regions of significant power (>95% confidence interval) compared to a background AR1 process.

Wavelet analysis of the 5-year smoothed deep (15-30 hPa) QBO amplitude modulation index (figure 3.19a) enhances the clarity of the long-term periodicity, showing statistically significant power at around 90 years in the interval between year numbers 500-800. The cross power between SSW_{5yr} and this QBO amplitude modulation index (figure 3.19) coincides extremely well with the signals observed in SSW_{5yr} at around 90 years. There are also coincident features at other timescales, although the feature between years 450-550 at periods of 60 years is less well captured. The phase-relationship arrows in the main region of long-term variability (periods around 90 years in the interval 450-800 years) point broadly to the left (π phase shift), indicating that the signals are approximately anti-phased (the slight downward pointing of the arrows suggests a small deviation from this lag-zero relationship and is discussed below). The anti-phase relationship is consistent with the HT relationship in which a westerly (positive) QBO anomaly corresponds to a reduction in the frequency of SSWs.

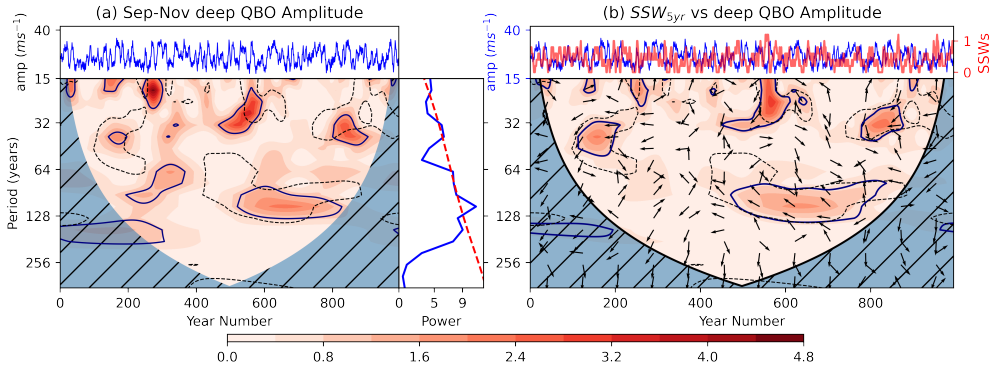


FIGURE 3.19: Like figure 3.11 for the Sep-Nov deep QBO (15–30 hPa) amplitude index smoothed with a 5-year window. **a**: QBO amplitude time series and associated wavelet power spectrum, **b**: Cross power spectrum between deep QBO amplitude and SSW_{5yr}.

In our earlier discussion, we linked long-term variability in SSW frequency to the existence of extended hiatus periods, during which the vortex is relatively undisturbed with no SSW events (figure 3.3). The cross-spectrum analysis with deep QBO amplitude modulation suggests a possible physical interpretation involving the Holton-Tan relationship varying on longer timescales, in which a series of consecutive years that exhibit a large amplitude, deep westerly QBO in early winter leads to a series of winters with reduced SSW frequency, i.e. a hiatus period. Correspondingly, a series of large-amplitude deep easterly QBO years would lead to a series of consecutive-event years.

We verify the results of the wavelet analyses described above by repeating the multi-linear regression (table 3.1) but using the 5-year smoothed QBO, ENSO and AL indices to measure their relative contributions to the 5-year smoothed SSW_{5yr} time series (table 3.2). The resulting regression coefficients for the deep QBO amplitude and AL remain significant at the 95% level, although the AL's contribution remains small and close to the significance boundary. The coefficient for Niño3.4 is not significant, suggesting that the connection between this ENSO index and the vortex variability

SSW_{5yr} regression		
Regression Variable	Coefficient	p-value
Niño3.4	-0.0127±0.032	0.688
AL	-0.072±0.021	0.046
deep QBO amp	-0.124±0.031	0.0001

TABLE 3.2: Summary of results from multi-linear regression analysis of SSW_{5yr}.

Filtered (>60-year periods) SSW_{5yr} regression		
Regression Variable	Coefficient	p-value
Niño3.4	∼0±0.01	∼1
AL	-0.0794±0.03	0.042
deep QBO amp	-0.199±0.01	0.00003

TABLE 3.3: Summary of results from multi-linear regression analysis of a Fourier filtered version of SSW_{5yr} retaining power corresponding to periods greater than 60 years.

is dominated by timescales less than 5 years. If we further isolate multi-decadal signals by Fourier filtering each time series, so that only periodicities longer than 60 years are retained (table 3.3), the Niño3.4 coefficient is near 0 while the deep QBO amplitude signal is near -0.2. This is consistent with our wavelet analysis which suggests a dominant role for QBO amplitude variations on these long timescales. The AL coefficient remains significant but smaller than that of the QBO (and outside error ranges). For completeness, we repeated the regression analysis using a 5-year smoothed PDO index instead of the AL but there was no significant change in the coefficients (not shown). This is consistent with the fact that the AL and PDO indices exhibit similar spectra and there is a high correlation between them ($r = -0.45$ unfiltered and $r = -0.68$ filtered), as also found by *Mantua et al.* [1997] and *Rodionov et al.* [2005].

To further clarify the role of the QBO, we note that an examination of figure 3.17 shows that the majority of the long-term amplitude variability in the 15-30

hPa deep QBO index lies in the amplitude of the westerly phase (the easterly phase amplitude is relatively constant with time). Also, as noted earlier, the simulation exhibits more hiatus intervals than consecutive-event intervals, which suggests that the observed long-term variability may arise primarily from the westerly QBO phase. To explore this hypothesis, we isolate the SSW hiatus intervals by modifying the SSW_{5yr} time series in the following way. All SSW rates above 0.54 events per season (the climatological mean) are re-set to 0.54 thereby removing variability in 5-year intervals that exhibit anomalously high SSW rates. Figure 3.20 shows the cross power spectrum between this modified SSW_{5yr} time series and the time series of deep QBO amplitude. It retains significant cross power within the portion of significant SSW_{5yr} power (figure 3.20 black dashed contours) when compared with figure 3.19b in which the full time series is used and also shows a phase relationship closer to anti-phased (i.e. pointing to the left).

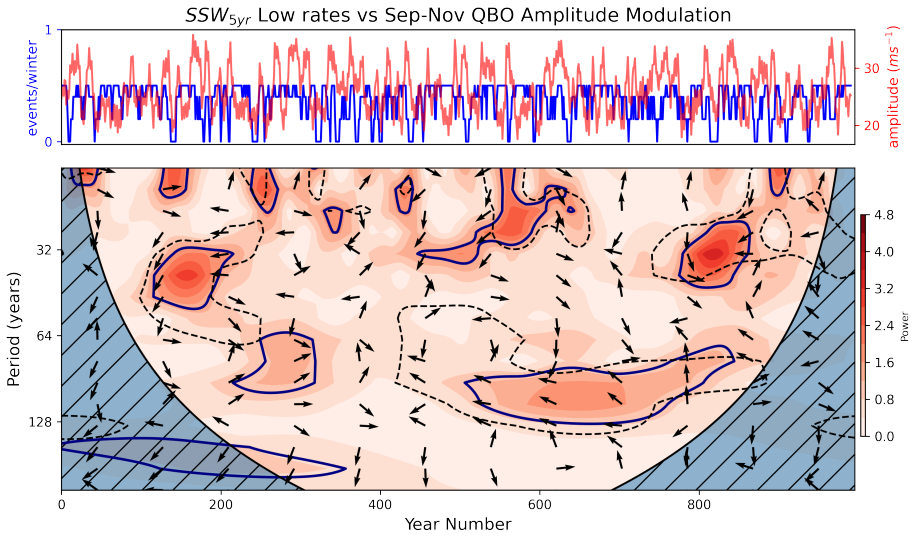


FIGURE 3.20: **Top**: SSW_{5yr} time series with variability in high SSW rate intervals removed by setting all rates above the climatological mean (0.54 events per season) to the mean (blue) and Sep-Nov deep QBO Hilbert Amplitude index smoothed with a 5-year window (red). **Bottom**: Cross wavelet power spectrum between the two time series.

This is further evidence to support the hypothesis that the deep QBO - SSW rela-

tionship on these long timescales in the model arises primarily from the SSW hiatus periods.

An obvious question is whether this sensitivity to deep QBO westerlies that we find in the model is also present in the real atmosphere. Examination of the ERA-Interim dataset shows limited support. Some winters in the 1990s are characterised by anomalously westerly Sep-Nov equatorial winds which are vertically coherent between the 15 and 30 hPa levels. However, this effect is intermittent and does not span the whole interval of the 1990s during which SSWs were markedly absent in the observational record (not shown). On the other hand, a mini hiatus that was present in the mid 2010s is associated with 3 years of deep westerly anomaly in the QBO. Overall, it is clear that the relationship, if present in the real atmosphere, is likely obscured by other factors including greenhouse gas increases and volcanic eruptions and the observational dataset is too short to provide useful validation for these long-timescale variations.

3.8 Summary and discussion

While there is much observational evidence for the impact of SSWs on the underlying tropospheric weather and climate, their multi-decadal variability and the associated forcing mechanisms are not well understood due to the short observational record. Analysis of long climate model simulations is currently the only available tool for understanding this variability. In this chapter, we have examined variability in the appearance of hiatus and intervals of consecutive SSWs in a 1000-year pre-industrial control simulation of one such model (UKESM).

We found realistic decadal and multi-decadal variability in the model, with hiatus intervals of 10 years or more in which no SSWs occurred, similar to the observed SSW record in the 1990s [*Pawson and Naujokat*, 1999; *Shindell et al.*, 1999] and also

intervals of consecutive-event periods in which at least one SSW occurred every year, as observed in the early 2000s [*Manney et al.*, 2005]. A 5-year smoothed representation of SSW frequency (SSW_{5yr}) was found to vary periodically for approximately 450 years of the 1000-year simulation with maxima in wavelet power corresponding to periodicity of around 60-90 years. A possible tropical SST source of this long-term variability was investigated. Wavelet and cross-spectrum analyses were performed using a variety of different tropical SST indices, including the ENSO 3.4 index, and also an index of the strength of the AL which is linked to large-scale planetary wave forcing of the winter stratosphere. While all of these indices displayed elements of long-term variability, some of which overlapped with the periodicity and time intervals seen in the SSW_{5yr} spectrum, none of them could fully account for the extended 450-year interval of significant power at 60-90 years seen in the SSW_{5yr} spectrum. The weak relationship between the AL and SSW occurrence is unexpected and modifying the metric by using a box average SLP measure utilised in *Garfinkel et al.* [2012b] did not recover a stronger connection. Further analysis of the AL-SSW relationship in the simulation would be useful to explore whether the AL exhibits a connection with the NH winter mean vortex winds or other continuous vortex metrics such as the NAM even though there is no apparent connection with SSW occurrence.

A second possible source of long-term variability involving variations in the QBO was also investigated. A range of QBO indices was considered, including the standard approach of using equatorial winds at a specified pressure level e.g. 50 hPa and also a 'deep QBO' index which takes the average QBO wind over 15-30 hPa, designed to capture the degree of vertical coherence in the QBO winds (following *Gray et al.* [2018] and *Andrews et al.* [2019]). A straightforward wavelet analysis of these QBO indices reveals no power at periodicity longer than 2-4 years. However, while there is evidently no long-term variability in the frequency of the QBO, visual examination of the QBO time series clearly shows the presence of long-term variability in the QBO

amplitudes. A measure of this amplitude modulation was extracted by taking the Hilbert Transform of the QBO index. Wavelet analysis of the amplitude variations from the Hilbert Transform of the QBO indices showed long-term periodicity matching that seen in the SSW_{5yr} wavelet analysis. In particular, the deep QBO index exhibited significant signals coincident with those in SSW_{5yr} corresponding to periodicities of around 90 years. This overlap accounted for nearly all 450 years of SSW variability present on the 90-year timescale. Regression analysis of 5-year smoothed and filtered indices confirmed the contribution of the deep QBO amplitude to variability in SSWs on timescales greater than 60 years.

Our analysis has therefore revealed an unexpected relationship between the strength and vertical coherence of the QBO and long-term variability in the frequency of SSWs. The relationship was found to be particularly sensitive to the QBO westerly phase. Extended periods of deep westerly QBO phases were associated with hiatus periods with few or no SSWs, consistent with the Holton Tan relationship. While this result appears compelling, it should be noted that the model showed some biases in its QBO associated with the period and descent rate of shear zones. The extended period of close to 3 years could introduce an element of phase locking between the QBO and seasonal cycle causing winter months to occur preferentially in one QBO phase over the other (evident from figure 3.6, legends). This may influence QBO-vortex coupling. However, these biases are common in modern GCMs [*Bushell et al.*, 2020] and *Rao et al.* [2019] show UKESM's representation of the HT effect is better than most major GCMs submitted to CMIP6 indicating this pi-control remains one of the most effective tools for studying multi-decadal variability in the stratosphere.

It is also unclear as to the true nature of the teleconnection between the vortex and equatorial stratosphere on 90-year timescales. Namely, our wavelet analysis is unable to determine the direction of causality in the connection so, while the association is consistent with a traditional HT link, there is still a possibility of a 2-way feedback

interaction between the vortex and QBO. The mechanisms at play are difficult to identify without targeted modelling experiments (which are proposed in section 6.2) however a possible pathway may involve similar processes as those discussed in *Lu et al.* [2008] and *Lu et al.* [2014] in which the strength of the association between the QBO and vortex is modulated over time via changes in the shape of the vortex itself and its subsequent effect on the mid-latitude planetary wave guide. Alternatively, The association between QBO and SSW signals may be due to the action of an unidentified 3rd factor which influences both the QBO and vortex on multi-decadal scales. ENSO is a natural candidate for a driver such as this as it has been shown to influence SSW occurrence (see section 2.5.3) as well as the QBO via modulation of equatorial upwelling. However, figure 3.11 indicates minimal spectral power in ENSO on the relevant timescales so this feature may not be driving variability. Further work could involve analysing other surface metrics whose signals may associate with either the QBO or vortex (or both) to establish whether the association uncovered in this chapter occurs purely via a HT link. Combining the results of all these analyses, our overall conclusion is that multi-decadal variability in SSW frequency in UKESM is primarily accounted for by long term variability in QBO-SSW coupling, particularly at periodicities of around 90 years and, to a lesser extent, by variability in the intensity of the AL at periodicities around 60 years, although coherence with the AL signals is far less persistent than with the QBO. Given the observed impact of SSWs on the underlying tropospheric weather and climate, improved understanding of the source and mechanisms of long-term variability in QBO-SSW interactions is likely to help improve future seasonal weather forecasts and decadal-scale climate predictions.

Outlook

While the results from this chapter provide a novel type of variability in SSWs and its possible origin, the work reveals a number of areas of further research which we aim

to address in subsequent chapters of this thesis.

Surface influence of SSW signals: While we suggest a set of drivers for periodic signals in SSWs, we do not assess the influence of signals in hiatuses on the surface. Of particular interest may be the NH Ocean basins given the timescales of signals considered in this study (similar to characteristic modes of variation such as the AMOC and AMV) as well as vortex variability's association with surface modes in this region [*Baldwin and Dunkerton*, 2001]. Analysis in the following chapter examines the interaction between signals in a vortex time series and key modes of tropospheric, surface and Atlantic variability.

Origins of QBO amplitude modulations: Open questions also remain regarding the role of signals in SSW time series in the earth system. If, as we propose here, amplitude modulation in a deep QBO metric is responsible for driving SSW signals, a natural area of further research could focus on understanding the cause of such amplitude variability. Categorising whether QBO signals are externally driven by features such as tropical upwelling, ENSO (as well as other tropical SST variability) and deep convection or internally generated within the stratosphere would likely be key for this understanding. Work in chapter 4 also includes a closer analysis of deep convection in the Pacific region to attempt to diagnose the source of QBO amplitude modulation fully.

The role of QBO vertical structure in teleconnections: Finally, the precise nature of QBO-SSW interactions is still not fully understood [*Anstey and Shepherd*, 2014]. While the importance of wave-mean flow interactions is widely recognised, further analysis is required to explore the relevance and usefulness of the deep QBO index highlighted in this chapter, that identifies vertically coherent QBO phases. It

appears to be especially relevant to long-term QBO-SSW interactions during the QBO-W phase and its importance is suggested in recent work [*Andrews et al.*, 2019]. Findings from a set of GCM experiments designed to explicitly analyse the role of vertical QBO structure in teleconnections are presented in chapter 5.

CHAPTER 4

Interactions between the stratospheric polar vortex and Atlantic circulation

Much of the work contained in this chapter is based upon *Dimdore-Miles et al.* [2021b], currently in review in *Atmospheric Chemistry and Physics*.

4.1 Introduction

Chapter 3 demonstrated that the appearance of SSWs, specifically intervals of hiatus in events, vary on multi-decadal timescales in a pi-control simulation of UKESM. Given the well studied downward influence of vortex variations over the Atlantic sector (see section 2.6), a natural question that follows from this finding is to what extent do these multidecadal signals influence modes of variability in tropospheric and surface climate? The majority of studies that have examined the associations between the stratospheric polar vortex and surface anomalies have considered the in-season impact of individual events (notably *Baldwin and Dunkerton* [2001]) however, the Atlantic region exhibits a key mode of multi-decadal variation, namely the AMOC (section

2.7) which is in turn a key driver of climate variability (e.g. *Frankignoul et al.* [2013]).

An association between stratospheric polar vortex variability and the AMOC on decadal timescales has been previously investigated [*Schimanke et al.*, 2011; *Reichler et al.*, 2012] but the mechanism of its influence remains unclear. For example, *Reichler et al.* [2012] examine the response of the AMOC to strong and weak polar vortex events and show a lagged, oscillatory response in the AMOC. They propose a pathway involving alterations of wind stress and ocean-atmosphere heat flux anomalies in the West Atlantic due to the changed NAO patterns following the vortex events. The effect is prominent in a pi-control simulation of a single model (GFDL-CM2.1) and, to some extent, in a suite of CMIP5 models. An impact of long-term changes in the NAO on the strength of the AMOC is supported by a number of studies [*Visbeck et al.*, 1998; *Delworth and Dixon*, 2000; *Delworth and Greatbatch*, 2000; *Eden and Willebrand*, 2001; *Lohmann et al.*, 2009; *Robson et al.*, 2012]. *Delworth and Zeng* [2016] used a set of idealised GCM experiments in which they impose a perpetual ocean-atmosphere heat flux pattern associated with different NAO phases. They find significantly different AMOC mean states depending on the imposed pattern (a stronger AMOC under positive NAO flux conditions than a control simulation). *Haase et al.* [2018] also analyse the in-season influence of SSW events on the NAO and ocean-atmosphere heat fluxes that then impacts the strength of deep convection in the North Atlantic, using the CESM1 WACCM model. The study notes the presence of an anomalously shallow mixed layer depth in the Labrador Sea following an SSW event.

A key result from *Reichler et al.* [2012] is the decadal modulation of the vortex-AMOC covariability. However, decadal to multi-decadal variability in vortex strength is not well understood. Some studies have focused on potential polar vortex impacts at the surface but suffer from low statistical significance due to the short observational record. *Garfinkel et al.* [2017], *Garfinkel et al.* [2015] and *Cohen et al.* [2009] link decadal fluctuations in vortex strength with modulation of the global warming signal in

Eurasian surface temperature in both reanalyses and CMIP3 models. *Schimanke et al.* [2011] demonstrate multi-decadal signals in SSW occurrence in a multi-century GCM simulation and propose an influence of these signals on similar period variability in Eurasian snow cover and Atlantic SSTs. However, results from this study are difficult to interpret given that the GCM used (EGMAM: ECHO-G with Middle Atmosphere Model) exhibits significant bias in its vortex representation with a mean SSW rate of only 2 events per decade compared to 6 events per decade in most reanalyses [*Ayarzagüena et al.*, 2019]. They note that repeating their study with a more advanced model is required to corroborate their findings. *Manzini et al.* [2012] examined decadal fluctuations in SSW events in a 260-year prescribed SST simulation of a GCM and analyse the impacts of these signals at the surface. They show that decadal vortex variability excites similar timescale variations in surface temperature and sea ice coverage between Greenland and Norway over the Atlantic sector. They propose this connection to be indicative of a delayed response of the AMOC to stratospheric forcing via the NAO which subsequently influences northward Atlantic heat transfer and sea ice melt rates as well as surface temperatures anomalies.

While a degree of connection between the vortex and AMOC has been proposed in the works outlined above, aspects of the interaction evade definitive explanation. Namely, the true mechanisms, as well as the timescales, involved. In this chapter we utilise the same 1000-year pi-control simulation as chapter 3, to extend the analysis there and examine the links between long-term vortex variability and the North Atlantic including oceanic modes. We first examine the near-surface in-season response to extreme vortex events to demonstrate that the model is able to reproduce corresponding anomalies in mean sea level pressure (MSLP), ocean-atmosphere heat flux and SSTs consistent with previous studies. We then study the interactions and feedback mechanisms between the stratosphere, troposphere and surface on different timescales using a combination of lag/lead composite analysis as well the wavelet

spectral decomposition method employed in chapter 3. The amplitude and lag of the AMOC response to a multi-year interval of strong polar vortex in the model are determined. This is then used to estimate the potential contribution of the observed 8 consecutive years with a very stable, undisturbed stratospheric vortex in the 1990s [*Pawson and Naujokat*, 1999] to the recent observed negative trend in the strength of the AMOC.

4.2 Data And methods

4.2.1 Model configuration and observation data

We analyse output from the same GCM simulation as presented in chapter 3 - the pi-control simulation of UKESM (see section 3.2.1). As in chapter 3, we choose the pi-control due to the length of integration relative to the timescales we wish to consider and to analyse the internal variability of the system in this model.

To estimate the contribution of stratospheric variations to recent observed AMOC trends we also make use of observation-based datasets of the atmosphere and oceans. First, we utilise reanalysis data from the ECMWF: ERA5 [*Hersbach et al.*, 2020] for observation-based geopotential height (GPH) fields. Similar to its predecessor, ERA-Interim (section 3.2.2), ERA5 consists of a set of observations assimilated through 4D-var using the ECMWF Integrated Forecast System (IFS). However, ERA5 utilises the latest version of the IFS which operates at a greater horizontal grid resolution to ERA-Interim (31km vs 80km) as well as a higher vertical resolution and maximum height (60 levels up to 0.1 hPa vs 137 levels to 0.01 hPa) [*Hersbach et al.*, 2020]. Most relevant for stratospheric representation is the inclusion of an improved gravity wave parameterisation scheme in the latest IFS, a model which exhibits marginal improvement in the predictability of SSW events compared to its predecessor [*Orr et al.*, 2010]. Despite these improvements in the underlying model, *Hersbach et al.*

[2020] reports no significant improvement in stratospheric representation between ERA5 and ERA-Interim due to a combination of IFS model bias in the middle to upper stratosphere and sparse observations in the same region. We choose to utilise ERA5 as opposed to ERA-Interim for analysis in this chapter as we consider observations of the AMOC and the vortex up to near present day. ERA5 provides data up till the present day while ERA-Interim has been discontinued as of 2019 so ERA5 is a preferable dataset in this case. Second, we use the Rapid Array Data set which provides time-depth profiles for the meridional overturning mass stream function in the Atlantic region at 26°N [*Moat et al.*, 2020]. These data are measured through a combination of ocean mooring, ship-based, satellite and submarine telephone cable observations to estimate the strength of primary contributions to the meridional overturning circulation: Ekman transport (through wind stress), transport through the Florida Straits and transport driven by East-West density gradients between the American and African continents [*McCarthy et al.*, 2015b].

4.2.2 Model diagnostics

We utilise the NAM (section 2.6.1) as a metric for the strength of the vortex as used by *Baldwin and Dunkerton* [2001] as well as numerous subsequent studies. The NAM is defined as the 1st principle component of the zonal mean, deseasonalised geopotential height field evaluated at latitudes north of $20°N$ over the NH winter season (Dec-Mar) on a given pressure level. To measure the vortex strength we evaluate the NAM on a level in close proximity to the vortex edge, 10 hPa, and the resulting index is henceforth known as NAM_{10}. We choose to utilise a continuous vortex metric for this work as opposed to the event-based measured used in chapter 3 as the NAM captures both types of anomalous vortex behaviour (strong and weak). Cross spectral analysis of the SSW time series and the QBO (figure 3.20) suggested an important role of SSW hiatuses in multi-decadal modes of variation. As a result, a continuous

metric that distinguishes between a weak, strong and neutral vortex is highly useful for this analysis. An individual vortex event (either strong or weak) is recorded when the daily NAM_{10} crosses +1.5 (strong) or -2 (weak). The day on which this reversal occurs is referred to as the central date. After this date, the NAM_{10} must recover to neutral (between -2 and 1.5) for a period of at least 10 consecutive days (which is the approximate radiative timescale of the mid-stratosphere) before another event can be recorded. The strong threshold value for events is chosen following the methodology of *Baldwin and Dunkerton* [2001] and the weak threshold is selected such that it results in approximately the same rate of weak events (SSWs) as is reported in chapter 3 (figure 3.2) using the same simulation of UKESM but with a zonal wind definition of SSWs (0.54 events/winter). A correlation analysis between the Dec-Mar mean NAM_{10} (a NAM based index of the seasonal mean strength of the vortex) and the SSWs per NH winter index utilised in chapter 3 gives $r = -0.72$ and confirms the relationship between the indices (the negative correlation is due to SSW_5yr being a weak vortex event metric). Differences between the NAM and SSW metrics likely originate from the ability of the NAM_{10} to capture anomalously strong and weak winters as well as those close to the climatological mean while the event based metric only indicates the presence of weak vortex events.

We also use the NAM_{10} to derive an index for the appearance of intervals of consecutive winters which show persistent vortex behaviour. The persistent NAM_{10} interval index is defined as follows: First, the NAM_{10} is averaged over each NH winter season (December-March), this gives a measure of mean vortex strength for each winter. Second, this index is smoothed using a Gaussian filter which is carried out through a convolution of the time series with a 1D Gaussian kernel in the time domain

given by

$$f(t,\sigma) = \frac{1}{\sqrt{2\pi\sigma^2}} e^{-\frac{1}{2}\left(\frac{t}{\sigma}\right)^2}, \tag{4.1}$$

where σ is the standard deviation of the distribution defined by the kernel. We choose $\sigma = 2$ years following the method of *Reichler et al.* [2012] and as a method analogous to the 5 year smoothing applied to an SSW time series in chapter 3. The selection of $\sigma = 2$ years allows contributions to the smoothed value from values approximately 7 years on either side of the central year as the value of the Gaussian window decays to near 0 approximately 3.5σ from its mean. However, the largest contributions come from 3-4 years either side of the central year. This allows the smoothing to capture instances of ∼6-8 consecutive years with persistent vortex behaviour, a similar length to intervals observed in reanalysis (e.g. the 1990s, *Pawson and Naujokat* [1999]).

We subsequently define persistent NAM_{10} intervals, when the vortex exhibits the same type of behaviour for a number of consecutive years, using extreme values of the smoothed NAM_{10} index. A persistent NAM_{10} interval is recorded when the smoothed NAM_{10} index value falls within the top or bottom 5^{th} percentile values. Once such an interval occurs, another cannot be recorded for 15 years after to avoid choosing multiple central years within the same interval. Using 5 percentile values gives approximately the same rate of persistent vortex intervals as is reported in *Reichler et al.* [2012] so we proceed with this threshold throughout for a direct comparison with this study. Tests were also carried out to assess the sensitivity of our results to this threshold and are reported in section 4.9.

We define an AMOC index following the procedure in *Reichler et al.* [2012]. The AMOC is defined using the overturning stream function field in the Atlantic sector. At each time point, the AMOC index is the maximum stream function value at any depth at a chosen latitude. We evaluate the index at 30°N, 45°N and 50°N and

measure the response and co-variability with the NAM_{10} time series and other climate indices defined below. We derive the observed AMOC index from the Rapid Array data as the maximum meridional stream function at each time point at 26N. We also utilise a definition of the NAO from *Hurrell et al.* [2003]. The NAO index is defined as the 1^{st} PC of the Dec-Mar MSLP in the region $20° - 80°N, 90°W - 40°E$. The PC is calculated by taking the first EOF of deseasonalised MSLP anomalies and projecting this EOF onto the anomaly field to produce the 1st PC. We additionally derive an Ocean-Atmosphere heat flux field defined as the sum of latent and sensible heat fluxes between the ocean surface and the atmosphere (i.e. positive values indicate an exchange of heat from the ocean to the atmosphere). We derive an index for the occurrence of deep convection anomalies in the equatorial eastern Pacific region. This index is defined by the top of atmosphere outgoing longwave radiation (OLR) averaged over the box 10° S–10° N, 240° –290° E. The OLR field is utilised as it acts as a proxy for the occurrence of convection anomalies - when deep convection is enhanced, cloud top height is increased and therefore OLR is reduced. The East Pacific box is selected following a preliminary sensitivity analysis to establish the equatorial OLR region which exhibits similar timescale variability (of near 90-year periods) to the QBO amplitude and SSW time series as shown in chapter 3 (figures 3.9 and 3.19). It is also a similar region to studies that consider East Pacific ENSO patterns which is identified as a separate mode of variability to the traditionally used central pacific ENSO region [*Johnson*, 2013].

We also utilise the same QBO metric as in the wavelet analysis of chapter 3 (see section 3.2.7). This is defined as the ZMZW averaged over the latitude range 5° S–5° N, and the pressure level range 15-30 hPa. As with chapter, 3 we also consider the Hilbert amplitude of the deep QBO as an instantaneous amplitude metric (see equations 3.13-3.15).

Finally, we analyse the relationship between the magnitude of smoothed strato-

spheric NAM_{10} extremes and lagged AMOC anomalies using linear regression with a single predictor (the lagged AMOC). We analyse the strength of linear relationship using a correlation coefficient, r, and estimate a significance level for this value using a bootstrapping method which calculates the probability of a given r if the phases in signals in the NAM_{10} and AMOC are randomly assigned but the overall autocorrelation structure is retained. We do this by comparing the r value calculated with real data with those produced from a set of synthetic NAM_{10} series. These synthetic data are generated by Fourier transforming the smoothed NAM_{10} index, randomly shuffling the Fourier phases and subsequently applying an inverse Fourier transform to generate a surrogate time series with the same Fourier power spectrum as the real data. Repeating this data generation and calculating the correlation between the magnitude of positive extremes in the surrogate NAM_{10}s and the lagged AMOC builds up a PDF for the r value which can be used to estimate the significance level for a real r value.

4.3 In-season surface responses to anomalous vortex events

We begin by diagnosing the in-season response to anomalous vortex events exhibited by surface variability in the model to assess its suitability for studying interactions on longer timescales. Figure 4.1 shows the mean sea level pressure (MSLP) composite differences between strong and weak polar vortex years (figure 4.1, top row). The composites have been determined by selecting MSLP values associated with events in which the daily NAM_{10} values cross the +1.5 (strong) or -2 (weak) threshold (see section 4.2.2). The composite differences demonstrate a significant lagged MSLP response with strong (weak) vortex years corresponding to a positive (negative) NAO pattern, in agreement with previous modelling and observational studies (see section 1). The NAO anomalies peak in magnitude at a lag of 1-2 months following the vortex anomalies with significant anomalies still visible for up to 3 months. There is also

a weak positive NAO pattern that leads the vortex anomalies by up to one month ($-1-0$ month lags). This may be an indication that an anomalous NAO pattern is a precursor for an anomalous vortex, or it could be a response to the initiation of the vortex anomaly since this usually commences in the upper stratosphere and pre-dates the event's central date defined at 10 hPa. Further exploration of this weak NAO signal is outside the scope of this paper. Additionally, a much stronger significant positive anomaly over the AL region is evident in the month leading up to the vortex anomaly consistent with previous work on this connection outlined in section 2.5.2. We also analysed this link in chapter 3 with composites of ZMZW under positive and negative AL (figure 3.7) as well as regression analysis (table 3.1) and found a similar statistically significant relationship between the AL and the frequency of SSWs but the regression coefficients were small in comparison with the QBO influence (table 3.1). Here, the association between the AL and the vortex strength appears marginally stronger (r = 0.39 with the NAM) which may be due to the NAM's ability to capture both types of vortex anomalies (strong and weak). In chapter 3, we also found that the AL exhibited minimal decadal to multi-decadal variability that was coherent with the same timescale variations in the vortex (figure 3.14) and for this reason, the role of the AL is not considered in detail in the remainder of this chapter.

The model also exhibits significant responses in ocean-atmosphere heat flux (figure 4.1, middle row). The largest flux anomalies are seen within 30 days (lag 0-1 month) and their spatial pattern resembles that of a North Atlantic tripole with positive anomalies over the sub-polar North Atlantic between approximately 50°-65°N, negative anomalies off the east coast of the USA and a second positive anomaly off the coast of northeast Africa. This pattern is consistent with the model response found by *Reichler et al.* [2012] to anomalous stratospheric NAM_{10} events as well as the pattern

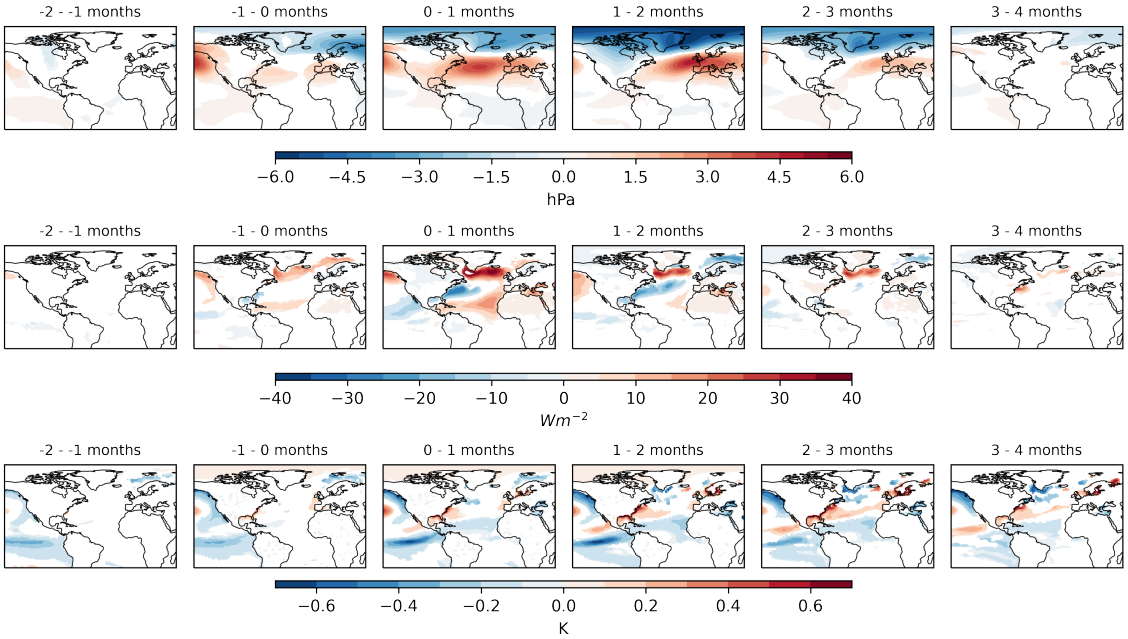


Figure 4.1: Surface patterns associated with anomalous winter stratospheric NAM_{10} events. **Top row**: Monthly mean sea level pressure anomaly (hPa), **middle row**: Ocean-Atmosphere heat flux defined as the sum of latent and sensible heat fluxes (Wm^{-2}) and **bottom row**: SSTs (K). Coloured shading shows where the composite differences between strong and weak NAM_{10} events are statistically significant to the 95% level under a 2 tailed students t-test. The title of each sub-figure indicates the month range relative to the central date of each NAM_{10} anomaly. Signals at negative times indicate that the surface anomaly leads the stratospheric NAM_{10} anomaly while positive times indicate that the stratospheric NAM_{10} anomaly leads the surface response.

associated with positive NAO phases in *Delworth and Zeng* [2016]. As with the MSLP composites, there are visible anomalies 30 days leading up to the identified events (lag -1 - 0 months) both over the North Atlantic and Pacific regions. The Atlantic pattern may correspond to early responses to a disrupted or strengthened vortex as well as possible precursors to events. The Pacific anomalies preceding events are considerably smaller than the Atlantic anomalies and are concentrated over the AL region.

The SST response to anomalous stratospheric NAM_{10} events (figure 4.1, bottom row) over the North Atlantic lags behind the heat flux anomalies by around 2 months, with the largest amplitude anomalies at around 2-4 month lags. The anomaly pattern resembles that of the heat flux anomalies (with a change of sign), consistent with a

mechanism in which the SSTs respond to the anomalous heat fluxes. A prominent negative tropical East Pacific anomaly is obvious in the months leading up to anomalous vortex events together with anomalies that resemble the Pacific Decadal Oscillation (PDO) in the region of the Aleutian Low [*Mantua et al.*, 1997] and these features persist for several months. Variability in this region is dominated by El Niño Southern Oscillation (ENSO) variations and a significant body of work (e.g. *Domeisen et al.* [2019]) has proposed teleconnections between ENSO and vortex strength, consistent with the type of association exhibited here, i.e. negative (positive) SSTs or la Niña (el Niño) conditions associated with an anomalously strong (weak) vortex.

4.4 Surface impacts of persistent vortex anomalies

The in-season anomaly patterns associated with anomalous stratospheric NAM_{10} events shown in figure 4.1 confirm that the model is able to reproduce the observed influence of vortex anomalies at the surface, particularly over the Atlantic region. We now extend the analysis to examine decadal-scale variability. Following the approach of *Reichler et al.* [2012], we smooth the NAM_{10} index (figure 4.2) and then select the upper and lower 5 percentiles of this index to identify intervals with a persistent consecutive strong or weak polar vortex (see section 4.2.2 for more details). The red and blue dots on figure 4.2 indicate the central year of intervals identified with persistent consecutive vortex anomalies (each dot represents the centre of intervals of approximately 8 years, see section 4.2.2). Characteristic surface responses associated with these intervals are then analysed by compiling composites surrounding the central year of each positive and negative interval at lags of -40 (before the intervals) and 40 (after intervals) years. Calculating the (positive minus negative) composite difference can then be used to assess the potential surface impacts to observed intervals of persistent consecutive vortex anomalies, such as the consecutive strong anomalies throughout most of the 1990s and the consecutive weak anomalies in the early 2000s.

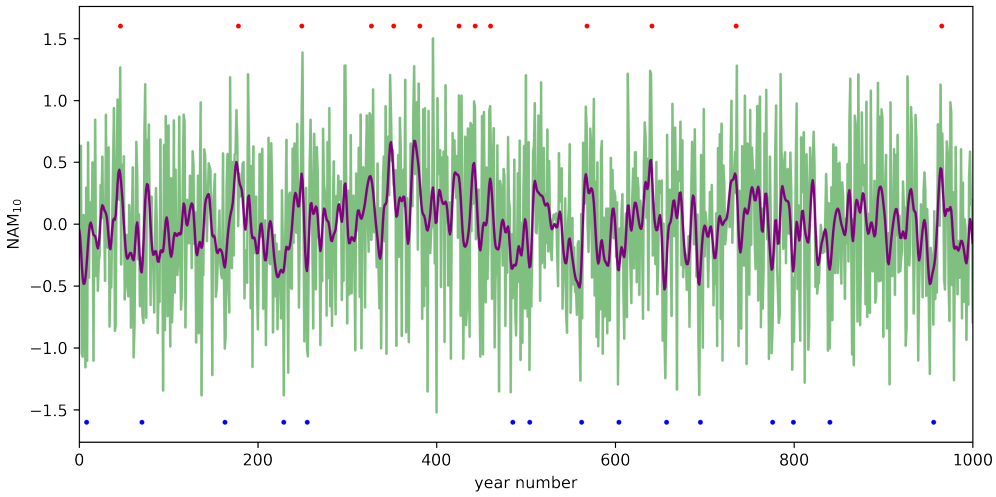


Figure 4.2: Time series of the December-March mean NAM_{10} index (green) and smoothed NAM_{10} (purple) evaluated on the 10 hPa level. The smoothed series is calculated by applying a Gaussian filter ($\sigma = 2$ years) to the green series. Red and blue dots indicate the occurrence of persistent strong and weak vortex intervals respectively defined as extreme values (top and bottom 5 percentiles) in the filtered NAM_{10} index. interval central years are selected such that at least 10 years lies between consecutive intervals.

A lead-lag analysis of composite differences in the AMOC strength at three different latitudes is shown in figure 4.3. The figure can be directly compared with figure 4c of *Reichler et al.* [2012] who suggest that decadal-scale variability in vortex strength acts to amplify a similar timescale of variability in the AMOC through resonance of the two signals. Similar to that work, an oscillatory AMOC response to the stratospheric anomalies is evident here, with significant positive anomalies in the AMOC at 45°N and 50°N at lags of approximately 3-5 years after persistent NAM_{10} intervals followed by negative anomalies at lags between 15 and 20 years. This response pattern is more clearly evident by taking the low pass filtered versions of the AMOC responses (figure 4.3b, d and f). Even after the high-frequency signals have been removed, there are significant composite differences of up to 1.5Sv at 15-20 year lags. (We note, however, that this low pass filtering of the AMOC time series reduces the overall variance so that the threshold for a composite difference to pass

the significance test is lower, and this may increase the responses that are deemed significant shown in figure 4.3).

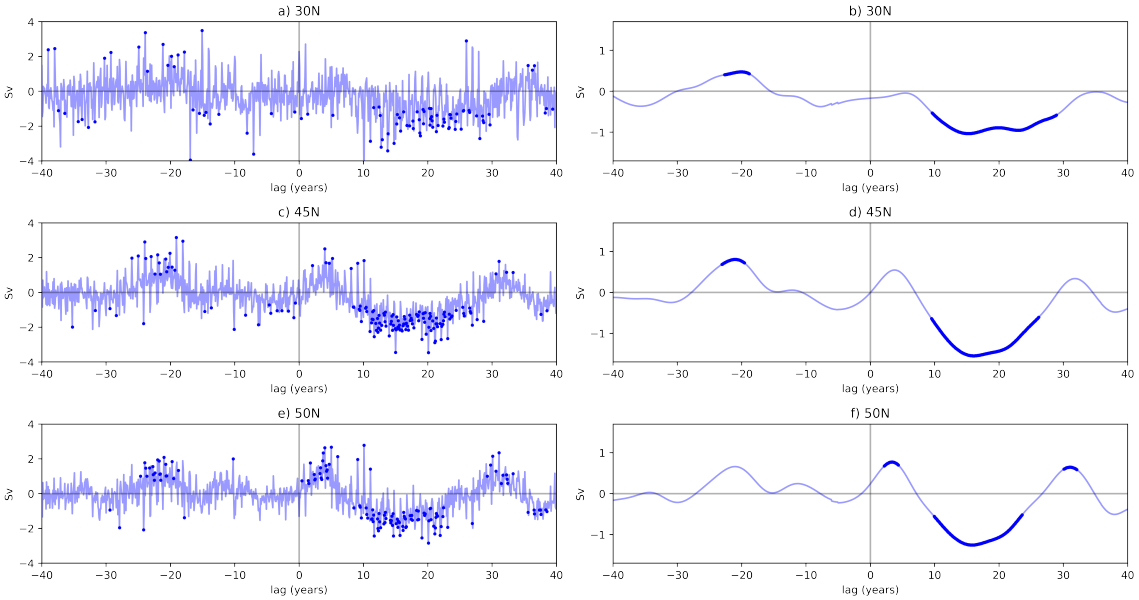


FIGURE 4.3: Lagged response of the AMOC index to persistent NAM_{10} intervals. Blue time series shows AMOC composite difference values between positive and negative NAM_{10} intervals defined in section 4.2.2. The x axis denotes the lead (negative values) or lag (positive values) relative to the interval's central year. Black dots denote composite differences significant at the 95% level under a 2-tailed Student's t-test. Panels a, c and e show monthly AMOC composites while b,d and f show smoothed AMOC composites using a Gaussian filter ($\sigma = 2$ years).

Oscillatory response behaviour is not exhibited clearly by the AMOC at 30°N, although negative anomalies at lags of 15-20 years after intervals are still visible. Response patterns at this latitude are also significantly smaller than those at 45°N and 50°N in the filtered composites (figure 4.3a and b). One possible explanation of this is that the coupling mechanism between the NAM_{10} and AMOC may involve an AMOC response that originates at higher latitudes and then propagates equator-ward therefore exerting less forcing on the AMOC evaluated further south. *Zhang* [2010] also note latitudinal differences in AMOC variability so these differences between 30°N, 45°N and 50°N are not unexpected. The AMOC signals at 45°N and 50°N also exhibit significant positive anomalies preceding the persistent vortex intervals, at a

lead of approximately 20 years and this is also present, albeit smaller in magnitude, in the low pass filtered indices. This precursor to persistent NAM_{10} intervals is not found in corresponding results from *Reichler et al.* [2012] and the role of this feature is considered in more detail in section 4.7.

We now examine this vortex-AMOC teleconnection in closer detail to explore possible physical pathways responsible for an AMOC response to persistent NAM_{10} intervals. Figure 4.4b shows that there is also an oscillatory response in the NAO. This consists of a positive zero-lag response difference (consistent with figure 4.1), a significant negative NAO anomaly between lags of 10-18 years followed by a positive NAO response at lags of around 28 years but with smaller amplitude than the zero-lag response. Also evident from figure 4.4b is that the oscillatory responses of the NAO and AMOC are similar, with the NAO leading the AMOC response by 2-3 years. Both responses vary with periods of 28-30 years but, interestingly, the negative responses in both signals are larger and longer-lasting at 10-20 year lags than those at zero and 28-30 year lags. This difference in the magnitude and persistence suggests that the NAO and AMOC response patterns cannot be explained as a straightforward oscillatory response to the NAM_{10} forcing at zero-lag. If this were the case then the response amplitude would be expected to decay with time and the negative response at 10-20 year lag would be smaller than the initial positive response. Instead, a form of feedback mechanism is required to explain the amplified 10-20 year lagged responses or a resonant mechanism as proposed in *Reichler et al.* [2012]. If such a feedback mechanism were present then one might also expect to see some oscillatory behaviour in the smoothed NAM_{10} time series, in response to the feedback from the surface. To investigate this, figure 4.4a shows the corresponding lead-lag difference analysis for the NAM_{10} index (i.e. the smoothed NAM_{10} composited around its own extreme values). This supports the presence of a feedback mechanism since it also exhibits oscillatory behaviour with the same period of around 30 years. However, this oscillation is largely

evident from the two positive peaks at zero-lag and 30-year-lag, with the latter being substantially damped. There is no significant response at lags of 10-20 years, where the NAO and AMOC responses were largest. This suggests that the negative NAO and AMOC responses at these lags are unlikely to be due to resonance with the NAM_{10} signal.

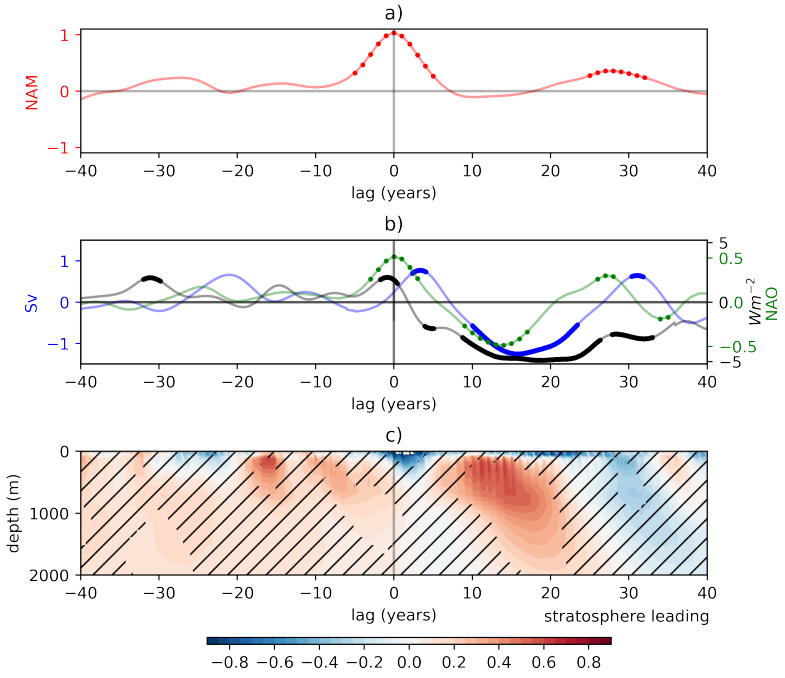


FIGURE 4.4: **a**: Composite differences of the smoothed NAM_{10} index around extreme NAM_{10} intervals (positive - negative intervals). **b**: Like figure 4.3f for the AMOC at 50°N (blue), the Dec-Mar mean NAO index (green) and ocean-atmosphere heat flux (sum of latent and sensible fluxes) averaged over an Atlantic box defined by 45°–65°N, 15°–60°W (black). **c**: composite differences of ocean temperature anomaly depth profiles averaged over the same Atlantic box. in panels a and b, points denote differences that are significant at the 95% level under a 2-tailed Student's t-test. Hatching on panel c indicates composite differences that are not significant at the 95% level

Alternatively, a possible physical pathway could involve an amplifying feedback mechanism between the NAO and AMOC responses. In this scenario, the positive zero-lag NAO response would drive a positive ocean-atmosphere heat flux anomaly over the sub-polar North Atlantic as seen in the response patterns to individual vortex events in figure 4.1. This heat flux anomaly would then lead to persistent negative

anomalies in the near-surface ocean temperatures as heat is removed from the ocean via variations in wind stress and evaporation. The black line in figure 4.4 shows the lead-lag difference for ocean-atmosphere heat flux in the region encompassing the sub-polar North Atlantic (45° –65° N, 15° –60° W). This region was selected to encompass the region with the largest heat flux response to individual vortex events in figure 4.1 (see middle row). Figure 4.4c shows the corresponding depth profile of ocean temperature response from the same region. A positive heat flux response, as well as an upper ocean (0-200m depth) cooling, is evident at 0-1-year lags. This heat flux perturbation would, in turn, drive a positive AMOC anomaly at 2-3 year lags via changes in the mixed layer depth and deep convection in the sub-polar North Atlantic, an effect discussed in *Delworth et al.* [1993] and *Medhaug et al.* [2012]. This increase in AMOC strength would subsequently increase the Labrador Sea temperature via poleward transport of heat. This is confirmed by the positive, deep (down to 2000m) ocean temperature anomaly at a lag of 10-20 years in figure 4.4c. In turn, the reversal of the Labrador Sea temperatures can feedback onto the NAO (see e.g. *Frankignoul et al.* [2013]), inducing a negative NAO phase at 10 years lags as the increased Labrador Sea heat content alters the ocean-atmosphere heat fluxes in the same region. Finally, this switch in the NAO phase would lead to a subsequent negative AMOC anomaly via the same heat flux mechanism outlined above for an opposite NAO phase. This sequence of feedbacks would thus act to enhance the persistence and magnitude of the secondary extreme in the NAO and AMOC. *Reichler et al.* [2012] also briefly suggest a similar mechanism to account for the AMOC response in their simulations, but involving a negative feedback of the AMOC onto itself as well as a role for the NAO.

4.5 Response to strong and weak vortex intervals

So far, we have considered composite difference responses to persistent strong and weak vortex intervals. However, we know that the vortex evolution during strong and

weak vortex years is very different and this is likely to lead to differing interactions with surface and ocean variability. The surface responses to the two extremes are therefore unlikely to be equal and opposite. For example, weak vortex winters are mostly associated with SSWs whose impact at the surface is observed on average 0-60 days after their central date [*Baldwin and Dunkerton*, 2001]. Furthermore, the vortex often exhibits a pre-conditioned state (see e.g. *Charlton and Polvani* [2007] and *Bancalá et al.* [2012]) in which it becomes anomalously strong in the weeks running up to an SSW. As a result, the timing of SSW events within a given season will dictate both the overall strength of the NAM_{10} measured over the winter season (which we use to construct the persistent NAM_{10} index) and the overall strength of the subsequent surface response. In contrast, winters that exhibit an anomalously strong vortex will, on average, exhibit such behaviour throughout the whole season so the impact on the surface will be present for a larger fraction of the winter season.

To assess the influence from each type of vortex extreme separately, figure 4.5 shows the lead-lag composite analysis of the NAO, AMOC, NAM_{10} and heat flux signals for the persistent positive (strong vortex) and persistent negative (weak vortex) NAM_{10} intervals separately. The AMOC patterns associated with each NAM_{10} type are slightly different. The persistently strong vortex composite shows clear oscillatory behaviour with a period of approximately 28 years. These patterns resemble many of the features observed in the AMOC composite differences (figure 4.4d). Specifically, a positive AMOC anomaly is present at lags of 2-3 years, a negative AMOC anomaly at 15-20 years and a second positive anomaly at approximately 30 years.

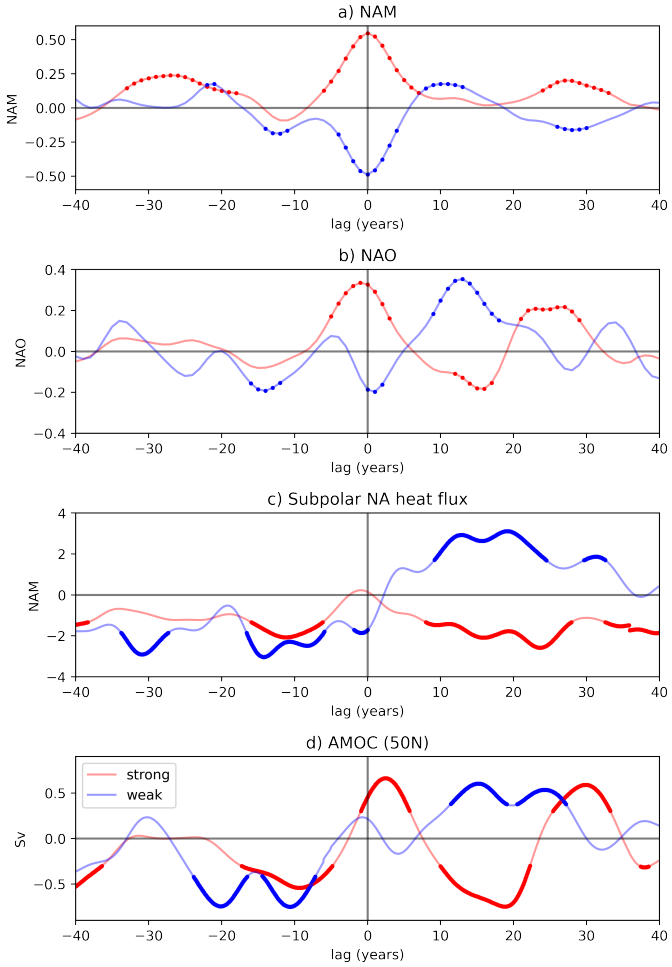


Figure 4.5: Composites of (**a**) Gaussian smoothed NAM_{10}, (**b**) NAO, (**c**) sub-polar NA heat flux (averaged over the same region as used in figure 4.4), (**d**) AMOC anomalies at 50°N associated with persistent vortex intervals of different types. On each sub-figure, the red (blue) plots show the lead/lag responses to composites of strong (weak) persistent NAM_{10} intervals. Solid dots denote composite anomalies are significant to the 95% level under a 2 tailed Student's t-test.

On the other hand, the persistently weak vortex composites exhibit a more complicated response, with double peaked minima at lags of -20 and -11 years and double-peaked maxima at 14 and 25 years. The weak vortex composites also exhibit no significant AMOC response at 2-3 year lags, unlike the strong vortex composites. Both event types are associated with NAO anomalies at zero-lag but the response to strong vortex intervals is larger in magnitude, which is consistent with the larger 2-3 year

lagged AMOC response to this event type. The 0-lag NAO response is followed by an extreme of the opposite sign at approximately 16-year and 14-year lags for strong and weak intervals respectively. As with the AMOC composites, the NAO response to persistently strong vortex intervals exhibits a pronounced oscillatory behaviour of periods around 28 years. The corresponding NAM_{10} analysis also shows oscillatory behaviour with periods of around 28 years. (We note that the NAM_{10} results show statistical significance at both lead and lag times. However, the lead/lag interpretation is less meaningful in this case since the NAM_{10} is used both as the signal and in the selection of the composites. The significance at both lead and lag times simply confirms that there is oscillatory behaviour). The double peaked behaviour of the AMOC associated with weak intervals is also reflected somewhat in the sub-polar North Atlantic heat flux response (figure 4.5c) with positive response peaks at approximately 11 and 20-year lags. There is also a 0-lag heat flux anomaly associated with weak vortex intervals corresponding to the negative NAO response but the corresponding response to strong intervals is not significant.

The asymmetry between the AMOC and NAO responses to persistently strong and persistently weak vortex intervals and the complexity of the separate responses show that the interactions between the NAM_{10} and these surface modes are complex, with some suggestion of oscillatory behaviour on different timescales. In the following sections, we address these complexities in more detail by analysing the frequency spectra of the time series and show that some of these complexities can be explained in terms of the non-stationarity of the signals.

4.6 Non-stationary variability

Analysis in chapter 3 showed that variability of the stratospheric polar vortex occurs on a range of timescales and is highly non-stationary (figure 3.9). Although the composite

analysis presented above shows oscillatory behaviour with periods of approximately 30 years, the results are likely complicated by the presence of non-stationary variability at other periodicities. We, therefore, analyse the frequency characteristics of the filtered NAM_{10} index. Figure 4.6 shows the wavelet power spectrum of this index. It reveals variability on a range of timescales. As expected from the composite analyses, the spectrum exhibits intermittent power throughout the whole simulation at periods between 15 and 40 years. There is also significant power corresponding to a period of approximately 90-100 years that persists for ∼300 years of the simulation (year numbers 520-820; approximately 3 cycles) as well as power at the 50-year timescale that persists for 120 years (year numbers 500-620; approximately 2 cycles).

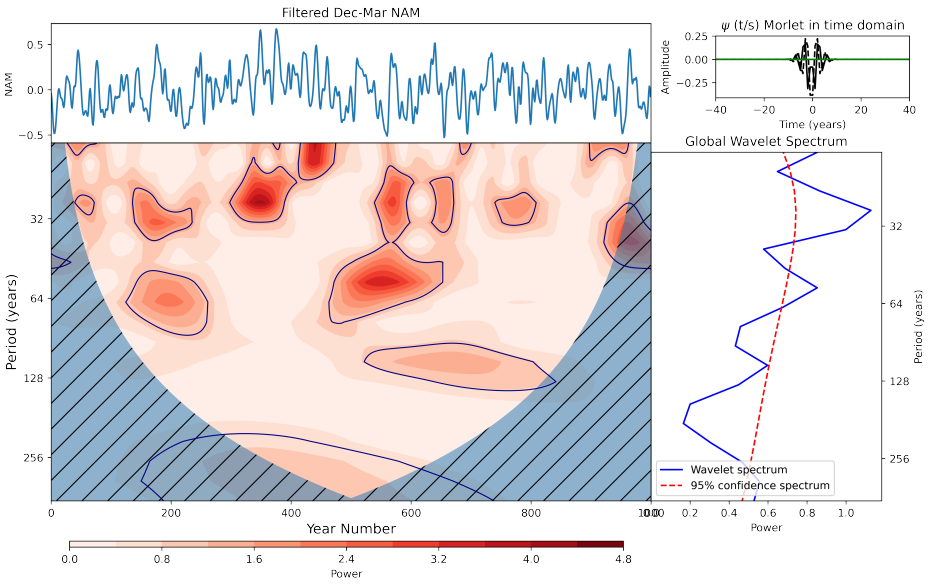


Figure 4.6: **Top left**: Dec-Mar NAM_{10} values smoothed with a Gaussian filter ($\sigma = 2$ years). **Bottom left**: Wavelet power spectrum of time series in top left. Hatching represents an area outside the cone of influence in which edge effects are significant and power should not be considered. Blue contours represent the 95% confidence level assuming mean background AR1 red noise. **Top Right**: Morlet wavelet used for the wavelet transform in the time domain. **Bottom right:** Global power spectrum, the wavelet power averaged over the whole simulation (blue line), and global 95% confidence spectrum (red dashed line).

We note that much of the ∼30-year periodicity seen in the strong composite analysis is likely associated with significant wavelet power in the interval between years

300 and 410 because this interval displays the largest number of positive extremes in the smoothed NAM_{10} time series (compare the 30-year wavelet power in figure 4.6 with the red dots in figure 4.2). The large number of elevated NAM_{10} extremes selected in this interval is also likely affected by the presence of extremely long timescales variability - qualitative inspection of figure 4.2 shows that the underlying NAM_{10} amplitude increases from around year 200, reaches a peak at ∼year 380 and thereafter declines. This means that years within this interval are more likely to reach the top 5 percentile in NAM_{10} and qualify as a persistent anomalously strong vortex. The origin of this multi-centennial variability is unclear and robust analysis of such a low-frequency signal is difficult as the wavelet power of this multi-century variability is located mostly outside the cone of influence (discussed in the previous chapter) that marks the boundary at which edge effects become significant.

We also analyse the frequency characteristics of AMOC variability. Figure 4.7 shows the corresponding wavelet spectra of the AMOC at 50°N and also the cross wavelet spectra between the filtered NAM_{10} and the AMOC which gives a time-varying measure of co-variability between the two indices at different periods. The wavelet spectrum for the AMOC at 50°N exhibits a peak in spectral power corresponding to approximately 130 years that persists for nearly 400 years of the simulation (and also at longer periods up to 250 years but boundary effects are an issue at these multi-centennial timescales, as discussed above). There are also portions of significant power at approximately 30-year and 50-year periods, both of which persist for approximately 2 cycles (∼60 years and ∼100 years respectively) which are also apparent in the global power spectrum. We also note that the main 30-year power comes from the 300-400 year interval, coinciding with the interval of most activity in both the NAM_{10} analysis (figure 4.6) and the selected high NAM_{10} percentiles (figure 4.2).

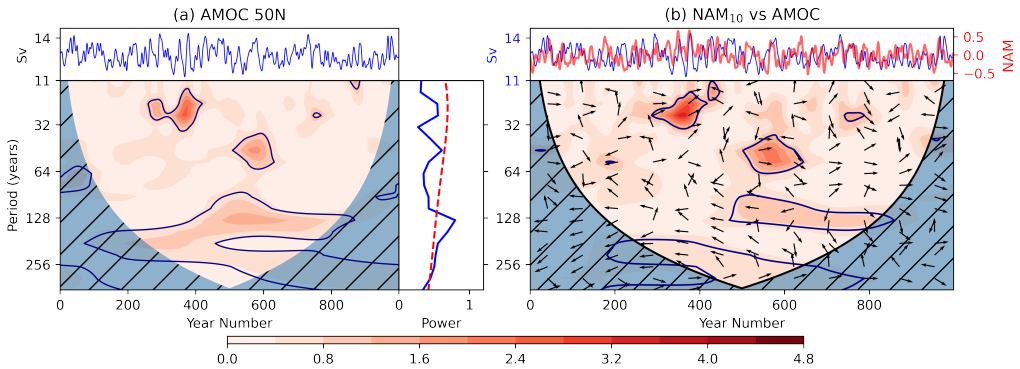


Figure 4.7: **(a, top)**: AMOC time series at 50°N, **(a, bottom left)**: Wavelet power spectrum (shaded contours represent wavelet power and navy contours the 95% significance level compared to an AR1 process), **(a, bottom right)**: global wavelet power spectrum (blue) and 95% confidence level (dashed red). **b**: Cross spectra between Filtered Dec-Mar NAM_{10} series and the AMOC index. **(b, top)**: NAM_{10} and AMOC time series. **b, bottom**: Cross power spectrum. Shading indicates cross power, yellow contours the 95% confidence interval and arrows the relative phase angle between signals in the time series (to the right: in phase, vertically upwards: $\frac{\pi}{2}$ out of phase with positive peaks in the NAM_{10} leading those in the AMOC, to the left: π out of phase, vertically downwards: $\frac{\pi}{2}$ out of phase with positive peaks in the AMOC leading those in the NAM).

The cross power spectrum between the filtered NAM_{10} and the AMOC shows 3 distinct features corresponding broadly to the three timescales prominent in the individual spectra of both indices. Significant cross power is evident at 90-100 year periods for approximately 350 years (between 450 and 800 years; 3-4 cycles). The phase relationship between the signals (indicated by arrows on figure 4.7 within this portion of the cross spectrum show a mixture of left-pointing arrows in the earlier portion, which indicate an anti-correlated relationship (π out of phase) and downward pointing arrows in the later portion that indicate a $\frac{\pi}{2}$ phase relationship. The latter relationship can be interpreted in a number of ways, with maxima in the AMOC leading the maxima in the NAM_{10}, minima in the NAM_{10} leading to maxima in the AMOC or maxima in the NAM_{10} index coinciding with maxima in the rate of change of the AMOC (see section 3.2.3 for more details of the cross spectra arrows and how they are derived). There is also significant cross spectral power centred around 30 years (between 300-400 years; 3 cycles) and 50 years (between 500-600 years; 2 cycles).

In contrast to the 90-year periodicity, the phase arrows point to the right and slightly upwards, indicating that maxima in the NAM_{10} index lead maxima in the AMOC by a small fraction of the cycle. This phase relationship is consistent with the composite analysis presented in figures 4.3 and 4.5 that indicated that a positive (negative) NAM_{10} leads to a positive (negative) AMOC response approximately 2-3 years later. The wavelet spectra for the AMOC at 30°N and 45°N are provided in figures 4.8a and 4.9a. They show broadly the same features as that of the AMOC at 50°N however it is notable that the AMOC at 30°N does not exhibit significant variability on the 50 and 30-year timescales. This is reflected in the cross spectrum with the smoothed NAM_{10} index which shows minimal cross power on these timescales (figure 4.8b).

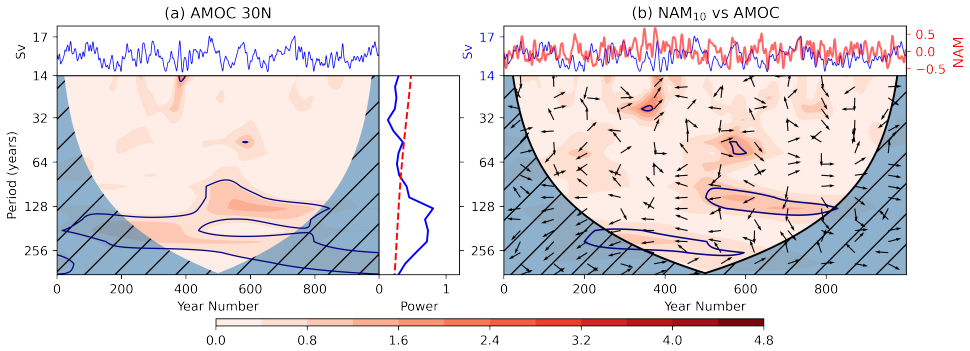


FIGURE 4.8: like figure 4.7 for the AMOC at 30°N. (a) shows the wavelet power spectrum of the AMOC and (b) the cross power spectrum between the AMOC and the NAM_{10} index.

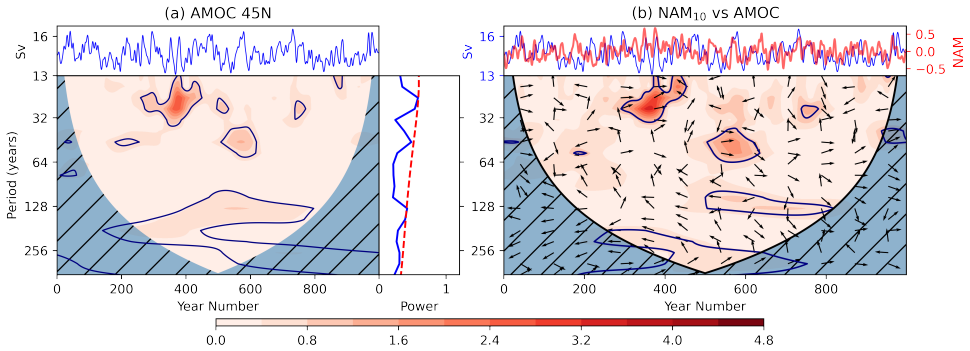


FIGURE 4.9: like figure 4.7 for the AMOC at 45°N. (a) shows the wavelet power spectrum of the AMOC and (b) the cross power spectrum between the AMOC and the NAM_{10} index.

To understand these non-stationary signals in the context of the proposed mechanism for vortex-AMOC interactions involving the NAO, we also analyse the power spectrum for the Dec-Mar NAO (figure 4.10). The wavelet power spectrum for the NAO (figure 4.10a) exhibits a portion of significant power at periods of 30 years between ∼300-400 years as well as a feature at 50 years between ∼500-600 years similar to the NAM_{10} and the AMOC. Furthermore, the cross power spectrum between the NAO and the NAM_{10} indicates that signals in the two indices on the ∼30 and ∼50-year periods are also coincident in time for the 70-100 years they persist for. The phase relationship between these signals is small (arrows pointing to the right) indicating an in-phase relationship between the indices, which is consistent with the zero-lag relationship between the NAO and filtered NAM_{10} extremes presented in the composite analysis (figures 4.4 and 4.5). The NAO wavelet analysis shows no significant power on the 90-100 year timescale. This suggests that the co-variability between the NAM_{10} and AMOC on these longer timescales does not involve the NAO and is likely to arise through different mechanisms. We return to examine this feature in more detail in section 4.7.

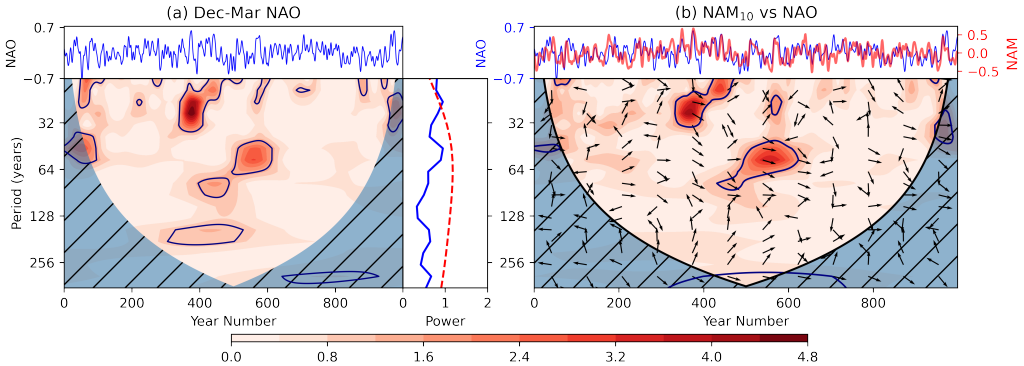


FIGURE 4.10: like figure 4.7 for the Dec-Mar NAO index. (a) shows the wavelet power spectrum of the NAO and (b) the cross power spectrum between the NAO and the NAM_{10} index.

The wavelet analysis suggests that while 30-year periodicity is most apparent in the composite patterns of figure 4.4 there may also be contributions involving the

50-year and 90-year periodicities. This complication is more clearly evident in figure 4.5 where the composites associated with persistent positive and negative NAM_{10} intervals were examined separately. Firstly, we note that the contribution to the composites from the interval exhibiting ∼30-year oscillatory behaviour (∼300-400 years) comes solely from a collection of persistent strong NAM_{10} intervals (see the red dots on figure 4.2). In contrast, a high proportion of the weak NAM_{10} contributions to the composite analysis (8 out of 13) occur within the interval between ∼500-600 years which exhibits variability at both 50-year and 90-year periodicity. The complicated double peaked behaviour of the AMOC response following persistent weak vortex intervals can now be better understood, taking into account the influence of the ∼50-year and ∼90-year periodicities. The double minima in AMOC response at 10-year and 20-year leads and at 15-year and 25-year lags can now be explained as manifestations of the 50-year and 90-year AMOC responses e.g. a half-cycle between the minimum at 10-year lead and maximum at 15-year lag (thus a half-cycle of 25 years) gives a periodicity of 50 years, while a half-cycle between the minimum at 20-year lead and 25-year lag (thus a half-cycle of 45 years) give a periodicity of 90 years. Additional support for this interpretation comes from the fact that the NAO composite analysis (figure 4.4b) shows a response that corresponds broadly with the AMOC minimum at 10-year lead and maximum at 15-year lag, suggesting a mechanism that involves the NAO on the 50-year timescale but there is no corresponding response in the NAO at the 90-year periodicity, in agreement with the wavelet spectra and cross spectra in figure 4.10 which indicates that the NAO does not exhibit variability on timescales of ∼90 years.

4.7 Surface forcing of the stratosphere

The absence of an NAO signal that corresponds to the 90-year periodicities seen in both the NAM_{10} and AMOC wavelet spectra and in the AMOC-NAM cross spectrum (figure 4.7) indicates that the mechanism for the stratosphere - AMOC teleconnection

on this longer timescale may be distinct in nature to those observed at the 30 and 50-year periodicities. As noted earlier, the phase relationship associated with this feature is also different to the shorter timescales ($\frac{\pi}{2}$ out of phase) suggesting that the direction of causality is also switched i.e. that the AMOC leads the stratospheric response on these timescales rather than vice versa. To study this more closely we investigate possible pathways involving variability on this timescale.

Our earlier analysis of this UKESM pi-control simulation (chapter 3) highlighted the ∼90-year variability in the frequency of SSWs and demonstrated that this was closely associated with similar timescale variations in the amplitude of the QBO (and in particular, the westerly QBO phase). Figure 4.11a shows the wavelet spectrum of the same QBO amplitude index employed in chapter 3 (the Hilbert amplitude of the deep QBO index) after smoothing with the same Gaussian filter utilised throughout this work (see section 3.2.7 for a description of how the QBO index was derived using the Hilbert amplitude). A portion of significant power at ∼90-year periods persists for approximately 200 years of the simulation between years 600-800, which coincides with the significant response in the same interval of the NAM_{10} and AMOC spectra at 90-year periodicity. Cross spectra of the QBO index with the smoothed NAM_{10} index (figure 4.11b) also corroborates the findings of chapter 3, with coincident signals at the 90-year timescales and right-pointing arrows that indicate an in-phase relationship, so that an interval of persistently strong positive (westerly) QBO anomalies coincides with an interval of persistent positive (strong) polar vortex anomaly. The sign of this teleconnection is consistent with a Holton-Tan teleconnection [*Lu et al.*, 2008, 2014] but it is present on much longer timescales.

While the long-timescale QBO-vortex teleconnection was demonstrated by work in chapter 3 (and confirmed here), the cause of the long-term westerly QBO variability was not established (see section 3.8). chapter 3 presented a wavelet analysis of equatorial SSTs in various regions (figure 3.13), including the equatorial East Pacific,

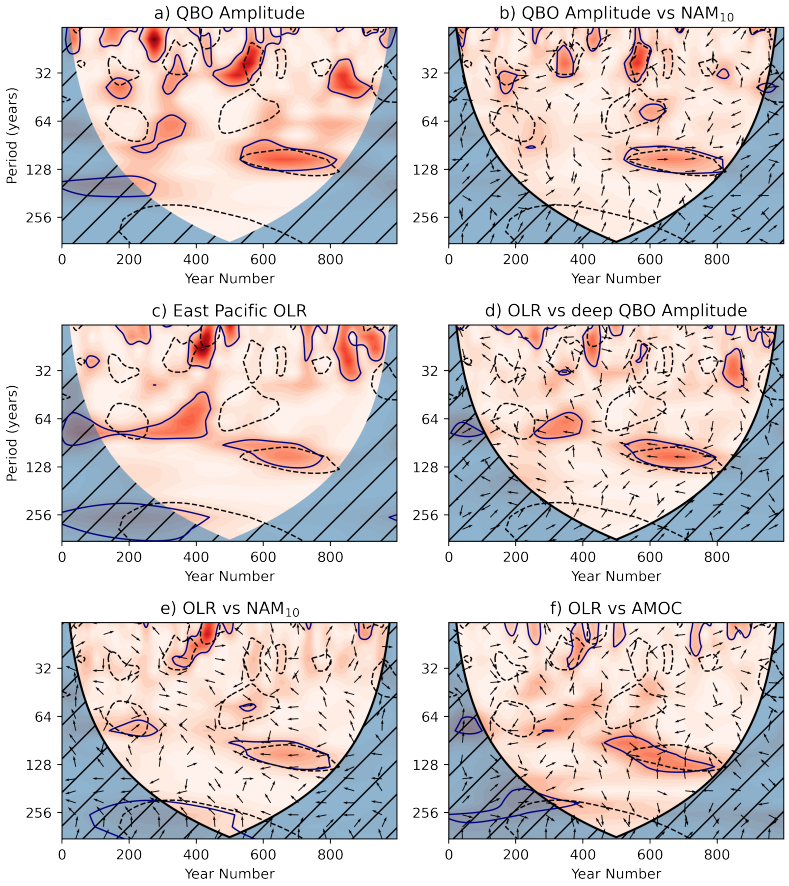


FIGURE 4.11: (a): Wavelet power spectrum for the Sep-Nov deep QBO amplitude (see section 3.2.7). (b) cross power spectra between deep QBO Amplitude (Sep-Nov) and smoothed NAM_{10} (Dec-Mar). (c): Wavelet power spectrum for the Sep-Nov Area weighted average equatorial East Pacific OLR (see section 4.2.2). **d-f**: cross power spectra between combinations of East Pacific OLR, deep QBO Amplitude (both Sep-Nov means), AMOC at 50°N (annual mean, all months) and NAM_{10} (Dec-Mar) indices all smoothed with the same Gaussian filter as is used throughout ($\sigma = 2$ years). Indices involved are indicated by the sub-figure titles. Shading indicates the cross power, using the same colour scale as in figures 4.6-4.9. Solid contours indicate the 95% confidence interval for the power spectrum and dashed contours show the 95% confidence interval for the NAM_{10} spectrum, for ease of comparison. Arrows indicate the relative phase angle between the signals in the indices.

to explore whether the ∼90-year QBO variability could be explained by SST triggering of convective activity that generates the gravity and other equatorial waves that contribute to the QBO. However, no 90-year periodicity in equatorial SSTs was found. Nevertheless, the extremely long period of the QBO and vortex variations suggests a driving mechanism that is likely linked to the ocean, because of the characteristic

long oceanic timescales.

To extend this investigation into 90-year timescale QBO modulation, we examine the variability of the East Pacific top-of-atmosphere OLR as a proxy for deep convection (instead of using the East Pacific SSTs, as in chapter 3). When deep convection is enhanced, cloud top height is increased and therefore OLR is reduced. Figure 4.11c shows the wavelet analysis of the Sep-Nov (the same months as utilised for the QBO amplitude) OLR in the East Pacific. It exhibits 90-year periodicity, as well as significant cross power with the smoothed QBO amplitude and the NAM_{10} index (figures 4.11d and e). The signals in the OLR and both the QBO and NAM_{10} are anti-correlated (left pointing arrows indicating a π phase difference). This is consistent with reduced OLR (increased deep convection) leading to greater QBO amplitude through increased wave forcing. The corresponding cross spectra between the AMOC and the OLR metric (figure 4.11f) also indicates a significant portion of cross power in the interval ∼600-800 years co-located with the feature seen in the NAM_{10} spectrum (see the dashed contours in figure 4.11 which indicate the region with significant power in the NAM_{10} spectrum). The phase difference, in this case, is mostly $\frac{\pi}{2}$ (the majority of arrows pointing upwards) indicating that one of the quantities depends on the time rate of change of the other. This result is similar to the study of *Timmermann et al.* [2005] who found a sensitivity of the equatorial Pacific region to periodic forcing of the AMOC. Their study showed a dependence of the Pacific thermocline on the rate of change of the AMOC. (We note, however, that the ∼7.5 Sv AMOC perturbation imposed in their study was considerably larger than the AMOC variations in our simulation). Similarly, a lagged cross-basin connection between the NA overturning circulation and Pacific Sea Surface Height (SSH) was proposed by *Cessi et al.* [2004] who interpreted it in terms of the propagation of oceanic Kelvin and Rossby waves with anomalies communicated between Atlantic and Pacific via the Indian Ocean as well as through the Drake Passage. We, therefore, suggest this as a possible pathway for the

influence of the AMOC on the polar vortex at 90-year timescales, via modulation of deep convection in the East Pacific that influences the amplitude of the QBO. A more detailed examination of the intermediate steps in this proposed physical pathway is required to confirm this, but this is outside the scope of the study.

4.8 Contribution of the stratosphere to recent AMOC changes

Our analysis of the UKESM simulation has identified co-variability between modes of variability in stratospheric circulation and the AMOC. Intervals in which the winter stratospheric polar vortex is consistently strong are, on average, followed by an extended negative anomaly in AMOC strength with a lag of approximately 15-20 years (figure 4.3f). Recent observations of the AMOC have shown a negative trend in circulation strength of approximately $-2.7Sv$ between 2004 and 2012 [*Smeed et al.*, 2018] before a marginal recovery after 2012 [*Smeed et al.*, 2019]. Modelling studies have proposed a key role for anthropogenic forcing in AMOC slowdown over the 20th century and into the future [*Liu et al.*, 2017; *Bakker et al.*, 2016; *Liu et al.*, 2019]. However, the drivers of observed AMOC trends in the 21st century are not well understood. The results shown in the previous sections suggest the possibility that stratospheric variability has also contributed to the observed AMOC changes, in response to nearly a decade of strong vortex years in the 1990s followed by a sequence of years with a weak, disturbed vortex in the early 2000s.

Using the relationship between the modelled NAM, NAO and AMOC, we can now compare the observed NAM, AMOC and NAO indices for the interval 1979-2020 from the ERA5 and RAPID array datasets (figure 4.12) and assess the potential contribution of stratospheric variability to the observed AMOC trend. The NAM_{10} index (red bars) is characterised by an interval of strong vortex winters between 1988 and 1997 in which all but 2 winters exhibited a positive NAM_{10}. This interval also

contains no SSWs [*Pawson and Naujokat*, 1999]. This is followed by a run of winters between 1998 and 2005 which exhibit anomalously weak NAM_{10} values with SSWs almost every year [*Manney et al.*, 2005]. The filtered NAM_{10} index (red dashed line) reflects the presence of these time intervals with a peak in positive values centred around 1995 followed by a negative extreme centred around 2003. The smoothed NAO (green dashed line) from the same dataset reflects some of these variations in the NAM_{10} with positive NAO extremes in the 1990s. The long-term envelope of the NAO does not remain positive for as long as the NAM, primarily due to the anomalous negative NAO in 1996 [*Halpert and Bell*, 1997]. The presence of this anomalous negative NAO in 1996 and the absence of a clear NAO anomaly in the following year despite the presence of strong positive anomalies in the stratospheric NAM_{10} is indicative of the fact that many other factors influence the NAO in addition to the stratospheric forcing. The AMOC strength estimated from the Rapid Array observations between 2005 and 2019 is also shown (blue curve) and shows a negative trend between 2005 and 2012 followed by a recovery from 2012 onwards [*Smeed et al.*, 2018, 2019].

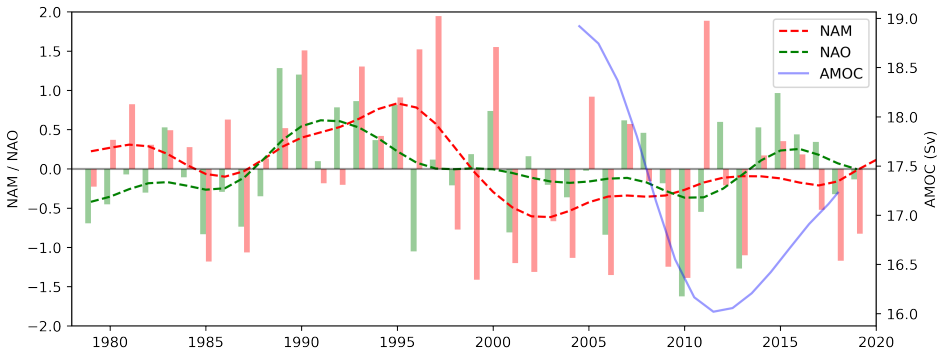


Figure 4.12: Time series of the Dec-Mar NAO index (green bars), NAM_{10} index (red bars) from the ERA5 dataset. Dashed lines correspond to indices shown by bars smoothed with a Gaussian filter ($\sigma = 2$ years). Also included is the annual AMOC time series at 26N from the rapid array dataset (blue).

The interval of observed consecutive strong NAM winters in the 1990s is anomalous

in the reanalysis period, although the available data record is rather short to allow a robust assessment. The amplitude and longevity of the observed anomaly are also large when compared to the UKESM simulation. Only 2 intervals in the UKESM simulation exhibit at least as many consecutive winters with strong (high NAM_{10}) conditions. These 2 intervals occur in the 300-400 year interval (centred around years 349 and 376) as shown in figure 4.13a. They each exhibit a sequence of 10 consecutive Dec-Mar anomalously positive NAM_{10} values. The 2nd interval exhibits 14 strong or marginally weak consecutive winters with the allowance for the small negative NAM_{10} value at year number 379. The presence of these two intervals is reflected in the smoothed NAM_{10} values (figure 4.13b) and they represent two of the three largest values of the filtered NAM_{10} index (0.66 and 0.67). The corresponding smoothed AMOC index during these 2 intervals (blue curve in figure 4.13a) shows a positive AMOC response at lags of 2-3 years followed by a negative response at 17-20 years, in good agreement with figure 4.3f. The negative responses at 17-20 years following these 2 intervals of strong NAM_{10} years are the 1st and 3rd greatest in magnitude compared to all other responses to persistent strong intervals. This is confirmed by figure 4.13c which shows the lagged AMOC response following all of the identified intervals with persistent positive NAM_{10} anomalies (the two identified around 349 and 376 years are shown in black).

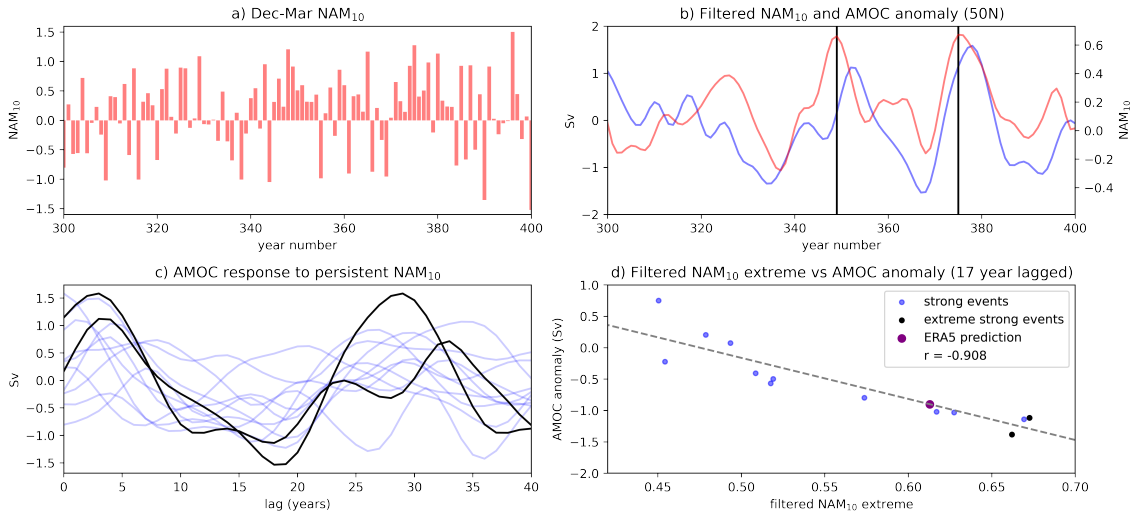


Figure 4.13: **a**: Dec-Mar NAM_{10} index (red bars) from the UKESM simulation between year numbers 300 and 400. **b**: AMOC (blue) and NAM_{10} (red) indices smoothed with the Gaussian filter ($\sigma = 2$ years) between year numbers 300 and 400 of the UKESM simulation. Black vertical lines show the location of the largest smoothed NAM_{10} extremes. **c**: AMOC response to persistent strong NAM_{10} intervals. Light blue lines denote lagged AMOC responses of the AMOC from the whole UKESM simulation, black lines show AMOC responses to NAM_{10} intervals marked in **b** by vertical black lines. **d**: Scatter plot of filtered NAM_{10} index values occurring at persistent strong NAM_{10} intervals throughout the whole UKESM simulation (x axis) against AMOC anomalies at 50°N lagged by 17 years after persistent intervals' central year (y axis). Blue points indicate persistent intervals and black dots represent the 2 intervals displayed in b. The dotted line represents the linear line of best fit for the points in black and blue. Also included is the 17-year lagged AMOC anomaly predicted by projecting the regression coefficients used to construct the linear fit onto the maximum smoothed NAM_{10} index in the ERA5 dataset (purple point).

To estimate the response amplitude of the AMOC to an interval of persistently strong vortex winters, figure 4.13d shows a scatter plot of the central NAM_{10} index of these intervals against the AMOC anomaly at 50°N lagged by 17 years. This reveals a strong linear relationship ($r = -0.908$) between the size of the persistent vortex anomaly and the subsequent negative anomaly in the AMOC at 50°N 17 years later. The PDF of surrogate correlations used to assess the statistical significance (following the method outlined in section 2) is displayed in figure 4.14a along with the correlation generated by the observed NAM_{10} data. It shows that the r value lies well outside the distribution of surrogate correlations, indicating the high level of significance of the

linear relationship. A similar analysis of the relationship between the magnitude of smoothed negative (weak) NAM_{10} extremes and the lagged AMOC response at 50°N (figure 4.14b) yields a much weaker relationship ($r = -0.21$) that is not statistically significant compared to the corresponding PDF of surrogate correlations (figure 4.14b). This asymmetry in the vortex-AMOC relationship between extreme positive and negative NAMs is perhaps not surprising, given that the surface impact of SSWs (that give rise to the negative NAM events) depends on the timing of the SSW within the winter season whereas strong positive NAM intervals exhibit strong vortex conditions throughout the winter.

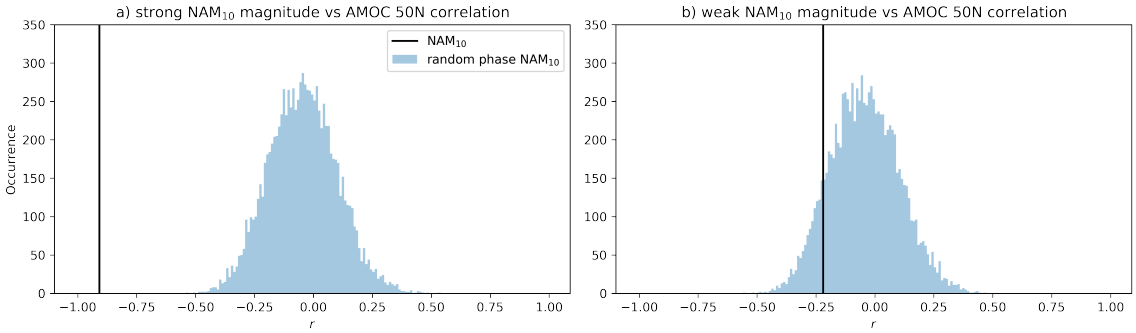


FIGURE 4.14: PDFs for correlations between the magnitude of NAM_{10} extreme positive (**a**) and negative (**b**) values from surrogate NAM_{10} data and anomalies in the AMOC at 50°N evaluated 17 years later. Each NAM_{10} surrogate is generated by Fourier transforming the smoothed NAM_{10} index, randomly shuffling the Fourier phases and inverse transforming. Each PDF is built with 10000 surrogates and the correlation between the NAM_{10} extreme magnitude and 17-year lagged AMOC anomaly at 50°N is shown by vertical black lines in both sub-figures.

A linear regression analysis on the data in figure 4.13d yields an estimated relationship between the variables which satisfies

$$AMOC'_{+17} = -6.54NAMmax + 3.11, \tag{4.2}$$

where $AMOC'_{+17}$ is the 17-year lagged AMOC anomaly at 50°N and $NAMmax$ is the magnitude of the positive extreme in smoothed NAM_{10} at the centre of each interval.

We can then use this relationship to predict the AMOC response to the observed sequence of strong vortex years in the 1990s exhibited by ERA5. The maximum smoothed NAM_{10} in ERA5 occurs in 1996 so, using this relationship, the maximum AMOC response associated with the stratosphere would be expected 17-years later (2013) with an amplitude of -0.89 Sv (figure 4.13d, purple point).

This prediction suggests that approximately 30% of the observed reduction in AMOC strength between 2005 and 2013 (0.89 Sv compared with 2.9 Sv in total) could be due to the response of the ocean to persistent forcing from consecutive strong vortex winters that occurred during the 1990s. We note, however, that our derivation of the modelled vortex-AMOC relationship is based on the AMOC response at 50°N, where the response amplitude is largest, whereas the Rapid Array dataset, that provides the most direct measurement of AMOC strength over the last 15 years, is based at 26N. Figure 4.15 shows the scatter plot of filtered NAM_{10} extreme magnitudes and lagged AMOC responses from the model at 30°N. At this latitude, the linear relationship is significantly weaker than at 50°N ($r = -0.652$ for 30°N vs $r = -0.908$ for 50°N) but the correlation coefficient remains significant at the 95% level. The predicted contribution from the strong vortex interval in the 1990s to the AMOC strength at 30°N is reduced to $-0.49Sv$, (figure 4.15, purple dot) suggesting that approximately 17% of the negative trend in the RAPID AMOC data may be due to stratospheric forcing from the 1990s. This is consistent with composite analysis in figures in 4.3a and b which indicate that the modulation of the AMOC by the smoothed NAM_{10} is less pronounced at 30°N than at higher latitudes.

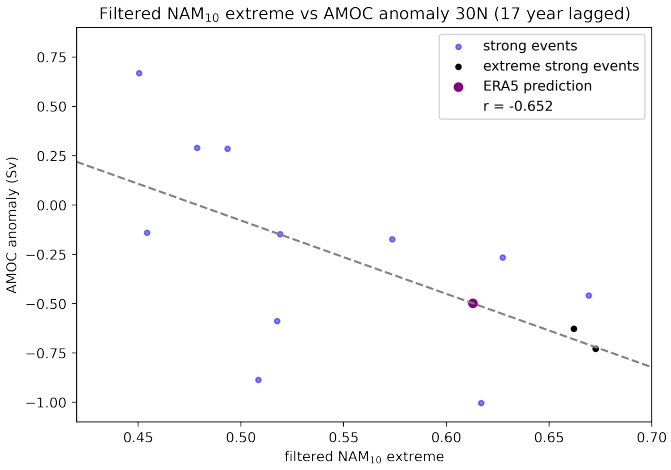


FIGURE 4.15: Like figure 4.13**d** for AMOC responses at 30°N: Scatter plot of filtered NAM_{10} index values occurring at persistent strong NAM_{10} intervals throughout the whole UKESM simulation (x axis) against AMOC anomalies at 30°N lagged 17 years after persistent intervals' central year (y axis). Blue points indicate persistent intervals and the dotted line represents the linear line of best fit for the points in black and blue. Also included is the 17-year lagged AMOC anomaly predicted by projecting the regression coefficients used to construct the linear fit onto the maximum smoothed NAM_{10} index in the ERA5 dataset (purple point).

4.9 Sensitivity to NAM thresholds and filtering

The results showing interactions between the vortex and the AMOC presented so far (figures 4.3 and 4.4) are derived from a stratospheric index which is highly processed. The NAM_{10} is both smoothed using a Gaussian filter and extreme values are subsequently selected to define intervals of anomalous vortex behaviour. Lagged responses of the AMOC are then obtained from these intervals. This processing relies on a number of parameters that need to be chosen: First, the filtering kernel width (the parameter σ, see equation 4.1) which dictates the number of years which contribute to smoothed NAM_{10} values. Second, the threshold value of the smoothed NAM_{10} used to define an interval of persistent vortex behaviour. Finally, for regression analysis such as that presented in figure 4.13d, the lag of the AMOC response in years used to correlate the magnitude of NAM_{10} extreme with the resulting AMOC anomaly also

needs to be selected.

So far, we have chosen these parameters in line with previous studies that utilise a similar smoothed NAM_{10} metric [*Reichler et al.*, 2012]. Namely, we utilise $\sigma = 2$ years to smooth all indices which allows contributions from approximately 6-8 years on either side of the interval centre which is approximately the length of the interval of persistent strong vortex behaviour in the 1990s of ERA5 (see figure 4.12). We also utilise the 5^{th} and 95^{th} percentiles to define weak and strong extremes respectively in the smoothed NAM_{10}. This yields approximately the same average rate of persistent vortex intervals in the pi-control of UKESM as appears in the modelling study of *Reichler et al.* [2012]. While values of these parameters may dictate some key physical features of the time series (for example interval width in years), there is little obvious justification for some parameter choices. In this section, we test the sensitivity of our results on vortex-AMOC interactions to choice of smoothing width (σ), NAM_{10} threshold and AMOC lag values.

First, we assess the impact of parameter choice on lagged response values of the AMOC at 50°N, the latitude at which the most prominent interactions were shown (see figure 4.3), following persistent NAM_{10} extremes. Parameter grids of the response to strong intervals for different combinations of lag and σ (figure 4.16a) show a similar response variation with lag (along the x axis of figure 4.16a) as that shown in figure 4.5 - positive responses peaking 2-3 years following stratospheric extremes followed by negative responses at 10-20 year lags. However, the largest negative response magnitude is observed when the NAM_{10} index is smoothed using $\sigma = \sim 5$ years at a lag of approximately 15 years instead of our original choice of $\sigma = 2$ years lagged by 17 years (as was used in figure 4.13d). This suggests that the AMOC responds most prominently to intervals which consist of contributions from approximately 10-15 years either side of the central year. Extremes intervals of this size are unlikely to consist of winters exhibiting all the same sign of vortex anomaly due to their length -

the largest run of consecutive positive NAM_{10} winters are shown in figure 4.13 and are only 10 years. Instead, these are likely intervals containing a combination of elevated NAM_{10} and neutral (near 0 smoothed NAM_{10}) winters - i.e. intervals that consist of winters with either a strong vortex or one that exhibits near climatological vortex winds and even those that may feature partial minor disruptions. This suggests that a key factor in the AMOC response to the vortex may not simply be the presence of ∼6-8 consecutive strong vortex seasons but the absence of major SSWs over a longer interval (∼10-15 years). While this result indicates a larger response using a wider smoothing window, applying this to observations like the analysis in section 4.8 may be difficult given the width of the window (including contributions from 10-15 years either side of the centre) in relation to the length of the observational record (approximately 40 years in ERA5). Furthermore, the observational record does not exhibit such a large interval of persistent vortex behaviour and the most prominent feature of the ERA5 NAM_{10} is the interval of approximately 8 years of strong NAM_{10} winters in the 1990s which is well captured using $\sigma = 2$ years.

The AMOC response magnitude is also sensitive to varying the percentile threshold used to define persistent vortex intervals. Figures 4.16b and c show the variation in response for different combinations of threshold and σ and threshold and lag. Both sub-figures indicate that the average AMOC response magnitude increases significantly with threshold percentiles over approximately 95%. This increase in magnitude is expected as increasing the threshold for events will include NAM_{10} intervals which on average contain more years with an anomalously strong vortex and likely a more persistent source of atmospheric forcing to the NAO and the ocean.

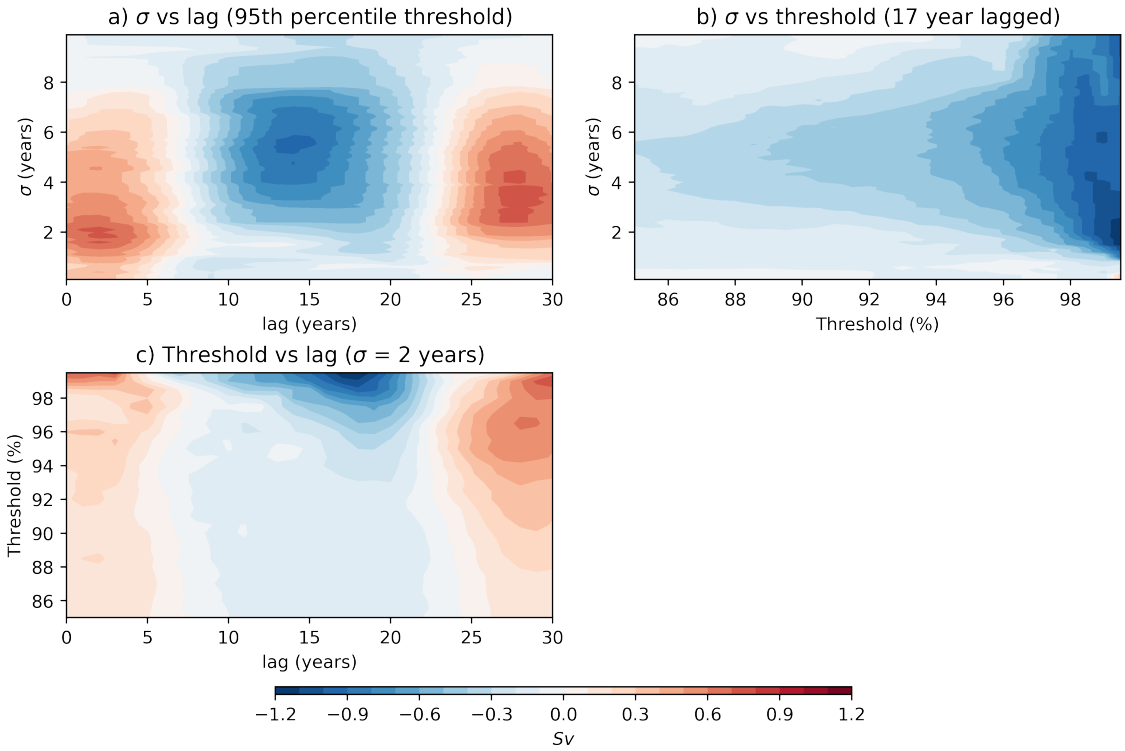


Figure 4.16: Response of the AMOC at 50°N to strong NAM_{10} intervals for combinations of **a):** smoothing width (σ) and lag both measured in years with percentile threshold held at 95%, **b):** σ and percentile threshold used to define persistent NAM_{10} extremes with a 17-year lag and **c):** Threshold and lag with $\sigma = 2$ years.

We also test the sensitivity of our key result outlined in section 4.8, that the magnitude of NAM_{10} extremes is directly proportional to the AMOC anomaly 17 years later, to parameter choices. Figure 4.17 shows the correlation between strong NAM_{10} extremes and the lagged AMOC anomaly at 50°N (black vertical lines) for a range of threshold percentile values used to define persistent vortex intervals (increasing in panels left to right on the figure) and smoothing widths (σ, increasing top to bottom). Each correlation's significance level is compared to a PDF of surrogate correlations constructed using the same procedure as for figure 4.14. For values of σ between 2 and 7 years, the real correlation lies on the edge of the surrogate correlation PDF for all values of the threshold percentile. This suggests the relationship between positive extremes in the smoothed NAM_{10} and the resulting AMOC response is robust to the

definition of strong persistent vortex interval for these values of smoothing width. For σ = 1 year, the correlation lies well within the distribution surrogate PDF for all sampled values of threshold percentile suggesting the vortex-AMOC interaction is significantly weakened for these parameter combinations. This weakening is accounted for by the fact that with a filtering kernel with $\sigma = 1$ year, contributions from only approximately 3 years either side of the interval centre (with the majority of contributions from 1-2 years either side) are included in smoothed NAM_{10} values. This may not be sufficient to provide atmospheric forcing persistent enough to induce significant correlations between NAM_{10} extremes and AMOC anomalies. For σ values larger than 7 years, the correlations are also deemed not significant against the bootstrapping test for the sampled values of percentile thresholds. This is because, at such large values of σ, each index is smoothed over time intervals similar to (and above) the lags considered in this analysis (17 years). As a result, variations in the NAM_{10} and AMOC on timescales up to and beyond 17 years are removed thus also removing significant correlations.

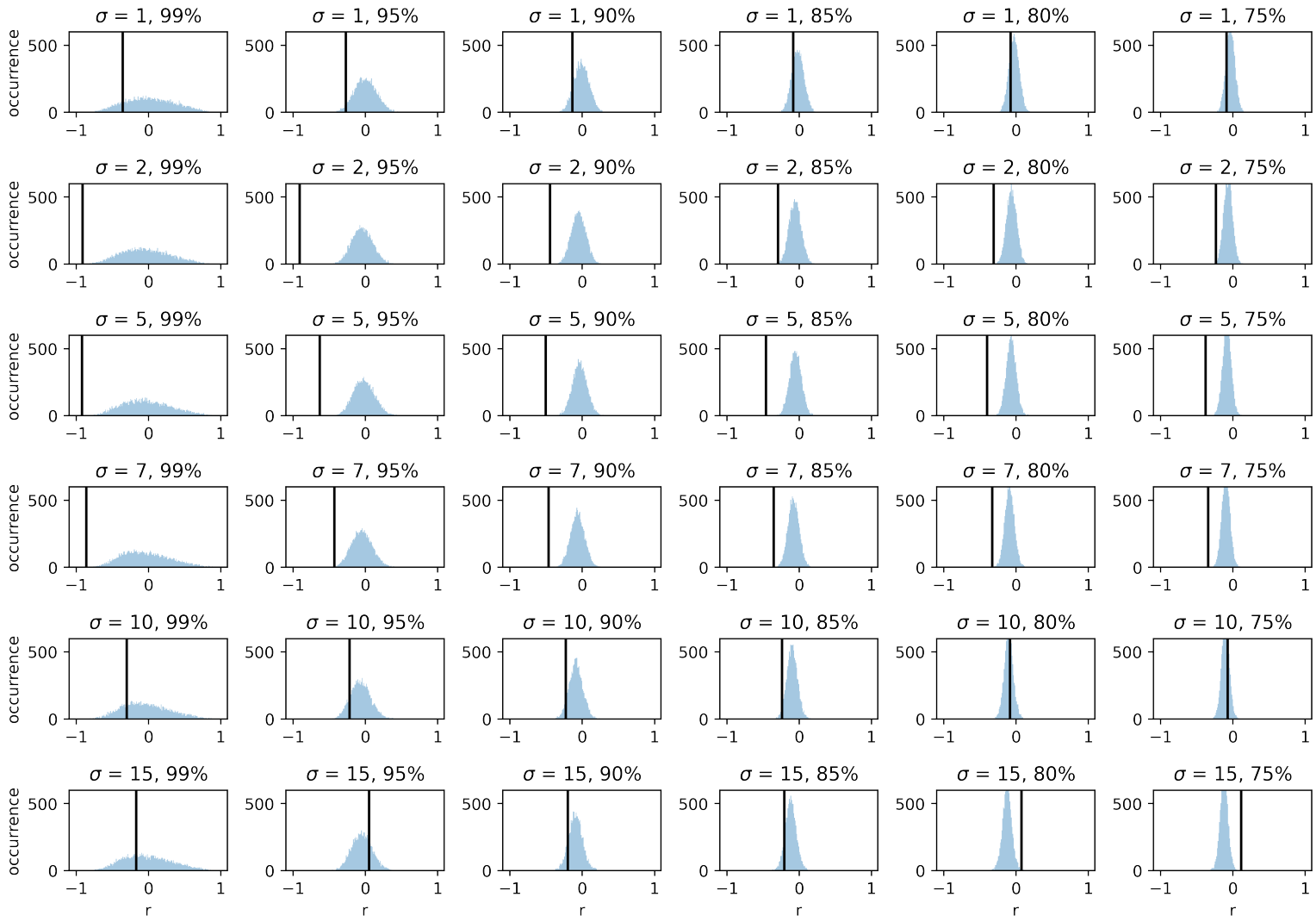


Figure 4.17: like figure 4.14a for different combinations of smoothing width (σ) (increasing in panels top to bottom) and percentile used to define NAM_{10} extremes (decreasing left to right). The title of each sub-figure indicates the pair of parameter values used.

We finally carry out a similar analysis on correlations between weak NAM_{10} extremes and the resulting AMOC anomaly (figure 4.18) which yielded low correlation with our original choice of parameters (σ =2 years, lag = 17 years, percentile threshold = 5%). In contrast to figure 4.17 for strong intervals, the majority of correlations for different parameter combinations lie well within the corresponding surrogate PDF. There are some exceptions, however, with significant negative correlations for σ= 5 years and threshold = 10% and 15% suggesting a possible connection between weak intervals of approximately 10 years with the AMOC. However, as discussed above, few intervals of this length exhibit exclusively negative NAM_{10} values (only 2 in the simulation) and instead these likely contain both weak and neutral vortex winters.

As discussed in section 4.8, the small correlations associated with weak intervals may be due to the different dynamical behaviour associated with weak persistent intervals which is highly dependant on SSW timing within each winter. Overall, the results presented from this sensitivity analysis once again suggests a key role for positive (strong) extremes in the vortex-AMOC interactions which are generally robust to reasonable choices of parameter values (threshold percentile and σ) while interactions involving anomalously weak vortex intervals appear less pronounced.

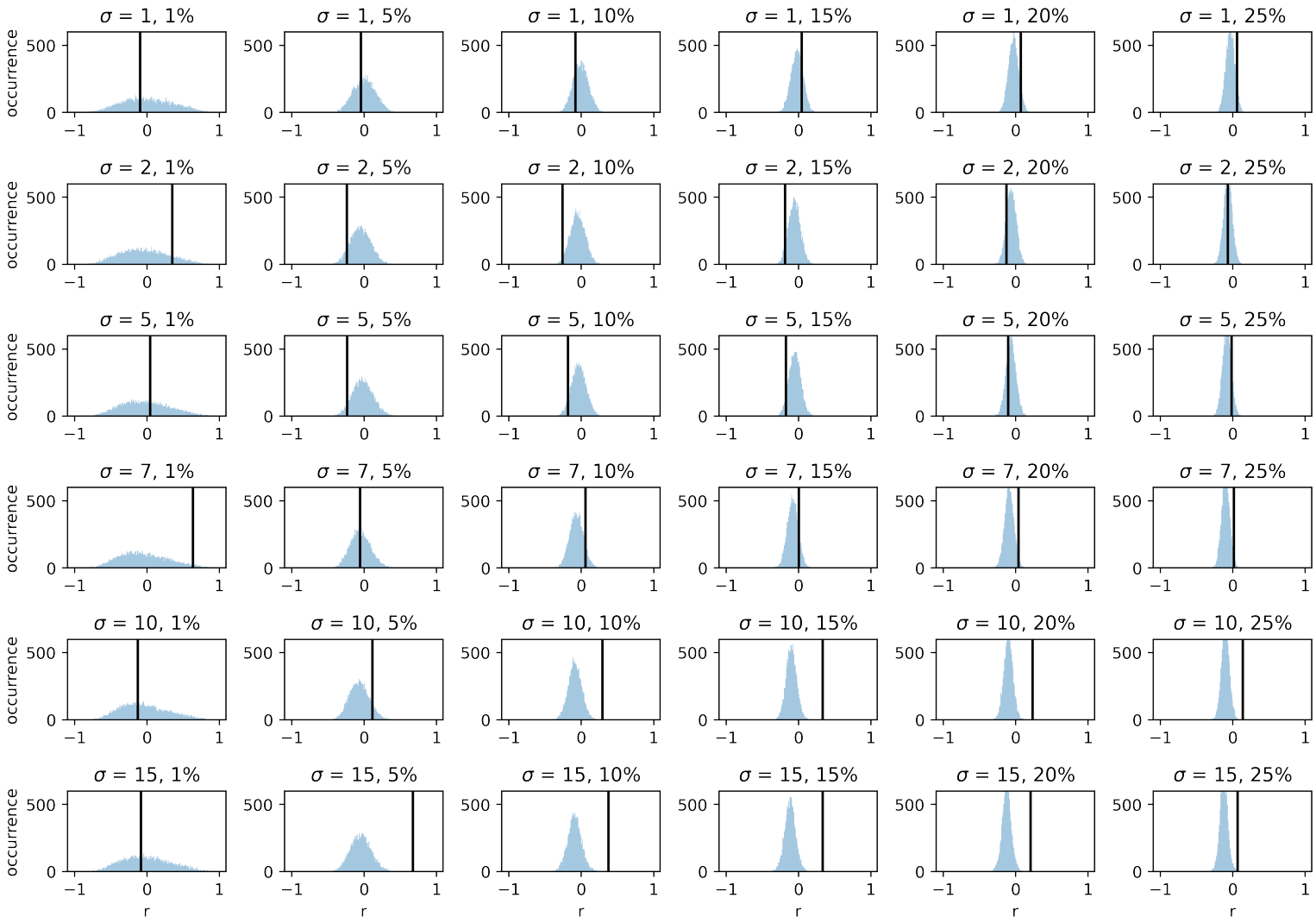


Figure 4.18: like figure 4.17 for correlations between NAM_{10} values associated with persistent weak intervals and 17-year lagged AMOC anomalies at 50°N.

4.10 Summary and discussion

In this chapter, we have analysed the influence of persistent polar vortex extremes on surface and ocean circulation in a 1000 year pi-control simulation of UKESM1. Persistent vortex anomalies are identified using a smoothed NAM_{10} index which characterises intervals of approximately 6-8 years during which the NH winter vortex is anomalously strong (positive NAM_{10} anomaly) or weak (negative NAM_{10} anomaly). While the surface impacts of stratospheric extremes in individual winters has received much attention [*Baldwin and Dunkerton*, 2001; *Domeisen*, 2019; *Charlton-Perez et al.*, 2018], the surface impacts of consecutive sets of persistently anomalous winters have been less well studied and teleconnections between the stratospheric vortex and ocean variability are not well characterised or understood.

We examine the AMOC response to long-term variations in the stratospheric polar vortex using composite analysis of the AMOC strength following persistent anomalous NAM_{10} intervals. We find oscillatory responses in the NAO and the AMOC consistent with previous work [*Reichler et al.*, 2012]. Diagnosis of the model supports a mechanism in which a persistently strong vortex (positive NAM) perturbs a positive NAO anomaly which subsequently induces a positive AMOC response at 2-3 year lags via an increase in sub-polar North Atlantic ocean-atmosphere heat flux. This, in turn, feeds back onto the NAO to drive a reversal in NAO phase (to negative) which leads to a subsequent negative AMOC anomaly at 15-20 year lags. The integrated effect of long-term oscillatory signals in the NAM_{10} and the associated NAO variations may thus act as a metronome for the AMOC, which is a natural mode of oscillation in ocean circulation that varies on similar timescales. Further diagnosis of the separate impacts from intervals of persistent positive NAM_{10} (strong vortex) and persistent negative NAM_{10} (weak vortex with repeated SSW occurrences) showed that persistent strong vortex intervals had a much larger impact on the AMOC, perhaps not surprisingly

because the vortex anomaly is consistently present throughout the whole winter.

We additionally find prominent non-stationary variations across multiple timescales in the AMOC, NAO and NAM_{10}. Wavelet analysis revealed extended intervals in which 30, 50 and 90-year periodicities were dominant, so the composite response patterns were complicated by the superposition of contributions from intervals exhibiting different timescale behaviour.

Interestingly, while the vortex (i.e. NAM_{10}), NAO and AMOC indices all co-varied at the 30 and 50-year periodicities, only the NAM_{10} and AMOC co-varied at the 90-year periodicity and co-spectra analysis suggested that the AMOC leads the vortex signal. This suggests a feedback of AMOC variability onto the vortex that does not involve the NAO. Chapter 3 found long-term (90-year) co-variability between the vortex and the QBO (figure 3.19) so suggesting the possibility that the 90-year AMOC-vortex relationship could act via an influence of the AMOC on equatorial wave forcing of the QBO. This would then influence the vortex through the Holton-Tan relationship. This was explored through wavelet and co-spectra analysis of variations in tropical east Pacific deep convection and QBO amplitude. These showed similar 90-year co-variability, indicating this as a plausible mechanism for the source of long-term variability in the QBO and the vortex, but further analysis of individual steps in the process, such as amplitude modulation of the various tropical waves that give rise to the QBO, would be required to confirm this.

Finally, we have applied the model results, that link a lagged AMOC response to the presence of persistent vortex anomalies (sets of consecutive strong or weak vortex winters), to assess the possible contribution of the interval of persistently strong vortex in the 1990s to the recent observed changes in the AMOC. Our analysis suggests a maximum AMOC response at 50°N with a lag of approximately 17 years. The lagged vortex-AMOC relationship is statistically significant using the AMOC response at

both 50°N ($r = -0.908$) and also at 30°N ($r = -0.652$), the latter being closer in latitude to the RAPID Array observations. Using a regression technique, we estimate that -0.89Sv (50°N) and -0.49Sv (30°N) of the observed RAPID Array AMOC trend by 2012 can be associated with the interval of persistent strong vortex behaviour centred on 1995. These estimates represent nearly 30% (50°N) and 17% (30°N) of the total decrease in AMOC transport between 2005 and 2013 in the RAPID array data. The observed negative trend in the AMOC has been attributed to a range of factors, including the influence of anthropogenic forcings [*Caesar et al.*, 2018, 2021], but to our knowledge, the potential role of vortex variability has not previously been considered. The origin of the interval of persistently strong vortex in the 1990s is unknown, but it was most likely due to internal variability. There is currently no consensus amongst climate models on how the vortex will respond to anthropogenic climate change [*Ayarzagüena et al.*, 2020], and the 1990s appear to have been an anomalous period with no clear long-term trend emerging [*Domeisen*, 2019]. As a result, our findings may indicate a significant role for internally generated signals in the recent negative AMOC trend.

There are a number of caveats to these results. Firstly, the results come from a single model - although there has been limited analysis of vortex-AMOC interactions in CMIP5 models [*Reichler et al.*, 2012], there is evidence that GCMs under-represent the influence of SSW events on the mid-latitude tropospheric jet, the NAO and surface temperatures, part of the "signal to noise" problem identified by *Scaife and Smith* [2018]. Nevertheless, the model showed a clear NAO signal up to 3 months following vortex anomalies, indicating a reasonable representation of stratosphere-surface interaction. Analysis in chapter 3 also noted an underestimation of SSW frequency compared to the ERA-Interim dataset (figure 3.2), which indicates a positive bias in the mean vortex strength as well as the NAM_{10}, leading to the possible over-representation of positive NAM_{10} intervals. The variability in the AMOC may also be under-represented

in the simulation, as *Roberts et al.* [2014] suggests that the models' decadal variability is smaller than that in the RAPID dataset. Additional analysis using a suite of CMIP6 models would clearly be useful to assess the robustness of the results presented here.

Overall, results from this chapter suggest a novel, non-stationary interaction between the vortex and Atlantic circulation as well as suggest a possible key role for the stratosphere in recent AMOC observations. Key limitations to the analysis presented here as well as further work following on from this study are explored in section 6.2.

CHAPTER 5

The role of vertical structure in QBO teleconnections

5.1 Introduction

Findings from chapter 3 indicated an association between a vertically integrated QBO index and the vortex (see figures 3.5 and 3.6). While a large body of work has aimed to understand teleconnections between the equatorial winds and the vortex (see section 2.5.1), aspects of the connection between the QBO and other parts of the stratosphere as well as the troposphere and surface, evade definitive explanation.

The QBO is typically defined by the equatorial ZMZW at a single level in the mid-stratosphere and the 50 hPa level is usually used for observational studies into teleconnections between the QBO and NH variability [*Baldwin et al.*, 2001]. However, some studies have also noted the importance of characterising the vertical structure of the QBO [*Fraedrich et al.*, 1993; *Wallace et al.*, 1993; *Baldwin and Dunkerton*, 1998; *Dunkerton*, 2017; *Gray et al.*, 2018; *Andrews et al.*, 2019]. In an observational-based study, *Gray et al.* [2018] find an enhanced association between the QBO and polar vortex as well as MSLP anomalies over the NH when a metric incorporating the vertical coherence of equatorial winds via empirical orthogonal functions is utilised.

Such an EOF method is first developed in *Fraedrich et al.* [1993] and *Wallace et al.* [1993] and analysed further in *Schenzinger* [2016]. *Gray et al.* [2018] proposes three distinct physical pathways by which the QBO exerts influence over tropospheric and surface variations: First, via modulation of NH winter vortex strength (the HT effect, see section 2.5.1) and the subsequent downward propagation of NAM anomalies from the vortex to the surface (see section 2.6). Second, through influence over tropical upwelling that results from the presence of different QBO phases in the lower stratosphere as seen in the observational study of *Liess and Geller* [2012]. Finally, via alterations in horizontal temperature gradients in the tropospheric subtropical jet region also caused by the induced meridional circulation, an effect suggested in *Garfinkel and Hartmann* [2011]. *Gray et al.* [2018] also shows that the nature of responses in the vortex and surface to the QBO vary significantly within the NH winter season with midwinter responses (in January) sensitive to QBO winds near 50 hPa in contrast to early and later winter (February and March) responses which are most sensitive to the QBO defined at 20 hPa and 70 hPa.

In a subsequent study, *Andrews et al.* [2019] introduce a similar but simpler methodology by defining the QBO as the average ZMZW between two vertical levels, which preferentially selects time intervals that display a vertically coherent QBO phase between the specified levels. This work (*Andrews et al.* [2019]) uses a reanalysis dataset as well as a historical simulation of the HadGEM3-GC2 model and defines NH winters occurring under QBOE and QBOW conditions as those which appear when the deep QBO metric exhibits magnitudes greater than $5ms^{-1}$. MSLP composites selected using the definition of QBO phase in NH winter are examined and enhanced responses to the QBO from the NAO and the AO are reported when the vertically integrated metric is used to define the QBO phase compared to a single level definition applied to the same datasets. However, this work does not analyse whether the vortex response is also enhanced when using the deep QBO metric and the pathways responsible for

the enhanced surface response as well as the mechanisms involved in the association are still not well understood.

In addition to the QBO, variations in the SAO (see section 2.4) also show associations with the vortex. The influence of the SAO on vortex variability and SSWs was first hypothesised in the observational study of *Gray et al.* [2001] which used rocketsonde data to establish a link between the vertical extent of the westerly SAO phase and vortex strength. However, these results were not statistically significant and the work stressed the need for more study with comprehensive observations as well as model simulations. Subsequent studies found similar links but with varying features: *Gray* [2003] found an influence of upper stratospheric equatorial winds on SSWs over the whole season but mostly in mid-winter. This was attributed to timing of the phase transition from westerly to easterly SAO. *Gray et al.* [2001] and *Hamilton* [1998] suggest that equatorial winds at all stratospheric levels (including the QBO and SAO regions) influence the vortex and a combination of QBO and SAO conditions is required to obtain a significant signal in vortex variability.

While many studies highlight statistical associations between QBO and SAO metrics with other parts of the climate system, they are less effective at demonstrating causal relationships. Indeed, *Andrews et al.* [2019] note the possibility that both the occurrence of deep QBO phases and NAO and AO anomalies may be driven by an unidentified third factor which gives rise to a robust statistical link between the phenomena without any direct physical connection. Studies which utilise observation based datasets to examine the QBO-NAO/AO interaction are also hampered by record length as well as the intrusion of other forcing factors associated with NH surface variations which obscure the signal from the QBO. These include Solar cycle variability [*Gray et al.*, 2016], volcanic eruptions [*Stenchikov et al.*, 2004], in particular stratospheric injection of aerosols, as well as surface variability in other regions such as ENSO [*Bell et al.*, 2009]. Some studies aim to overcome these potential pitfalls and

explicitly test the nature of teleconnections with forced model setups, where momentum forcing or nudging is applied to winds in specific regions of the atmosphere. Such works further suggest the importance of the SAO and QBO region when considering the vortex. *Pascoe et al.* [2005] finds improved vortex representation in model runs with forced winds in the equatorial stratosphere (both QBO and SAO regions separately) and *Gray et al.* [2020] shows that nudging model winds in the SAO region (as well as specifying tropospheric wave forcing) towards reanalysis for a single winter, allows the model to capture an SSW observed in that winter with high degrees of accuracy in its timing and magnitude.

Despite the significant body of work presented above into the QBO and its relation to other parts of the climate system, the role of vertical structure in teleconnections is not fully understood. In this chapter, we utilise a set of nudging experiments to explicitly test the importance of vertical coherence in the equatorial stratosphere's influence over the vortex as well as tropospheric and surface variability. Results from this analysis may aid in establishing the true nature of QBO teleconnections as well as develop understanding of a potentially powerful source of forecast predictive skill for NH surface weather.

5.2 Model configuration

To explicitly test the effect of QBO vertical coherence on teleconnections, we perform a set of simulations of a modified version of the UKESM GCM analysed in chapters 3 and 4. As with the pi-control simulation examined so far, the model component for the atmosphere is GA7.1, GHG concentrations are set to 1850 levels (see section 3.2.1) and volcanic eruptions are absent (however a constant background volcanic aerosol level is imposed). The primary difference between the pi-control and the configuration utilised here is the experiments run with no coupled ocean component. Instead, SSTs

are prescribed using monthly mean climatological fields obtained from an interval of the pi-control (year numbers 96-126) [*O'Connor et al.*, 2021]. Sea Ice extents are also prescribed to climatological values using the same interval of the pi-control. All simulations are initialised using conditions from the start of the 30-year interval of the pi-control used to calculate SST and sea ice climatologies (year number 96). We choose to impose SST and sea ice conditions in our experiments as this removes contributions to the NAO/AO from interannual to decadal variability at the surface such as ENSO. The absence of volcanic eruptions similarly prevents influence of stratospheric injection of volcanic aerosols on the NAO. Removing these contributions, in turn, helps to isolate the effects of the QBO on surface variability. We utilise three simulations using the above configuration with different forced setups:

- First, an unforced control simulation referred to as the **pre-industrial clim control** (pi-clim cntrl). This simulation is produced as part of CMIP6 and is run for 45 years. It is documented in full in *O'Connor et al.* [2021].

- Second, a forced run which fixes the state of the equatorial winds to a vertically coherent idealised QBO (see next section for details of the idealised winds). This simulation is referred to as the **deep QBO experiment** (or simply the deep experiment) and is run for 50 years.

- A forced run which fixes the state of the equatorial winds to an idealised QBO with a low degree of vertical coherence (i.e. with opposite phases in the upper and lower stratosphere, see next section). This simulation is referred to as the **shallow QBO experiment** (or simply the shallow experiment). This simulation is also run for 50 years.

We choose to simulate both forced runs for 50 years to ensure the simulations cover a sufficient number of the QBO cycles to carry out a robust statistical analysis

on QBO teleconnections while also working within restrictions on computing time. The pi-clim cntrl was produced as part of CMIP6 as opposed to created specifically for this analysis and was run for 45 years. This discrepancy in simulation length is relatively small and should not affect the comparison between the experiments.

5.2.1 Nudging

In order to impose the vertical structure of the QBO in the deep and shallow experiments, we employ a method to constrain atmospheric conditions in a GCM simulation known as nudging. In this method, an atmospheric quantity, Y, is constrained via Newtonian-relaxation which pushes the model state for Y towards some imposed value at each model timestep such that

$$\Delta Y = G\Delta t(Y_{imposed} - Y_{model}), \tag{5.1}$$

where ΔY is the change in Y applied by the nudging scheme, $Y_{imposed}$ is the state of Y from the imposed field, Y_{model} is the value of Y the model has evolved to since the last timestep (when it was last nudged), Δt is the model timestep and G is the relaxation parameter [*Telford et al.*, 2008]. G is a measure of the strength of the relaxation towards $Y_{imposed}$ at each timestep and can also be expressed as $G = \frac{1}{\tau}$ where τ is known as the relaxation timescale, a measure of the speed at which the relaxed field will reach its target value. When choosing the relaxation timescale, a balance is required between constraining the model sufficiently to the imposed state (i.e. a short enough τ such that the model's Y avoids evolving freely) and avoiding the introduction of large gradients (a large enough τ to avoid model instability). The MetOffice Unified model, of which the model configurations presented here are a part, typically uses a relaxation timescale of 6 hours at all vertical levels [*Telford et al.*, 2008]. This has been shown to produce good quality nudging results in a range of

studies employing such a method despite the different radiative timescales present across atmospheric levels [*Gray et al.*, 2020] so we proceed with this value for our experiments. In our experiments, we nudge the zonal wind, u, towards an idealised version of the QBO wind fields expressed as

$$u_{qbo}(t,p) = F(p)sin(\frac{2\pi(t+s(p))}{period}), \tag{5.2}$$

where $s(p)$ is a parameter which varies with pressure level and sets the rate of phase shift in the QBO with descending height. For simplicity, we choose $s(p)$ such that a linear descent rate with increasing $log(p)$ is achieved. This is achieved by setting $s(p) = klog(p/p_0)$, where k is a constant and p_0 is a reference pressure level (in this case 1 hPa) from which we measure the descending phase difference. We then select different values for the parameter k to achieve deep QBO and shallow QBO structures: For the deep experiment, $k = 2.5$ achieves a higher degree of vertical phase coherence while for the shallow experiment, $k = 5$ which leads to a larger phase shift with descending pressure level (and therefore less vertical coherence). The choices of values for this parameter are informed by previous studies into the descent rate of QBO phases. Notably, *Kinnersley and Pawson* [1996] and *Coy et al.* [2020] show in observations that the rate of change of winds with respect to the height coordinate (z), that measures the time variation of vertical shear in the QBO, ranges from approximately $-15 - 15ms^{-1}km^{-1}$. We therefore aim to reproduce idealised winds with rates of change in this range. We choose the period of the QBO in both experiments to be 32 months for consistency with the QBO period exhibited in the UKESM pi-control which is extended compared to reanalysis (see section 3.3) as well as that of the pi-clim cntrl which is analysed in the following section. $F(p)$ is a momentum forcing vertical profile applied to reproduce the variation in magnitude of the QBO with pressure level (the QBO peaks in magnitude at around the 20 hPa

level in ERA-Interim). We choose our $F(p)$ in line with the methodology of *Pascoe et al.* [2005] who design similar idealised QBO fields and utilise a $F(z)$ (with altitude in km as the height coordinate) which takes the form of a Weibull function given by

$$F(z) = R_D \frac{1}{\gamma \beta^{\alpha}} Z_D^{\alpha-1} e^{-Z_D/\beta}, \tag{5.3}$$

where the parameters are set to $\alpha = 3.5, \beta = 0.27, \gamma = 3.2335, R_D = 40.0 ms^{-1}, Z_D = (z - 15)/20$ and we make an appropriate conversion between vertical coordinates z and p.

The idealised time-height QBO profiles generated for both experiments are shown in figure 5.1 and highlight the key differences between the idealised QBOs: The deep QBO winds (figure 5.1a) exhibit the same sign of wind throughout the middle atmosphere for the majority of the series while the shallow QBO (figure 5.1c) shows different phases between the upper and middle stratosphere. The deep experiment exhibits significantly faster descent rates of the zero wind line (thick black lines on figure 5.1) than the idealised shallow experiment and the rates of change of phase with height (z) for both experiments, which measures the time variation of the vertical shear, lie within the range reported by observational studies into the QBO - i.e. up to a magnitude of $15 ms^{-1} km^{-1}$ as in *Kinnersley and Pawson* [1996]. The corresponding 5 year sample of equatorial ZMZMW from ERA-Interim is also included for comparison (figure 5.1e). This sample highlights that the observed QBO exhibits deep and shallow characteristics at different times, i.e. vertical coherence similar to the deep QBO near month number 50 and different phases is the lower and upper stratosphere near month number 15 similar to the shallow QBO. Both idealised QBOs also exhibit a peak magnitude near the 20 hPa pressure level due to the implementation of the momentum forcing profile, $F(p)$, seen in figures 5.1b and d.

In both experiments we apply the relaxation in equation 5.1 towards the corre-

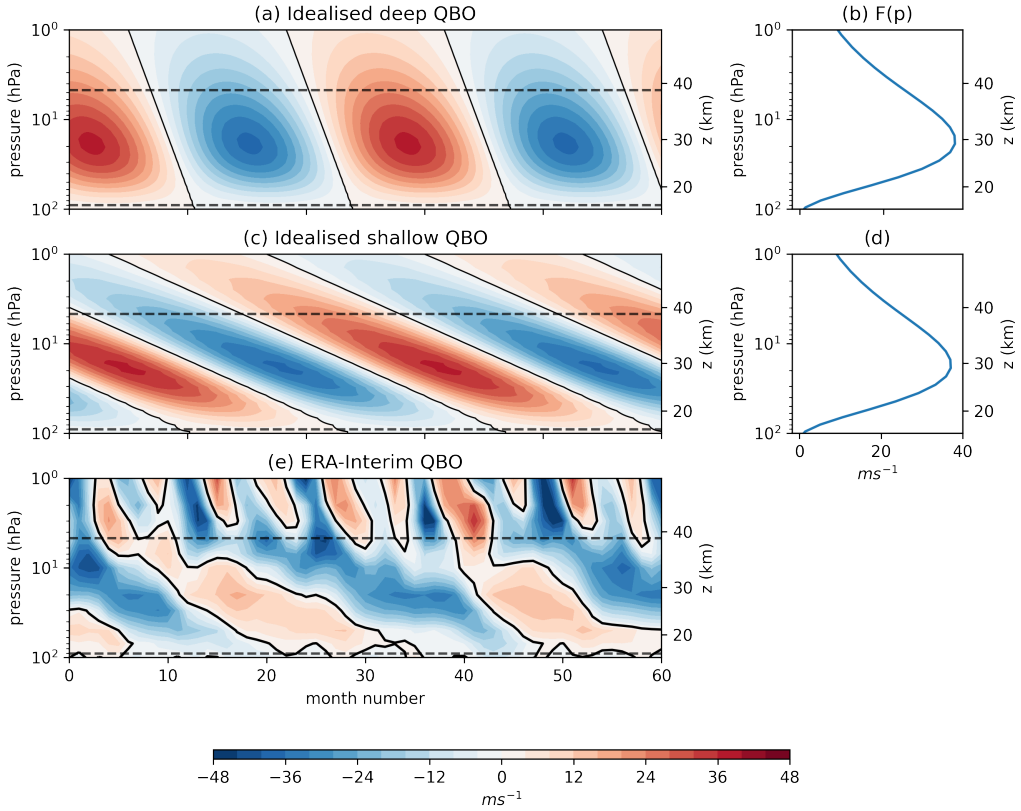


Figure 5.1: Sample time series of idealised equatorial ZMZW and associated momentum forcing profile for the deep (a and b respectively) and shallow (c and d respectively) QBO experiments. Panel e shows a corresponding 5 year sample of ZMZW from ERA-Interim. Horizontal dashed lines on (a), (c) and (e) denote the 6 hPa and 90 hPa pressure levels between which we implement nudging towards the idealised wind in each experiment. Solid back lines denote the zero-wind line.

sponding QBO winds over the set of model levels approximately corresponding to the pressure level range 90-6 hPa and the latitudinal range 10° S–10° N. The relaxation is applied at all longitudes. At the boundary between the nudging region and the rest of the atmosphere we apply a tapered version of the relaxation with a value of the parameter G that decreases linearly with increased distance from the relaxation region. This tapering is applied on the 2 atmospheric levels at the bottom and top of the vertical region and 5° either side of the latitudinal region. This tapering is applied

to avoid introducing large vertical and latitudinal gradients in zonal wind and prevent potential model instability.

5.3 QBO characteristics

We first analyse the equatorial winds in each experiment and verify whether the implementation of nudging has resulted in the desired equatorial ZMZW profiles. Figures 5.2a and c show a 5 year sample of the equatorial winds in each experiment that results from implementing QBO nudging between the 90 hPa and 6 hPa levels. These winds reflect many of the key features of the idealised winds (figure 5.1); the deep experiment (figure 5.2a) exhibits vertical coherence in the middle stratosphere while the shallow simulation (figure 5.2b) shows opposite phases of the QBO in the upper and lower sections of the nudging region (9 hPa-6 hPa). The period of ZMZW variations in both experiments is indicated by the Fourier power spectra shown in figures 5.2b and d. The mid-stratospheric winds (∼90-10 hPa) exhibits peak Fourier power corresponding to a period close to the value specified by the idealised winds (32 months) in both experiments. The QBO variations produced by the nudging experiments also show good agreement in phase amplitude and period with that of the pi-clim cntrl (figures 5.2e and f). It also broadly resembles the winds in ERA-Interim (figures (5.2g and h)) although the QBO from this dataset exhibits varying degrees of vertical coherence - a deep QBO phase is observed near month number 50 while a shallow QBO is evident near month number 15. These QBO samples confirm that the implementation of the nudging in our experiment has been effective in imposing different degrees of vertical coherence while retaining some of the characteristics of the QBOs in the un-nudged run and ERA-Interim.

While the QBO of both simulations reflects some of the main characteristics of the target nudging winds, there is a notable asymmetry in the amplitudes of the two QBO

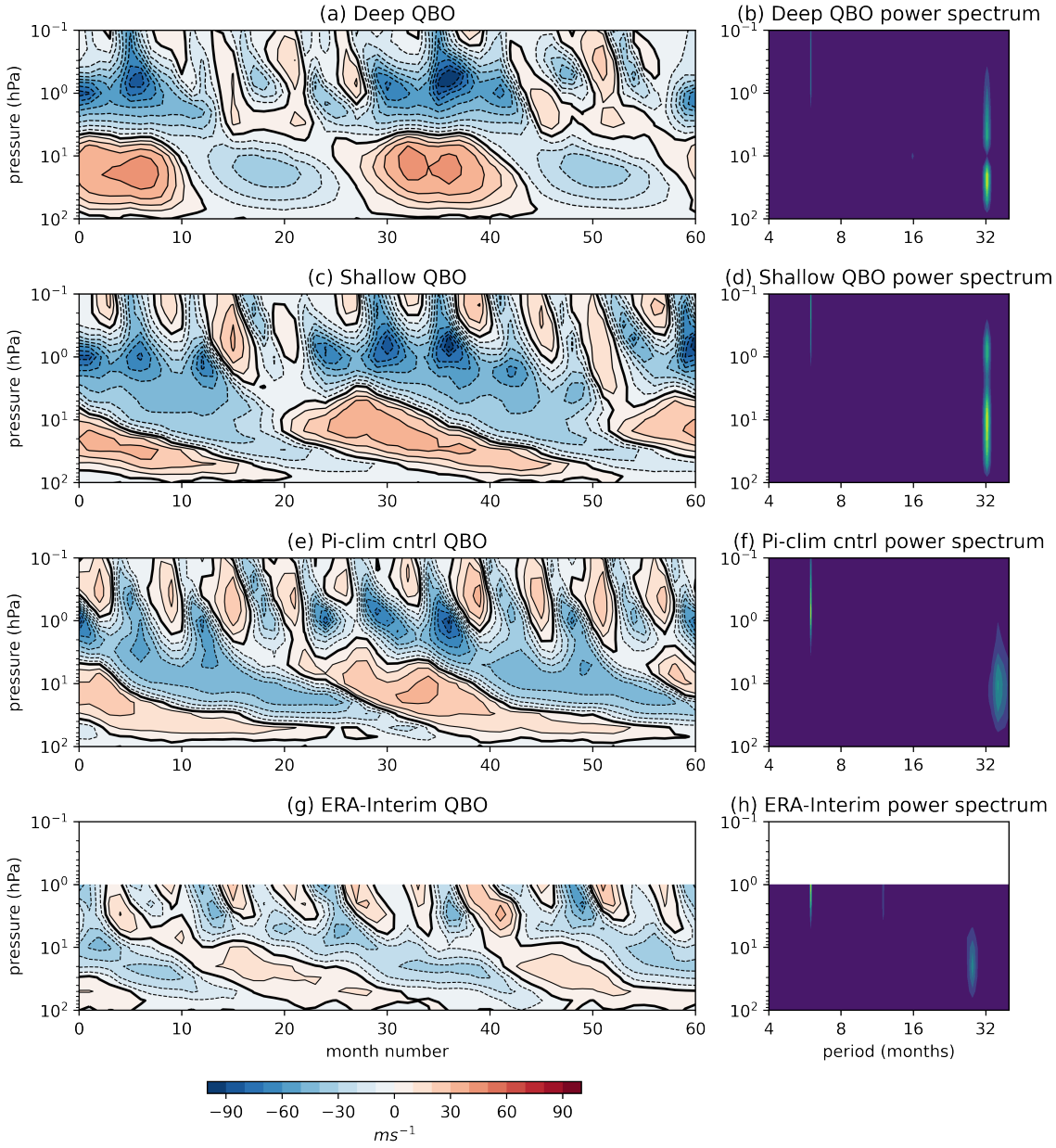


FIGURE 5.2: 5 year sample of ZMZW averaged between 5° S–5° N latitude from the deep QBO (a), shallow QBO (c) and pi-clim cntrl (e) simulations and ERA-Interim (g). Thick black contours denote the 0-wind line where westerlies meet easterlies. Sub-figures b, d, f and h show Fourier Power spectra for equatorial winds at various levels from the same datasets.

phases in both experiments with the westerly phase amplitude appearing larger in all QBO cycles throughout each simulation. This is an unexpected result - we defined

the target nudging field using equation 5.2 which ensures each phase of the idealised QBO exhibits identical magnitude (i.e. $F(p)$ in equation 5.2 is constant in time). To examine this asymmetry further, we analyse the time series of simulated (model output) and idealised (nudging input) winds on individual pressure levels (Figures 5.3 and 5.4). In the deep experiment (figure 5.3), the easterly phase of the QBO is in good agreement (within $\sim$1%) with the idealised winds on each of the pressure levels sampled. In contrast, the magnitude of the westerly phase resulting from the simulation systematically 'overshoots' compared to the nudging winds. This effect is apparent throughout much of the mid-stratosphere (10 hPa-50 hPa) and suggests the possibility of a westerly momentum forcing term in the model which acts to override the influence of the nudging scheme. This in turn may suggest that our selection of nudging timescale, $\tau = 6$ hours, is too long in relation to timescales over which other forcing terms act. The effect is less pronounced in the shallow experiment with only the QBO at 50 hPa exhibiting notable over-representation in westerly amplitude. The source of this additional forcing term is unclear but is likely closely associated with Kelvin or gravity wave forcing as this is the primary source of the westerly QBO phase (see section 2.4). This may indicate the requirement for a shorter nudging timescale for future nudged QBO experiments using this configuration as the model appears insufficiently constrained at the positive extremes of the QBO. This is a surprising result; *Telford et al.* [2008] present an evaluation of the efficacy of the MetOffice Unified Model (of which our simulations are a member) nudging scheme and show that, using $\tau = 6$ hours, zonal winds in the mid-stratosphere can be nudged towards reanalysis fields with a high degree of correlation ($r > 0.98$) between model output and target winds. Further work beyond the scope of this study is required to establish the source of this discrepancy but *Telford et al.* [2008] points out that the primary reason for the choice of $\tau = 6$ hours is due to the time resolution of the reanalysis data as opposed to necessarily due to model instability. In our experiments, the time

resolution of the nudging fields are not constrained by data availability as they are synthetically generated and, as a result, experiments with a smaller τ are feasible and may rectify the biases evident from figures 5.3 and 5.4.

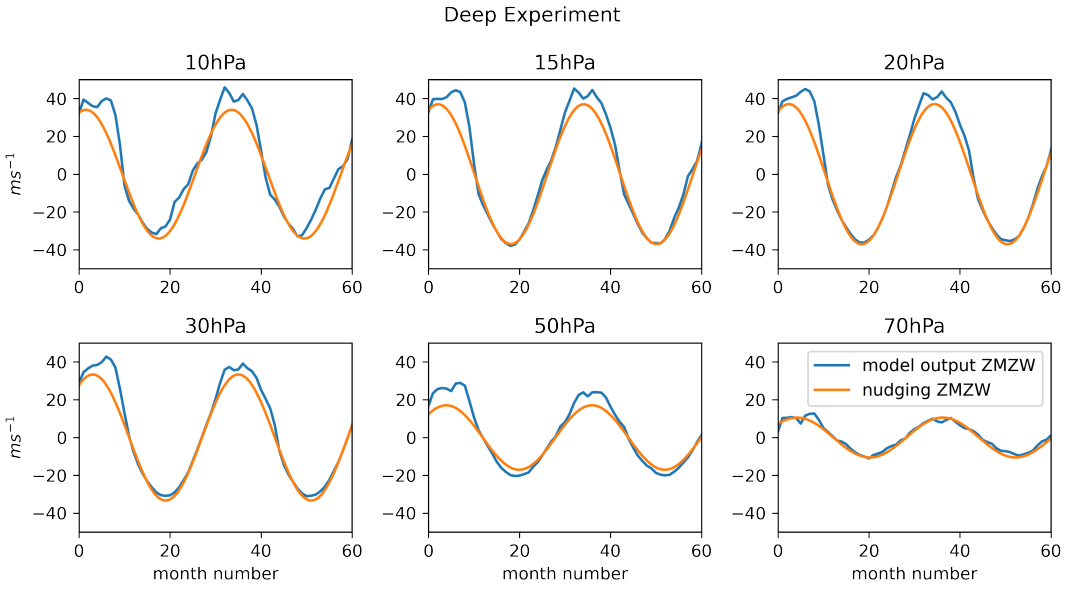


FIGURE 5.3: 5 year sample of ZMZW on individual pressure levels averaged between 5° S–5° N latitude from the deep QBO experiments (blue) and the Idealised wind field used for nudging in the same experiment (orange).

While this bias does lead to marginal asymmetries in QBO phases, the desired vertical structures are still obtained in both experiments which is the focus of this study and therefore we proceed with the simulations for analysis of QBO teleconnections in the next section. The possible detrimental effect of this amplitude bias is that NH winters may preferentially occur under one QBO phase more than the other if we define a QBO phase using equatorial winds over a given threshold ($5ms^{-1}$ is commonly used). As a result, in all analysis of these simulations, we note the number of NH winters exhibiting each QBO phase and only draw major conclusions in cases where their abundance is broadly comparable.

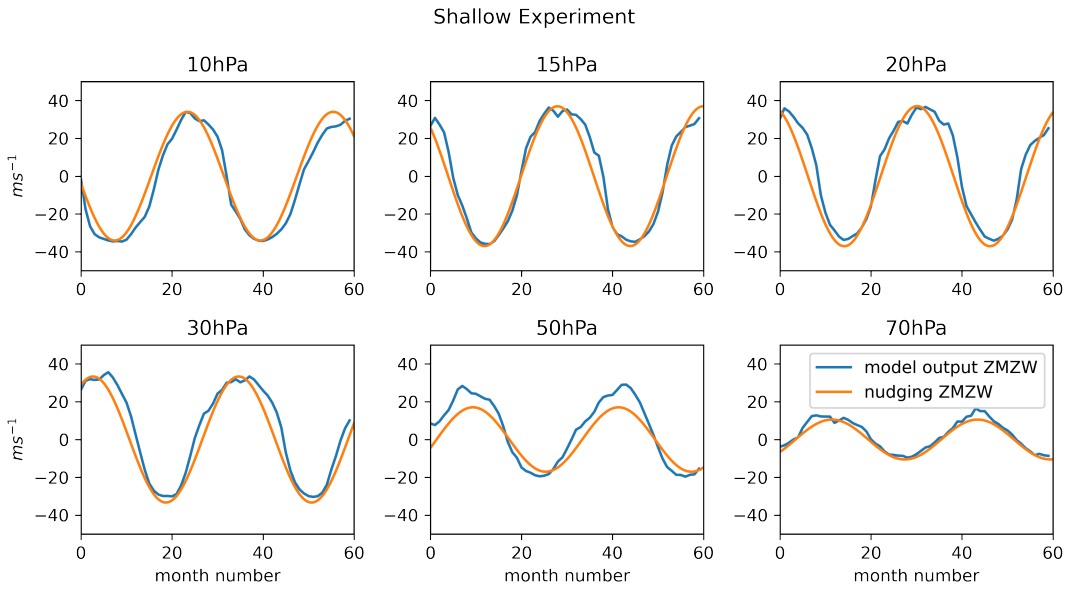


FIGURE 5.4: Like figure 5.3 for the shallow QBO experiment.

5.4 Other atmospheric characteristics

In addition to the imposed QBO states, both experiments also exhibit variations in ZMZW on the 1 hPa level and above corresponding to a period of ∼6 months which indicates the presence of an SAO like variation (see figure 5.2). Previous work suggests a key role for this region in equator-vortex teleconnections (e.g. *Gray et al.* [2020]) as well as elements of synchronisation between the QBO and SAO [*Kuai et al.*, 2009]. As each experiment imposes significantly different QBO states, features of SAO in the experiments may play a key role in dictating responses from the vortex, troposphere and surface.

SAO differences can be formally diagnosed by analysing the climatological seasonal cycle in equatorial winds (figure 5.5, note that the pressure level scale in this figure starts at 10 hPa while that of figure 5.2 starts at 100 hPa). This indicates the mean state of each simulation's SAO; the westerly phase of the SAO appearing in early NH winter (Sep-Nov), which is attributed to the dissipation of Kelvin waves and

small scale inertia-gravity waves [*Dunkerton*, 1979; *Hitchman and Leovy*, 1988], is significantly weaker and exhibits less vertical extent in the deep experiment compared to the shallow - difference plots of the nudged experiments' seasonal cycles (figure 5.5c) show significant differences in Sep-Oct near the 0.1 hPa level. The timing of phase transitions from westerly to easterly in early NH winter (denoted by the climatological zero wind line on approximately the 0.1 hPa level) is also marginally later in the shallow experiment. These differences in the extent of the westerly SAO phase could play a key role in equator-vortex interactions in each experiment as these features, particularly phase transition timings, have been shown to associate with the timing of SSWs [*Gray et al.*, 2001; *Hamilton*, 1998]. The largest differences between the experiment SAOs are evident in the magnitude of the easterly phase, driven by summer hemisphere easterly meridional advection by the BDC, in mid-late NH winter (Jan-Mar) near the 1 hPa level. Here, the shallow experiment's easterlies are significantly larger however easterly phases in both experiments are stronger than those in the pi-clim cntrl (figure 5.5C). While these differences highlight the potential impact that the degree of vertical coherence in the QBO may have on the SAO, the role these variations play in teleconnections with the vortex in each experiment is less clear and explored further in sections 5.6 and 5.7.

Another key mode of variation we consider in each experiment is the vortex and the frequency of SSWs. Figure 5.6 shows the average NH winter season SSW rates in each experiment. Over the whole winter season (figure 5.6a), each experiment exhibits an SSW rate which lies within 1 standard error of each other as well as the rate exhibited by ERA-Interim (red bars). The deep experiment shows the most SSWs (0.61 events per winter) however the differences between each SSW rate are not deemed significant to the 95% level using the bootstrap and parametric significance tests outlined in section 3.2.6.

We also analyse the seasonal distribution of SSWs (figure 5.6b). Each simulation

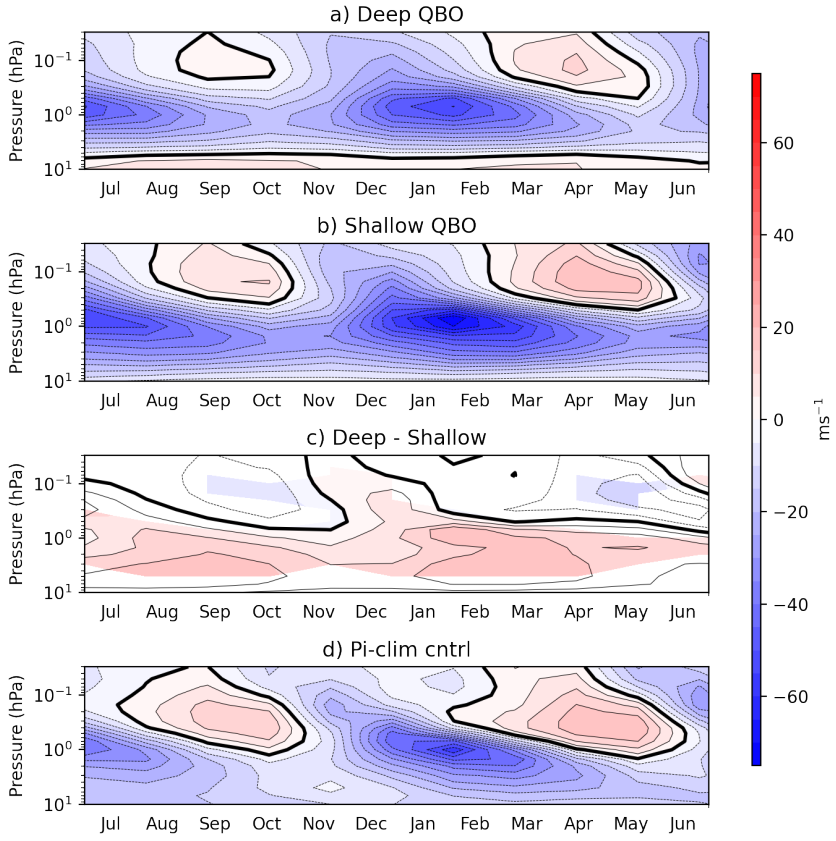


FIGURE 5.5: Climatological seasonal cycle of ZMZW averaged between 5° S–5° N latitude from the deep (a) and shallow (b) QBO experiments. Panel c shows climatological differences between deep and shallow seasonal cycles and the cycle from the pi-clim cntrl is provided in panel d. Coloured shading on difference panel c denote differences significant to the 95% level under a 2-tailed Student's t-test. Thick black lines on each panel indicate the zero-wind line.

shows a significant overestimation in November SSWs, a similar effect to that shown in the pi-control and discussed in section 3.3 (see figure 3.2). This November SSW bias is similar across all simulations and may influence the vortex in mid-late winter as it recovers from a disruption in November which precludes significant planetary wave driving. This effect is evident in the December SSW rates for all simulations which is marginally lower than in ERA-Interim. How these November and December rates may interact with QBO teleconnections is unclear however, their influence may be non-negligible; potential signals from the QBO in mid-late winter may be obscured if

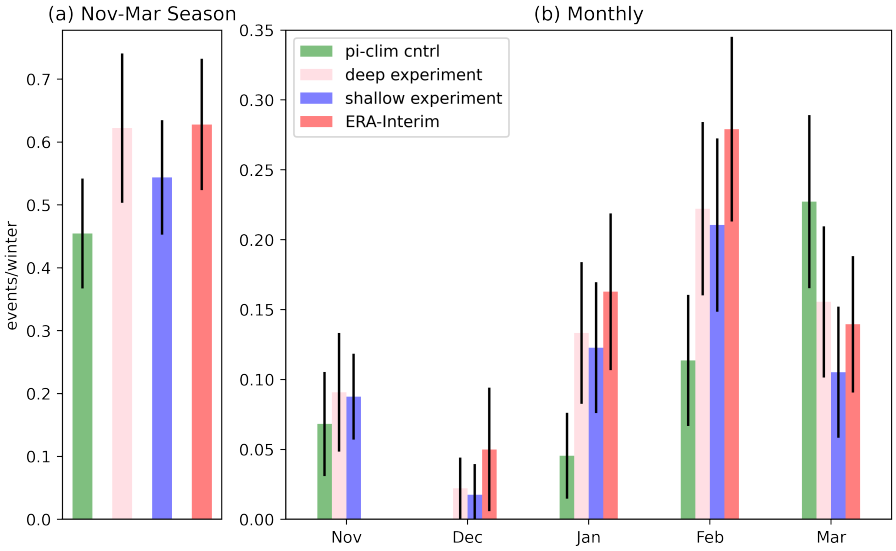


Figure 5.6: **a**: SSWs per NH winter season (Nov-Mar) in the deep QBO, shallow QBO and pi-clim cntrl simulations. **b**: SSW rates separated by months. Error bars on (a) and (b) signify the standard error on rates calculated as $\frac{\sigma}{\sqrt{N}}$ where σ is the standard deviation of the SSW per winter time series and N is the number of years in the simulation. SSW rates from ERA-Interim are also included for comparison.

the vortex of each experiment tends to be disrupted unrealistically early in the winter. As a result, in all diagnostics in the following sections, sensitivity tests were performed to assess whether removing years which contain November SSWs significantly changed the response patterns. Over the remainder of the winter season (Jan-Mar), the pi-clim cntrl exhibits steadily increasing SSW rates between mid and late winter. Introducing both a perpetually deep and shallow QBO in the nudged experiments appears to recover the seasonal distribution exhibited by ERA-Interim, increasing rates between Dec-Feb followed by a decrease in Mar. The reason for this is unclear and may point to significant late winter interactions between the QBO and the vortex in these simulations which are examined in closer detail in section 5.6.

5.5 Surface responses to deep and shallow QBOs

So far, we have shown that both nudged experiments exhibit the desired vertical structure in the QBO as well as realistic variations in the SAO and the vortex. The focus of this study, however, is the different teleconnections that arise between the equatorial stratosphere and other parts of the climate system. In particular, we focus on the key finding of *Andrews et al.* [2019]; that the NAO and AO response to the QBO is enhanced when the QBO exhibits a higher degree of vertical coherence.

To test this phenomenon explicitly, we analyse diagnostics of surface variability (specifically MSLP) under different QBO conditions in each simulation to compare the nature of teleconnections in each case. First, we examine whether the un-nudged simulation (the pi-clim cntrl) exhibits connection between the QBO and the surface. Figure 5.7 shows composites of NH MSLP associated with different QBO phases (top two rows) as well as the composite difference (QBOE - QBOW, bottom row) from the pi-clim cntrl. The QBO phase is defined using early winter (Nov-Dec) equatorial winds on the 50 hPa level, a standard level used in previous studies [*Anstey and Shepherd*, 2014] and located in the middle of the nudging region for both relaxed experiments (we analyse the variation of results with QBO height in the following sections). There are marginally more occurrences of early winter QBOW phases in each month (parentheses in figure 5.7, top 2 rows) indicating a degree of locking of the QBO to the seasonal cycle, an effect discussed by *Rajendran et al.* [2016]. However, the abundance of each phase is comparable enough to carry out composite analysis.

In early winter (Nov), the response to the QBO is marginal; there is a significant positive differences in MSLP for QBOE-QBOW over the Icelandic region which corresponds to a negative NAO however this covers a relatively small region compared to some of the same composites presented in *Andrews et al.* [2019] and *Gray et al.* [2018] that show a coherent NAO response to the 50 hPa QBO in ERA-Interim that

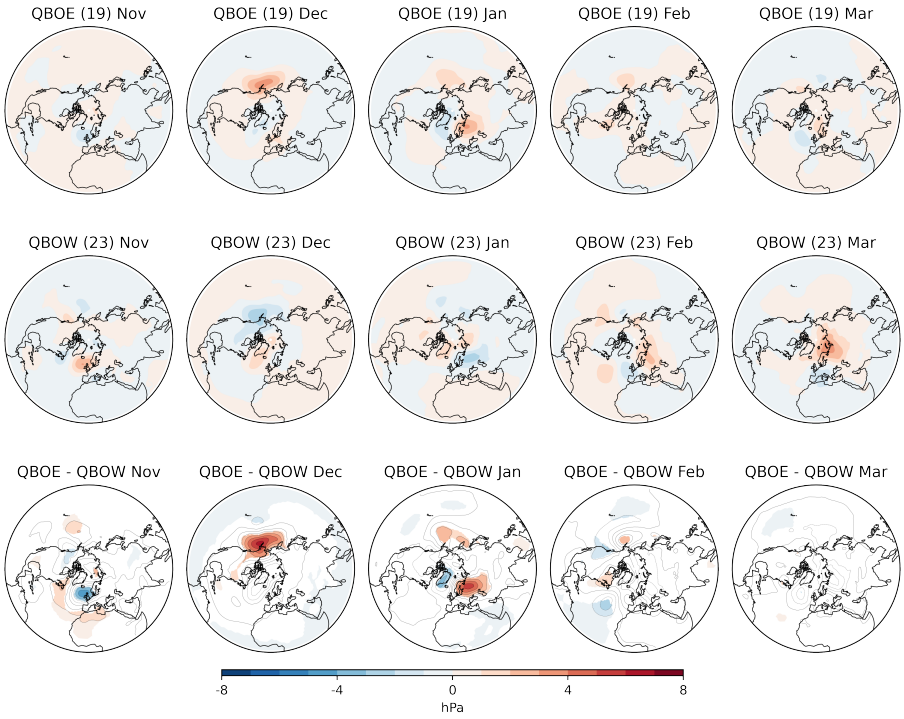


Figure 5.7: NH deseasonalised MSLP anomaly composites for the QBO East (top row), QBO West (middle row) phases and composite differences (QBOE - QBOW, bottom row) for the pi-clim cntrl simulation. The QBO phase is defined as any Nov-Dec mean equatorial (5° S–5° N average) ZMZW on the 50 hPa that exceeds a magnitude of $5ms^{-1}$, i.e. $+5ms^{-1}$ threshold for QBOW and $-5ms^{-1}$ threshold for QBOE. Anomalies associated with each QBO phase are presented in various months which are indicated in sub-figure titles. Numbers in parentheses indicate the number of NH winters that occur under each phase which make up the composite. Coloured shading in the bottom row indicates MSLP differences significant above the 95% confidence level under a 2 tail Student's t-test.

peaks in January. In mid-winter (Dec-Feb), the composite differences do not resemble a coherent NAO/AO pattern with the exception of responses in December which exhibit positive differences over the AL region. A QBO signal is also absent in later winter (Mar), a month in which *Gray et al.* [2018] highlight a coherent Pacific MSLP response in ERA-Interim. These disparate patterns are not significantly altered by the exclusion of NH winters which exhibit November SSWs (not shown) suggesting the lack of signal is likely not linked to the model SSW bias seen in figure 5.6.

In contrast, the corresponding MSLP composites from the deep experiment (figure

5.8) exhibit a prominent signal in the NAO region indicated by a significant composite difference of up to 8 hPa over the North Atlantic region. This signal is most apparent in mid-late winter (Jan-Mar), although a similar anomaly is visible in November. This feature corresponds to positive (negative) MSLP anomalies under QBOE (QBOW) conditions centred over the southern node of the NAO (a region encompassing the Azores). As with the pi-clim cntrl, there is a small discrepancy in the abundance of winters exhibiting different QBO phases with the QBOW phase marginally more prominent. However, this difference is small and indicates that the asymmetry in phase amplitudes demonstrated in figure 5.2 has not had a significant impact on the preferential occurrence of NH winters under each phase.

These patterns indicate a shift towards a positive NAO pattern under QBOE conditions and negative NAO under QBOW - the opposite sign to a response expected via a Holton-Tan mechanism which predicts a weakened (strengthened) vortex and subsequent negative (positive) NAO under QBOE (QBOW) phases. Furthermore, *Andrews et al.* [2019] show a response consistent with a Holton-Tan link and of the opposite sign to those shown here (positive NAO phase under QBOW conditions) using a deep QBO metric in observations and a free-running model. As a result, our results are somewhat surprising and warrant further study into their origins which is presented in the following sections.

The corresponding Atlantic responses from the shallow QBO experiment (figure 5.9) are markedly different to its deep counterpart: The magnitude of responses to individual QBO phases (top two rows) as well as differences (bottom row) are smaller than in the deep experiment (up to $\sim$4 hPa) and a smaller region of composite differences are deemed significant under a 2 tailed t-test (also bottom row). There is also a MSLP response in the North Pacific in both nudged experiments concentrated over the AL region which corresponds to the Pacific node of the AO (see figure 2.5). As with the Atlantic response, the deep experiment exhibits anomalies with larger

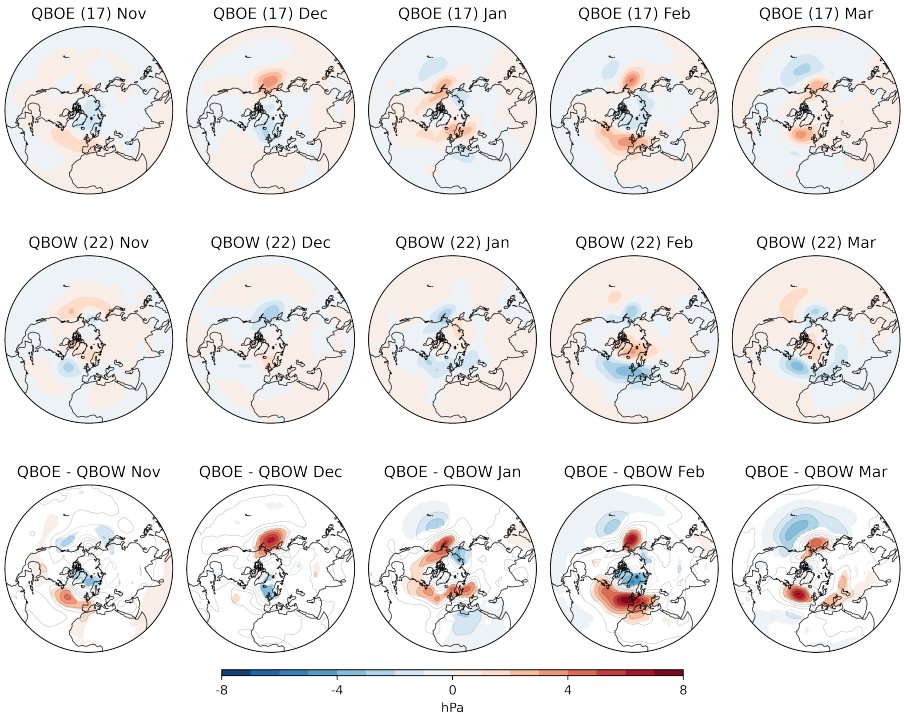


Figure 5.8: Like figure 5.7 for the deep QBO experiment.

amplitude than those in the shallow. Both experiments' Pacific responses are most prominent in mid-NH winter (Dec-Feb) consistent with similar findings in *Gray et al.* [2018] that show significant anomalies over this region peak in February. The sign of the anomalies in this region for both experiments indicate that a positive (negative) Pacific pattern corresponds to QBOE (QBOW) conditions; again, an opposite response to that seen in *Andrews et al.* [2019] and *Gray et al.* [2018]. As with the pi-clim cntrl, both experiments' MSLP responses are not significantly affected by the removal of November SSWs. Overall, results comparing MSLP composites in our two nudged experiments indicate enhanced amplitudes of response patterns to a perpetually deep QBO. However, the Atlantic and Pacific responses in the deep experiment is of the opposite sign to the expected HT mechanism as well as that in [*Andrews et al.*, 2019] and therefore a closer examination of possible pathways involved in this response is required to understand the role of vertical coherence in the QBO in our simulations.

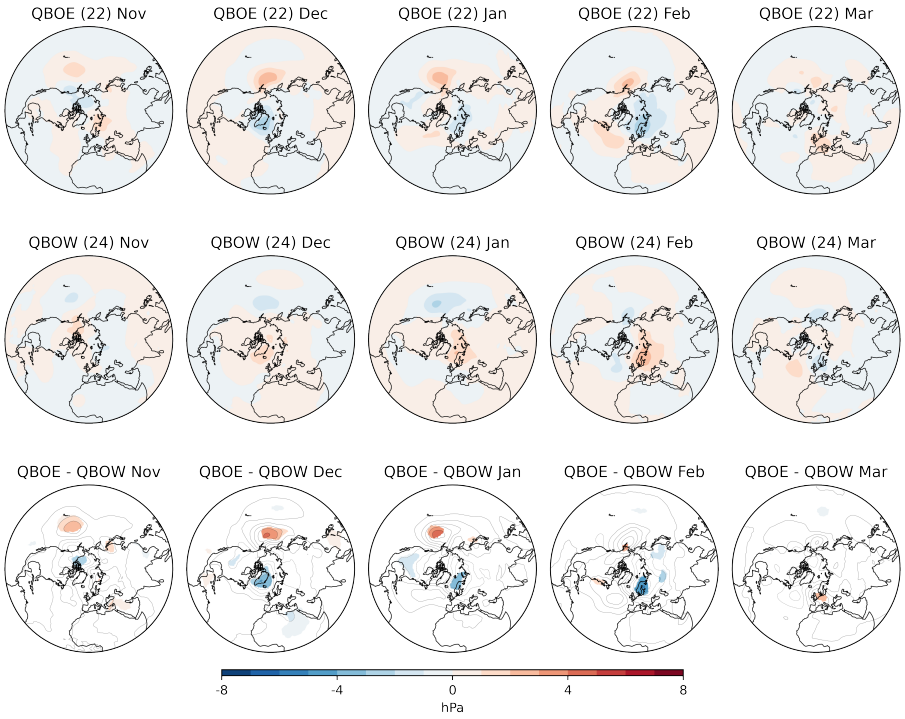


FIGURE 5.9: Like figure 5.7 for the shallow QBO experiment.

5.6 Vortex responses to the QBO

We next analyse the interaction between the QBO and the vortex in each experiment to further understand the possible mechanisms involved in the surface responses seen in the previous section. Figure 5.10 shows a measure of the strength of the Holton-Tan effect in the pi-clim cntrl simulation - composite differences between NH winter ZMZW under QBOE and QBOW conditions. The phase of the QBO is defined in early winter (Nov-Dec) on various pressure levels (rows in figure 5.10) and ZMZW differences are evaluated for a range of NH winter months (columns). The response from the vortex in this un-nudged simulation broadly reflects the composites from the fully coupled pi-control simulation of UKESM (figure 3.5) with negative composite differences in the vortex when the QBO is defined on the 20 hPa and 30 hPa levels. This is consistent with the HT effect discussed in section 2.5.1 in which the easterly QBO phase is

associated with a weakened vortex (see figure 5.10, left column). The majority of these negative differences are concentrated in early-mid winter months (Nov-Jan), a finding also reported in *Gray et al.* [2018]. There are negative composite differences to the QBO at 70 hPa and 50 hPa also in early winter which extend from the subtropics to as far north as 50°N. In late winter (Feb-Mar), the response of the vortex reduces and even reverse to positive on the 70 hPa level (again, an effect reported in *Gray et al.* [2018]). The equatorial anomalies associated with QBO phases in this simulation are characterised by a four-fold structure in height with alternating QBOE/W phases evident throughout the mid-stratosphere and extending into the lower-mesosphere.

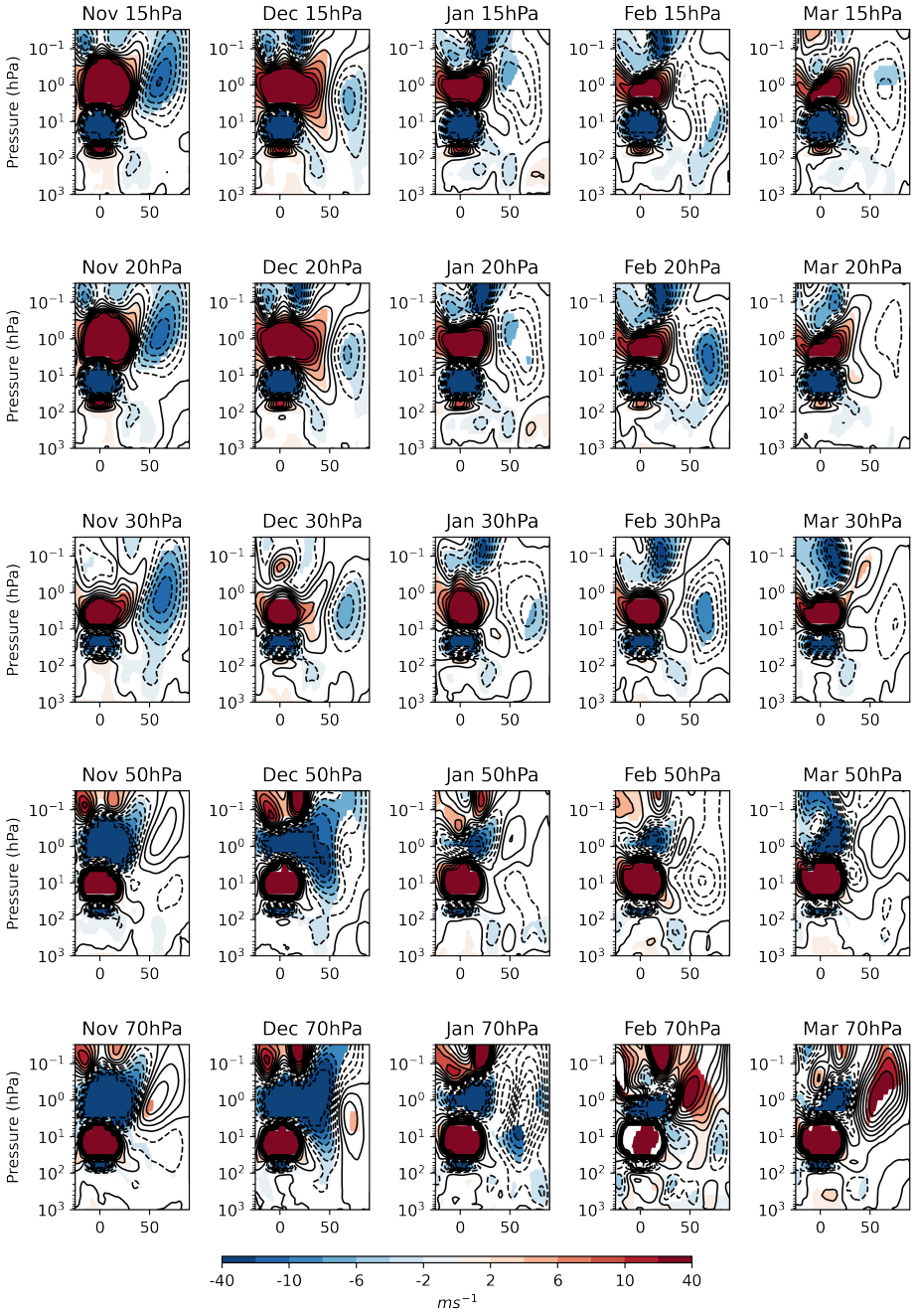


FIGURE 5.10: ZMZW composite differences for QBOE - QBOW conditions from the pi-clim cntrl simulation. The QBO phase is defined as any Nov-Dec mean equatorial (5° S–5° N average) ZMZW that exceeds a magnitude of $5ms^{-1}$, i.e. $+5ms^{-1}$ threshold for QBOW and $-5ms^{-1}$ threshold for QBOE on various pressure levels which are indicated by sub-figure titles. Differences are evaluated in a range of NH winter months (also indicated in sub-figure titles). Coloured shading indicates ZMZW differences significant above the 95% confidence level under a 2 tail Student's t-test.

The pi-clim cntrl composites also reflect some of the key features of corresponding ZMZW responses from ERA-Interim (figure 5.11). Namely, the ERA-Interim composites also exhibit a seasonal progression with negative composite differences for QBOE-QBOW which increase from November and peak in January before reversing in March. However, the amplitude of vortex responses in the model is weaker than in ERA-Interim, which is a feature in common with other models [*Anstey et al.*, 2021], although it's not clear whether this is due to a true underestimation of the response by the models or whether it is due to internal variability since the strength of the observed HT effect has been shown to vary over time (e.g. *Lu et al.* [2008] and *Lu et al.* [2014]). ERA-Interim responses are also most prominent using a QBO metric defined on the 50 hPa level in contrast to the model which exhibits largest responses to the QBO defined at a higher level (20 hPa and 30 hPa). This discrepancy is seen in many models studied under QBOI (see section 2.4) and attributed to QBO phases in GCMs that fail to penetrate down with a large enough amplitude to the 50 hPa level [*Anstey et al.*, 2021]. Nevertheless, the pi-clim cntrl composites indicate that the un-nudged configuration of the model is able to reproduce a clear coupling between the QBO and the vortex suggesting the suitability of this model configuration for QBO-vortex analysis with nudged QBO simulations.

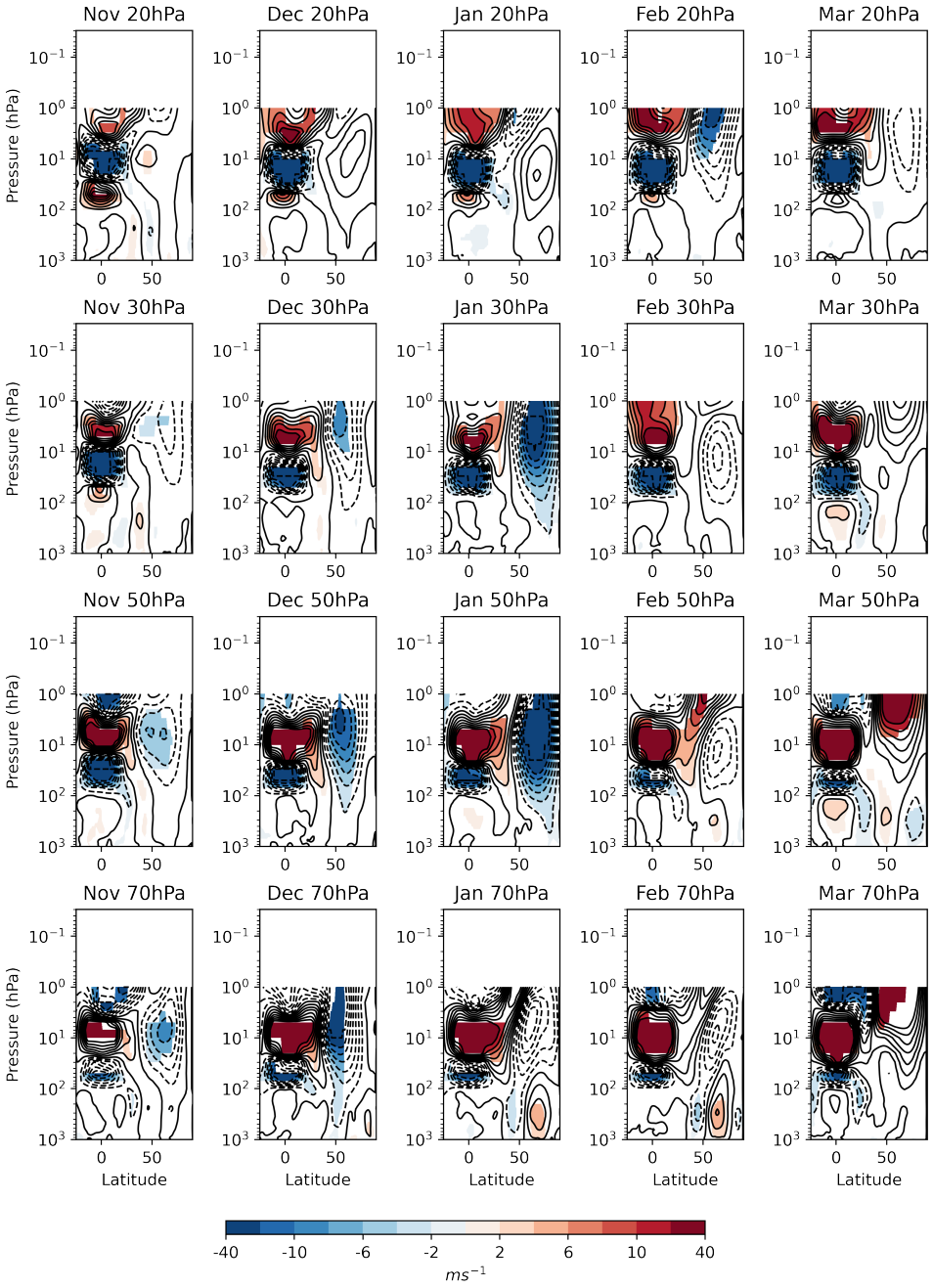


FIGURE 5.11: Like figure 5.10 for ERA-Interim. Composites for the QBO defined on the 15 hPa level are not included as this is not a standard level output for ERA-Interim.

The corresponding ZMZW composite differences between QBO phases in the deep and shallow QBO experiments (figure 5.12 and 5.13 respectively) show distinct

response patterns. In early winter (November), both simulations exhibit negative composite differences in the vortex for QBOE - QBOW, in good agreement with a HT mechanism [*Holton and Tan*, 1980] as well as the pi-clim cntrl (figure 5.10). The magnitude of vortex responses in November is marginally larger in the deep experiment compared to that of the shallow and pi-clim cntrl. The equatorial response patterns in the deep experiment predominantly exhibit a two-fold structure in early winter (Nov-Dec) with anomalies in the lower-mid stratosphere and opposite anomalies above in the upper stratosphere and lower mesosphere. In later winter (Jan-Mar), an additional phase above the 0.1 hPa level is evident forming a three-fold structure. The corresponding equatorial responses in the shallow experiment shows a combination of two, three and four-fold patterns of anomalies.

In mid-late winter (Jan-Mar), the deep experiment exhibits remarkably large positive composite differences in the vortex region. This notable feature is largely absent in the pi-clim cntrl (figure 5.10) as well as the shallow experiment (figure 5.13). There is a response to the QBO at 30 hPa in the shallow experiment with positive differences evident for February and March but these are significantly smaller in magnitude than those in the deep QBO simulation. These positive differences in the deep experiment are of the opposite sign to the expected HT relation however they do reflect the seasonal progression between early and later NH winter in QBO-vortex interactions suggested in *Gray et al.* [2018]. This seasonal progression in both experiments is unaffected by the removal of November SSWs and may also account for the positive (negative) NAO pattern MSLP responses to QBOE (QBOW) in late NH winter in figure 5.8: In these months, the vortex appears strengthened (weakened) under QBOE (QBOW) conditions which may, in turn, induce a positive (negative) NAO through the vortex's in-season influence over the NAO [*Baldwin and Dunkerton*, 2001; *Charlton-Perez et al.*, 2018].

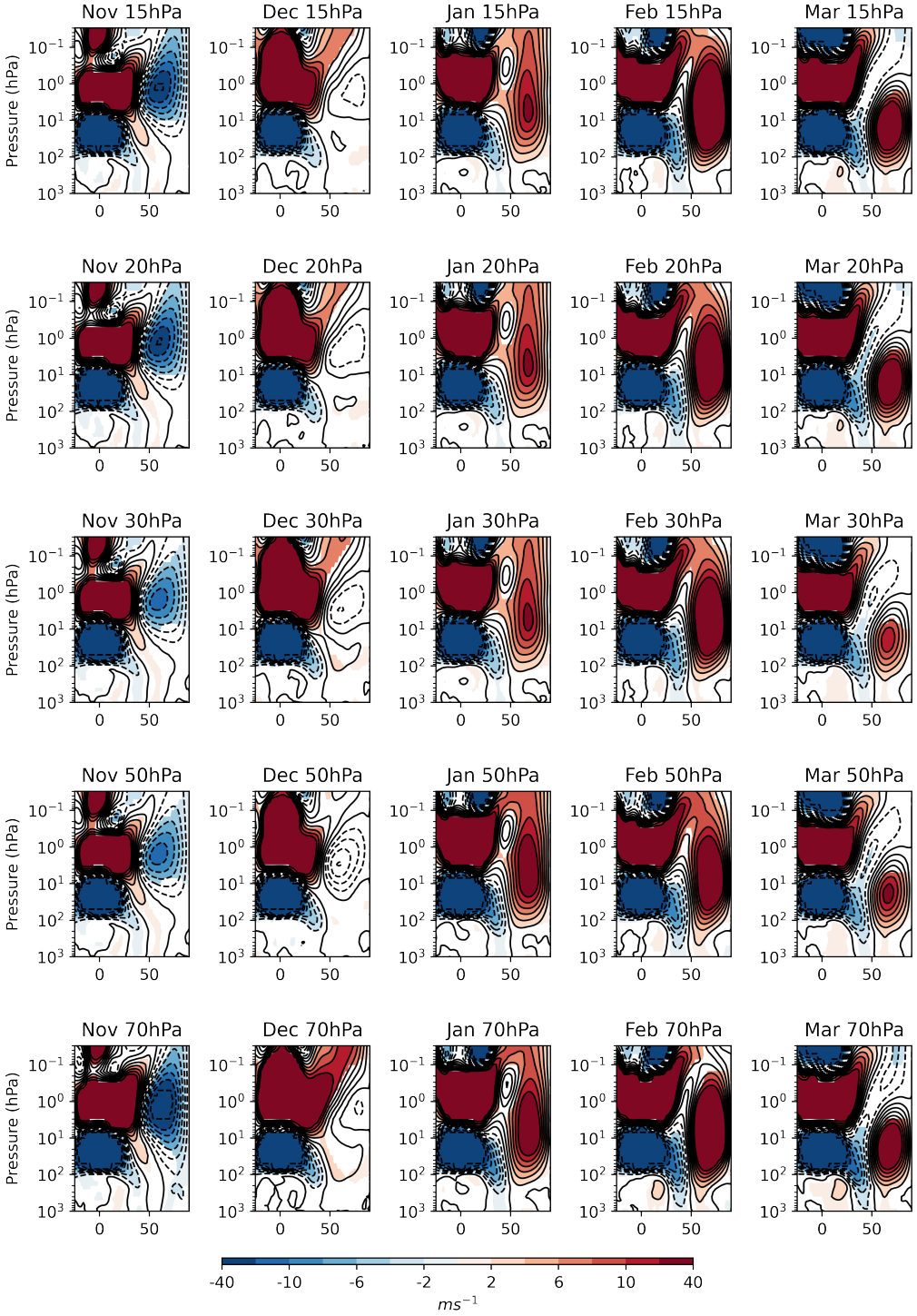


FIGURE 5.12: Like figure 5.10 for the deep experiment

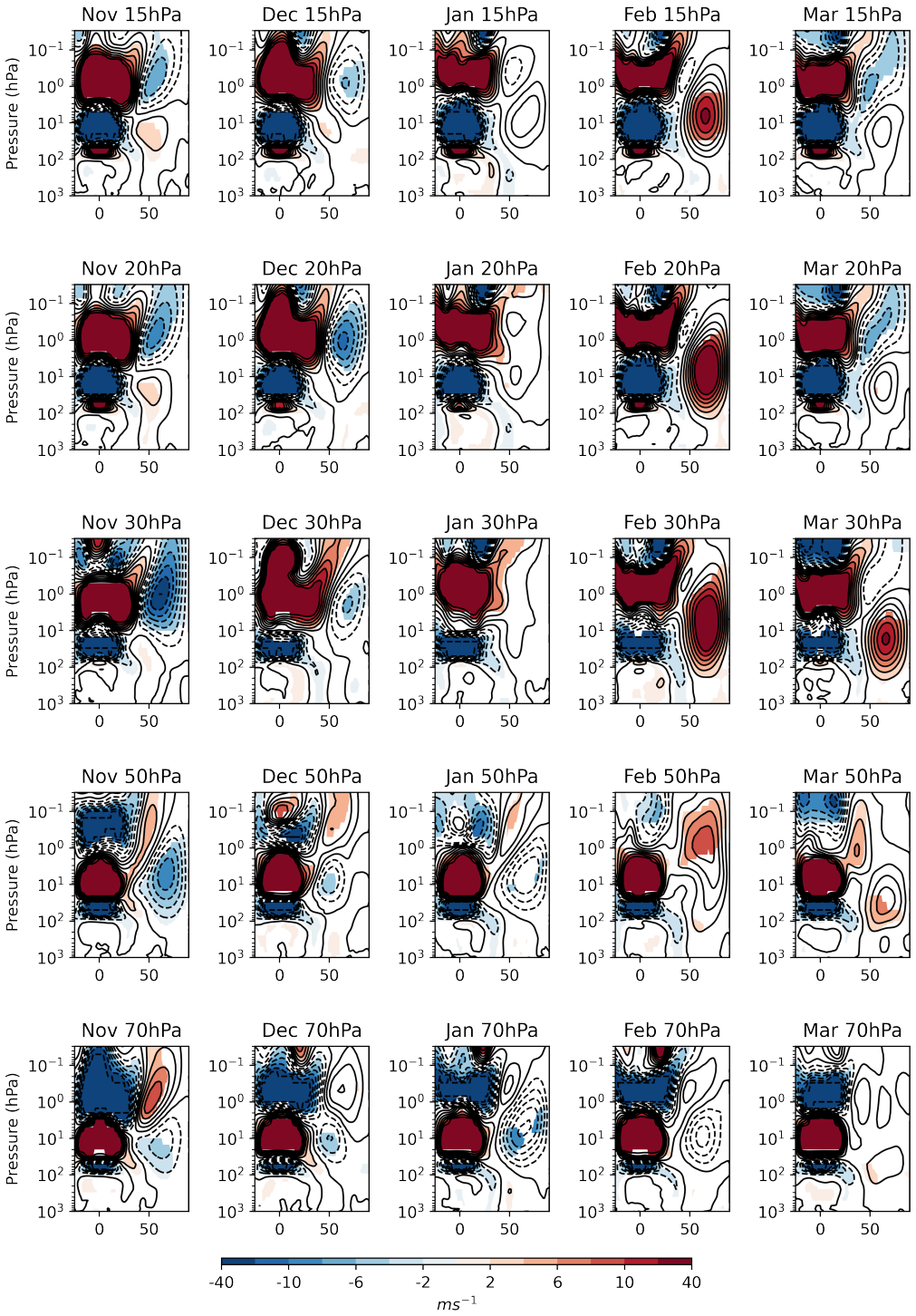


Figure 5.13: Like figure 5.10 for the shallow QBO experiment.

To examine these large mid-winter vortex responses in the deep simulation more closely, we analyse the responses of planetary wave propagation to different QBO phases. figure 5.14 shows composites of meridional and vertical EP flux arrows and EP flux divergence under QBOE (top row) and QBOW conditions (middle row) as well as differences between the phases (bottom row) from the deep experiment. In addition, we include the zero wind line of ZMZW composites under QBO phases on figure 5.14 to examine the association between wind anomalies and the direction of wave propagation.

The largest differences in EP flux are visible in January. In this month, there is greater EP flux divergence (i.e. larger negative $\nabla \cdot F$) over the vortex region (near 60°N on the 10 hPa level) for QBOW indicating increased wave driving of the vortex under this phase compared to QBOE. This confirms that the mid-winter HT link in the deep experiment is reversed compared to ERA-Interim with greater wave driving of the vortex and a subsequent weakening under QBOW compared to QBOE. The precise causes for this reversal are as yet unexplained however, QBOE conditions are associated with enhanced equatorward EP flux propagation near 40°N between the 1 hPa and 0.1 hPa levels compared to QBOW. This indicates that under QBOW conditions, more planetary waves are permitted to propagate towards the equator and away from the vortex. In this same region, QBOW phases are associated with an arm of the easterly SAO phase which encroaches poleward into the extra-tropics near the 0.8 hPa level (indicated by the zero wind line on composites). The role that variability in this region may play in accounting for responses patterns to the QBO is explored in further detail in section 5.7.

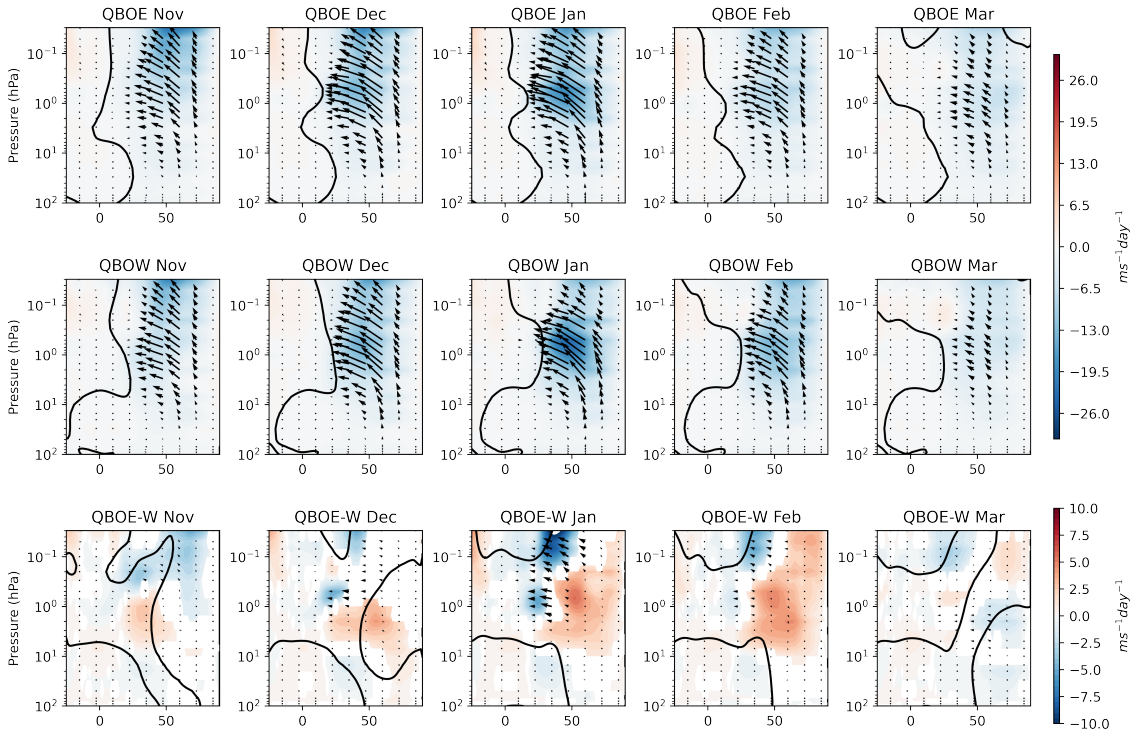


Figure 5.14: Deep QBO experiment composites of EP flux divergence (coloured shading) and EP fluxes (arrows with units of m^2s^{-2}), which indicate the direction of wave propagation, under QBOE (top row) and QBOW (middle row) conditions as well as the difference between QBOE and QBOW composites (bottom row) for November-March. QBO phases are defined as any Nov-Dec equatorial winds which exceeds a magnitude of $5ms^{-1}$ on the 50 hPa level. Thick black lines denote the 0-wind line of ZMZW composites evaluated using the same QBO phases.

Also evident in the ZMZW composites from the deep experiment (figure 5.12) are elements of connection between the QBO and the surface: Between ∼45-55°N latitudes, a limb of anomalies associated with QBO phases descends into the troposphere (below 100 hPa) and to the surface. These anomalies are of the same sign as the QBO anomaly in the middle equatorial stratosphere and increases in magnitude as well as propagation towards the surface throughout the winter season with significant composite differences reaching the surface in February and March. This feature is not evident in the composites of the shallow experiment but is observed in the pi-clim cntrl albeit at a lower magnitude and only for a selection of months (February and

March using a 30 hPa QBO, for example). This feature may be evidence in support of a subtropical pathway between the QBO and surface suggested in *Gray et al.* [2018] but, on the other hand, it is only ever present with significant vortex anomalies, so it may simply be a secondary response to the vortex anomaly involving a latitudinal shift of the mid-latitude jet (as in *Baldwin and Dunkerton* [2001]).

5.7 The role of the SAO region

ZMZW composites in figure 5.12 show positive (negative) vortex responses to QBOE (QBOW) conditions in late winter which are significantly enhanced in the deep experiment. They are also consistent with enhanced late winter MSLP responses in the deep experiment (figure 5.8) which are opposite to those seen in the observations [*Gray et al.*, 2018] and in earlier experiments [*Andrews et al.*, 2019]. However, the causes of these responses in the vortex are as yet unclear.

A prominent feature of the ZMZW composites in the deep simulation (figure 5.12) is the presence of anomalies in the SAO region (above the 1 hPa level): Composite differences in the upper equatorial stratosphere in this experiment exhibit large anomalies of the opposite sign to the QBO phase below. These anomalies are evident throughout NH winter season and are not sensitive to the choice of QBO level. This is consistent with the idea of vertically coherent QBO phases filtering out waves with the same phase speed direction as the QBO by preventing propagation through the QBO region according to the Charney-Drazin Criteria. Conversely, wave forcing of the opposite phase speed of the deep QBO is permitted to propagate into the lower mesosphere where momentum is transferred to the mean flow leading to SAO anomalies of the opposite sign to the QBO.

This modulation of the SAO by the QBO can be further demonstrated by examining a time series of deseasonalised equatorial ZMZW anomalies in each simulation

(figure 5.15). Once the seasonal cycle in SAO winds is removed, both the deep and shallow QBO variations (sub-figures a and c) are seen to extend beyond the nudging region up to near the 0.1 hPa level. This is also reflected in the Fourier power spectra (figures 5.15b and d) which show significant power corresponding to the QBO period up into the mesosphere, an effect reported in *Kuai et al.* [2009] who show elements of synchronisation between the QBO and SAO. QBO signals in the SAO region are less prominent in the pi-clim cntrl and ERA-Interim winds (figures 5.15e-h) with QBO variations extending to approximately the 1 hPa level in the Fourier spectra.

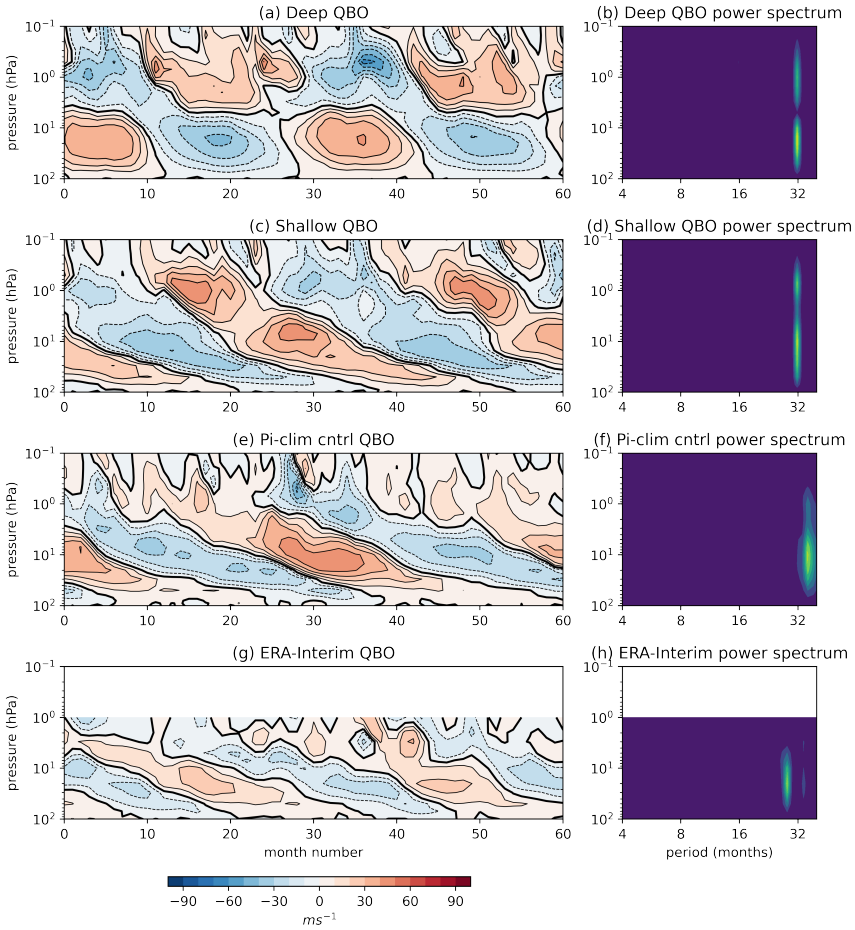


Figure 5.15: 5 year sample of deseasonalised ZMZW anomalies averaged between 5° S–5° N latitude from the deep QBO (a), shallow QBO (c) and pi-clim cntrl (e) simulations and ERA-Interim (g). Thick black contours denote the zero-wind line where westerlies meet easterlies. Sub-figures b, d, f and h show Fourier Power spectra for equatorial wind anomalies at various levels from the same datasets.

There are also significant extra-tropical ZMZW anomalies associated with these QBO-like variations in the upper stratosphere/lower mesosphere (USLM) region. Figure 5.16 show ZMZW composite differences between USLM QBOE and USLM QBOW conditions defined using extremes in the deseasonalised winds on the 1 hPa level (to remove the effect of the seasonal cycle). The largest responses in the vortex region are apparent in the deep experiment (figure 5.16, top row). In mid-late winter, large anomalies are apparent near 60°N for USLM QBOE - QBOW composite differences. These responses correspond to a weakened (strengthened) vortex for USLM QBOE (QBOW) anomalies. In the equatorial region, large USLM anomalies are evident near the 1 hPa level (resulting from the design of the composites). These USLM anomalies also significantly encroach into the extra-tropical region with significant composite differences apparent out to latitudes of ∼45°N. Between 100 hPa and 10 hPa, significant QBO anomalies are evident of the opposite sign to those in the USLM region above. This provides further evidence of the mechanisms described above by which the QBO and SAO co-vary significantly. The vortex responses to the USLM QBO in the other experiments are significantly smaller than the corresponding responses in the deep QBO simulation - negative vortex composite differences are only evident in late winter (Feb-Mar) in the shallow simulation (figure 5.16, middle row) and there are no vortex responses deemed significant under a Student's t-test in the pi-clim cntrl (bottom row). Composite differences in the equatorial USLM region in these experiments are also more confined to the equatorial region than those in the deep experiment. These composites indicate that variability in the SAO region may play a key role in modulating vortex strength, particularly in the deep experiment which exhibits larger and more widespread USLM anomalies than the other two experiments.

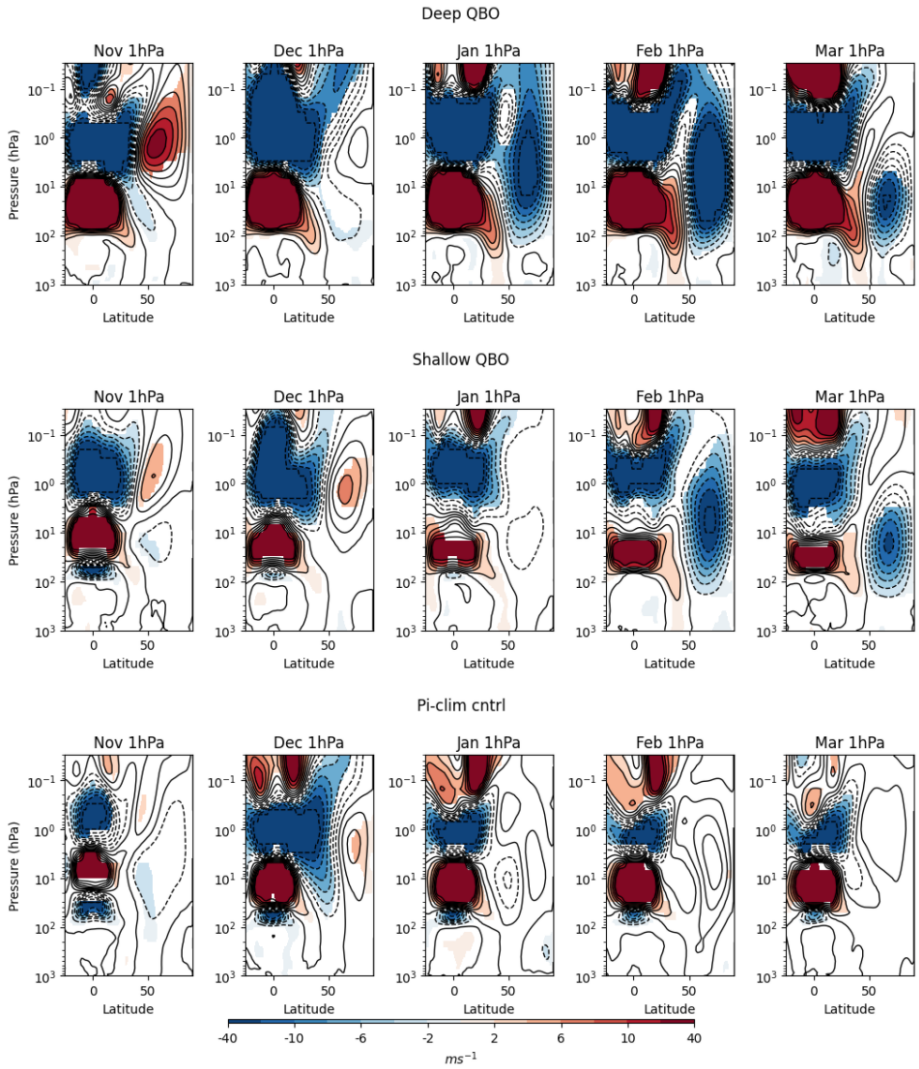


Figure 5.16: ZMZW composite differences between anomalous easterly and westerly USLM QBO conditions from the deep QBO (top row), shallow QBO (middle row) and pi-clim cntrl (bottom row) simulations. The USLM QBO phase is defined as any deseasonalised Nov-Dec monthly equatorial (5° S–5° N average) ZMZW that exceeds a magnitude of 5 ms^{-1} on the 1 hPa level. Composite differences are evaluated in a range of NH winter months (indicated in sub-figure titles). Coloured shading indicates ZMZW differences significant above the 95% confidence level under a 2 tail Student's t-test.

Gray et al. [2020] show a similar association between the SAO region and the vortex using a set of nudging experiments and suggest a connection via modulation of planetary wave propagation by SAO variations. To verify whether this mechanism may apply in the deep experiment (the simulation which exhibits the largest vortex responses to the equatorial USLM region) we analyse EP flux patterns associated with

different phases of the USLM QBO. Figure 5.17 shows composites of EP flux arrows and divergence under USLM QBOE, USLM QBOW and USLM QBOE-QBOW. The EP flux divergence composite patterns are of the opposite sign to those associated with the QBO in the middle stratosphere (figure 5.14) with greater flux divergence (i.e. larger negative $\nabla \cdot F$) over the vortex region under USLM QBOE in January and February. The composites in these months are characterised by enhanced pole-wards propagation of mid-latitude EP flux arrows between the 1 hPa and 0.1 hPa levels under USLM QBOE as well as an encroachment of the equatorial summer easterlies near the 1 hPa level, denoted by the zero-wind line on figure 5.17, into the NH extra-tropics also under this phase. These are opposite to patterns associated with the 50 hPa QBO which indicates enhanced equatorward flux on the same levels under QBOE. These composites indicate that under USLM QBOE (QBOW) conditions, mid-latitude waves are directed towards (away from) the vortex leading to increased (decreased) wave driving of the vortex and a subsequent weakening (strengthening) of vortex winds.

Combining the results from this section provides a potential mechanism by which the equatorial USLM modulates the later winter vortex response to mid-stratosphere QBO phases in the deep experiment (as seen in composites in figure 5.12): The design of the deep QBO experiment has resulted in an unexpectedly strong modulation of the equatorial USLM region, through the filtering of equatorial waves as they propagate vertically through the deep QBO region. As a result, there is a two-fold vertical structure in the equatorial ZMZW QBO anomaly, with a strong westerly (easterly) bias in the USLM overlying the QBOE (QBOW) anomaly in the lower stratosphere. This, in turn, permits more (less) equatorward propagation of mid-latitude planetary waves in the upper stratosphere leading to reduced (increased) wave driving of the vortex and a subsequent strengthening (weakening) of the vortex. It thus appears that, in this experiment, the influence from QBO variations in the equatorial USLM overwhelm the influence from the QBO variations in the lower stratosphere. Finally,

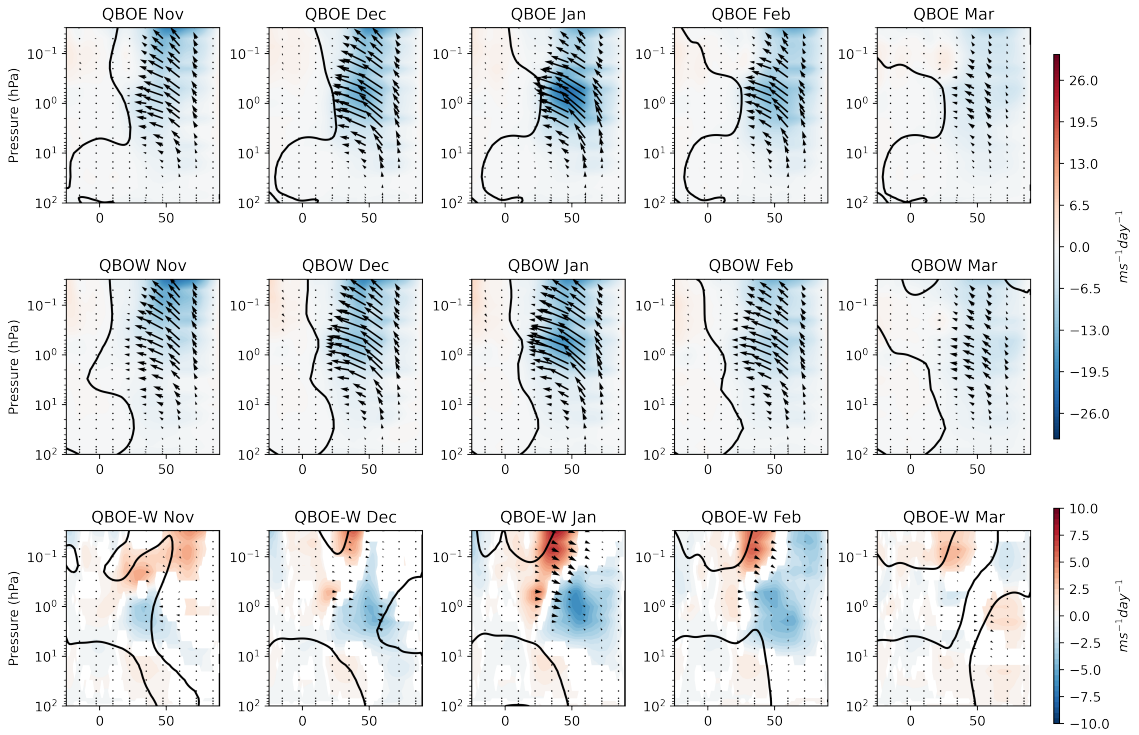


Figure 5.17: Deep QBO experiment composites of EP flux divergence (coloured shading) and EP fluxes (arrows with units of m^2s^{-2}), which indicate the direction of wave propagation, under USLM QBOE (top row) and USLM QBOW (middle row) conditions as well as the difference between QBOE and QBOW composites (bottom row) for November-March. QBO phases are defined as any deseasonalised Nov-Dec equatorial wind anomaly which exceeds a magnitude of $5ms^{-1}$ on the 1 hPa level. Thick black lines denote the 0-wind line of ZMZW composites evaluated using the same USLM QBO phases.

these vortex anomalies (that are of opposite sign to the traditional HT relationship) propagate to the surface and result in the MSLP response patterns to QBO phases in figure 5.8 thus explaining the incorrect sign of the MSLP anomalies when compared to the observed response. On the other hand, however, anomalies in the equatorial USLM may also be in response to the vortex anomalies - i.e. the vortex may respond to QBO phases and subsequently modulate the direction of EP flux equatorwards leading to USLM anomalies associated with different mid-stratosphere QBO phases. This complex interplay of potential mechanisms makes it difficult to definitively explain the responses to the QBO in our deep experiment.

5.8 Results in the context of previous work

Our analysis so far indicates that a perpetually deep QBO leads to large responses in the vortex and NH MSLP of the opposite sign to a HT link as well as those shown by previous work [*Andrews et al.*, 2019] and that variability in the USLM region may be key to modulating this response. *Andrews et al.* [2019] did not study the HT relationship or other atmospheric responses to the QBO explicitly but showed an enhanced MSLP response consistent with a HT link (i.e. QBOE phase associated with a negative NAO pattern) using a deep QBO metric in both reanalysis and a free-running model. Accounting for the discrepancy in responses between our experiments and those of *Andrews et al.* [2019] may be key to understanding the mechanisms involved in QBO teleconnections but requires closer examination of the stratospheric responses in their model simulation.

An analogous measure of the effect of a deep QBO metric to that in *Andrews et al.* [2019] is to analyse the UKESM pi-control simulation utilised in chapters 3 and 4. Indeed, *Andrews et al.* [2019] use the HadGEM3-GC2 model [*Williams et al.*, 2018], a predecessor of UKESM1, and the length of the pi-control (1000 years) allows for robust composite analysis. Figure 5.18 shows MSLP composites for different QBO conditions using a QBO metric at 50 hPa, a standard level which also shows significant vortex responses from previous analysis (see figure 3.5), from the pi-control simulation. These composites show that this model does not exhibit coherent MSLP anomaly patterns over the Atlantic - there is little to no response in this region to either phase and marginal composite differences which peak in magnitude at $\sim$1.5 hPa compared to $\sim$ 3.5 hPa in the same region from ERA-Interim [*Andrews et al.*, 2019]. A significant Pacific response is evident in January which peaks in magnitude at $\sim$2 hPa composite difference, a similar magnitude to that in ERA-Interim also shown in *Andrews et al.* [2019]. The sign of this Pacific anomaly is consistent with that found in *Gray et al.*

[2018] with QBOE(W) associated with positive MSLP anomalies [1].

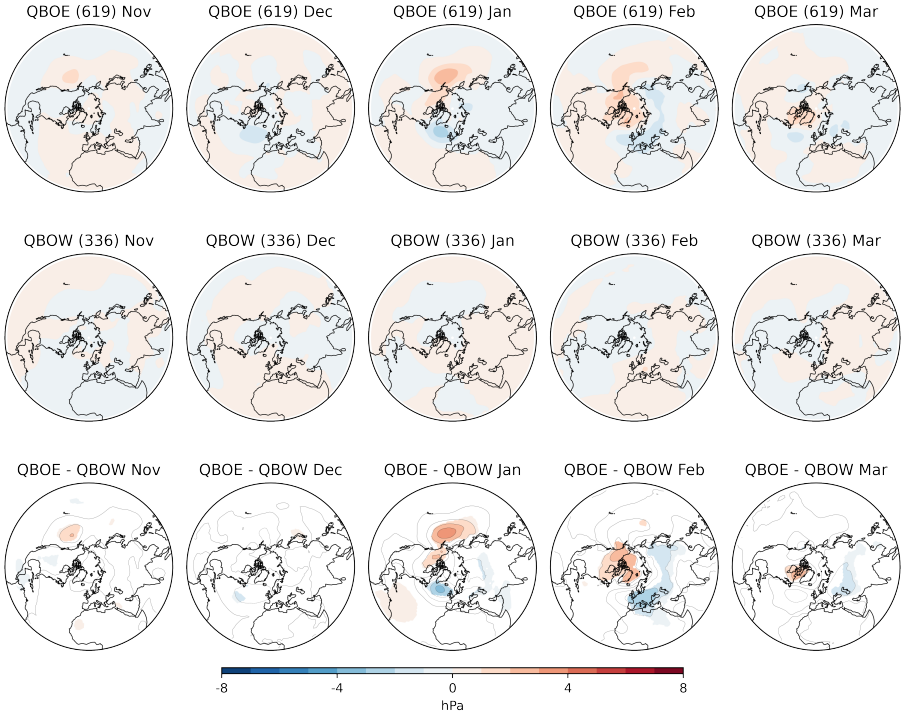


Figure 5.18: like figure 5.7 for the pi-control simulation. QBO phases for each composite are defined as any monthly equatorial (5° S–5° N average) ZMZW that exceeds a magnitude of 5 $\mathrm{m\,s^{-1}}$ on the 50 hPa level.

We compare this single level definition to an analogous plot using a deep QBO metric. Figure 5.19 shows the MSLP composites when the QBO phase is defined using the deep QBO definition of *Andrews et al.* [2019], i.e. by taking the average of the winds between 15-30 hPa instead of the single 50 hPa level. Anomalies associated with each phase of this deep metric are significantly enhanced compared to figure 5.18: Clear negative anomalies are visible over the northern node of the NAO (in the Icelandic region) for QBOW conditions peaking in January and similar anomalies are also apparent in February. There is also a coherent response to the deep QBO in the north Pacific which is first evident in December and increases in magnitude until a

[1]There is an asymmetry in the abundance of QBOE and QBOW months that make up the composites - Significantly more QBOE phases are observed in NH winter which is consistent with similar composite analysis in chapter 3 (figure 3.6) in which this feature is discussed further.

peak in February. The structure of this anomaly is distinct to that shown when using the 50 hPa QBO - under QBOW, a north-south dipole is evident with negative MSLP over the AL region and positive anomalies directly south of the Aleutian islands.

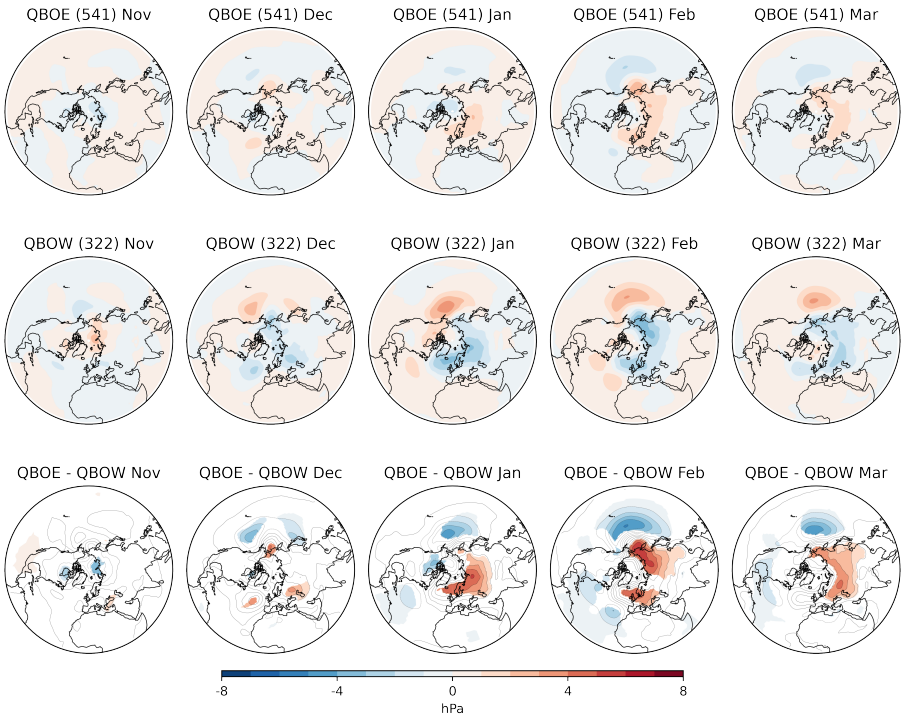


FIGURE 5.19: Like figure 5.18 but defining QBO phases using the same deep metric as employed in *Andrews et al.* [2019], any monthly equatorial (5° S–5° N average) ZMZW averaged between the 15 hPa and 30 hPa levels that exceeds a magnitude of 5 $\mathrm{m\,s^{-1}}$.

Importantly, the MSLP responses using the deep QBO metric are consistent with the results of *Andrews et al.* [2019] (their figure 6). Namely, in the NAO region, the deep QBOE (QBOW) phase is associated with positive (negative) anomalies over the Icelandic low region and therefore a negative (positive) NAO. The structure of the Pacific responses is also consistent with their results; the QBOE (QBOW) phase is associated with decreased (increased) pressure over the AL region and increased (decreased) MSLP further south in the mid-Pacific. We can, therefore, confidently use this model simulation to extend the study of *Andrews et al.* [2019] by exploring whether the stronger MSLP response to a deep QBO definition is accompanied by a

correspondingly stronger HT response in the stratosphere, or whether there is some other mechanism that comes into play. We can also examine the amplitude of the associated equatorial USLM anomaly and compare it with the large unusual two and three-fold structures seen in our deep QBO experiments (figure 5.12), so that we can further understand the unexpected reversal of the MSLP response in that experiment.

The pi-control also exhibits QBO-vortex coupling consistent with an expected HT effect - analysis from chapter 3 (figure 3.5) showed a negative composite difference in vortex winds for QBOE-QBOW conditions over the whole winter using both the single level (50 hPa) and deep QBO metrics. Interestingly, the magnitude of the high NH latitude response using the deep metric is similar to that exhibited for the 50 hPa QBO when measured over the whole season (figure 3.5). When the ZMZW composites from the pi-control are split up by month (figure 5.20), the responses are also comparable in magnitude and both peak in January although anomalies associated with the deep metric are evident throughout the winter season while single level vortex responses are most evident in December and January.

A marked difference between these composites is the presence of a tropospheric sub-tropical anomaly using the deep metric which is present for all sampled months and absent when using the single level definition. This suggests that the enhanced MSLP responses using a deep QBO measure in the pi-control may arise via the subtropical pathway (which is absent using the 50 hPa QBO) in addition to a modulation of the high-latitude pathway via the HT link. Furthermore, the subtropical tropospheric anomalies are also present in the deep QBO experiment (figure 5.12) and absent in the shallow simulation (figure 5.13) which further suggests the potential importance of this pathway when considering deep QBO teleconnections.

There are also some significant anomalies in the equatorial USLM in both the single level (50 hPa) composites and the deep QBO composites in figure 5.20. While they

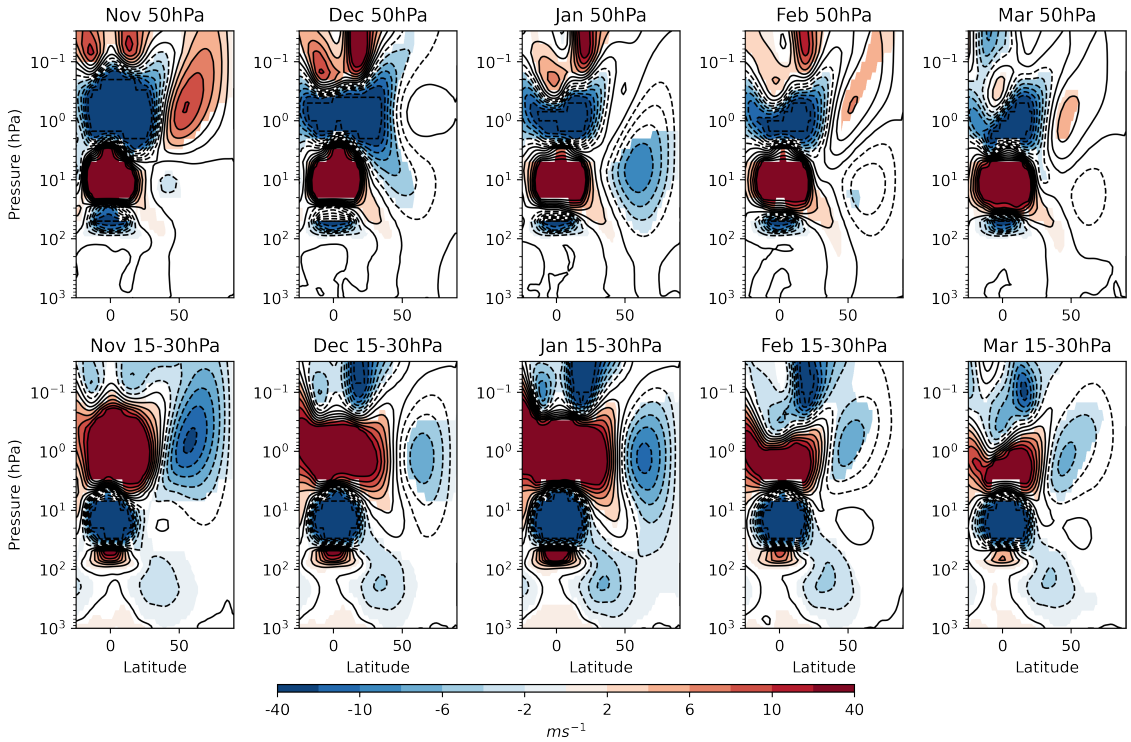


FIGURE 5.20: ZMZW composite differences for QBOE - QBOW from for the pi-control simulation of UKESM. QBO phases are defined using the Nov-Dec monthly equatorial (5° S–5° N average) ZMZW on the 50 hPa level (top row) and the same deep metric as employed in *Andrews et al.* [2019], the ZMZW averaged between the 15 hPa and 30 hPa levels (bottom row). Differences are evaluated in a range of NH winter months (indicated in sub-figure titles). Coloured shading indicates ZMZW differences significant above the 95% confidence level under a 2 tail Student's t-test.

both show QBOE minus QBOW differences, the vertical structure of the equatorial anomalies is very different, because of the different levels used in the composite selection: 50 hPa vs 15-30 hPa. Both composites have a four-fold anomaly structure in the vertical at equatorial latitudes but they have opposite polarities. For example, the deep QBO composite defined at 15-30 hPa has a positive anomaly in the lowermost stratosphere while the single-level composite defined at 50 hPa has a negative anomaly in this height region. The fact that the deep QBO composite has a stronger and longer-lasting HT response of the expected sign at high latitudes suggests that this lowermost anomaly is not important in determining the HT response (because the equatorial anomaly there is westerly but the vortex response is to weaken). This suggests that

the HT response is more likely a complex response to the whole vertical wind structure over the equator. This has been noted previously, in the context that planetary waves are deep structures and most likely are influenced by the equatorial winds over a significant depth of the stratosphere and possibly even the lower mesosphere. However, with such a complex vertical structure, it is not possible to isolate the most important height region. Returning to the idealised experiments, the deep experiment had a simpler two/three-fold structure in the vertical that suggested the equatorial USLM winds were most influential in determining the sign of the high latitude HT response, since easterly winds in the USLM led to a weaker vortex, and vice versa. Nevertheless, without a better understanding of the HT mechanism, it is still not clear which is the most important influence i.e. whether the response depends upon the amplitude of an anomaly, the height region of an anomaly or maybe even the location / strength of the vertical wind shear (or perhaps some combination of these). While our nudged simulations help to point to a possible influence from the equatorial USLM region, further experiments and analysis are needed to confirm this.

5.9 Summary and discussion

In this chapter, we analysed the influence of vertical structure of the QBO in teleconnections with the vortex and surface using a set of relaxation experiments which prescribed different degrees of QBO vertical coherence. While many studies have suggested the importance of QBO metrics that incorporate the vertical structure of the QBO [*Schenzinger et al.*, 2017; *Gray et al.*, 2018; *Andrews et al.*, 2019], many of them identify statistical associations between QBO metrics and other climate variability but encounter problems proving causality in teleconnections. As a result, the true nature of QBO teleconnections including many of the mechanisms involved are still not fully understood.

We found that an un-nudged configuration of the model (the pi-clim cntrl) was able to simulate some elements of connection between the QBO and the surface however, the MSLP response patterns did not closely resemble that of the NAO or AO and were significantly less coherent and persistent than those reported in previous modelling and observational studies (namely *Andrews et al.* [2019]). A simulation which prescribed a QBO with perpetual vertical coherence (the deep QBO experiment) exhibited significantly larger anomalies in MSLP than both the un-nudged simulation and one that prescribed a shallow QBO (with different QBO phases near the 100 hPa and 10 hPa levels respectively). These large anomalies in the deep experiment corresponded to an NAO pattern in late NH concentrated over the southern node in the Azores region. Surprisingly, QBOE phases were associated with a positive NAO pattern, an opposite response to that found in studies using a deep QBO metric [*Andrews et al.*, 2019] as well as that expected from a pathway involving the vortex and the Holton-Tan association [*Holton and Tan*, 1980].

We aimed to account for this opposite sign in QBO responses by examining the vortex response to QBO phases in each experiment. As with the MSLP response, the deep QBO experiment showed larger magnitude vortex responses from the vortex to QBO phases (figure 5.12) than in the shallow and un-nudged simulations (figures 5.10 and 5.13). These responses also evolve within the NH winter with negative responses to QBOE in early winter (in line with an expected HT link) and large amplitude positive responses in Jan-Mar. This switch in vortex response may account for the NAO patterns in late winter; the positive vortex response to QBOE in later winter leads to a positive NAO via the vortex's influence over the NAO [*Charlton-Perez et al.*, 2018].

Additionally, we noted that the late winter vortex response in this deep experiment (which was largely absent in the other experiments) was associated with significant equatorial USLM anomalies, likely induced via preferential filtering of equatorial waves

by the opposite deep QBO phase below. In the same simulation, the vortex was shown to respond to variations in the USLM QBO and an analysis of EP fluxes revealed that anomalies in the easterly phase of the USLM QBO were also associated with anomalies in poleward propagation of planetary waves in the upper stratosphere. This lead to increased wave driving of the vortex under USLM QBOE conditions and a weakening in late NH winter. This gives a potential mechanism to account for the late winter vortex strengthening (weakening) and subsequent positive (negative) NAO under mid-stratospheric QBOE (QBOW) phases. However, it is unclear whether the vortex anomalies drive the USLM variations or vice versa.

A comparison of responses to the QBO in our deep nudged experiment with the use of a deep QBO metric in a free-running pi-control (similar to that used in *Andrews et al.* [2019]) highlighted a number of key differences: The sign of the HT link and MSLP responses were consistent with previous work in the pi-control and the equatorial anomalies induced by the QBO Exhibited a different four-fold structure as opposed to the two-fold pattern in height exhibited by responses in the deep nudged experiment. There is a possibility that the perpetually deep QBO in our experiment acted to perturb the equatorial ULSM region with an unrealistic structure of anomalies which, in turn, lead to large magnitude responses in the vortex and MSLP of the opposite sign to a HT link. However, showing this connection explicitly is challenging with the simulations analysed here and further targeted experiments are required to study this effect more closely. Nevertheless, this feature provided further evidence of the role of the USLM QBO in vortex variability (in agreement with *Gray et al.* [2020]).

Overall, while our experiments suggest that the magnitudes of QBO responses are enhanced by the presence of a perpetually deep QBO, mid-late winter teleconnections in the deep experiment are dominated by responses which are inconsistent with previous work [*Gray et al.*, 2018; *Andrews et al.*, 2019]. The source of this discrepancy may lie in the modulation of large USLM anomalies by the perpetually deep QBO

below that, in turn, lead to large vortex anomalies obscuring the signal from other pathways. This prevents a comprehensive evaluation of the role of QBO vertical coherence in teleconnections.

To overcome this, further relaxation experiments which impose a deep or shallow QBO and also constrain the SAO winds may be useful. For example, repeating the deep QBO experiment but with a vertical extension of the relaxation into the USLM where winds were nudged towards either climatological ZMZW from a different simulation or using a reanalysis product. These simulations would eradicate the large USLM responses to QBO phase and isolate the effect of vertical QBO structure on teleconnections through other possible pathways. For example, the subtropical route suggested by *Gray et al.* [2018] was prominent in the deep experiment (figure 5.12, below the 100 hPa level) but whose effect may have been obscured by the USLM anomalies and subsequent vortex and MSLP response. Biases in the underlying model used for each experiment may also influence our results: Each simulation, similarly to the pi-control, exhibit a significant number of November SSWs. This has the potential to alter the evolution of the vortex throughout the remainder of winter as the vortex recovers from a November disruption. However, these November warmings occurred at similar rates in all experiments and we accounted for this bias by testing the sensitivity of results to removing years containing a November SSW finding that the key features of QBO responses were generally unaffected.

A similar limitation to our approach in this analysis is the fact that perpetual deep or shallow QBO conditions may not be fully representative of the real climate system - Reanalyses exhibit a QBO with deep and shallow attributes at different times and composite analysis which samples conditioned on the appearance of these characteristics produces coherent teleconnection patterns [*Andrews et al.*, 2019]. Where possible, we have imposed reasonable characteristics in both the deep and shallow QBOs; their descent rates, for example, were chosen within a range from an observational study

[*Kinnersley and Pawson*, 1996] and the period was selected in line with the pi-control and pi-clim cntrl for ease of comparison. Nevertheless, our simulations are designed to isolate the effect of these structures on teleconnections from noise in the climate system and, to this end, their representation may not fully mirror that of the real atmosphere. If carefully designed, targeted sensitivity experiments such as ours remain a useful tool to examine causality between features in the QBO and extra-tropical variability.

CHAPTER 6

Conclusions

6.1 Summary of results

The main findings of this thesis are summarised as follows:

Multi-decadal variations in polar vortex strength: While most works focus on seasonal effects of vortex variability, their non-uniform distribution in time in reanalysis datasets suggests the possibility of longer-term variations. We showed that, in a pi-control integration of a GCM (UKESM), the strength of the vortex exhibits spectral power on timescales between 30 and 100 years. This power is particularly apparent when the vortex index, either in the form of an event-based SSW time series (as is analysed in chapter 3) or a continuous metric (e.g. the NAM_{10}, chapter 4), is smoothed to capture the occurrences of intervals of consecutive NH winters exhibiting the same type of anomalous behaviour. These signals are highly non-stationary with the most persistent spectral feature appearing for approximately 450 years on the $\sim$90-year timescale.

Drivers of multi-decadal variability in the vortex: We identified co-variations between 90-year period signals in vortex variability with amplitude variations in a deep QBO metric. The deep QBO metric was defined by taking the average equatorial wind between 15 hPa and 30 hPa and identifies NH winters during which the vertical structure of the QBO is anomalously coherent (i.e. showing agreement in phase across pressure levels). Amplitude variations appear most pronounced in the westerly phase of the QBO and exhibit the most coherent behaviour with the appearance of hiatus intervals of SSWs. This association is consistent with the well-studied Holton-Tan relationship in which the presence of the westerly QBO phase in NH winter leads to greater latitudinal dispersion of vertically propagating planetary wave activity and subsequently a stronger vortex. The vortex indices exhibited minimal co-variability with major modes of surface variation on multi-decadal timescales and wavelet spectra for ENSO and the AL fail to account for large portions of the SSW and NAM wavelet power spectra on these multi-decadal timescales.

Surface influence of multi-decadal vortex variability: We analysed possible influences of multi-decadal signals in the vortex on tropospheric, surface and ocean variability with a particular focus on the Atlantic sector given the timescales involved (which were similar to the AMOC's characteristic periods) as well as the in-season association between the vortex and this region. We found that intervals of approximately 6-8 years that exhibit persistent anomalous vortex behaviour were found to lead to oscillatory responses in the Atlantic Meridional Overturning Circulation (AMOC) which were mediated through feedbacks with variations in ocean-atmosphere heat fluxes and the NAO. These AMOC responses peak in magnitude at lags of 2-3 years and $\sim$17 years following the vortex anomalies and were also characterised by non-stationary variations at periods of 30 and 50 years in the vortex, NAO and AMOC. We also found that the AMOC varies on longer timescales, similar to the 90-year

vortex variability, but power at this periodicity was not present in the NAO suggesting that mechanisms on these longer timescales may be different to those at 50 and 30-year periods.

AMOC influence on the QBO: We subsequently analysed possible sources of this 90-year variability of amplitude modulation in the deep QBO to determine whether variations were internally generated in the atmosphere or driven by low-frequency surface modes. While indices of major surface variation such as ENSO and the AL failed to account for large parts of the QBO and vortex wavelet spectra, significant co-variations between the QBO amplitude and deep convection indices over the eastern Pacific region were found. This co-variation supports the hypothesis that tropical upwelling and deep convection influence the vertical structure of the QBO and hence the formation of a deep QBO structure, providing a source of 90-year oscillations in the vortex from the surface. Co-variability between the AMOC and East Pacific deep convection was also shown at 90-year periods and AMOC variability on this timescale was distinct to that at 50 and 30-year periods as it is not accompanied by similar NAO variations. This result suggests a physical pathway by which 90-year timescale variations in the AMOC influence the vortex via modulation of tropical east pacific convection and modulation of the deep QBO amplitude.

Stratospheric role in recent AMOC trends: Using the lagged response of the AMOC to anomalous vortex intervals in the UKESM pi-control simulation, we estimated the potential contribution to recent observed trends in the AMOC from the interval of anomalously strong vortex winters in the 1990s. We found that the magnitude of the filtered NAM_{10} extremes in the model, which captures both the strength and persistence of the vortex anomaly, was directly proportional to the AMOC anomaly 17 years later with a remarkable degree of correlation (r = -0.908).

Furthermore, using this estimation of the lag yielded an estimate of the stratospheric contributions to the AMOC downturn between 2004 and 2012 of $-0.89Sv$ at 50°N ($-0.5Sv$ at 30°N). This contribution represents approximately 30% (17% at 30°N) of the total negative trend and suggests a key role for the vortex, a mode of internal variability, in driving observed AMOC variations.

Importance of QBO vertical structure in teleconnections: We designed a set of nudging experiments to explicitly test the influence of vertical coherence in the QBO on the strength of teleconnections with the vortex and the surface (the AO and NAO).

The QBO responses of the deep experiment were dominated by large-amplitude anomalies in the vortex and MSLP with QBOE(W) phases associated with a stronger (weaker) vortex and positive NAO and AO patterns. These are of the opposite sign to an expected HT link as well as the results of similar previous works [*Gray et al.*, 2018; *Andrews et al.*, 2019]. We found that these unexpected responses were associated with large amplitude anomalies in the SAO region likely caused by preferential filtering of equatorial waves by the deep QBO phase below. These equatorial USLM winds were associated with significant anomalies in vortex strength, consistent with a possible influence from this region. However, the design of the idealised deep QBO experiment resulted in a simple two/three-fold vertical structure of the equatorial QBO, which is unrealistic. The influence from the USLM may therefore have been overestimated in this experiment.

Examination of the HT relationship using a deep QBO metric in the 1000-year UKESM pi-control simulation showed a more realistic four-fold vertical QBO structure, as well as the correct sign of the HT relationship and MSLP response. The analysis of this simulation showed a consistent HT - vortex - Atlantic MSLP relationship, confirming the likely role of the polar route for stratospheric influence on the NAO via

vortex variations, but also identified a possible contribution to both the Atlantic and Pacific MSLP response via a subtropical route, where the induced meridional QBO circulation influences the lowermost stratosphere.

We, therefore, concluded that, while the deep QBO experiment confirmed a possible influence of the deep QBO from the equatorial USLM, its design obscured the response from other height regions. The analysis highlights the complexity of the QBO influence on both vortex and surface variability and suggests that the observed QBO influence at the surface is likely to be the result of a combination of processes that involve different height regions of the equatorial atmosphere.

6.2 Limitations and further investigations

The work presented in this thesis has also raised a number of questions, and its limitations motivate further investigation. Some of these ideas are discussed below:

Determining causality in teleconnections: While time series analyses such as those presented in chapters 3 and 4 can highlight associations between key modes of climate variability, they are less effective at determining causality in connections. Where possible, we have selected indices that confirm well-known in-season causality, such as an early winter QBO index compared with a mid-winter SSW index (as in chapter 3) or the vortex impact on Atlantic MSLP and subsequent links to the AMOC (chapter 4). Nevertheless, determining causality on longer timescales is difficult as the climate system is extremely complex, with many different interactions between modes of variability. These complexities can hamper simple statistical analysis such as multi-linear regression (as used in chapter 3 on SSW, QBO and surface time series) as it fails to capture the non-stationary nature of signals and suffers from the potential non-orthogonality of explanatory variables (ENSO, the QBO and the AL). While we employed more sophisticated techniques such as wavelet analysis to account for

non-stationarity, establishing causal connections remains an issue.

Further work into determining causality could involve tailor-made statistical methods such as the Causal Effect Network (CEN) framework [*Kretschmer et al.*, 2016] which has been developed for the analysis of causal connections in complex systems of time series data. This method identifies connections between pairs of time-series selected from a large group of indices while filtering out spurious correlations that arise between series which are not causally linked. For example, a correlation may arise between two variables that have no direct physical link if they are both driven by the same underlying process or via autocorrelation effects [*Runge et al.*, 2014]. Implementation of the CEN technique on indices such as those analysed in chapter 4 (the NAM_{10}, NAO, sub-polar North Atlantic heat flux and the AMOC) may aid in improving understanding of the physical pathways involved in interactions. For example, it may establish whether the NAO-AMOC interaction, which was shown to arise following a filtered NAM_{10} extreme, is prominent in the absence of a stratospheric anomaly or if the extreme vortex behaviour is a necessary triggering mechanism.

Targeted experiments: To overcome these issues with demonstrating causality in teleconnections, we also recommend a set of targeted sensitivity experiments using GCM simulations whose design is informed by our results. These experiments impose different multi-decadal signals on key climate indices using a similar nudging method as utilised in chapter 5 [*Telford et al.*, 2008].

- To test the connection between multi-decadal signals in QBO amplitude modulation and SSWs suggested in chapter 3, a set of simulations which impose variability in QBO amplitude: For example, one simulation could prescribe oscillating QBO amplitude on the 90-year timescales while another imposes a constant QBO amplitude. Comparison of multi-decadal signals in SSW fre-

quency in these experiments could establish whether the signals in the pi-control (chapter 3) are causally linked.

- Similar model setups designed to test the robustness of vortex-AMOC interactions could also be implemented. A simulation in which variability in vortex strength is imposed on decadal timescales with a pre-defined period may be appropriate in this case: Comparisons of the AMOC in such simulations with runs that imposed no decadal variability in the vortex could explicitly test the role of NAM_{10} variations in multi-decadal AMOC variability.

Understanding AMOC-SST-OLR connections: Analysis in section 4.7 showed variations in equatorial East Pacific OLR on 90-year timescales which were coincident with QBO and vortex variations as well as the AMOC at 50N. However, one would expect that an AMOC-OLR pathways would also involve modulation of SSTs in the same region via sea surface heating but analysis in chapter 3 showed no significant signals on the 90-year timescale in East Pacific SSTs. As a result, a more general approach to diagnosing variation in Pacific SSTs and their role in the AMOC-OLR-QBO-vortex teleconnection is required to fully understand this pathway. For example, future work could consider the spatial correlation pattern of Pacific SSTs against time series of interest; for instance the AMOC at 50N as utilised in chapter 4. This may reveal that the response of the Pacific SSTs to the AMOC is not concentrated over an East Pacific box but exhibits a more complex spatial structure. An extension to this analysis could also involve using the correlation map as a loading pattern to define an SST metric that tracks the time variation of the SST response pattern to the AMOC. Wavelet analysis of this new metric may indicate 90-year signals coincident with East Pacific OLR as well as the QBO and vortex and aid in understanding the exact role of Pacific SSTs in the physical pathways discussed in chapter 4 in which the AMOC leads to OLR anomalies and subsequent variations in the QBO and vortex.

The true role of the stratosphere in observed AMOC trends: Our results regarding the role of the SSW hiatus in the 1990s in recent AMOC trends also carry a number of limitations. For example, the AMOC response to extreme NAM_{10} intervals appear heavily weighted towards 30-year timescale variations. Variations on this timescale are highly non-stationary and it is unclear whether similar signals are present in the observational record, not least due to the short record of direct observations of the AMOC. Furthermore, as with the multi-decadal interactions, our analysis determined a strong statistical link between the phenomena but struggles to explicitly prove causality. Further sensitivity analysis may address some of these issues. Namely, relaxation experiments which impose an SSW hiatus interval of $\sim$ 9years and, at the end of this interval, allows the model to evolve freely to measure the lagged AMOC response compared to a control simulation with no stratospheric perturbation. Similar experiments which measure the response to consecutive NH winters with the same NAO pattern [*Delworth and Zeng*, 2016] showed promising results with significant AMOC anomalies from a control simulation evident. Our proposed experiments would test whether an SSW hiatus interval provides a large enough perturbation to induce significant NAO/AMOC anomalies.

Limitations of a single model approach: The results from chapters 3 and 4 regarding the interaction between multi-decadal variations in the polar vortex and other parts of the climate system is derived from a single simulation of a single GCM - the UKESM pi-control. This poses a potentially significant issue as the model exhibits biases in its representation of some key modes of climate variability. For example, November SSWs are significantly over-represented (figure 3.2) which may affect the progression of its strength through the winter as the vortex recovers from a November disruption which precludes further significant wave driving. The mean period of the QBO in the model is also longer than that exhibited by ERA-Interim [*Bushell et al.*,

2020]. This could lead to an over-inflated HT strength due to the longer persistence of QBO phases altering the mid-latitude waveguide through, on average, a larger portion of NH winter. Finally, the model under-represents decadal-scale variation in AMOC over the historical period [*Robson et al.*, 2020].

These biases may result in teleconnections in the model that are not fully representative of the real atmosphere. Recent work has also shown a large degree of inter-model variability exists in representations of the QBO [*Bushell et al.*, 2020] as well as SSWs [*Ayarzagüena et al.*, 2020] suggesting the possibility that results from our studies are model dependant. Further work could consider a suite of CMIP6 models and examine the multi-decadal signals in the vortex, QBO, NAO and AMOC to test the robustness of the various teleconnections established in the analysis of this thesis.

More effective QBO nudging: In chapter 5, we designed a set of nudging experiments which relaxed the QBO winds towards idealised fields (the deep and shallow QBO). However, a comparison of these fields with the model winds (figures 5.3 and 5.4) revealed the westerly phase of the QBO is under-represented in the model output despite the applied relaxation. This problem was particularly prevalent when nudging towards a deep QBO and poses potential issues with future QBO studies as it leads to significant asymmetries in nudged QBO phases.

Further analysis into rectifying this bias could involve a set of sensitivity experiments that implement nudging of the QBO towards the same idealised fields using smaller values for nudging timescales (τ in equation 5.1) than we used in our experiments ($\tau = 6$ hours). τ is generally set to 6 hours in line with the temporal resolution of reanalysis files commonly used for nudging (and is similar to that used in other families of models) [*Telford et al.*, 2008] however, using idealised fields, which can be generated at any temporal resolution, removes this constraint. Assessing the reduction in QBO bias achieved by reducing τ as well as the possible model

instability introduced by using a short nudging timescale, could aid in implementing more effective QBO nudging in future studies.

Constraining the USLM QBO: While our QBO experiments successfully imposed a deep and shallow QBO in the lower-mid stratosphere (figure 5.2), the deep experiment induced large anomalies in the equatorial USLM region (figure 5.12). These anomalies were shown to lead to large vortex and surface responses of the opposite sign to the expected HT link as well as the results of *Andrews et al.* [2019]. This USLM QBO signal obscured other possible physical pathways associated with the QBO and prevented a definitive evaluation of the role of vertical coherence in QBO teleconnections.

To analyse other possible pathways closer, we recommend further simulations which impose a deep QBO in the lower and mid stratosphere and also nudges the SAO winds. In the SAO region, winds could be nudged towards climatological values calculated from another simulation (the pi-clim cntrl, for example) in order to remove the large anomalies induced by the deep QBO in our experiment. Eradicating the influence of these USLM responses may aid in isolating the influence from other height regions involved in QBO teleconnections, including the potential influence from the induced meridional QBO circulation via the subtropical route described in *Gray et al.* [2018]. Isolation of these other effects may develop a better understanding of the mechanisms at play in the presence of a vertically coherent QBO.

Bibliography

Akinwande, O., H. Dikko, and S. Agboola (2015), Variance Inflation Factor: As a Condition for the Inclusion of Suppressor Variable(s) in Regression Analysis, *Open Journal of Statistics*, *05*, 754–767, doi:10.4236/ojs.2015.57075.

Alexander, M. A., and J. D. Scott (2008), The Role of Ekman Ocean Heat Transport in the Northern Hemisphere Response to ENSO, *Journal of Climate*, *21*(21), 5688–5707, doi:10.1175/2008JCLI2382.1.

Alexander, M. A., I. Bladé, M. Newman, J. R. Lanzante, N.-C. Lau, and J. D. Scott (2002), The Atmospheric Bridge: The Influence of ENSO Teleconnections on Air–Sea Interaction over the Global Oceans, *Journal of Climate*, *15*(16), 2205–2231, doi:10.1175/1520-0442(2002)015<2205:TABTIO>2.0.CO;2.

Alley, R. B. (2007), Wally Was Right: Predictive Ability of the North Atlantic "Conveyor Belt" Hypothesis for Abrupt Climate Change, *Annual Review of Earth and Planetary Sciences*, *35*(1), 241–272, doi:10.1146/annurev.earth.35.081006.131524.

Ambaum, M. H. P., B. J. Hoskins, and D. B. Stephenson (2001), Arctic Oscillation or North Atlantic Oscillation?, *Journal of Climate*, *14*(16), 3495–3507, doi:10.1175/1520-0442(2001)014<3495:AOONAO>2.0.CO;2.

Andrews, D. G., and M. E. McIntyre (1976), Planetary Waves in Horizontal and Vertical Shear: The Generalized Eliassen-Palm Relation and the Mean Zonal Acceleration, *Journal of the Atmospheric Sciences*, *33*(11), 2031–2048, doi:10.1175/1520-0469(1976)033<2031:PWIHAV>2.0.CO;2.

Andrews, D. G., J. R. Holton, and C. B. Leovy (1987), *Middle Atmosphere Dynamics*, Academic Press.

Andrews, M. B., J. R. Knight, A. A. Scaife, Y. Lu, T. Wu, L. J. Gray, and V. Schenzinger (2019), Observed and Simulated Teleconnections Between the Stratospheric Quasi-Biennial Oscillation and Northern Hemisphere Winter Atmospheric Circulation, *Journal of Geophysical Research: Atmospheres*, *124*(3), 1219–1232, doi:10.1029/2018JD029368.

Andrews, M. B., J. K. Ridley, R. A. Wood, T. Andrews, E. W. Blockley, B. Booth, E. Burke, A. J. Dittus, P. Florek, L. J. Gray, S. Haddad, S. C. Hardiman, L. Hermanson, D. Hodson, E. Hogan, G. S. Jones, J. R. Knight, T. Kuhlbrodt, S. Misios, M. S. Mizielinski, M. A. Ringer, J. Robson, and R. T. Sutton (2020), Historical simulations with HadGEM3-GC3.1 for CMIP6, *Journal of Advances in Modeling Earth Systems*, *12*(6), doi:10.1029/2019MS001995.

Anstey, J. A., and T. G. Shepherd (2008), Response of the northern stratospheric polar vortex to the seasonal alignment of QBO phase transitions, *Geophysical Research Letters*, *35*(22), doi:10.1029/2008GL035721.

Anstey, J. A., and T. G. Shepherd (2014), High-latitude influence of the quasi-biennial oscillation, *Quarterly Journal of the Royal Meteorological Society*, *140*(678), 1–21, doi:10.1002/qj.2132.

Anstey, J. A., I. R. Simpson, J. H. Richter, H. Naoe, M. Taguchi, F. Serva, L. J. Gray, N. Butchart, K. Hamilton, S. Osprey, O. Bellprat, P. Braesicke, A. C. Bushell, C. Cagnazzo, C.-C. Chen, H.-Y. Chun, R. R. Garcia, L. Holt, Y. Kawatani, T. Kerzenmacher, Y.-H. Kim, F. Lott, C. McLandress, J. Scinocca, T. N. Stockdale, S. Versick, S. Watanabe, K. Yoshida, and S. Yukimoto (2021), Teleconnections of the Quasi-Biennial Oscillation in a multi-model ensemble of QBO-resolving models, *Quarterly Journal of the Royal Meteorological Society*, *SPECIAL SECTION QBO MODELLING INTERCOMPARISON*(n/a), 1–25, doi:10.1002/qj.4048.

Ayarzagüena, B., S. Ineson, N. J. Dunstone, M. P. Baldwin, and A. A. Scaife (2018), Intraseasonal Effects of El Niño–Southern Oscillation on North Atlantic Climate, *Journal of Climate*, *31*(21), 8861–8873, doi:10.1175/JCLI-D-18-0097.1.

Ayarzagüena, B., F. M. Palmeiro, D. Barriopedro, N. Calvo, U. Langematz, and K. Shibata (2019), On the representation of major stratospheric warmings in reanalyses, *Atmospheric Chemistry and Physics*, *19*(14), 9469–9484, doi:10.5194/acp-19-9469-2019.

Ayarzagüena, B., A. Charlton-Perez, A. Butler, P. Hitchcock, I. Simpson, L. Polvani, N. Butchart, E. Gerber, L. Gray, B. Hassler, P. Lin, F. Lott, E. Manzini, R. Mizuta, C. Orbe, S. Osprey, D. Saint-Martin, M. Sigmond, M. Taguchi, and S. Watanabe (2020), Uncertainty in the Response of Sudden Stratospheric Warmings and Stratosphere-Troposphere Coupling to Quadrupled CO 2 Concentrations in CMIP6 Models, *Journal of Geophysical Research: Atmospheres*, *125*, 103–121, doi:10.1029/2019JD032345.

Bakker, P., A. Schmittner, J. T. M. Lenaerts, A. Abe-Ouchi, D. Bi, M. R. van den Broeke, W.-L. Chan, A. Hu, R. L. Beadling, S. J. Marsland, S. H. Mernild, O. A. Saenko, D. Swingedouw, A. Sullivan, and J. Yin (2016), Fate of the Atlantic Meridional Overturning Circulation: Strong decline under continued warming and Greenland melting, *Geophysical Research Letters*, *43*(23), 12,252–12,260, doi:10.1002/2016GL070457.

Baldwin, M., L. Gray, T. Dunkerton, K. Hamilton, P. Haynes, W. Randel, J. Holton, M. Alexander, I. Hirota, T. Horinouchi, D. Jones, J. Kinnersley, C. Marquardt, K. Sato, and M. Takahashi (2001), The Quasi-Biennial Oscillation, *Reviews Geophys.*, *39*(2), 179–229, doi:10.1029/1999RG000073.

Baldwin, M. P., and T. J. Dunkerton (1991), The quasi-biennial oscillations above 10mb, *Geophysical Research Letters*, *18*(7), 1205–1208, doi:10.1029/91GL01333.

Baldwin, M. P., and T. J. Dunkerton (1998), Quasi-biennial modulation of the southern hemisphere stratospheric polar vortex, *Geophysical Research Letters*, *25*(17), 3343–3346, doi:10.1029/98GL02445.

Baldwin, M. P., and T. J. Dunkerton (1999), Propagation of the Arctic Oscillation from the stratosphere to the troposphere, *Journal of Geophysical Research: Atmospheres*, *104*(D24), 30,937–30,946, doi:10.1029/1999JD900445.

Baldwin, M. P., and T. J. Dunkerton (2001), Stratospheric Harbingers of Anomalous Weather Regimes, *Science*, *294*(5542), 581–584, doi:10.1126/science.1063315.

Baldwin, M. P., and L. J. Gray (2005), Tropical stratospheric zonal winds in ECMWF ERA-40 reanalysis, rocketsonde data, and rawinsonde data, *Geophysical Research Letters*, *32*, L09,806, doi:10.1029/2004GL022328.

Baldwin, M. P., and D. W. J. Thompson (2009), A critical comparison of stratosphere–troposphere coupling indices, *Quarterly Journal of the Royal Meteorological Society*, *135*(644), 1661–1672, doi:10.1002/qj.479.

Baldwin, M. P., B. Ayarzagüena, T. Birner, N. Butchart, A. H. Butler, A. J. Charlton-Perez, D. I. V. Domeisen, C. I. Garfinkel, H. Garny, E. P. Gerber, M. I. Hegglin, U. Langematz, and N. M. Pedatella (2021), Sudden Stratospheric Warmings, *Reviews of Geophysics*, *59*(1), e2020RG000,708, doi:10.1029/2020RG000708.

Ballish, B. A., and V. K. Kumar (2008), Systematic Differences in Aircraft and Radiosonde Temperatures: Implications for NWP and Climate Studies, *Bulletin of the American Meteorological Society*, *89*(11), 1689–1708, doi:10.1175/2008BAMS2332.1.

Bancalá, S., K. Krüger, and M. Giorgetta (2012), The preconditioning of major sudden stratospheric warmings, *Journal of Geophysical Research (Atmospheres)*, *117*, 4101, doi:10.1029/2011JD016769.

Bell, C. J., L. J. Gray, A. J. Charlton-Perez, M. M. Joshi, and A. A. Scaife (2009), Stratospheric Communication of El Niño Teleconnections to European Winter, *Journal of Climate*, *22*(15), 4083–4096, doi:10.1175/2009JCLI2717.1.

Belmont, A. D., and D. G. Dartt (1968), VARIATION WITH LONGITUDE OF THE QUASI-BIENNIAL OSCILLATION, *Monthly Weather Review*, *96*(11), 767–777, doi:10.1175/1520-0493(1968)096<0767:VWLOTQ>2.0.CO;2.

Berrisford, P., D. Dee, P. Poli, R. Brugge, M. Fielding, M. Fuentes, P. Kållberg, S. Kobayashi, S. Uppala, and A. Simmons (2011), The ERA-Interim archive version 2.0, *ERA Report Series*, (1), 23.

Biastoch, A., C. W. Böning, J. Getzlaff, J.-M. Molines, and G. Madec (2008), Causes of Interannual–Decadal Variability in the Meridional Overturning Circulation of the Midlatitude North Atlantic Ocean, *Journal of Climate*, *21*(24), 6599–6615, doi:10.1175/2008JCLI2404.1.

Biondi, F., A. Gershunov, and D. R. Cayan (2001), North Pacific Decadal Climate Variability since 1661, *Journal of Climate*, *14*(1), 5–10, doi:10.1175/1520-0442(2001)014<0005:NPDCVS>2.0.CO;2.

Böning, C. W., M. Scheinert, J. Dengg, A. Biastoch, and A. Funk (2006), Decadal variability of subpolar gyre transport and its reverberation in the North Atlantic overturning, *Geophysical Research Letters*, *33*(21), doi:10.1029/2006GL026906.

Bouttier, F., and G. Kelly (2001), Observing-system experiments in the ECMWF 4D-Var data assimilation system, *Quarterly Journal of the Royal Meteorological Society*, *127*(574), 1469–1488, doi:10.1002/qj.49712757419.

Buckley, M. W., and J. Marshall (2016), Observations, inferences, and mechanisms of the Atlantic Meridional Overturning Circulation: A review, *Reviews of Geophysics*, *54*(1), 5–63, doi:10.1002/2015RG000493.

Bushell, A. C., J. A. Anstey, N. Butchart, Y. Kawatani, S. M. Osprey, J. H. Richter, F. Serva, P. Braesicke, C. Cagnazzo, C.-C. Chen, H.-Y. Chun, R. R. Garcia, L. J. Gray, K. Hamilton, T. Kerzenmacher, Y.-H. Kim, F. Lott, C. McLandress, H. Naoe, J. Scinocca, A. K. Smith, T. N. Stockdale, S. Versick, S. Watanabe, K. Yoshida, and S. Yukimoto (2020), Evaluation of the Quasi-Biennial Oscillation in global climate models for the SPARC QBO-initiative, *Quarterly Journal of the Royal Meteorological Society*, *1*, 1–31, doi:10.1002/qj.3765.

Butchart, N. (2014), The Brewer-Dobson circulation, *Reviews of Geophysics*, *52*(2), 157–184, doi:10.1002/2013RG000448.

Butchart, N., J. Austin, J. R. Knight, A. A. Scaife, and M. L. Gallani (2000), The response of the stratospheric climate to projected changes in the concentrations of well-mixed greenhouse gases from 1992 to 2051, *Journal of Climate*, *13*(13), 2142–2159, doi:10.1175/1520-0442.

Butchart, N., A. J. Charlton-Perez, I. Cionni, S. C. Hardiman, P. H. Haynes, K. Krüger, P. J. Kushner, P. A. Newman, S. M. Osprey, J. Perlwitz, M. Sigmond, L. Wang, H. Akiyoshi, J. Austin, S. Bekki, A. Baumgaertner, P. Braesicke, C. Brhl, M. Chipperfield, M. Dameris, S. Dhomse, V. Eyring, R. Garcia, H. Garny, P. Jöckel, J. F. Lamarque, M. Marchand, M. Michou, O. Morgenstern, T. Nakamura, S. Pawson, D. Plummer, J. Pyle, E. Rozanov, J. Scinocca, T. G. Shepherd, K. Shibata, D. Smale, H. Teyssèdre, W. Tian, D. Waugh, and Y. Yamashita (2011), Multimodel climate and variability of the stratosphere, *Journal of Geophysical Research Atmospheres*, doi:10.1029/2010JD014995.

Butchart, N., J. A. Anstey, K. Hamilton, S. Osprey, C. McLandress, A. C. Bushell, Y. Kawatani, Y.-H. Kim, F. Lott, J. Scinocca, T. N. Stockdale, M. Andrews, O. Bellprat, P. Braesicke, C. Cagnazzo, C.-C. Chen, H.-Y. Chun, M. Dobrynin, R. R. Garcia, J. Garcia-Serrano, L. J. Gray, L. Holt, T. Kerzenmacher, H. Naoe, H. Pohlmann, J. H. Richter, A. A. Scaife, V. Schenzinger, F. Serva, S. Versick, S. Watanabe, K. Yoshida, and S. Yukimoto (2018), Overview of experiment design and comparison of models participating in phase 1 of the SPARC Quasi-Biennial Oscillation initiative (QBOi), *Geoscientific Model Development*, *11*(3), 1009–1032, doi:10.5194/gmd-11-1009-2018.

Butler, A. H., and L. M. Polvani (2011), El Niño, La Niña, and stratospheric sudden warmings: A reevaluation in light of the observational record, *Geophysical Research Letters*, *38*(13), doi:10.1029/2011GL048084.

Butler, A. H., D. J. Seidel, S. C. Hardiman, N. Butchart, T. Birner, and A. Match (2015), Defining Sudden Stratospheric Warmings, *Bulletin of the American Meteorological Society*, *96*(11), 1913–1928, doi:10.1175/BAMS-D-13-00173.1.

Butler, A. H., J. P. Sjoberg, D. J. Seidel, and K. H. Rosenlof (2017), A sudden stratospheric warming compendium, *Earth System Science Data*, *9*(1), 63–76, doi:10.5194/essd-9-63-2017.

Caesar, L., S. Rahmstorf, A. Robinson, G. Feulner, and V. Saba (2018), Observed fingerprint of a weakening Atlantic Ocean overturning circulation, *Nature*, *556*(7700), 191–196, doi:10.1038/s41586-018-0006-5.

Caesar, L., G. D. McCarthy, D. J. R. Thornalley, N. Cahill, and S. Rahmstorf (2021), Current Atlantic Meridional Overturning Circulation weakest in last millennium, *Nature Geoscience*, *14*(3), 118–120, doi:10.1038/s41561-021-00699-z.

Cessi, P., K. Bryan, and R. Zhang (2004), Global seiching of thermocline waters between the Atlantic and the Indian-Pacific Ocean Basins, *Geophysical Research Letters*, *31*(4), doi:10.1029/2003GL019091.

Charlton, A., L. Polvani, J. Perlwitz, F. Sassi, E. Manzini, K. Shibata, S. Pawson, J. Nielsen, and D. Rind (2007), A new look at stratospheric sudden warmings. Part II: Evaluation of numerical model simulations, *Journal of Climate*, *10*, 470–488, doi:doi:10.1175/JCLI3994.1.

Charlton, A. J., and L. M. Polvani (2007), A New Look at Stratospheric Sudden Warmings. Part I: Climatology and Modeling Benchmarks, *Journal of Climate*, *20*(3), 449–469, doi:10.1175/JCLI3996.1.

Charlton-Perez, A. J., M. P. Baldwin, T. Birner, R. X. Black, A. H. Butler, N. Calvo, N. A. Davis, E. P. Gerber, N. Gillett, S. Hardiman, J. Kim, K. Krüger, Y.-Y. Lee, E. Manzini, B. A. McDaniel, L. Polvani, T. Reichler, T. A. Shaw, M. Sigmond, S.-W. Son, M. Toohey, L. Wilcox, S. Yoden, B. Christiansen, F. Lott, D. Shindell, S. Yukimoto, and S. Watanabe (2013), On the lack of stratospheric dynamical variability in low-top versions of the CMIP5 models, *Journal of Geophysical Research: Atmospheres*, *118*(6), 2494–2505, doi:10.1002/jgrd.50125.

Charlton-Perez, A. J., L. Ferranti, and R. W. Lee (2018), The influence of the stratospheric state on North Atlantic weather regimes, *Quarterly Journal of the Royal Meteorological Society*, *144*(713), 1140–1151, doi:10.1002/qj.3280.

Charney, J. G., and P. G. I. Drazin (1961), Propagation of planetary-scale disturbances from the lower into the upper atmosphere, *Journal of Geophysical Research*, *66*(1), 83–109, doi:doi:10.1029/JZ066i001p00083.

Chen, S., W. Chen, R. Wu, B. Yu, and H.-F. Graf (2020), Potential Impact of Preceding Aleutian Low Variation on El Niño–Southern Oscillation during the Following Winter, *Journal of Climate*, *33*(8), 3061–3077, doi:10.1175/JCLI-D-19-0717.1.

Chen, X., and J. M. Wallace (2015), ENSO-Like Variability: 1900–2013, *Journal of Climate*, *28*(24), 9623–9641, doi:10.1175/JCLI-D-15-0322.1.

Cheng, H., R. L. Edwards, W. S. Broecker, G. H. Denton, X. Kong, Y. Wang, R. Zhang, and X. Wang (2009), Ice Age Terminations, *Science*, *326*(5950), 248–252, doi:10.1126/science.1177840.

Cohen, J., M. Barlow, and K. Saito (2009), Decadal Fluctuations in Planetary Wave Forcing Modulate Global Warming in Late Boreal Winter, *Journal of Climate*, *22*(16), 4418–4426, doi:10.1175/2009JCLI2931.1.

Courtier, P., E. Andersson, W. Heckley, D. Vasiljevic, M. Hamrud, A. Hollingsworth, F. Rabier, M. Fisher, and J. Pailleux (1998), The ECMWF implementation of three-dimensional variational assimilation (3D-Var). I: Formulation, *Quarterly Journal of the Royal Meteorological Society*, *124*(550), 1783–1807, doi:10.1002/qj.49712455002.

Coy, L., P. A. Newman, S. Strahan, and S. Pawson (2020), Seasonal Variation of the Quasi-Biennial Oscillation Descent, *Journal of Geophysical Research: Atmospheres*, *125*(18), e2020JD033,077, doi:10.1029/2020JD033077.

Daubechies, I. (1990), The wavelet transform, time-frequency localization and signal analysis, *IEEE Transactions on Information Theory*, *36*(5), 961–1005, doi:10.1109/18.57199.

Davini, P., C. Cagnazzo, and J. A. Anstey (2014), A blocking view of the stratosphere-troposphere coupling, *Journal of Geophysical Research: Atmospheres*, *119*(19), 11,100–11,115, doi:10.1002/2014JD021703.

de Boyer Montégut, C., G. Madec, A. S. Fischer, A. Lazar, and D. Iudicone (2004), Mixed layer depth over the global ocean: An examination of profile data and a profile-based climatology, *Journal of Geophysical Research: Oceans*, *109*(C12), doi:10.1029/2004JC002378.

Dee, D. P., S. M. Uppala, A. J. Simmons, P. Berrisford, P. Poli, S. Kobayashi, U. Andrae, M. A. Balmaseda, G. Balsamo, P. Bauer, P. Bechtold, A. C. Beljaars, L. van de Berg, J. Bidlot, N. Bormann, C. Delsol, R. Dragani, M. Fuentes, A. J. Geer, L. Haimberger, S. B. Healy, H. Hersbach, E. V. Hólm, L. Isaksen, P. Kållberg, M. Köhler, M. Matricardi, A. P. Mcnally, B. M. Monge-Sanz, J. J. Morcrette, B. K. Park, C. Peubey, P. de Rosnay, C. Tavolato, J. N. Thépaut, and F. Vitart (2011), The ERA-Interim reanalysis: Configuration and performance of the data assimilation system, *Quarterly Journal of the Royal Meteorological Society*, *137*(656), 553–597, doi:10.1002/qj.828.

Delworth, T., S. Manabe, and R. J. Stouffer (1993), Interdecadal Variations of the Thermohaline Circulation in a Coupled Ocean-Atmosphere Model, *Journal of Climate*, *6*(11), 1993–2011, doi:10.1175/1520-0442(1993)006<1993:IVOTTC>2.0.CO;2.

Delworth, T. L., and K. W. Dixon (2000), Implications of the Recent Trend in the Arctic/North Atlantic Oscillation for the North Atlantic Thermohaline Circulation, *Journal of Climate*, *13*(21), 3721–3727, doi:10.1175/1520-0442(2000)013<3721:IOTRTI>2.0.CO;2.

Delworth, T. L., and R. J. Greatbatch (2000), Multidecadal Thermohaline Circulation Variability Driven by Atmospheric Surface Flux Forcing, *Journal of Climate*, *13*(9), 1481–1495, doi:10.1175/1520-0442(2000)013<1481:MTCVDB>2.0.CO;2.

Delworth, T. L., and M. E. Mann (2000), Observed and simulated multidecadal variability in the Northern Hemisphere, *Climate Dynamics*, *16*(9), 661–676, doi:10.1007/s003820000075.

Delworth, T. L., and F. Zeng (2016), The Impact of the North Atlantic Oscillation on Climate through Its Influence on the Atlantic Meridional Overturning Circulation, *Journal of Climate*, *29*(3), 941–962, doi:10.1175/JCLI-D-15-0396.1.

Deser, C. (2000), On the teleconnectivity of the "Arctic Oscillation", *Geophysical Research Letters*, *27*(6), 779–782, doi:10.1029/1999GL010945.

Deser, C., I. R. Simpson, K. A. McKinnon, and A. S. Phillips (2017), The Northern Hemisphere Extratropical Atmospheric Circulation Response to ENSO: How Well Do We Know It and How Do We Evaluate Models Accordingly?, *Journal of Climate*, *30*(13), 5059–5082, doi:10.1175/JCLI-D-16-0844.1.

Dimdore-Miles, O., L. Gray, and S. Osprey (2021a), Origins of multi-decadal variability in sudden stratospheric warmings, *Weather and Climate Dynamics*, *2*(1), 205–231, doi:10.5194/wcd-2-205-2021.

Dimdore-Miles, O., L. Gray, S. Osprey, J. Robson, R. Sutton, and B. Sinha (2021b), Interactions between the stratospheric polar vortex and Atlantic circulation on seasonal to multi-decadal timescales, *Atmospheric Chemistry and Physics Discussions*, pp. 1–40, doi:10.5194/acp-2021-688.

Domeisen, D. I. V. (2019), Estimating the Frequency of Sudden Stratospheric Warming Events From Surface Observations of the North Atlantic Oscillation, *Journal of Geophysical Research: Atmospheres*, *124*(6), 3180–3194, doi:10.1029/2018JD030077.

Domeisen, D. I. V., A. H. Butler, K. Fröhlich, M. Bittner, W. A. Müller, and J. Baehr (2015), Seasonal Predictability over Europe Arising from El Niño and Stratospheric Variability in the MPI-ESM Seasonal Prediction System, *Journal of Climate*, *28*(1), 256–271, doi:10.1175/JCLI-D-14-00207.1.

Domeisen, D. I. V., C. I. Garfinkel, and A. H. Butler (2019), The Teleconnection of El Niño Southern Oscillation to the Stratosphere, *Reviews of Geophysics*, *57*(1), 5–47, doi:10.1029/2018RG000596.

Dunkerton, T. (1979), On the Role of the Kelvin Wave in the Westerly Phase of the Semiannual Zonal Wind Oscillation, *Journal of the Atmospheric Sciences*, *36*(1), 32–41, doi:10.1175/1520-0469(1979)036<0032:OTROTK>2.0.CO;2.

Dunkerton, T. J. (2017), Nearly identical cycles of the quasi-biennial oscillation in the equatorial lower stratosphere, *Journal of Geophysical Research: Atmospheres*, *122*(16), 8467–8493, doi:10.1002/2017JD026542.

Ebdon, R. A. (1960), Notes on the wind flow at 50 mb in tropical and sub-tropical regions in January 1957 and January 1958, *Quarterly Journal of the Royal Meteorological Society*, *86*(370), 540–542, doi:10.1002/qj.49708637011.

Ebdon, R. A., and R. G. Veryard (1961), Fluctuations in Equatorial Stratospheric Winds, *Nature*, *189*(4767), 791–793, doi:10.1038/189791a0.

Eden, C., and T. Jung (2001), North Atlantic Interdecadal Variability: Oceanic Response to the North Atlantic Oscillation (1865–1997), *Journal of Climate*, *14*(5), 676–691, doi:10.1175/1520-0442(2001)014<0676:NAIVOR>2.0.CO;2.

Eden, C., and J. Willebrand (2001), Mechanism of Interannual to Decadal Variability of the North Atlantic Circulation, *Journal of Climate*, *14*(10), 2266–2280, doi:10.1175/1520-0442(2001)014<2266:MOITDV>2.0.CO;2.

Eichinger, R., H. Garny, P. Šácha, J. Danker, S. Dietmüller, and S. Oberländer-Hayn (2020), Effects of missing gravity waves on stratospheric dynamics; part 1: Climatology, *Climate Dynamics*, *54*(5), 3165–3183, doi:10.1007/s00382-020-05166-w.

Esler, J. G., and N. Matthewman (2011), Stratospheric Sudden Warmings as Self-Tuning Resonances. Part I: Vortex Splitting Events, *Journal of the Atmospheric Sciences*, *68*(11), 2481–2504, doi:10.1175/JAS-D-11-07.1.

Esler, J. G., and R. K. Scott (2005), Excitation of Transient Rossby Waves on the Stratospheric Polar Vortex and the Barotropic Sudden Warming, *Journal of the Atmospheric Sciences*, *62*(10), 3661–3682, doi:10.1175/JAS3557.1.

Fleming, S. W. (2014), A non-uniqueness problem in the identification of power-law spectral scaling for hydroclimatic time series, *Hydrological Sciences Journal*, *59*(1), 73–84, doi:10.1080/02626667.2013.851384.

Fletcher, C. G., and P. J. Kushner (2011), The Role of Linear Interference in the Annular Mode Response to Tropical SST Forcing, *Journal of Climate*, *24*(3), 778–794, doi:10.1175/2010JCLI3735.1.

Fletcher, C. G., and P. J. Kushner (2013), Linear interference and the Northern Annular Mode response to tropical SST forcing: Sensitivity to model configuration, *Journal of Geophysical Research: Atmospheres*, *118*(10), 4267–4279, doi:10.1002/jgrd.50385.

Fraedrich, K., S. Pawson, and R. Wang (1993), An EOF Analysis of the Vertical-Time Delay Structure of the Quasi-Biennial Oscillation, *Journal of the Atmospheric Sciences*, *50*(20), 3357–3365, doi:10.1175/1520-0469(1993)050<3357:AEAOTV>2.0.CO;2.

Frankignoul, C., and K. Hasselmann (1977), Stochastic climate models, Part II Application to sea-surface temperature anomalies and thermocline variability, *Tellus*, *29*(4), 289–305, doi:10.3402/tellusa.v29i4.11362.

Frankignoul, C., G. Gastineau, and Y.-O. Kwon (2013), The Influence of the AMOC Variability on the Atmosphere in CCSM3, *Journal of Climate*, *26*(24), 9774–9790, doi:10.1175/JCLI-D-12-00862.1.

Freedman, D., R. Pisani, and R. Purves (2007), *Statistics, 4th Edition International Student Edition | Wiley*.

Frierson, D. M. W., Y.-T. Hwang, N. S. Fučkar, R. Seager, S. M. Kang, A. Donohoe, E. A. Maroon, X. Liu, and D. S. Battisti (2013), Contribution of ocean overturning circulation to tropical rainfall peak in the Northern Hemisphere, *Nature Geoscience*, *6*(11), 940–944, doi:10.1038/ngeo1987.

Fujiwara, M., J. S. Wright, G. L. Manney, L. J. Gray, J. Anstey, T. Birner, S. Davis, E. P. Gerber, V. L. Harvey, M. I. Hegglin, C. R. Homeyer, J. A. Knox, K. Krüger, A. Lambert, C. S. Long, P. Martineau, A. Molod, B. M. Monge-Sanz, M. L. Santee, S. Tegtmeier, S. Chabrillat, D. G. H. Tan, D. R. Jackson, S. Polavarapu, G. P. Compo, R. Dragani, W. Ebisuzaki, Y. Harada, C. Kobayashi, W. McCarty, K. Onogi, S. Pawson, A. Simmons, K. Wargan, J. S. Whitaker, and C.-Z. Zou (2017), Introduction to the SPARC Reanalysis Intercomparison Project (S-RIP) and overview of the reanalysis systems, *Atmospheric Chemistry and Physics*, *17*(2), 1417–1452, doi:10.5194/acp-17-1417-2017.

Garcia, R. R., T. J. Dunkerton, R. S. Lieberman, and R. A. Vincent (1997), Climatology of the semiannual oscillation of the tropical middle atmosphere, *Journal of Geophysical Research: Atmospheres*, *102*(D22), 26,019–26,032, doi:10.1029/97JD00207.

Garcia, R. R., A. K. Smith, D. E. Kinnison, Á. de la Cámara, and D. J. Murphy (2017), Modification of the Gravity Wave Parameterization in the Whole Atmosphere Community Climate Model: Motivation and Results, *Journal of the Atmospheric Sciences*, *74*(1), 275–291, doi:10.1175/JAS-D-16-0104.1.

García-Herrera, R., N. Calvo, R. R. Garcia, and M. A. Giorgetta (2006), Propagation of ENSO temperature signals into the middle atmosphere: A comparison of two general circulation models and ERA-40 reanalysis data, *Journal of Geophysical Research: Atmospheres*, *111*(D6), doi:10.1029/2005JD006061.

Garfinkel, C. I., and D. L. Hartmann (2008), Different ENSO teleconnections and their effects on the stratospheric polar vortex, *Journal of Geophysical Research: Atmospheres*, *113*(D18), doi:10.1029/2008JD009920.

Garfinkel, C. I., and D. L. Hartmann (2011), The Influence of the Quasi-Biennial Oscillation on the Troposphere in Winter in a Hierarchy of Models. Part I: Simplified Dry GCMs, *Journal of the Atmospheric Sciences*, *68*(6), 1273–1289, doi:10.1175/2011JAS3665.1.

Garfinkel, C. I., D. L. Hartmann, and F. Sassi (2010), Tropospheric Precursors of Anomalous Northern Hemisphere Stratospheric Polar Vortices, *Journal of Climate*, *23*(12), 3282–3299, doi:10.1175/2010JCLI3010.1.

Garfinkel, C. I., T. A. Shaw, D. L. Hartmann, and D. W. Waugh (2012a), Does the Holton–Tan Mechanism Explain How the Quasi-Biennial Oscillation Modulates the Arctic Polar Vortex?, *Journal of the Atmospheric Sciences*, *69*(5), 1713–1733, doi:10.1175/JAS-D-11-0209.1.

Garfinkel, C. I., A. H. Butler, D. W. Waugh, M. M. Hurwitz, and L. M. Polvani (2012b), Why might stratospheric sudden warmings occur with similar frequency in El Niño and La Niña winters?, *Journal of Geophysical Research: Atmospheres*, *117*(D19), doi:10.1029/2012JD017777.

Garfinkel, C. I., M. M. Hurwitz, and L. D. Oman (2015), Effect of recent sea surface temperature trends on the Arctic stratospheric vortex, *Journal of Geophysical Research: Atmospheres*, *120*(11), 5404–5416, doi:10.1002/2015JD023284.

Garfinkel, C. I., S.-W. Son, K. Song, V. Aquila, and L. D. Oman (2017), Stratospheric variability contributed to and sustained the recent hiatus in Eurasian winter warming, *Geophysical Research Letters*, *44*(1), 374–382, doi:10.1002/2016GL072035.

Garfinkel, C. I., C. Schwartz, D. I. V. Domeisen, S.-W. Son, A. H. Butler, and I. P. White (2018), Extratropical atmospheric predictability from the quasi-biennial oscillation in subseasonal forecast models, *Journal of Geophysical Research: Atmospheres*, *123*(15), 7855–7866.

Gerber, E. P., L. M. Polvani, and D. Ancukiewicz (2008a), Annular mode time scales in the Intergovernmental Panel on Climate Change Fourth Assessment Report models, *Geophysical Research Letters*, *35*(22), doi:10.1029/2008GL035712.

Gerber, E. P., S. Voronin, and L. M. Polvani (2008b), Testing the Annular Mode Autocorrelation Time Scale in Simple Atmospheric General Circulation Models, *Monthly Weather Review*, *136*(4), 1523–1536, doi:10.1175/2007MWR2211.1.

Gerber, E. P., C. Orbe, and L. M. Polvani (2009), Stratospheric influence on the tropospheric circulation revealed by idealized ensemble forecasts, *Geophysical Research Letters*, *36*(24), doi:10.1029/2009GL040913.

Giorgetta, M. A., E. Manzini, E. Roeckner, M. Esch, and L. Bengtsson (2006), Climatology and Forcing of the Quasi-Biennial Oscillation in the MAECHAM5 Model, *Journal of Climate*, *19*(16), 3882–3901, doi:10.1175/JCLI3830.1.

Gray, L. J. (2003), The influence of the equatorial upper stratosphere on stratospheric sudden warmings, *Geophysical Research Letters*, *30*(4), doi:10.1029/2002GL016430.

Gray, L. J., S. J. Phipps, T. J. Dunkerton, M. P. Baldwin, E. F. Drysdale, and M. R. Allen (2001), A data study of the influence of the equatorial upper stratosphere on northern-hemisphere stratospheric sudden warmings, *Quarterly Journal of the Royal Meteorological Society*, *127*(576), 1985–2003, doi:10.1002/qj.49712757607.

Gray, L. J., S. Crooks, C. Pascoe, S. Sparrow, and M. Palmer (2004), Solar and QBO Influences on the Timing of Stratospheric Sudden Warmings, *Journal of the Atmospheric Sciences*, *61*(23), 2777–2796, doi:10.1175/JAS-3297.1.

Gray, L. J., T. J. Woollings, M. Andrews, and J. Knight (2016), Eleven-year solar cycle signal in the NAO and Atlantic/European blocking, *Quarterly Journal of the Royal Meteorological Society*, *142*(698), 1890–1903, doi:10.1002/qj.2782.

Gray, L. J., J. A. Anstey, Y. Kawatani, H. Lu, S. Osprey, and V. Schenzinger (2018), Surface impacts of the Quasi Biennial Oscillation, *Atmospheric Chemistry and Physics*, *18*(11), 8227–8247, doi:10.5194/acp-18-8227-2018.

Gray, L. J., M. J. Brown, J. Knight, M. Andrews, H. Lu, C. O'Reilly, and J. Anstey (2020), Forecasting extreme stratospheric polar vortex events, *Nature Communications*, *11*(1), 4630, doi:10.1038/s41467-020-18299-7.

Grinsted, A., J. C. Moore, and S. Jevrejeva (2004), Application of the cross wavelet transform and wavelet coherence to geophysical time series, *Nonlinear Processes in Geophysics*, *11*(5/6), 561–566, doi:10.5194/npg-11-561-2004.

Gruzdev, A. N., and V. A. Bezverkhny (2000), Two regimes of the quasi-biennial oscillation in the equatorial stratospheric wind, *Journal of Geophysical Research: Atmospheres*, *105*(D24), 29,435–29,443, doi:10.1029/2000JD900495.

Gu, K., H. K. T. Ng, M. L. Tang, and W. R. Schucany (2008), Testing the ratio of two poisson rates, *Biometrical Journal. Biometrische Zeitschrift*, *50*(2), 283–298, doi:10.1002/bimj.200710403.

Haase, S., K. Matthes, M. Latif, and N.-E. Omrani (2018), The Importance of a Properly Represented Stratosphere for Northern Hemisphere Surface Variability in the Atmosphere and the Ocean, *Journal of Climate*, *31*(20), 8481–8497, doi: 10.1175/JCLI-D-17-0520.1.

Halpert, M. S., and G. D. Bell (1997), Climate Assessment for 1996, *Bulletin of the American Meteorological Society*, *78*(5s), S1–S50, doi:10.1175/1520-0477-78.5s.S1.

Hamilton, K. (1998), Effects of an Imposed Quasi-Biennial Oscillation in a Comprehensive Troposphere–Stratosphere–Mesosphere General Circulation Model, *Journal of the Atmospheric Sciences*, *55*(14), 2393–2418, doi:10.1175/1520-0469(1998)055<2393:EOAIQB>2.0.CO;2.

Hamouda, M. E., C. Pasquero, and E. Tziperman (2021), Decoupling of the Arctic Oscillation and North Atlantic Oscillation in a warmer climate, *Nature Climate Change*, *11*(2), 137–142, doi:10.1038/s41558-020-00966-8.

Hegyi, B. M., and Y. Deng (2011), A dynamical fingerprint of tropical Pacific sea surface temperatures on the decadal-scale variability of cool-season Arctic precipitation, *Journal of Geophysical Research: Atmospheres*, *116*(D20), doi: 10.1029/2011JD016001.

Hersbach, H., B. Bell, P. Berrisford, S. Hirahara, A. Horányi, J. Muñoz-Sabater, J. Nicolas, C. Peubey, R. Radu, D. Schepers, A. Simmons, C. Soci, S. Abdalla, X. Abellan, G. Balsamo, P. Bechtold, G. Biavati, J. Bidlot, M. Bonavita, G. D. Chiara, P. Dahlgren, D. Dee, M. Diamantakis, R. Dragani, J. Flemming, R. Forbes, M. Fuentes, A. Geer, L. Haimberger, S. Healy, R. J. Hogan, E. Hólm, M. Janisková, S. Keeley, P. Laloyaux, P. Lopez, C. Lupu, G. Radnoti, P. de Rosnay, I. Rozum, F. Vamborg, S. Villaume, and J.-N. Thépaut (2020), The ERA5 global reanalysis, *Quarterly Journal of the Royal Meteorological Society*, *146*(730), 1999–2049, doi: 10.1002/qj.3803.

Hitchcock, P., and I. R. Simpson (2014), The Downward Influence of Stratospheric Sudden Warmings, *Journal of the Atmospheric Sciences*, *71*(10), 3856–3876, doi: 10.1175/JAS-D-14-0012.1.

Hitchman, M. H., and C. B. Leovy (1988), Estimation of the Kelvin Wave Contribution to the Semiannual oscillation, *Journal of the Atmospheric Sciences*, *45*(9), 1462–1475, doi:10.1175/1520-0469(1988)045<1462:EOTKWC>2.0.CO;2.

Holton, J. R., and H. C. Tan (1980), The influence of the equatorial quasi-biennial oscillation on the global circulation at 50 mb, *Journal of Atmospheric Sciences*, *37*(20), 2200–2208, doi:10.1175/1520-0469.

Holton, J. R., and H.-C. Tan (1982), The quasi-biennial oscillation in the northern hemisphere lower stratosphere, *Journal of the Meteorological Society of Japan*, *60*(1), 140–148, doi:10.2151/jmsj1965.60.1_140.

Holton, J. R., and W. M. Wehrbein (1980), A numerical model of the zonal mean circulation of the middle atmosphere, *pure and applied geophysics*, *118*(1), 284–306, doi:10.1007/BF01586455.

Horan, M. F., and T. Reichler (2017), Modeling seasonal sudden stratospheric warming climatology based on polar vortex statistics, *Journal of Climate*, *30*(24), 10,101–10,116.

Hu, D., and Z. Guan (2018), Decadal Relationship between the Stratospheric Arctic Vortex and Pacific Decadal Oscillation, *Journal of Climate*, *31*(9), 3371–3386, doi:10.1175/JCLI-D-17-0266.1.

Hu, Y., and K. K. Tung (2002), Tropospheric and equatorial influences on planetary-wave amplitude in the stratosphere, *Geophysical Research Letters*, *29*(2), 6–1–6–4, doi:10.1029/2001GL013762.

Huffman, M. D. (1984), An Improved Approximate Two-Sample Poisson Test, *Journal of the Royal Statistical Society. Series C (Applied Statistics)*, *33*(2), 224–226, doi:10.2307/2347448.

Hurrell, J., Y. Kushnir, G. Ottersen, and M. Visbeck (2003), *The North Atlantic Oscillation: Climatic Significance and Environmental Impact*, *Geophysical Monograph Series*, vol. 134, American Geophysical Union, doi:10.1029/GM134.

Ineson, S., and A. A. Scaife (2009), The role of the stratosphere in the European climate response to El Niño, *Nature Geoscience*, *2*(1), 32–36, doi:10.1038/ngeo381.

Iza, M., and N. Calvo (2015), Role of Stratospheric Sudden Warmings on the response to Central Pacific El Niño, *Geophysical Research Letters*, *42*(7), 2482–2489, doi:10.1002/2014GL062935.

Iza, M., N. Calvo, and E. Manzini (2016), The Stratospheric Pathway of La Niña, *Journal of Climate*, *29*(24), 8899–8914, doi:10.1175/JCLI-D-16-0230.1.

Johnson, N. C. (2013), How Many ENSO Flavors Can We Distinguish?, *Journal of Climate*, *26*(13), 4816–4827, doi:10.1175/JCLI-D-12-00649.1.

Kang, W., and E. Tziperman (2017), More frequent sudden stratospheric warming events due to enhanced MJO forcing expected in a warmer climate, *Journal of Climate*, *30*(21), 8727–8743, doi:10.1175/JCLI-D-17-0044.1.

Kao, H.-Y., and J.-Y. Yu (2009), Contrasting Eastern-Pacific and Central-Pacific Types of ENSO, *Journal of Climate*, *22*(3), 615–632, doi:10.1175/2008JCLI2309.1.

Kawatani, Y., K. Hamilton, and S. Watanabe (2011), The Quasi-Biennial Oscillation in a Double CO2 Climate, *Journal of the Atmospheric Sciences*, *68*(2), 265–283, doi:10.1175/2010JAS3623.1.

Kawatani, Y., K. Hamilton, K. Miyazaki, M. Fujiwara, and J. A. Anstey (2016), Representation of the tropical stratospheric zonal wind in global atmospheric reanalyses, *Atmospheric Chemistry and Physics*, *16*(11), 6681–6699, doi:10.5194/acp-16-6681-2016.

Kidston, J., A. Scaife, S. Hardiman, D. Mitchell, N. Butchart, M. Baldwin, and L. Gray (2015), Stratospheric influence on tropospheric jet streams, storm tracks and surface weather, *Nature Geoscience*, *8*, 433–440, doi:10.1038/ngeo2424.

Kim, H.-Y. (2018), Statistical notes for clinical researchers: Simple linear regression 2 – evaluation of regression line, *Restorative Dentistry & Endodontics*, *43*(3), e34, doi:10.5395/rde.2018.43.e34.

Kim, J., S. W. Son, E. P. Gerber, and H. S. Park (2017), Defining sudden stratospheric warming in climate models: Accounting for biases in model climatologies, *Journal of Climate*, doi:10.1175/JCLI-D-16-0465.1.

King, A. D., A. H. Butler, M. Jucker, N. O. Earl, and I. Rudeva (2019), Observed Relationships Between Sudden Stratospheric Warmings and European Climate Extremes, *Journal of Geophysical Research: Atmospheres*, *124*(24), 13,943–13,961, doi:10.1029/2019JD030480.

Kinnersley, J. S., and S. Pawson (1996), The Descent Rates of the Shear Zones of the Equatorial QBO, *Journal of the Atmospheric Sciences*, *53*(14), 1937–1949, doi:10.1175/1520-0469(1996)053<1937:TDROTS>2.0.CO;2.

Knight, J. R., R. J. Allan, C. K. Folland, M. Vellinga, and M. E. Mann (2005), A signature of persistent natural thermohaline circulation cycles in observed climate, *Geophysical Research Letters*, *32*(20), doi:10.1029/2005GL024233.

Kodera, K., K. Yamazaki, M. Chiba, and K. Shibata (1990), Downward propagation of upper stratospheric mean zonal wind perturbation to the troposphere, *Geophysical Research Letters*, *17*(9), 1263–1266, doi:10.1029/GL017i009p01263.

Kolstad, E. W., T. Breiteig, and A. A. Scaife (2010), The association between stratospheric weak polar vortex events and cold air outbreaks in the Northern Hemisphere, *Quarterly Journal of the Royal Meteorological Society*, *136*(649), 886–893, doi:10.1002/qj.620.

Kren, A. C., D. R. Marsh, A. K. Smith, and P. Pilewskie (2016), Wintertime Northern Hemisphere Response in the Stratosphere to the Pacific Decadal Oscillation Using the Whole Atmosphere Community Climate Model, *Journal of Climate*, *29*(3), 1031–1049, doi:10.1175/JCLI-D-15-0176.1.

Kretschmer, M., D. Coumou, J. F. Donges, and J. Runge (2016), Using causal effect networks to analyze different arctic drivers of midlatitude winter circulation, *Journal of Climate*, doi:10.1175/JCLI-D-15-0654.1.

Krzywinski, N., M & Altman (2015), Multiple linear regression, *Nature Methods*, *12*, 1103–1104.

Kuai, L., R. Shia, X. Jiang, K. Tung, and Y. Yung (2009), Nonstationary Synchronization of Equatorial QBO with SAO in Observations and a Model, *undefined*.

Kuhlbrodt, T., A. Griesel, M. Montoya, A. Levermann, M. Hofmann, and S. Rahmstorf (2007), On the driving processes of the Atlantic meridional overturning circulation, *Reviews of Geophysics*, *45*(2), doi:10.1029/2004RG000166.

Kuttippurath, J., and G. Nikulin (2012), A comparative study of the major sudden stratospheric warmings in the Arctic winters 2003/2004-2009/2010, *Atmospheric Chemistry & Physics*, *12*, 8115–8129, doi:10.5194/acp-12-8115-2012.

Latif, M., and N. S. Keenlyside (2011), A perspective on decadal climate variability and predictability, *Deep Sea Research Part II: Topical Studies in Oceanography*, *58*(17), 1880–1894, doi:10.1016/j.dsr2.2010.10.066.

Lau, K.-M., and H. Weng (1995), Climate Signal Detection Using Wavelet Transform: How to Make a Time Series Sing, *Bulletin of the American Meteorological Society*, *76*(12), 2391–2402, doi:10.1175/1520-0477(1995)076<2391:CSDUWT>2.0.CO;2.

Lavoie, D., N. Lambert, and D. Gilbert (2019), Projections of Future Trends in Biogeochemical Conditions in the Northwest Atlantic Using CMIP5 Earth System Models, *Atmosphere-Ocean*, *57*(1), 18–40, doi:10.1080/07055900.2017.1401973.

Lawrence, Z. D., J. Perlwitz, A. H. Butler, G. L. Manney, P. A. Newman, S. H. Lee, and E. R. Nash (2020), The Remarkably Strong Arctic Stratospheric Polar Vortex of Winter 2020: Links to Record-Breaking Arctic Oscillation and Ozone Loss, *Journal of Geophysical Research: Atmospheres*, *125*(22), e2020JD033,271, doi:10.1029/2020JD033271.

Lehtonen, I., and A. Y. Karpechko (2016), Observed and modeled tropospheric cold anomalies associated with sudden stratospheric warmings, *Journal of Geophysical Research: Atmospheres*, *121*(4), 1591–1610, doi:10.1002/2015JD023860.

Liess, S., and M. A. Geller (2012), On the relationship between QBO and distribution of tropical deep convection, *Journal of Geophysical Research: Atmospheres*, *117*(D3), doi:10.1029/2011JD016317.

Limpasuvan, V., and D. L. Hartmann (1999), Eddies and the annular modes of climate variability, *Geophysical Research Letters*, *26*(20), 3133–3136, doi:10.1029/1999GL010478.

Limpasuvan, V., D. W. J. Thompson, and D. L. Hartmann (2004), The Life Cycle of the Northern Hemisphere Sudden Stratospheric Warmings, *Journal of Climate*, *17*(13), 2584–2596, doi:10.1175/1520-0442(2004)017<2584:TLCOTN>2.0.CO;2.

Lindzen, R. S., and J. R. Holton (1968), A theory of the quasi-biennial oscillation, *Journal of Atmospheric Sciences*, *25*(6), 1095–1107, doi:10.1175/1520-0469(1968)025<1095:ATOTQB>2.0.CO;2.

Liu, W., S.-P. Xie, Z. Liu, and J. Zhu (2017), Overlooked possibility of a collapsed Atlantic Meridional Overturning Circulation in warming climate, *Science Advances*, *3*(1), e1601,666, doi:10.1126/sciadv.1601666.

Liu, W., A. Fedorov, and F. Sévellec (2019), The Mechanisms of the Atlantic Meridional Overturning Circulation Slowdown Induced by Arctic Sea Ice Decline, *Journal of Climate*, *32*(4), 977–996, doi:10.1175/JCLI-D-18-0231.1.

Liu, Y., X. San Liang, and R. H. Weisberg (2007), Rectification of the Bias in the Wavelet Power Spectrum, *Journal of Atmospheric and Oceanic Technology*, *24*(12), 2093–2102, doi:10.1175/2007JTECHO511.1.

Lohmann, K., H. Drange, and M. Bentsen (2009), Response of the North Atlantic subpolar gyre to persistent North Atlantic oscillation like forcing, *Climate Dynamics*, *32*(2), 273–285, doi:10.1007/s00382-008-0467-6.

Long, C. S., M. Fujiwara, S. Davis, D. M. Mitchell, and C. J. Wright (2017), Climatology and interannual variability of dynamic variables in multiple reanalyses evaluated by the SPARC Reanalysis Intercomparison Project (S-RIP), *Atmospheric Chemistry and Physics*, *17*(23), 14,593–14,629, doi:10.5194/acp-17-14593-2017.

Lu, H., M. P. Baldwin, L. J. Gray, and M. J. Jarvis (2008), Decadal-scale changes in the effect of the QBO on the northern stratospheric polar vortex, *Journal of Geophysical Research: Atmospheres*, *113*(D10), doi:10.1029/2007JD009647.

Lu, H., T. J. Bracegirdle, T. Phillips, A. Bushell, and L. Gray (2014), Mechanisms for the Holton-Tan relationship and its decadal variation, *Journal of Geophysical Research: Atmospheres*, *119*(6), 2811–2830, doi:10.1002/2013JD021352.

Manney, G. L., K. Krüger, J. L. Sabutis, S. A. Sena, and S. Pawson (2005), The remarkable 2003–2004 winter and other recent warm winters in the Arctic stratosphere since the late 1990s, *Journal of Geophysical Research: Atmospheres*, *110*(D4), doi:10.1029/2004JD005367.

Manney, G. L., M. J. Schwartz, K. Krüger, M. L. Santee, S. Pawson, J. N. Lee, W. H. Daffer, R. A. Fuller, and N. J. Livesey (2009), Aura Microwave Limb Sounder observations of dynamics and transport during the record-breaking 2009 Arctic stratospheric major warming, *Geophysical Research Letters*, *36*(12), doi:10.1029/2009GL038586.

Mantua, N. J., S. R. Hare, Y. Zhang, J. M. Wallace, and R. C. Francis (1997), A Pacific Interdecadal Climate Oscillation with Impacts on Salmon Production*, *Bulletin of the American Meteorological Society*, *78*(6), 1069–1080, doi:10.1175/1520-0477(1997)078<1069:APICOW>2.0.CO;2.

Manzini, E., M. A. Giorgetta, M. Esch, L. Kornblueh, and E. Roeckner (2006), The Influence of Sea Surface Temperatures on the Northern Winter Stratosphere: Ensemble Simulations with the MAECHAM5 Model, *Journal of Climate*, *19*(16), 3863–3881, doi:10.1175/JCLI3826.1.

Manzini, E., C. Cagnazzo, P. G. Fogli, A. Bellucci, and W. A. Müller (2012), Stratosphere-troposphere coupling at inter-decadal time scales: Implications for the North Atlantic Ocean, *Geophysical Research Letters*, *39*(5), doi:10.1029/2011GL050771.

Matsuno, T. (1971), A Dynamical Model of the Stratospheric Sudden Warming, *Journal of the Atmospheric Sciences*, *28*(8), 1479–1494, doi:10.1175/1520-0469(1971)028<1479:ADMOTS>2.0.CO;2.

Maycock, A. C., and P. Hitchcock (2015), Do split and displacement sudden stratospheric warmings have different annular mode signatures?, *Geophysical Research Letters*, *42*(24), 10,943–10,951, doi:10.1002/2015GL066754.

Maycock, A. C., G. I. T. Masukwedza, P. Hitchcock, and I. R. Simpson (2020), A Regime Perspective on the North Atlantic Eddy-Driven Jet Response to Sudden Stratospheric Warmings, *Journal of Climate*, *33*(9), 3901–3917, doi:10.1175/JCLI-D-19-0702.1.

McCarthy, G., E. Frajka-Williams, W. E. Johns, M. O. Baringer, C. S. Meinen, H. L. Bryden, D. Rayner, A. Duchez, C. Roberts, and S. A. Cunningham (2012), Observed interannual variability of the Atlantic meridional overturning circulation at 26.5°N, *Geophysical Research Letters*, *39*(19), doi:10.1029/2012GL052933.

McCarthy, G. D., I. D. Haigh, J. J.-M. Hirschi, J. P. Grist, and D. A. Smeed (2015a), Ocean impact on decadal Atlantic climate variability revealed by sea-level observations, *Nature*, *521*(7553), 508–510, doi:10.1038/nature14491.

McCarthy, G. D., D. A. Smeed, W. E. Johns, E. Frajka-Williams, B. I. Moat, D. Rayner, M. O. Baringer, C. S. Meinen, J. Collins, and H. L. Bryden (2015b), Measuring the Atlantic Meridional Overturning Circulation at 26°N, *Progress in Oceanography*, *130*, 91–111, doi:10.1016/j.pocean.2014.10.006.

McIntyre, M. E., and T. N. Palmer (1983), Breaking planetary waves in the stratosphere, *Nature*, *305*(5935), 593–600, doi:10.1038/305593a0.

Medhaug, I., H. R. Langehaug, T. Eldevik, T. Furevik, and M. Bentsen (2012), Mechanisms for decadal scale variability in a simulated Atlantic meridional overturning circulation, *Climate Dynamics*, *39*(1), 77–93, doi:10.1007/s00382-011-1124-z.

Menary, M. B., W. Park, K. Lohmann, M. Vellinga, M. D. Palmer, M. Latif, and J. H. Jungclaus (2012), A multimodel comparison of centennial Atlantic meridional overturning circulation variability, *Climate Dynamics*, *38*(11), 2377–2388, doi: 10.1007/s00382-011-1172-4.

Menary, M. B., T. Kuhlbrodt, J. Ridley, M. B. Andrews, O. B. Dimdore-Miles, J. Deshayes, R. Eade, L. Gray, S. Ineson, J. Mignot, C. D. Roberts, J. Robson, R. A. Wood, and P. Xavier (2018), Preindustrial Control Simulations With HadGEM3-GC3.1 for CMIP6, *Journal of Advances in Modeling Earth Systems*, *10*(12), 3049–3075, doi:10.1029/2018MS001495.

Mielke, C., E. Frajka-Williams, and J. Baehr (2013), Observed and simulated variability of the AMOC at 26°N and 41°N, *Geophysical Research Letters*, *40*(6), 1159–1164, doi:10.1002/grl.50233.

Minobe, S. (1999), Resonance in bidecadal and pentadecadal climate oscillations over the North Pacific: Role in climatic regime shifts, *Geophysical Research Letters*, *26*(7), 855–858, doi:10.1029/1999GL900119.

Mitchell, D. M., L. J. Gray, and A. J. Charlton-Perez (2011a), The structure and evolution of the stratospheric vortex in response to natural forcings, *Journal of Geophysical Research Atmospheres*, doi:10.1029/2011JD015788.

Mitchell, D. M., A. J. Charlton-Perez, and L. J. Gray (2011b), Characterizing the variability and extremes of the stratospheric polar vortices using 2D moment analysis, *Journal of the Atmospheric Sciences*, *68*(6), 1194–1213, doi:10.1175/2010JAS3555.1.

Moat, B. I., E. Frajka-Williams, D. Smeed, D. Rayner, A. Sanchez-Franks, W. E. Johns, M. O. Baringer, D. L. Volkov, and J. Collins (2020), Atlantic meridional overturning circulation observed by the RAPID-MOCHA-WBTS (RAPID-Meridional Overturning Circulation and Heatflux Array-Western Boundary Time Series) array at 26N from 2004 to 2018 (v2018.2)., doi:10.5285/AA57E879-4CCA-28B6-E053-6C86ABC02DE5.

Mulcahy, J. P., C. Jones, A. Sellar, B. Johnson, I. A. Boutle, A. Jones, T. Andrews, S. T. Rumbold, J. Mollard, N. Bellouin, C. E. Johnson, K. D. Williams, D. P. Grosvenor, and D. T. McCoy (2018), Improved Aerosol Processes and Effective Radiative Forcing in HadGEM3 and UKESM1, *Journal of Advances in Modeling Earth Systems*, *10*(11), 2786–2805, doi:10.1029/2018MS001464.

Nakagawa, K. I., and K. Yamazaki (2006), What kind of stratospheric sudden warming propagates to the troposphere?, *Geophysical Research Letters*, *33*(4), 3–6, doi: 10.1029/2005GL024784.

Newman, M., M. A. Alexander, T. R. Ault, K. M. Cobb, C. Deser, E. D. Lorenzo, N. J. Mantua, A. J. Miller, S. Minobe, H. Nakamura, N. Schneider, D. J. Vimont, A. S. Phillips, J. D. Scott, and C. A. Smith (2016), The Pacific Decadal Oscillation, Revisited, *Journal of Climate*, *29*(12), 4399–4427, doi:10.1175/JCLI-D-15-0508.1.

Nigam, S. (1990), On the Structure of Variability of the Observed Tropospheric and Stratospheric Zonal-Mean Zonal Wind, *Journal of the Atmospheric Sciences*, *47*(14), 1799–1813, doi:10.1175/1520-0469(1990)047<1799:OTSOVO>2.0.CO;2.

Nishii, K., H. Nakamura, and T. Miyasaka (2009), Modulations in the planetary wave field induced by upward-propagating Rossby wave packets prior to stratospheric sudden warming events: A case-study, *Quarterly Journal of the Royal Meteorological Society*, *135*(638), 39–52, doi:10.1002/qj.359.

O'Connor, F. M., N. L. Abraham, M. Dalvi, G. A. Folberth, P. T. Griffiths, C. Hardacre, B. T. Johnson, R. Kahana, J. Keeble, B. Kim, O. Morgenstern, J. P. Mulcahy, M. Richardson, E. Robertson, J. Seo, S. Shim, J. C. Teixeira, S. T. Turnock, J. Williams, A. J. Wiltshire, S. Woodward, and G. Zeng (2021), Assessment of pre-industrial to present-day anthropogenic climate forcing in UKESM1, *Atmospheric Chemistry and Physics*, *21*(2), 1211–1243, doi:10.5194/acp-21-1211-2021.

Orr, A., P. Bechtold, J. Scinocca, M. Ern, and M. Janiskova (2010), Improved Middle Atmosphere Climate and Forecasts in the ECMWF Model through a Nonorographic Gravity Wave Drag Parameterization, *Journal of Climate*, *23*(22), 5905–5926, doi:10.1175/2010JCLI3490.1.

Osprey, S. M., L. J. Gray, S. C. Hardiman, N. Butchart, A. C. Bushell, and T. J. Hinton (2010), The Climatology of the Middle Atmosphere in a Vertically Extended Version of the Met Office's Climate Model. Part II: Variability, *Journal of the Atmospheric Sciences*, *67*(11), 3637–3651, doi:10.1175/2010JAS3338.1.

Osprey, S. M., L. J. Gray, S. C. Hardiman, N. Butchart, A. C. Bushell, and T. J. Hinton (2019), Stratospheric role in interdecadal changes of El Niño impacts over Europe, *Clim Dyn*, *52*, 1173—1186.

Overland, J., J. Adams, and N. Bond (1999), Decadal Variability of the Aleutian Low and Its Relation to High-Latitude Circulation, *Journal of Climate - J CLIMATE*, *12*, 1542–1548, doi:10.1175/1520-0442(1999)012<1542:DVOTAL>2.0.CO;2.

Overland, J. E., D. B. Percival, and H. O. Mofjeld (2006), Regime shifts and red noise in the North Pacific, *Deep Sea Research Part I: Oceanographic Research Papers*, *53*(4), 582–588, doi:10.1016/j.dsr.2005.12.011.

Pascoe, C. L., L. J. Gray, S. A. Crooks, M. N. Juckes, and M. P. Baldwin (2005), The quasi-biennial oscillation: Analysis using ERA-40 data, *Journal of Geophysical Research: Atmospheres*, *110*(D8), doi:10.1029/2004JD004941.

Pawson, S., and B. Naujokat (1999), The cold winters of the middle 1990s in the northern lower stratosphere, *Journal of Geophysical Research: Atmospheres*, *104*(D12), 14,209–14,222, doi:10.1029/1999JD900211.

Pawson, S., K. Kodera, K. Hamilton, T. Shepherd, S. Beagley, B. Boville, J. Farrara, T. Fairlie, A. Kitoh, W. Lahoz, U. Langematz, E. Manzini, D. Rind, A. Scaife, S. Kiyotaka, P. Simon, R. Swinbank, L. Takacs, R. Wilson, and F. Wu (2000), The GCM–reality intercomparison project for SPARC (GRIPS): Scientific issues and initial results, *Bulletin of the American Meteorological Society*, *81*, 781–796, doi:10.1175/1520-0477(2000)081<0781:TGIPFS>2.3.CO;2.

Plumb, R. (1984), The quasi-biennial oscillation, in *Dynamics of the Middle Atmosphere*, pp. 217–251, Tokyo.

Polvani, L. M., L. Sun, A. H. Butler, J. H. Richter, and C. Deser (2017), Distinguishing Stratospheric Sudden Warmings from ENSO as Key Drivers of Wintertime Climate Variability over the North Atlantic and Eurasia, *Journal of Climate*, *30*(6), 1959–1969, doi:10.1175/JCLI-D-16-0277.1.

Raible, C., T. Stocker, M. Yoshimori, M. Renold, U. Beyerle, C. Casty, and J. Luterbacher (2005), Northern hemispheric trends of pressure indices and atmospheric circulation patterns in observations, reconstructions, and coupled GCM simulations, *Journal of Climate*, *18*, doi:10.1175/JCLI3511.1.

Rajendran, K., I. M. Moroz, P. L. Read, and S. M. Osprey (2016), Synchronisation of the equatorial QBO by the annual cycle in tropical upwelling in a warming climate, *Quarterly Journal of the Royal Meteorological Society*, *142*(695), 1111–1120, doi:10.1002/qj.2714.

Rao, J., and R. Ren (2016), A decomposition of ENSO's impacts on the northern winter stratosphere: Competing effect of SST forcing in the tropical Indian Ocean, *Climate Dynamics*, *46*(11), 3689–3707, doi:10.1007/s00382-015-2797-5.

Rao, J., and R. Ren (2018), Varying stratospheric responses to tropical Atlantic SST forcing from early to late winter, *Climate Dynamics*, *51*(5), 2079–2096, doi:10.1007/s00382-017-3998-x.

Rao, J., C. I. Garfinkel, and R. Ren (2019), Modulation of the Northern Winter Stratospheric El Niño–Southern Oscillation Teleconnection by the PDO, *Journal of Climate*, *32*(18), 5761–5783, doi:10.1175/JCLI-D-19-0087.1.

Ray, E. A., M. J. Alexander, and J. R. Holton (1998), An analysis of the structure and forcing of the equatorial semiannual oscillation in zonal wind, *Journal of Geophysical Research: Atmospheres*, *103*(D2), 1759–1774, doi:10.1029/97JD02679.

Reed, R. J. (1965), The Quasi-Biennial Oscillation of the Atmosphere Between 30 and 50 km Over Ascension Island, *Journal of the Atmospheric Sciences*, *22*(3), 331–333, doi:10.1175/1520-0469(1965)022<0331:TQBOOT>2.0.CO;2.

Reichler, T., J. Kim, E. Manzini, and J. Kröger (2012), A stratospheric connection to Atlantic climate variability, *Nature Geoscience*, *5*(11), 783–787, doi:10.1038/ngeo1586.

Richter, J. H., C. Deser, and L. Sun (2015), Effects of stratospheric variability on El Niño teleconnections, *Environmental Research Letters*, *10*(12), 124,021, doi:10.1088/1748-9326/10/12/124021.

Ridley, J. K., E. W. Blockley, A. B. Keen, J. G. L. Rae, A. E. West, and D. Schroeder (2018), The sea ice model component of HadGEM3-GC3.1, *Geoscientific Model Development*, *11*(2), 713–723, doi:10.5194/gmd-11-713-2018.

Roberts, C. D., L. Jackson, and D. McNeall (2014), Is the 2004–2012 reduction of the Atlantic meridional overturning circulation significant?, *Geophysical Research Letters*, *41*(9), 3204–3210, doi:10.1002/2014GL059473.

Robson, J., R. Sutton, K. Lohmann, D. Smith, and M. D. Palmer (2012), Causes of the Rapid Warming of the North Atlantic Ocean in the Mid-1990s, *Journal of Climate*, *25*(12), 4116–4134, doi:10.1175/JCLI-D-11-00443.1.

Robson, J., Y. Aksenov, T. J. Bracegirdle, O. Dimdore-Miles, P. T. Griffiths, D. P. Grosvenor, D. L. R. Hodson, J. Keeble, C. MacIntosh, A. Megann, S. Osprey, A. C. Povey, D. Schröder, M. Yang, A. T. Archibald, K. S. Carslaw, L. Gray, C. Jones, B. Kerridge, D. Knappett, T. Kuhlbrodt, M. Russo, A. Sellar, R. Siddans, B. Sinha, R. Sutton, J. Walton, and L. J. Wilcox (2020), The Evaluation of the North Atlantic Climate System in UKESM1 Historical Simulations for CMIP6, *Journal of Advances in Modeling Earth Systems*, *12*(9), e2020MS002,126, doi:10.1029/2020MS002126.

Rodionov, S. N., J. E. Overland, and N. A. Bond (2005), Spatial and temporal variability of the Aleutian climate, *Fisheries Oceanography*, *14*(s1), 3–21, doi:10.1111/j.1365-2419.2005.00363.x.

Runge, J., V. Petoukhov, and J. Kurths (2014), Quantifying the Strength and Delay of Climatic Interactions: The Ambiguities of Cross Correlation and a Novel Measure Based on Graphical Models, *Journal of Climate*, *27*(2), 720–739, doi:10.1175/JCLI-D-13-00159.1.

Santoso, A., M. J. Mcphaden, and W. Cai (2017), The Defining Characteristics of ENSO Extremes and the Strong 2015/2016 El Niño, *Reviews of Geophysics*, *55*(4), 1079–1129, doi:10.1002/2017RG000560.

Scaife, A. A., and D. Smith (2018), A signal-to-noise paradox in climate science, *npj Climate and Atmospheric Science*, *1*(1), 1–8, doi:10.1038/s41612-018-0038-4.

Scaife, A. A., A. Y. Karpechko, M. P. Baldwin, A. Brookshaw, A. H. Butler, R. Eade, M. Gordon, C. MacLachlan, N. Martin, N. Dunstone, and D. Smith (2016), Seasonal winter forecasts and the stratosphere, *Atmospheric Science Letters*, *17*(1), 51–56, doi:10.1002/asl.598.

Scaife, A. A., R. E. Comer, N. J. Dunstone, J. R. Knight, D. M. Smith, C. MacLachlan, N. Martin, K. A. Peterson, D. Rowlands, E. B. Carroll, S. Belcher, and J. Slingo (2017), Tropical rainfall, Rossby waves and regional winter climate predictions, *Quarterly Journal of the Royal Meteorological Society*, *143*(702), 1–11, doi:10.1002/qj.2910.

Schenzinger, V. (2016), Tropical stratosphere variability and extratropical teleconnections, Ph.D. thesis, University of Oxford / University of Oxford.

Schenzinger, V., S. Osprey, L. Gray, and N. Butchart (2017), Defining metrics of the Quasi-Biennial Oscillation in global climate models, *Geoscientific Model Development*, *10*(6), 2157–2168, doi:10.5194/gmd-10-2157-2017.

Scherhag, R. (1952), Die explosionsartigen Stratosparenerwarmungen des Spatwinters, *38*, 51–63.

Schimanke, S., J. Zittel, T. Spangehl, and U. Cubasch (2011), Multi-decadal variability of sudden stratospheric warmings in an AOGCM, *Geophysical Research Letters - GEOPHYS RES LETT*, *38*(1), doi:10.1029/2010GL045756.

Schmidt, H., S. Rast, F. Bunzel, M. Esch, M. Giorgetta, S. Kinne, T. Krismer, G. Stenchikov, C. Timmreck, L. Tomassini, and M. Walz (2013), Response of the middle atmosphere to anthropogenic and natural forcings in the CMIP5 simulations with the Max Planck Institute Earth system model, *Journal of Advances in Modeling Earth Systems*, doi:10.1002/jame.20014.

Scott, R. K., and L. M. Polvani (2006), Internal Variability of the Winter Stratosphere. Part I: Time-Independent Forcing, *Journal of the Atmospheric Sciences*, *63*(11), 2758–2776, doi:10.1175/JAS3797.1.

Seviour, W. J., L. J. Gray, and D. M. Mitchell (2016), Stratospheric polar vortex splits and displacements in the high-top CMIP5 climate models, *Journal of Geophysical Research*, doi:10.1002/2015JD024178.

Seviour, W. J. M. (2017), Weakening and shift of the Arctic stratospheric polar vortex: Internal variability or forced response?, *Geophysical Research Letters*, *44*(7), 3365–3373, doi:10.1002/2017GL073071.

Seviour, W. J. M., D. M. Mitchell, and L. J. Gray (2013), A practical method to identify displaced and split stratospheric polar vortex events, *Geophysical Research Letters*, *40*(19), 5268–5273, doi:10.1002/grl.50927.

Shaw, T. A., and J. Perlwitz (2013), The Life Cycle of Northern Hemisphere Downward Wave Coupling between the Stratosphere and Troposphere, *Journal of Climate*, *26*(5), 1745–1763, doi:10.1175/JCLI-D-12-00251.1.

Shindell, D. T., R. L. Miller, G. A. Schmidt, and L. Pandolfo (1999), Simulation of recent northern winter climate trends by greenhouse-gas forcing, *Nature*, *399*, 452–455, doi:10.1038/20905.

Simmons, A. J., P. Poli, D. P. Dee, P. Berrisford, H. Hersbach, S. Kobayashi, and C. Peubey (2014), Estimating low-frequency variability and trends in atmospheric temperature using ERA-Interim, *Quarterly Journal of the Royal Meteorological Society*, *140*(679), 329–353, doi:10.1002/qj.2317.

Smeed, D., B. I. Moat, D. Rayner, W. E. Johns, M. O. Baringer, D. L. Volkov, and E. Frajka-Williams (2019), Atlantic meridional overturning circulation observed by the RAPID-MOCHA-WBTS (RAPID-Meridional Overturning Circulation and Heatflux Array-Western Boundary Time Series) array at 26N from 2004 to 2018., doi:10.5285/8CD7E7BB-9A20-05D8-E053-6C86ABC012C2.

Smeed, D. A., S. A. Josey, C. Beaulieu, W. E. Johns, B. I. Moat, E. Frajka-Williams, D. Rayner, C. S. Meinen, M. O. Baringer, H. L. Bryden, and G. D. McCarthy (2018), The North Atlantic Ocean Is in a State of Reduced Overturning, *Geophysical Research Letters*, *45*(3), 1527–1533, doi:10.1002/2017GL076350.

Smith, A. K., L. A. Holt, R. R. Garcia, J. A. Anstey, F. Serva, N. Butchart, S. Osprey, A. C. Bushell, Y. Kawatani, Y.-H. Kim, F. Lott, P. Braesicke, C. Cagnazzo, C.-C. Chen, H.-Y. Chun, L. Gray, T. Kerzenmacher, H. Naoe, J. Richter, S. Versick, V. Schenzinger, S. Watanabe, and K. Yoshida (2019), The equatorial stratospheric semiannual oscillation and time-mean winds in QBOi models, *Quarterly Journal of the Royal Meteorological Society*, *1*(special section QBO modelling Intercomparison), 1–17, doi:10.1002/qj.3690.

Smith, K. L., and P. J. Kushner (2012), Linear interference and the initiation of extratropical stratosphere-troposphere interactions, *Journal of Geophysical Research: Atmospheres*, *117*(D13), doi:10.1029/2012JD017587.

Song, K., and S.-W. Son (2018), Revisiting the ENSO–SSW Relationship, *Journal of Climate*, *31*(6), 2133–2143, doi:10.1175/JCLI-D-17-0078.1.

Stenchikov, G., K. Hamilton, A. Robock, V. Ramaswamy, and M. D. Schwarzkopf (2004), Arctic oscillation response to the 1991 Pinatubo eruption in the SKYHI general circulation model with a realistic quasi-biennial oscillation, *Journal of Geophysical Research: Atmospheres*, *109*(D3), doi:10.1029/2003JD003699.

Storkey, D., A. Blaker, P. Mathiot, A. Megann, Y. Aksenov, E. W. Blockley, D. Calvert, T. Graham, H. Hewitt, P. Hyder, T. Kuhlbrodt, J. G. L. Rae, and B. Sinha (2018), UK global ocean GO6 and GO7: A traceable hierarchy of model resolutions, *Geoscientific Model Development Discussions*, pp. 1–43, doi:10.5194/gmd-2017-263.

Strong, C., and G. Magnusdottir (2009), The Role of Tropospheric Rossby Wave Breaking in the Pacific Decadal Oscillation, *Journal of Climate*, *22*(7), 1819–1833, doi:10.1175/2008JCLI2593.1.

Sugimoto, S., and K. Hanawa (2009), Decadal and interdecadal variations of the aleutian low activity and their relation to upper oceanic variations over the north pacific, *Journal of the Meteorological Society of Japan. Ser. II*, *87*(4), 601–614, doi:10.2151/jmsj.87.601.

Sung, M.-K., B.-M. Kim, and S.-I. An (2014), Altered atmospheric responses to eastern Pacific and central Pacific El Niños over the North Atlantic region due to stratospheric interference, *Climate Dynamics*, *42*(1), 159–170, doi:10.1007/s00382-012-1661-0.

Sutton, R. T., and D. L. R. Hodson (2005), Atlantic Ocean Forcing of North American and European Summer Climate, *Science*, *309*(5731), 115–118, doi:10.1126/science.1109496.

Taguchi, M. (2008), Is There a Statistical Connection between Stratospheric Sudden Warming and Tropospheric Blocking Events?, *Journal of the Atmospheric Sciences*, *65*(4), 1442–1454, doi:10.1175/2007JAS2363.1.

Takahashi, M. (1996), Simulation of the stratospheric Quasi-Biennial Oscillation using a general circulation model, *Geophysical Research Letters*, *23*, 661–664, doi:10.1029/95GL03413.

Telford, P. J., P. Braesicke, O. Morgenstern, and J. A. Pyle (2008), Technical Note: Description and assessment of a nudged version of the new dynamics Unified Model, *Atmospheric Chemistry and Physics*, *8*(6), 1701–1712, doi:10.5194/acp-8-1701-2008.

Thompson, D. W. J., and J. M. Wallace (1998), The Arctic oscillation signature in the wintertime geopotential height and temperature fields, *Geophysical Research Letters*, *25*(9), 1297–1300, doi:10.1029/98GL00950.

Thompson, D. W. J., and J. M. Wallace (2000), Annular Modes in the Extratropical Circulation. Part I: Month-to-Month Variability, *Journal of Climate*, *13*(5), 1000–1016, doi:10.1175/1520-0442(2000)013<1000:AMITEC>2.0.CO;2.

Thompson, D. W. J., M. P. Baldwin, and J. M. Wallace (2002), Stratospheric Connection to Northern Hemisphere Wintertime Weather: Implications for Prediction, *Journal of Climate*, *15*(12), 1421–1428, doi:10.1175/1520-0442(2002)015<1421:SCTNHW>2.0.CO;2.

Timmermann, A., S.-I. An, U. Krebs, and H. Goosse (2005), ENSO Suppression due to Weakening of the North Atlantic Thermohaline Circulation, *Journal of Climate*, *18*(16), 3122–3139, doi:10.1175/JCLI3495.1.

Tomassini, L., E. P. Gerber, M. P. Baldwin, F. Bunzel, and M. Giorgetta (2012), The role of stratosphere-troposphere coupling in the occurrence of extreme winter cold spells over northern Europe, *Journal of Advances in Modeling Earth Systems*, *4*(4), doi:10.1029/2012MS000177.

Torrence, C., and G. P. Compo (1998), A practical guide to wavelet analysis, *Bulletin of the American Meteorological Society*, *79*(12), 61–78, doi:10.1175/1520-0477.

Trenberth, K., and J. Hurrell (1994), Decadal atmosphere-ocean variations in the pacific, *Climate Dynamics*, *9*, 303–319, doi:10.1007/BF00204745.

Trenberth, K. E., and D. P. Stepaniak (2001), Indices of El Niño Evolution, *Journal of Climate*, *14*(8), 1697–1701, doi:10.1175/1520-0442(2001)014<1697:LIOENO>2.0.CO;2.

Tsuyoshi, N., and Y. Shingo (1989), Recent warming of tropical sea surface temperature and its relationship to the northern hemisphere circulation, *Journal of the Meteorological Society of Japan*, *67:3*, doi:10.2151/jmsj1965.67.3_375.

Tulloch, R., and J. Marshall (2012), Exploring Mechanisms of Variability and Predictability of Atlantic Meridional Overturning Circulation in Two Coupled Climate Models, *Journal of Climate*, *25*(12), 4067–4080, doi:10.1175/JCLI-D-11-00460.1.

Uppala, S. M., P. W. KÅllberg, A. J. Simmons, U. Andrae, V. D. C. Bechtold, M. Fiorino, J. K. Gibson, J. Haseler, A. Hernandez, G. A. Kelly, X. Li, K. Onogi, S. Saarinen, N. Sokka, R. P. Allan, E. Andersson, K. Arpe, M. A. Balmaseda, A. C. M. Beljaars, L. V. D. Berg, J. Bidlot, N. Bormann, S. Caires, F. Chevallier, A. Dethof, M. Dragosavac, M. Fisher, M. Fuentes, S. Hagemann, E. Hólm, B. J. Hoskins, L. Isaksen, P. A. E. M. Janssen, R. Jenne, A. P. Mcnally, J.-F. Mahfouf, J.-J. Morcrette, N. A. Rayner, R. W. Saunders, P. Simon, A. Sterl, K. E. Trenberth, A. Untch, D. Vasiljevic, P. Viterbo, and J. Woollen (2005), The ERA-40 re-analysis, *Quarterly Journal of the Royal Meteorological Society*, *131*(612), 2961–3012, doi:10.1256/qj.04.176.

Vial, J., T. Osborn, and F. Lott (2013), Sudden Stratospheric Warmings and tropospheric blockings in a multi-century simulation of the IPSL-CM5A coupled climate model, *Climate Dynamics*, *40*, doi:10.1007/s00382-013-1675-2.

Vimont, D. J. (2005), The Contribution of the Interannual ENSO Cycle to the Spatial Pattern of Decadal ENSO-Like Variability, *Journal of Climate*, *18*(12), 2080–2092, doi:10.1175/JCLI3365.1.

Visbeck, M., H. Cullen, G. Krahmann, and N. Naik (1998), An ocean model's response to North Atlantic Oscillation-like wind forcing, *Geophysical Research Letters*, *25*(24), 4521–4524, doi:10.1029/1998GL900162.

Wallace, J. M., R. L. Panetta, and J. Estberg (1993), Representation of the Equatorial Stratospheric Quasi-Biennial Oscillation in EOF Phase Space, *Journal of the Atmospheric Sciences*, *50*(12), 1751–1762, doi:10.1175/1520-0469(1993)050<1751:ROTESQ>2.0.CO;2.

Walters, D., A. J. Baran, I. Boutle, M. Brooks, P. Earnshaw, J. Edwards, K. Furtado, P. Hill, A. Lock, J. Manners, C. Morcrette, J. Mulcahy, C. Sanchez, C. Smith, R. Stratton, W. Tennant, L. Tomassini, K. Van Weverberg, S. Vosper, M. Willett, J. Browse, A. Bushell, K. Carslaw, M. Dalvi, R. Essery, N. Gedney, S. Hardiman, B. Johnson, C. Johnson, A. Jones, C. Jones, G. Mann, S. Milton, H. Rumbold, A. Sellar, M. Ujiie, M. Whitall, K. Williams, and M. Zerroukat (2019), The Met Office Unified Model Global Atmosphere 7.0/7.1 and JULES Global Land 7.0 configurations, *Geoscientific Model Development*, *12*(5), 1909–1963, doi:10.5194/gmd-12-1909-2019.

Wang, Z., Y. Lu, F. Dupont, J. W. Loder, C. Hannah, and D. G. Wright (2015), Variability of sea surface height and circulation in the North Atlantic: Forcing mechanisms and linkages, *Progress in Oceanography*, *132*, 273–286, doi:10.1016/j.pocean.2013.11.004.

Wang, Z., D. Brickman, and B. J. W. Greenan (2019), Characteristic evolution of the Atlantic Meridional Overturning Circulation from 1990 to 2015: An eddy-resolving ocean model study, *Deep Sea Research Part I: Oceanographic Research Papers*, *149*, 103,056, doi:10.1016/j.dsr.2019.06.002.

Watson, P. A., and L. J. Gray (2014), How does the quasi-biennial oscillation affect the stratospheric polar vortex?, *Journal of the Atmospheric Sciences*, *71*(1), 391–409, doi:10.1175/JAS-D-13-096.1.

White, I., C. I. Garfinkel, E. P. Gerber, M. Jucker, V. Aquila, and L. D. Oman (2019), The downward influence of sudden stratospheric warmings: Association with tropospheric precursors, *Journal of Climate*, *32*(1), 85–108, doi:10.1175/JCLI-D-18-0053.1.

White, I. P., C. I. Garfinkel, E. P. Gerber, M. Jucker, P. Hitchcock, and J. Rao (2020), The Generic Nature of the Tropospheric Response to Sudden Stratospheric Warmings, *Journal of Climate*, *33*(13), 5589–5610, doi:10.1175/JCLI-D-19-0697.1.

Williams, K. D., D. Copsey, E. W. Blockley, A. Bodas-Salcedo, D. Calvert, R. Comer, P. Davis, T. Graham, H. T. Hewitt, R. Hill, P. Hyder, S. Ineson, T. C. Johns, A. B. Keen, R. W. Lee, A. Megann, S. F. Milton, J. G. L. Rae, M. J. Roberts, A. A. Scaife, R. Schiemann, D. Storkey, L. Thorpe, I. G. Watterson, D. N. Walters, A. West, R. A. Wood, T. Woollings, and P. K. Xavier (2018), The Met Office Global Coupled Model 3.0 and 3.1 (GC3.0 and GC3.1) Configurations, *Journal of Advances in Modeling Earth Systems*, *10*(2), 357–380, doi:10.1002/2017MS001115.

Woo, S.-H., M.-K. Sung, S.-W. Son, and J.-S. Kug (2015), Connection between weak stratospheric vortex events and the Pacific Decadal Oscillation, *Climate Dynamics*, *45*(11), 3481–3492, doi:10.1007/s00382-015-2551-z.

Xu, X., E. P. Chassignet, W. E. Johns, W. J. Schmitz, and E. J. Metzger (2014), Intraseasonal to interannual variability of the Atlantic meridional overturning circulation from eddy-resolving simulations and observations, *Journal of Geophysical Research: Oceans*, *119*(8), 5140–5159, doi:10.1002/2014JC009994.

Yang, J. (2015), Local and remote wind stress forcing of the seasonal variability of the Atlantic Meridional Overturning Circulation (AMOC) transport at 26.5°N, *Journal of Geophysical Research: Oceans*, *120*(4), 2488–2503, doi:10.1002/2014JC010317.

Yang, M., and Y. Yu (2016), Attribution of variations in the quasi-biennial oscillation period from the duration of easterly and westerly phases, *Climate Dynamics*, *47*, 1943–1959, doi:10.1007/s00382-015-2943-0.

Yool, A., E. E. Popova, and T. R. Anderson (2013), MEDUSA-2.0: An intermediate complexity biogeochemical model of the marine carbon cycle for climate change and ocean acidification studies, *Geoscientific Model Development*, doi:10.5194/gmd-6-1767-2013.

Yool, A., J. Palmiéri, C. G. Jones, A. A. Sellar, L. de Mora, T. Kuhlbrodt, E. E. Popova, J. P. Mulcahy, A. Wiltshire, S. T. Rumbold, M. Stringer, R. S. R. Hill, Y. Tang, J. Walton, A. Blaker, A. J. G. Nurser, A. C. Coward, J. Hirschi, S. Woodward, D. I. Kelley, R. Ellis, and S. Rumbold-Jones (2020), Spin-up of UK Earth System Model 1 (UKESM1) for CMIP6, *Journal of Advances in Modeling Earth Systems*, *12*(8), e2019MS001,933, doi:10.1029/2019MS001933.

Zhang, R. (2010), Latitudinal dependence of Atlantic meridional overturning circulation (AMOC) variations, *Geophysical Research Letters*, *37*(16), doi:10.1029/2010GL044474.

Zhang, R., R. Sutton, G. Danabasoglu, Y.-O. Kwon, R. Marsh, S. G. Yeager, D. E. Amrhein, and C. M. Little (2019), A Review of the Role of the Atlantic Meridional Overturning Circulation in Atlantic Multidecadal Variability and Associated Climate Impacts, *Reviews of Geophysics*, *57*(2), 316–375, doi:10.1029/2019RG000644.

Zhang, Y., J. M. Wallace, and D. S. Battisti (1997), ENSO-like Interdecadal Variability: 1900–93, *Journal of Climate*, *10*(5), 1004–1020, doi:10.1175/1520-0442(1997)010<1004:ELIV>2.0.CO;2.